Search for low-mass resonances in four-muon final state and generic heavy Higgs bosons in same-sign two-lepton final state with the ATLAS detector

Dissertation Submitted to

Tsinghua University

in partial fulfillment of the requirement

for the degree of

Doctor of Philosophy

in

Physics

by

Xu Yue

Dissertation Supervisor: Associate Professor Chen Xin

June, 2022

ABSTRACT

LHCb announced the discovery of new di-J/ψ resonances around 6.9 GeV in 2020, which can be seen as a $cc\bar{c}\bar{c}$ tetraquark. The final state of di-charmonium to four muons can significantly suppress backgrounds, which is also of great benefit to the search of new resonances and can also be used to search for rare decays of bottomonium η_b and χ_{b0}. A search for low mass resonances in the four-muon final state, using 139 fb^{-1} of pp collision data at $\sqrt{s} = 13$ TeV collected by the ATLAS detector, is also performed in both di-J/ψ and J/ψ+$\psi(2S)$ channels. Backgrounds are estimated using a data-driven method and method of control regions, and checked before opening the signal regions window by window. A peak with mass of 6.9 GeV is observed in the first signal region in the di-J/ψ channel, which is consistent with the $X(6900)$ observed by LHCb. An excess of data is also seen in the J/ψ+$\psi(2S)$ channel. A 95% confidence level upper limit on $\sigma(pp \to \eta_b/\chi_{b0} + X) \times \text{BR}(\eta_b/\chi_{b0} \to 2J/\psi)$ is set in the second signal region.

ATLAS and CMS experiment groups in LHC announced the discovery of the Higgs boson in 2012, which completes the last piece of the Standard Model (SM). The SM theoretical prediction is in good agreement with experimental results, but it's still incomplete. Thus, theorists build up various Beyond Standard Models (BSM), most of which contain at least one Higgs boson. Experimentalists have been searching for BSM heavy Higgs bosons in different final states. A search for model-independent heavy Higgs boson decaying into W/Z bosons is performed, including both phenomenological and experimental searches. The heavy Higgs boson has both dimension-four and dimension-six interactions with SM particles. The dimension-six operators can significantly enhance the Higgs boson momentum, and therefore suppress the SM background. In the associated VH (V = W, Z) production, the effect of dimension-six operators is largest and the signal sensitivity is highest. In the phenomenological search, three signal regions with at least two leptons in final states are studied. At the 95% confidence level (CL), the expected exclusion regions at three heavy Higgs boson mass points (300 GeV, 600 GeV and 900 GeV) are shown. The experimental search focuses on the final state containing two same-sign leptons ($W^{\pm}H \to \ell^{\pm}\nu\ell^{\pm}\nu jj$) in association with one large-R jet or two small-R jets with an invariant mass consistent with a hadronically decaying W boson, using 139 fb^{-1} of pp collision data at $\sqrt{s} = 13$ TeV collected by the ATLAS detector. The upper limits of $\sigma(pp \rightarrow VH) \times \mathrm{BR}(H \rightarrow VV)$ at the 95% CL are calculated as a function of the resonance mass and the upper limits on BSM HVV coupling modifiers are derived.

Keywords: LHC; ATLAS; Beyond Standard Model; Heavy Higgs boson; four muons

TABLE OF CONTENTS

LIST OF SYMBOLS AND ACRONYMS

ATLAS	A Toroidal LHC ApparatuS
BDT	Boosted Decision Tree
CERN	European Organization for Nuclear Research
CMS	Compact Muon Solenoid
CR	Control Region
ECAL	Electroweak Calorimeter
HCAL	Hadron Calorimeter
HL-LHC	High Luminosity LHC
HLT	High Level Trigger
LHC	Large Hadron Collider
LHCb	Large Hadron Collider beauty
MC	Monte Carlo
MSSM	Minimal Supersymmetric extended Standard Model
NF	Normalization Factor
NP	Nuisance Parameter
PDF	Parton Distribution Functions
PDG	Particle Data Group
Pixel	Pixel detector
PLV	Prompt Lepton Veto
QCD	Quantum Chromodynamics
QED	Quantum Electrodynamics
SCT	The SemiConductor Tracker
SM	Standard Model
SR	Signal Region
TRT	Transition Ratiation Tracker
VBF	Vector Boson Fusion
VH	Associated Production with Vector Boson
VR	Validation Region
2HDM	Two Higgs Doublet Model

CHAPTER 1 INTRODUCTION

From the discovery of the atom to the discovery of quarks, physicists are always interested in the question about "what does matter consist of". Particle physics is dedicated to studying the structure, properties and interactions of matter in the microworld. The Standard Model (SM) is the most fundamental and successful model describing three fundamental interactions and all the known elementary particles. In quantum field theory, Weak and electromagnetic interactions are defined in the electroweak theory (EW), while the quantum chromodynamics theory (QCD) defines the strong interaction which describes the interaction between quarks and gluons.

In 1964-1971, EW theory was developed. The introduction of the Higgs mechanism explains the origin of the mass of gauge bosons (W and Z). In 2012, ATLAS and CMS announced the discovery of the Higgs boson, completing the final piece of the SM. However, there are still many open questions that need to be answered through experimental and theoretical research, e.g. is the observed Higgs boson with mass of 125 GeV the SM one?

The SM is successful in both theory and experiment, but it still has some shortcomings. It can't explain the questions of neutrino mass, charge conjugation parity (CP) asymmetry, dark matter, and so on. To answer these questions, beyond Standard Models (BSM) have been defined. Many BSM contain more than one Higgs boson, such as Two Higgs Doublet Models (2HDM) and Minimal Supersymmetric Standard Model (MSSM). In these BSM, the properties of the lightest Higgs boson are similar with the SM one, and mass of the other Higgs bosons is between hundreds GeV and several TeV, within the detectable range of LHC.

The search for heavy Higgs bosons can not only verify the SM, but also help us understand the universe better. Since it's not very efficient to search for heavy Higgs bosons model by model, it's essential to search for heavy Higgs bosons model-independently. The heavy Higgs boson can have both dim-4 and dim-6 effective interactions with SM particles. The introduction of dim-6 operators can significantly enhance the momentum of heavy Higgs bosons and suppress SM backgrounds. For my first work I performed a phenomenology study of generic heavy Higgs bosons. Then, based on the phenomenology study, my second work is to use ATLAS Run2 data to search for generic heavy Higgs bosons.

In 1972-1974, QCD was developed. The quark model of conventional hadrons successfully describes mesons and baryons as being composed of two or three valence quarks. At the same time, theorists also predicted the existence of exotic hadrons with more than three quarks, whose properties would not fit the standard picture of the quark model. The study of exotic hadrons can provide a unique insight into the nature of strong interactions. In 2020, LHCb announced the observation of a narrow structure around 6.9 GeV in the di-J/ψ to 4μ spectrum, presumably a full-charm tetraquark (TQ). The confirmation from other experiments e.g. CMS and ATLAS, is important. My third work is to search for low mass resonances in the 4μ spectrum with ATLAS Run2 data.

CHAPTER 2 STANDARD MODEL AND BEYOND STANDARD MODEL

Particle physics aims at studying the fundamental structure and interactions of matter, based on the Quantum Field Theory (QFT). There are four fundamental interactions in nature(weak, electromagnetic, strong and gravitational interactions). The SM of particle physics describes three of the four fundamental interactions excluding gravity. This chapter's Section 2.1 introduces the SM and the corresponding interactions. Section 2.2 introduces some BSM briefly.

2.1 The Standard Model

The SM[1-2] is a complex theory, combining strong, electromagnetic and weak interactions, and including all the discovered fundamental particles. Its gauge group is $SU(3)_C \times SU(2)_L \times U(1)_Y$, corresponding to three interactions. It's developed from the late 20th century; in 1954, non-Abelian gauge field was proposed by Chen Ning Yang and Robert Mills to explain strong interaction[3]; in 1961, Sheldon Glashow contributed to the unification of the electromagnetic and weak interactions, known as electroweak theory[4-5]; in 1967, Abdus Salam and Steven Weinberg introduced the Higgs mechanism to electroweak theory; in the mid-1970s, strong interaction[6-7] developed quickly, thanks to the confirmation that hadron consists of quarks[8-9]. Whereafter, experimenters discovered W and Z bosons in 1983, top quark in 1995 and τ neutrino in 2000. In July 2012, the ATLAS and CMS experiments at CERN announced the discovery of a Higgs boson with a 125 GeV mass value which was confirmed as the SM one. So far, all the fundamental particles predicted by the SM have been discovered.

2.1.1 Fundamental particles

Matter is composed of atoms; the atom is composed of electrons and the nucleus; Protons and neutrons, known as nucleons, are the components of the nucleus. Electrons and nucleons are combined by electromagnetic interaction with the photon as force carrier. The proton and the neutron consist of quarks. According to spin property, fundamental particles can be classified into two types: fermion which has an odd half-integer (1/2, 3/2, 5/2...) spin and follows Fermi-Dirac statistics and boson which has an integer (0, 1, 2...)

spin and follows Bose-Einstein statistics. Each fundamental particle has an antiparticle with the same spin and mass, but different electric charge and color charge.

2.1.1.1 Fermion

In SM, there are 12 fermions with spin 1/2 and their corresponding antiparticles, including 6 quarks and 6 leptons. Both quarks and leptons can be divided into 3 generations as shown in Table 2.1.

Table 2.1 Three generations of leptons and quarks.

Lepton					
1st generation		2nd generation		3rd generation	
Name	Symbol	Name	Symbol	Name	Symbol
electron	e^-	muon	μ^-	tau	τ^-
electron neutrino	ν_e	muon neutrino	ν_μ	tau neutrino	ν_τ
Quarks					
up quark	u	charm quark	c	top quark	t
down quark	d	strange quark	s	bottom quark	b

Quarks have both electric charge and color charge, so they can join both electroweak interaction and strong interaction. Top quark is the heaviest quark with mass of 173 GeV with high precision. Due to color confinement, quarks are never found in isolation. They can combine to form hadrons, including mesons and baryons; mesons are usually composed of one quark and one antiquark; baryons are usually composed of three quarks; Proton and neutron are the lightest baryons.

Leptons don't undergo strong interactions, due to no color charge. Leptons can be further classified into electrically charged leptons and neutral leptons (known as neutrinos); electron, muon and tau are charged leptons with mass of 0.511 MeV, 105.7 MeV and 1.78 GeV; neutrinos (electron neutrino, muon neutrino and tau neutrino) are hard to be detected and very light whose masses are still unknown.

2.1.1.2 Gauge bosons

In the SM, fundamental interactions are mediated by force carriers (known as gauge bosons). Four known gauge bosons exist: gluon, photon, W boson and Z boson. They are all with a spin of 1.

Gluons carry color charge and act as exchange particles for the strong interaction between quarks. They bind quarks together to form hadrons. The photon is massless and mediates the electromagnetic interaction.

Z boson is neutral, labeled as Z^0, with mass around 91 GeV. W boson is charged, labeled as W^- (its antiparticle labeled as W^+), with mass around 80 GeV. Therefore, there are three force carriers for weak interaction (W^-, W^+ and Z^0) whose lifetimes are around 10^{-24} s.

The emission or absorption of a W boson can change a particle's electric charge or quark's type, such as the β^- decay process shown in Figure 2.1.

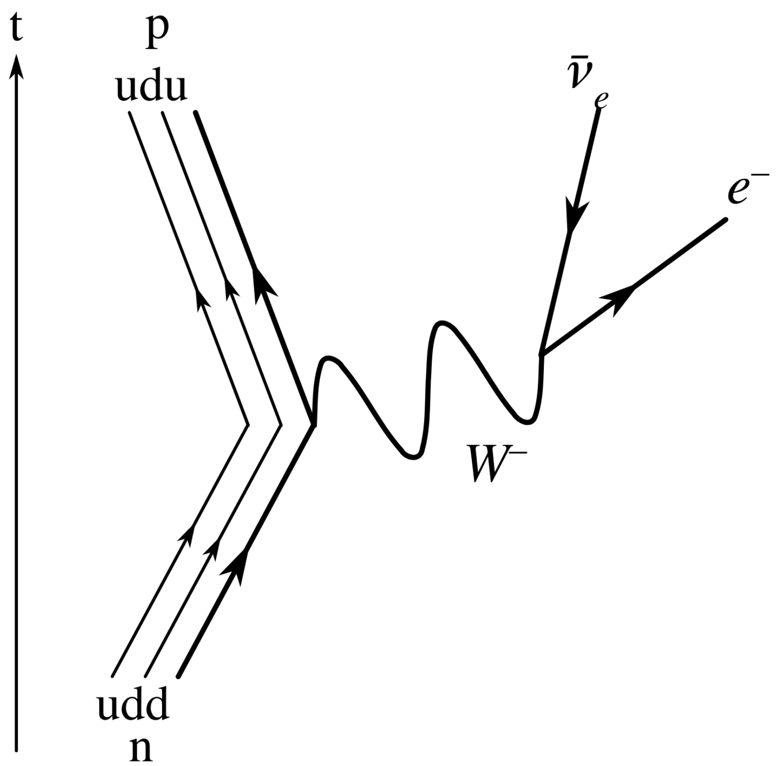

Figure 2.1 Feynman diagram for β^- decay.

Z boson can't change the charge of a particle, but it can change the spin, momentum and energy.

2.1.1.3 Higgs boson

The Higgs boson is the only scalar particle in the SM. It interacts with SM particles and gives them mass via the Higgs mechanism. In the LHC, the Higgs boson is mainly produced through gluon-gluon fusion (ggF), vector-boson fusion (VBF) and associated production with vector boson (VH) production channels. Figure 2.2 shows the Feynman diagrams for the three production channels.

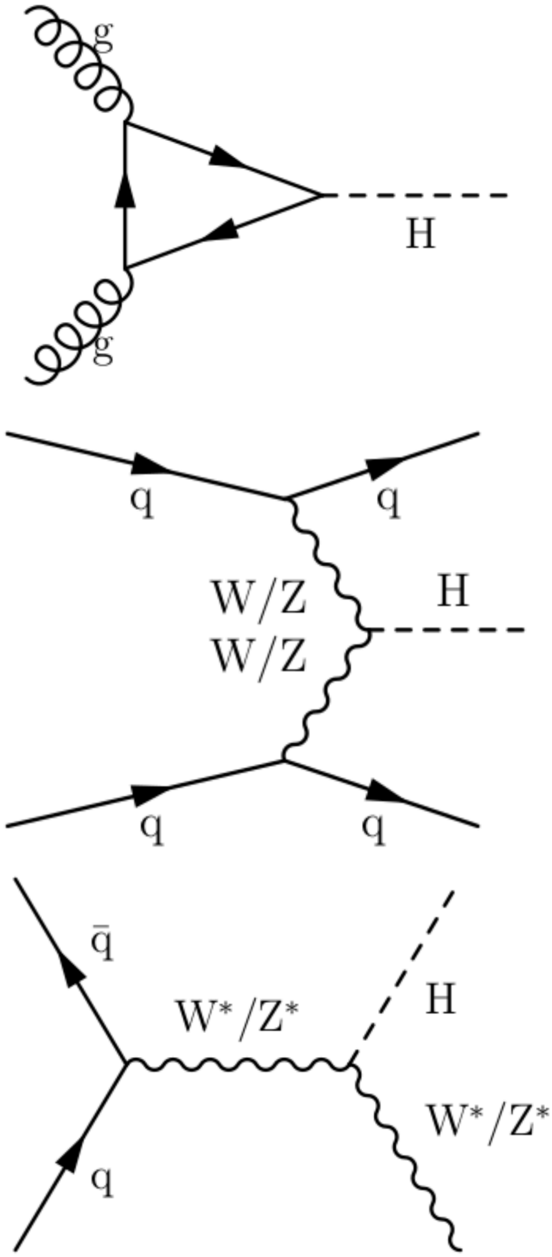

Figure 2.2 Feynman diagrams for main production channels of the Higgs boson: ggF(top), VBF(middle) and VH(bottom).

2.1.2 Interactions

The SM is a $SU(3)_C \times SU(2)_L \times U(1)_Y$ gauge field theory, including quantum chromodynamics (QCD) and electroWeak gauge theory (EW).

2.1.2.1 Quantum chromodynamics

QCD is the gauge field theory describing strong interactions of quarks and gluons, is the $SU(3)_C$ sector of the SM[10]. The QCD Lagrangian is given by:

$$\mathcal{L}_{QCD} = \sum_{Q} \bar{Q}(i\gamma^{\mu} D_{\mu} - m_Q)Q - \frac{1}{4} G^{a}_{\mu\nu} G^{a,\mu\nu}, \quad Q = d, u, s, c, b, t \quad a = 1...8 \tag{2.1}$$

where Q is the quark field but the color indices are not shown here. $D_{\mu} = \partial_{\mu} - i g_s G^{a}_{\mu} t^{a}$ is the covariant derivative and g_s is the coupling constant of strong interaction. $t^{a} = \lambda^{a}/2$ are the generators of $SU(3)_C$ group and correspond to 8 Gell-Mann matrices:

$$\begin{aligned}
\lambda_1 &= \begin{pmatrix} 0 & 1 & 0 \\ 1 & 0 & 0 \\ 0 & 0 & 0 \end{pmatrix}, \ \lambda_2 = \begin{pmatrix} 0 & -i & 0 \\ i & 0 & 0 \\ 0 & 0 & 0 \end{pmatrix}, \\
\lambda_3 &= \begin{pmatrix} 1 & 0 & 0 \\ 0 & -1 & 0 \\ 0 & 0 & 0 \end{pmatrix}, \ \lambda_4 = \begin{pmatrix} 0 & 0 & 1 \\ 0 & 0 & 0 \\ 1 & 0 & 0 \end{pmatrix}, \\
\lambda_5 &= \begin{pmatrix} 0 & 0 & -i \\ 0 & 0 & 0 \\ i & 0 & 0 \end{pmatrix}, \ \lambda_6 = \begin{pmatrix} 0 & 0 & 0 \\ 0 & 0 & 1 \\ 0 & 1 & 0 \end{pmatrix}, \\
\lambda_7 &= \begin{pmatrix} 0 & 0 & 0 \\ 0 & 0 & -i \\ 0 & i & 0 \end{pmatrix}, \ \lambda_8 = \frac{1}{\sqrt{3}} \begin{pmatrix} 1 & 0 & 0 \\ 0 & 1 & 0 \\ 0 & 0 & -2 \end{pmatrix}
\end{aligned} \tag{2.2}$$

The matrices satisfy the commutation relation:

$$[\frac{\lambda^a}{2}, \frac{\lambda^b}{2}] = i f^{abc} \frac{\lambda^c}{2} \tag{2.3}$$

where f^{abc} are the structure constants of SU(3) group, completely antisymmetric in the three indices.

$G^{a}_{\mu\nu}$ represents the gauge invariant gluon field strength tensor, given by:

$$G^{a}_{\mu\nu} \equiv \partial_{\mu} G^{a}_{\nu} - \partial_{\nu} G^{a}_{\mu} + g_s f^{abc} G^{b}_{\mu} G^{c}_{\nu} \tag{2.4}$$

2.1.2.2 Electroweak gauge theory

The EW theory describes the electroweak interactions in SM, based on the gauge group $SU(2)_L \times U(1)_Y$ [10]. The generators of $SU(2)_L$ and $U(1)_Y$ are weak isospin (T^a) and weak hypercharge (Y), satisfying the relation:

$$Q = T^3 + \frac{1}{2} Y \tag{2.5}$$

where Q is electric charge.

The gauge bosons mediating the electroweak interactions are three W bosons of weak isospin (W_μ^a $(a = 1, 2, 3)$) and B_μ boson of weak hypercharge. They both have spin 1 and their corresponding gauge coupling constants are g and g'.

Before spontaneous symmetry breaking of the electroweak symmetry, the gauge bosons are massless. However, the spontaneous symmetry breaking makes W_μ^3 and B_μ coalesce into A_μ and Z_μ, and makes W_μ^1 and W_μ^2 coalesce into $W_\mu^\pm$ as shown in Equation 2.6.

$$\begin{pmatrix} A_\mu \\ Z_\mu \end{pmatrix} = \begin{pmatrix} cos\theta_W & sin\theta_W \\ -sin\theta_W & cos\theta_W \end{pmatrix} \begin{pmatrix} B_\mu \\ W_\mu^3 \end{pmatrix}, \; sin\theta_W = \frac{g'}{\sqrt{g^2 + g'^2}} \tag{2.6}$$

$$W_\mu^\pm = (W_\mu^1 \mp i W_\mu^2)/\sqrt{2} \tag{2.7}$$

where θ_W is the weak mixing angle, also known as Weinberg angle. A_μ, Z_μ and $W_\mu^\pm$ correspond to photon, Z^0 and $W^\pm$ bosons, respectively.

To give gauge bosons and fermions mass, the Higgs scalar field is introduced. It is a complex doublet.

$$\Phi = \begin{pmatrix} \phi^+ \\ \phi^0 \end{pmatrix} \tag{2.8}$$

The corresponding gauge invariant Lagrangian is

$$\mathcal{L}_H = (D^\mu \Phi)^\dagger (D_\mu \Phi) - V_H(\Phi), \; V_H(\Phi) = -\mu^2 \Phi^\dagger \Phi + \lambda (\Phi^\dagger \Phi)^2 \tag{2.9}$$

where $D_\mu = \partial_\mu - igW_\mu^a T^a - i\frac{1}{2}g' B_\mu$, $T^a = \sigma^a/2$. $V_H(\Phi)$ represents the potential of the Higgs field.

The vacuum expectation value reads:

$$\langle \Phi \rangle = \frac{1}{\sqrt{2}} \begin{pmatrix} 0 \\ v \end{pmatrix}, \; v \approx 246 \text{ GeV} \tag{2.10}$$

When the Higgs boson gains a non-zero vacuum expectation value, the symmetry breaking becomes manifest. The Higgs field under unitary gauge reads:

$$\Phi(x) = \frac{1}{\sqrt{2}} \begin{pmatrix} 0 \\ v + H(x) \end{pmatrix} \tag{2.11}$$

where $H(x)$ is the real scalar field perturbation along the real axis of ϕ^0. Equation (2.9) is simplified as:

$$\begin{aligned}
\mathcal{L}_H &= \frac{1}{2}(\partial^\mu H)(\partial_\mu H) + m_W^2 W_\mu^+ W^{-,\mu} + \frac{1}{2} m_Z^2 Z_\mu Z^\mu \\
&+ \frac{2m_W^2}{v} H W_\mu^+ W^{-,\mu} + \frac{m_Z^2}{v} H Z_\mu Z^\mu \\
&+ \frac{m_W^2}{v^2} H^2 W_\mu^+ W^{-,\mu} + \frac{m_Z^2}{2v^2} H Z_\mu Z^\mu \\
&+ \frac{1}{4}\mu^2 v^2 - \frac{1}{2} m_H^2 H^2 - \frac{m_H^2}{2v} H^3 - \frac{m_H^2}{8v^2} H^4
\end{aligned} \tag{2.12}$$

where H is the Higgs boson with mass equal to $m_H \equiv \sqrt{2}\mu = \sqrt{\lambda}v$. m_Z and m_W represent the mass of Z^0 and $W^\pm$ bosons:

$$\begin{aligned}
m_W &\equiv \frac{1}{2} g v \\
m_Z &\equiv \frac{1}{2}\sqrt{g^2 + g'^2}\, v
\end{aligned} \tag{2.13}$$

The Higgs boson can interact with fermions. This interaction is known as Yukawa interaction whose Lagrangian is

$$\mathcal{L}_{Yukawa} = -\tilde{y}_d^{ij} \overline{Q}_{iL} d'_{jR} \Phi - y_{u_i} d_i \overline{Q}_{iL} u_{iR} \widetilde{\Phi} - y_{\ell_i} \overline{L}_{iL} \ell_{iR} \Phi + h.c., \; \widetilde{\Phi} \equiv i\sigma^2 \Phi^* \tag{2.14}$$

After symmetry breaking, the up like quarks (u, c, and t), down like quarks (d, s and b) and charged leptons can obtain mass ($m_{u_i} = y_{u_i} v/\sqrt{2}$, $m_{d_i} = y_{d_i} v/\sqrt{2}$ and $m_{\ell_i} = y_{\ell_i} v/\sqrt{2}$).

2.2 Beyond Standard Model

The SM is believed to be self-consistent in theory and greatly successful in experiment, predicting the existence of the Higgs boson and explaining most of the experimental results. However, it leaves some questions unsolved and only includes three of the four known fundamental interactions. Gravity, most related to our daily life, is not included in the SM. The question about dark matter and dark energy also can not be explained. In the model of the universe, dark energy composes 68% of the total energy and dark matter composes 27%, but the known matter only composes 5%.

For the known 5%, the SM can't explain the observed large CP asymmetry. In the SM, only weak interaction can lead to CP asymmetry, but it's not large enough to explain the observed phenomenon. New sources of CP violation are needed. Many BSM provide extra sources of CP violation, such as two Higgs doublet model (2HDM)[11] and minimal supersymmetric Standard Model (MSSM)[12]. And many of these BSM contain more than one Higgs boson. For example, 2HDM extends the Higgs field into two doublets, including five scalar particles:

1. CP-even neutral Higgs boson: h and H. H is heavier than h.
2. CP-odd pseudo-scalar particle A and two charged Higgs bosons $H^{\pm}$.

Theorists propose new models to explain the experimental phenomena inconsistent with the SM. Experimenters search for new physics or confirm the SM, and look for new particles based on these BSM predictions.

CHAPTER 3 PARTICLE DETECTOR

Physics is an experiment-based discipline. The ability of detecting particles and measuring their properties directly affects our progress in understanding nature. The LHC is the largest particle collider in the world, providing experimenters with a wealth of data to search for new particles and measure their properties. This chapter starts with the overview of the LHC in Section 3.1, and is followed by the introduction of ATLAS detector in Section 3.2.

3.1 The LHC

The European Organization for Nuclear Research, known as CERN was established in 1954, based in the northwest of Geneva. It has the world's largest particle physics experiment. Besides LHC, current active machines of CERN are:

1. The Linac 3 linear accelerator: generate low energy particles and inject ions into the Low Energy Ion Ring (LEIR).
2. The LEIR: accelerate ions from Linac 3.
3. The Proton Synchrotron Booster: increase the particles' energy before transferred to other accelerators.
4. The 28 GeV Proton Synchrotron (PS): CERN's first accelerator, built in 1954.
5. The Super Proton Synchrotron (SPS): a circular accelerator with a diameter of 2 kilometers. It delivers an energy of 450 GeV, and injects protons and heavy ions into the LHC.
6. The On-Line Isotope Mass Separator (ISOLDE): used to study unstable nuclei and produce radioactive ions.
7. The Antiproton Decelerator (AD): reduces the velocity of antiprotons and is used to search for antimatter.

The LHC[13], build by CERN during 1998-2008, is the world's largest particle collider with the highest energy, lying in a tunnel of 27 kilometers in circumference and as deep as 100 meters underground. The particle beam is firstly accelerated by linear accelerators, PS and SPS. Then, it is separated into two beams traveling in opposite directions and injected into the LHC. In 2009, two proton beams are collided successfully at the first time, with world's highest energy achieving 1.18 TeV per beam; in 2010, proton beams are accelerated to 3.5 TeV per beam, achieving the center-of-mass energy 7 TeV. in 2012, the center-of-mass energy was increased to 8 TeV. The data taking during 2009 and 2013 is called Run1. After Run1, LHC was shut down for a 2-years upgrade, during which the center-of-mass energy was increased to 13 TeV with bunch collisions every 25 ns. The data taking during 2015-2018 is called Run2. During 2018-2022 (the second long shutdown), the LHC was upgraded with 13.6 TeV collision energy. The new data taking started in April, 2022.

At the LHC, there are four major detectors: ATLAS[14], CMS[15], LHCb[16] and ALICE[17]. ATLAS and CMS are the two largest general-purpose detectors, which aim to search for the Higgs boson and new physics. LHCb is proposed to study physics related to bottom quark and CP violation. ALICE aims at the product of heavy ion collision, such quark-gluon plasma (QGP). Besides the four main detectors, there are also some small experiments, such as MoEDAL[18], TOTEM[19], FASER[20], and so on.

The data used in the thesis is from the proton-proton (pp) collisions collected with the ATLAS detector during Run2, with an integrated luminosity of 139 fb^{-1}.

3.2 The ATLAS detector

The ATLAS detector[14,21-22] is one of the two general-purpose detectors at the LHC. The 7000-tonne ATLAS detector, at 44 m long, 25 m high and 25 m wide, is the largest volume particle detector ever constructed. It investigates a wide range of physics, from the Higgs boson to extra dimensions and particles that could make up dark matter.

Figure 3.1 shows the overall layout of the ATLAS detector. It contains five sub-detectors from inside out: Inner Detector (ID), electromagnetic (EM) Calorimeter (ECal), Hadronic Calorimeter (HCal), Muon Spectrometer (MS), Forward Detectors (FD). The resolution and η coverage of each sub-detector are summarized in Table 3.1. The inner detector has the best resolution, but it only covers the range of $|\eta| < 2.5$. Calorimeters cover a wide range, but the resolutions are a bit worse.

3.2.1 The ATLAS coordinate system

The ATLAS coordinate system is a right-handed coordinate system with the z axis along the tunnel (beam direction), the x axis pointing towards the centre of the LHC ring, and the y axis pointing vertically upwards, as shown in Figure 3.2[23]. In the x-y plane, the polar coordinate (r, ϕ) is applied, where the azimuthal angle ϕ is measured from the

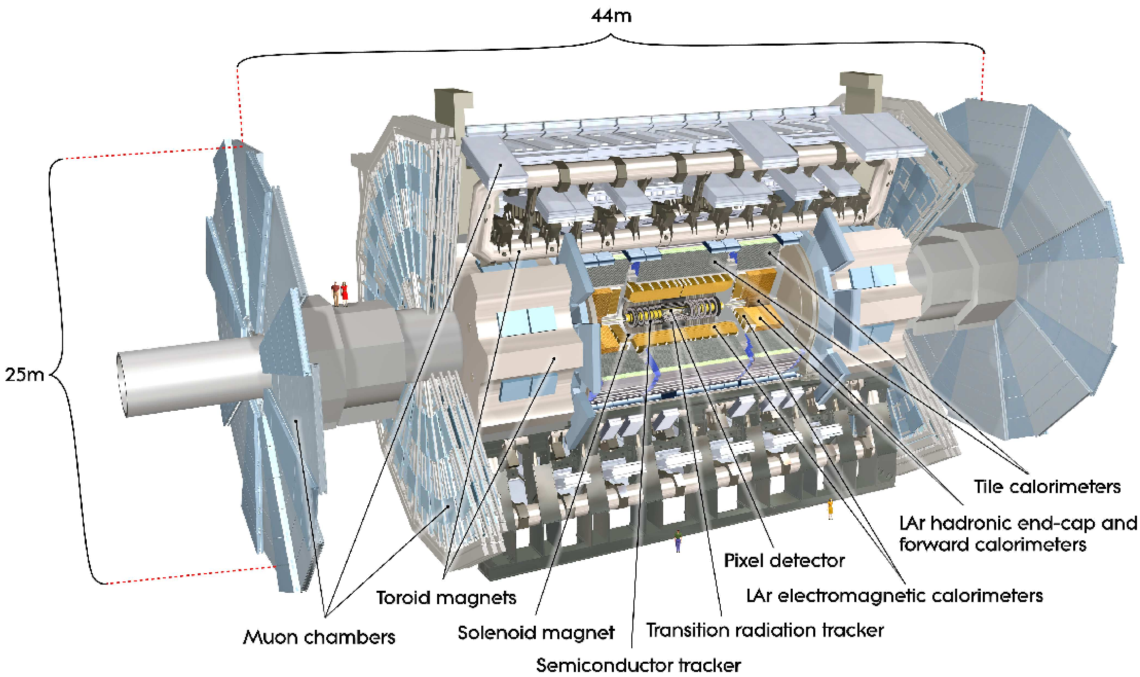

Figure 3.1 Cut-away view of the ATLAS detector[14].

Table 3.1 General performance goals of the ATLAS detector: resolution and coverage[14].

sub-detector	Required resolution	η coverage	
		Measurement	Trigger
ID	$\sigma_{p_T}/p_T = 0.05\% p_T \oplus 1\%$	±2.5	–
ECal	$\sigma_E/E = 10\%/\sqrt{E} \oplus 0.7\%$	±3.2	±2.5
HCal (barrel and end-cap)	$\sigma_E/E = 50\%/\sqrt{E} \oplus 3\%$	±3.2	±3.2
HCal (forward)	$\sigma_E/E = 100\%/\sqrt{E} \oplus 10\%$	$3.1 < \lvert\eta\rvert < 4.9$	$3.1 < \lvert\eta\rvert < 4.9$
MS	$\sigma_{p_T}/p_T = 10\%$ at $p_T = 1$ TeV	±2.7	±2.4

x axis. The pseudorapidity η is defined with θ measured from the positive z axis: $\eta = -ln\,tan(\theta/2)$. For massive objects, the rapidity y is defiend as $y = 0.5ln[(E+p_z)/(E-p_z)]$. The transverse momentum p_T, transverse energy E_T and transverse missing energy E_T^{miss} are the corresponding components in the x-y plane. The angular distance between two physics objects (ΔR) is defined as $\Delta R = \sqrt{\Delta\eta^2 + \Delta\phi^2}$.

3.2.2 The inner detector

There are approximately 1000 particles emerging from the collision point per 25 ns within $|\eta| < 2.5$, which causes a very high track density in the inner detector. To achieve the required momentum and energy resolution, the ID was installed in the ATLAS to precisely measure the trajectory and momentum of charged particles. It's immersed in a

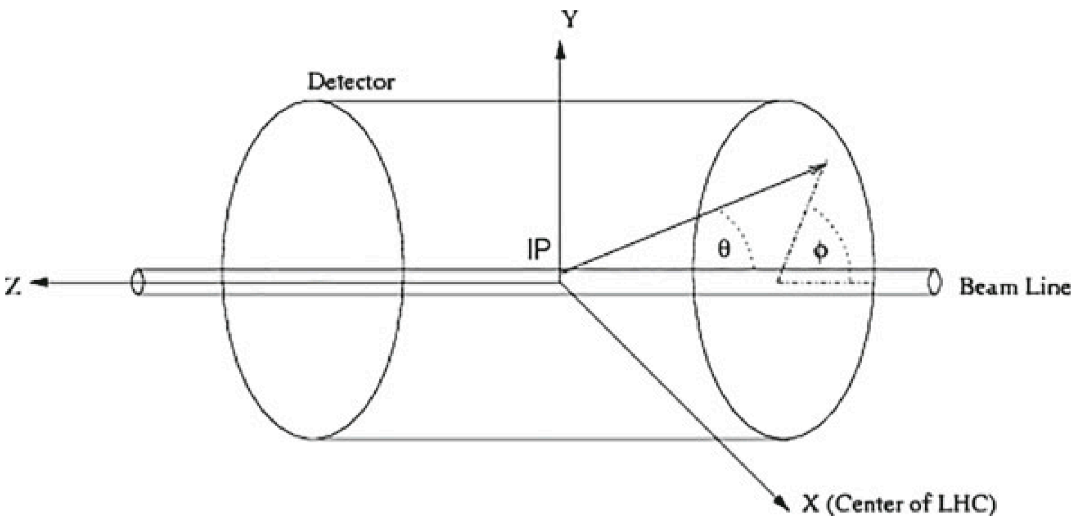

Figure 3.2 Illustration of the ATLAS coordinate system[23].

2T magnetic field, so the tracks of charged particles in the ID are curved. As the particles pass through the ID, they leave behind a series of hits due to the interaction of the charged particles with the ID material. Tracks can be reconstructed with these hits using softwares developed by ATLAS. Figure 3.3 shows the cut-away view of the ID, which consists of the pixel detectors (Pixels), the semiconductor tracker (SCT) and the transition radiation tracker (TRT).

The highest granularity is achieved using the silicon pixel detectors, which have four layers with many pixel sensors in each layer and have approximately 92 million readout channels. The innermost layer of the Pixels is the insertable B-Layer (IBL)[24]. Its pixel size is $50 \times 250\mu m^2$ ($R - \phi \ \times \ z$) and its intrinsic resolutions are $8\mu m$ ($R - \phi$) and $40\mu m$ (z). For the external layers, all pixel sensors have a minimum pixel size of $50 \times 400\mu m^2$ ($R - \phi \times z$) and intrinsic resolutions of $10\mu m$ ($R - \phi$) and $115\mu m$ (z). The SCT has eight strip layers with totally 6 million readout channels and its intrinsic resolutions are $17\mu m$ ($R - \phi$) and $580\mu m$ (z). The TRT is composed of 4 mm diameter drifts, but it can only provide information in the $R - \phi$ plane with accuracy of $130\mu m$. There are approximately 350,000 readout channels in the TRT.

3.2.3 Calorimetry

The cut-away view of the calorimeters is shown in Figure 3.4. Calorimeters cover the range of $|\eta| < 4.9$ and consider the detection requirements of different physical processes and the radiation environment of different regions. According to the type of interactions

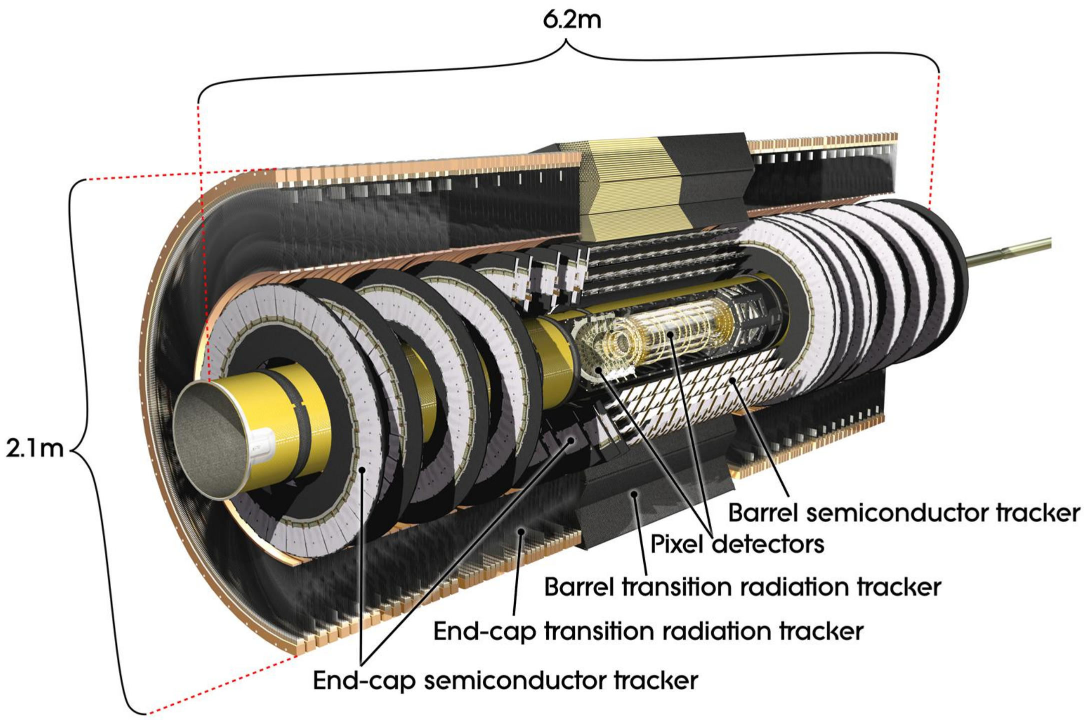

Figure 3.3 Cut-away view of the ATLAS inner detector[14].

between detector material and particles, calorimeters are classified into electromagnetic calorimeters and hadronic calorimeters.

3.2.3.1 Electromagnetic calorimeter

The EM calorimeter uses lead and liquid argon as absorbers which absorb electrons and photons via electromagnetic interactions. It's divided into a barrel part ($|\eta| < 1.475$) and two end-cap parts ($1.375 < |\eta| < 3.2$). The barrel calorimeter is 6.4 m long and 53 cm thick, and is composed of two identical half-barrels which are separated at $z = 0$ with a small gap of 4 mm. Each end-cap part consists of two coaxial wheels with outer wheel covering the region of $1.375 < |\eta| < 2.5$ and inner wheel covering the region of $2.5 < |\eta| < 3.2$. A presampler detector is located at the region of $|\eta| < 1.8$, used to correct the energy loss of electrons and photons, and composed of a liquid argon layer with 1.1 cm thick in the barrel region and 0.5 cm thick in the end-cap region.

3.2.3.2 Hadronic calorimeter

The hadronic calorimeters are used to absorb hadrons and measure their energy, consisting of three parts:

1. Tile calorimeter: it uses steel as the absorber and scintillator as the active material,

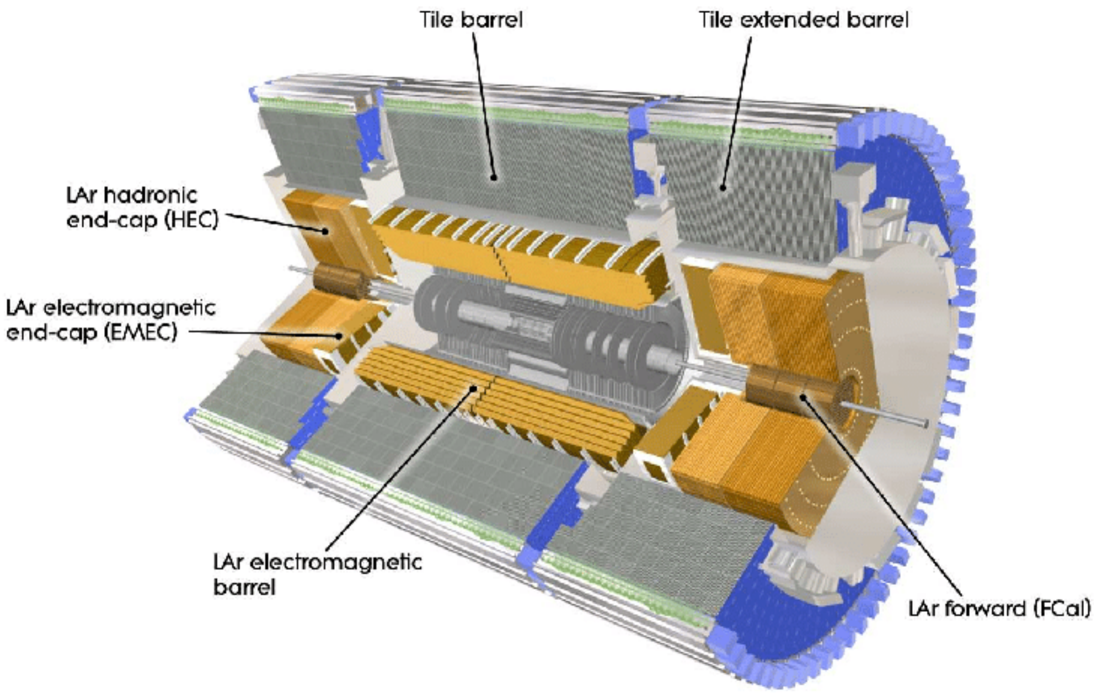

Figure 3.4 Cut-away view of the ATLAS calorimeter system[14].

consists of one barrel part ($|\eta| < 1.0$) and two extended barrel parts ($0.8 < |\eta| < 1.7$) and wraps around the barrel EM calorimeter with an inner radius of 2.28 m and an outer radius of 4.25 m.

2. LAr hadronic end-cap calorimeter: it covers the range of $1.5 < |\eta| < 3.2$, located right behind the end-cap EM calorimeter, and use copper as the absorber and liquid argon as the active material.
3. Forward calorimeter: it consists of three modules with the first one made of copper and the others made of tungsten. It extends the end-cap part, covers the region of $3.1 < |\eta| < 4.9$ and can reduce the radiation background in the muon spectrometer.

3.2.4 Muon spectrometer

The outermost sub-detector is the muon spectrometer, covering the region of $|\eta| < 2.7$. Muons are reconstructed based on the magnetic deflection of muon tracks in the high precision tracking chambers. The muon spectrometer consists of toroid magnets and four chambers, as shown in Figure 3.5.

The toroid magnets provide the magnetic field for the muon spectrometer, consisting of one large barrel toroid providing 1.5 to 5.5 Tm of bending power and two end-cap magnets providing 1 to 7.5 Tm of bending power.

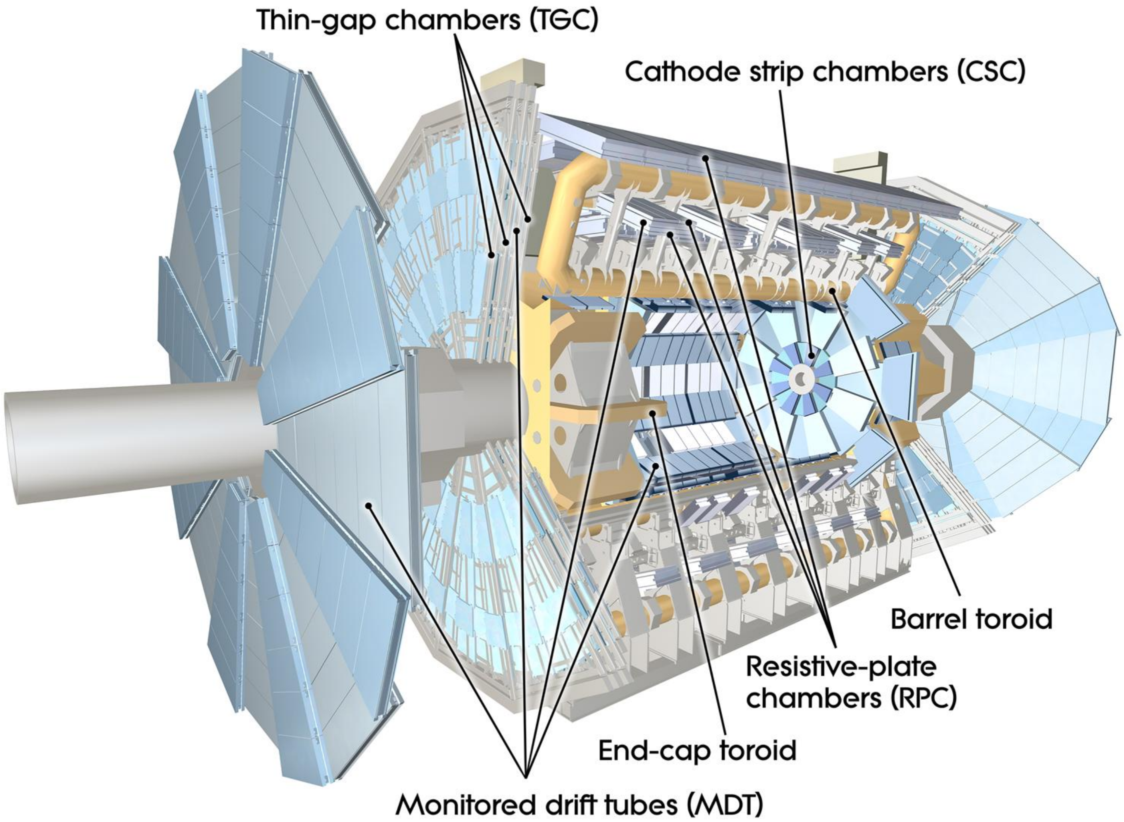

Figure 3.5 Cut-away view of the ATLAS muon system[14].

The four chambers are Monitored Drift Tubes (MDT), Cathode Strip Chambers (CSC), Resistive Plate Chambers (RPC) and Thin Gap Chambers (TGC); MDT covers the largest region ($|\eta| < 2.7$) and provides precision measurement of the track coordinates; CSC also measures the track coordinates, but it only covers the region of $2.0 < |\eta| < 2.7$; RPC and TGC are trigger chambers, covering the region of $|\eta| < 1.05$ and $1.05 < |\eta| < 2.7$, respectively, and provide bunch-crossing identification, well-defined p_T threshold and measurement of the muon coordinate.

3.2.5 Forward detectors

As shown in Figure 3.6, four smaller detectors cover the forward region of ATLAS[25-26]: the Luminosity measurement using Cerenkov Integrating Detector (LUCID), the ZeroDegree Calorimeter (ZDC), ATLAS Forward Proton Detector (AFP) and the Absolute Luminosity For ATLAS (ALFA).

LUCID and ALFA are used to measure the luminosity, located at ± 17 m and ± 240 m from the interaction point, respectively. LUCID is the first online relative-luminosity monitor of ATLAS and detects inelastic pp scattering in the forward region. ALFA con-

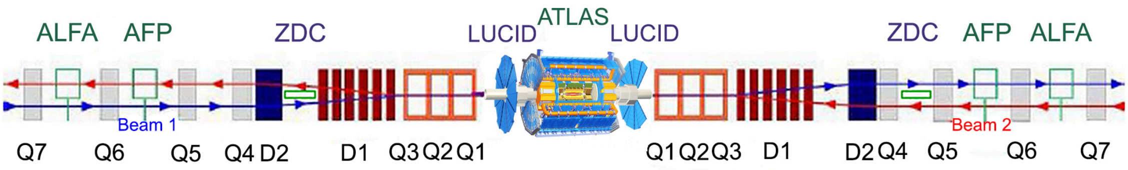

Figure 3.6 Illustration of the ATLAS forward detectors[27].s

sists of scintillating fiber trackers and determines the absolute luminosity via elastic scattering in small angles. ZDC located at ±140 m can measure neutral particles in the region of $|\eta| \geq 8.2$, playing an important role in measuring the centrality of heavy ion collisions. AFP is located at ±210 m, measuring the proton diffraction processes.

3.2.6 Trigger and data acquisition systems

The trigger and data acquisition (TDAQ) systems[28-29] are used to apply online selections and store event data. In Run2, due to the increasing of instantaneous luminosity and collision energy, the event rate is increased significantly. ATLAS upgraded the trigger system to reduce the rate to around 1 kHz. The upgraded system uses a two-stage trigger to select events: First Level Trigger (L1) based on hardware and High Level Trigger (HLT) based on software. The L1 trigger reduces the rate from the bunch crossing rate of 40 MHz to the detector maximum read-out rate of 100 kHz within $2.5\mu s$. Then, the HLT further reduces the rate to a physics output rate of 1 kHz within $200\mu s$.

3.2.7 Undering events and pile-up

Events not from the initial hard scattering all are called underlying events[30], whose momentum are usually low. Correctly simulating the underlying events is very important for understanding high momentum physics. Currently, due to the lack of understanding about parton density function (PDF), initial state radiation, final state radiation and multi-partonic interactions (MPI), the uncertainty of underlying events simulation at the LHC is large.

In each bunch-crossing, there may be multiple proton-proton collisions. The average number of collisions per bunch-crossing is called pile-up[31]. Figure 3.7 shows the pile-up distributions of ATLAS in Run2. The pile-up can be classified into two types: in-time pile-up and out-of-time pile-up. The former is the collisions happening in the same bunch-crossing as the hard scattering, while the latter is the collisions occurring in another bunch-crossing (before or after the hard scattering).

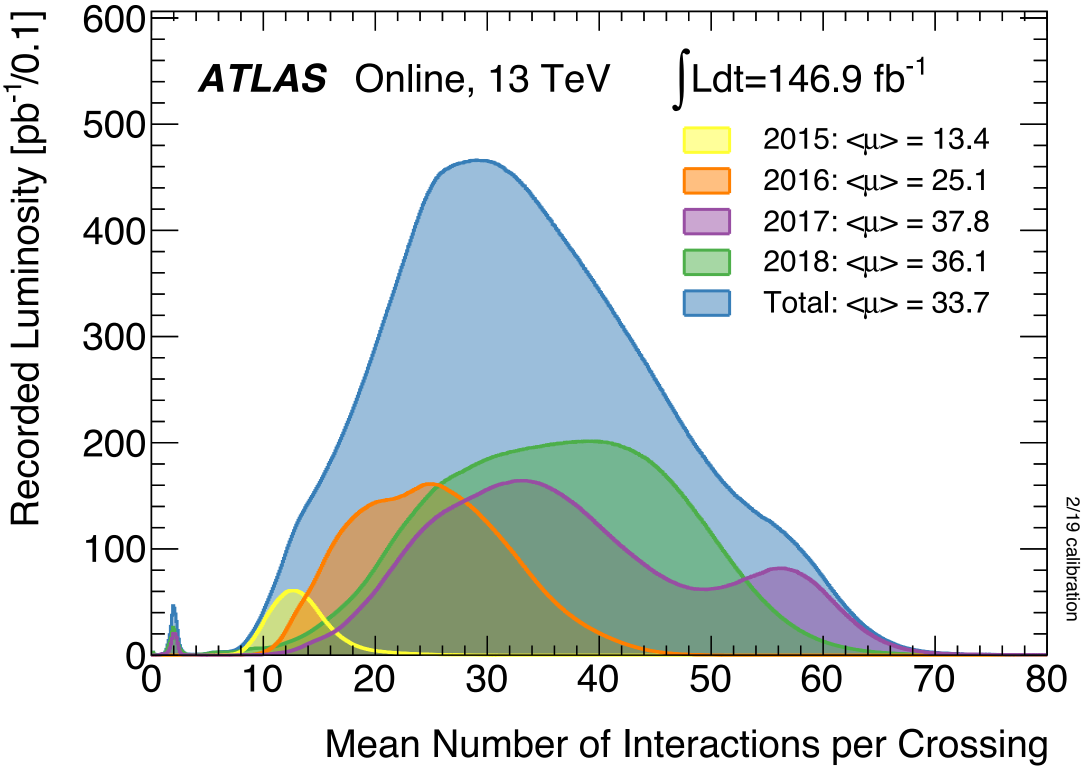

Figure 3.7 Mean number of interactions per crossing recorded by the ATLAS detector in Run2[32].

3.3 Monte Carlo simulation

Monte Carlo (MC) method is used to generate events to interpret the ATLAS data in the context of the SM or BSM. The softwares developed to generate events are known as generators, such as MadGraph5_aMC@NLO[33], Pythia[34], SHERPA[35] and POWHEG[36-37]. For precise prediction of the detector, the generated events are passed to dedicated frameworks for detector response simulation and object reconstruction. For all the simulated MC samples used in this thesis, the detector response is modeled with a detector simulation framework based on GEANT4[38]. The object reconstruction is based on the software, the same as the one used for data[39]. The effect of pileup is simulated by Pythia and included in all samples.

CHAPTER 4 OBJECT RECONSTRUCTION

At the detector level, we can only observe electrical signals from the interaction between particles and detector material. We need to use a large and modular suite of software tools to reconstruct physics objects, such as photons and electrons, with these electrical signals as input. The physics objects are used directly in physics analysis. The electrical signals from the inner detector are utilized to reconstruct the tracks and momentum of charged particles. The electromagnetic and hadronic calorimeters are for the energy reconstruction of electrons, photons and hadrons. With the muon spectrometer and the inner detector, muons can be reconstructed. ATLAS has also developed a series of identification methods for distinguishing prompt leptons (called “leptons” in this thesis) from non-prompt leptons. Prompt leptons originate from hard scattering or boson decays and are usually used in physics analysis. Non-prompt leptons come from the decay of hadronized quarks (known as jets) and misidentification of leptons. This chapter introduces the reconstruction of physics objects in ATLAS, mainly focusing on the reconstruction and identification of electrons, muons and jets.

4.1 Track and vertex

As charged particles pass through the inner detector, they interact with the detector material. The produced electrical signals can be used to reconstruct the track of each particle and thus the primary vertex. The reconstruction procedure is divided into three steps[14,40]:

1. Pre-processing: the electrical signals in Pixel and SCT are converted into clusters which are transferred into space points. The electrical signals from TRT are turned into drift circles.
2. Track finding: firstly, the space points from Pixel and SCT are combined into track seeds which are extended throughout the SCT, The track candidates are formed from these seeds. Secondly, track candidates are fitted with outlier clusters removed and ambiguities resolved, by applying track quality selections, such as the number of related clusters. The selected tracks are further extended to the TRT. Finally, the tracks are refitted with the total information of Pixel, SCT and TRT.
3. Post-processing: the primary vertex is reconstructed with a dedicated vertex finder

algorithm[41].

4.2 Electron and photon

The reconstruction of photon and electron relies on the inner detector and the EM calorimeter[42]. In the EM calorimeter, a seed cluster is reconstructed among all the clusters depositing EM energy and it finds a matching track from all the reconstructed tracks. In the inner detector, photon can convert into an electron and a positron. This type of photon is called the converted photon, and the others are called the unconverted photon. If the seed cluster is matched to a track which doesn't come from the converted photon, it's reconstructed as an electron. If the seed cluster is related to tracks from the converted photon, it's reconstructed as a converted photon. If there are no tracks matching to the seed cluster, it's reconstructed as an unconverted photon.

The reconstruction of electron clusters starts from the seed cluster. Clusters are formed around the seed cluster by expanding the cluster size in ϕ in the barrel region ($|\eta| < 1.37$) using window of size 5×7, or expanding the size in η in the end-cap region ($1.52 < |\eta| < 2.47$) using a window of size 5×5. In the transition region ($1.37 < |\eta| < 1.52$), both windows are used. The electron energy is obtained from the calibrated clusters and the ϕ and η directions are taken from the corresponding track.

To distinguish prompt electrons and non-prompt electrons, a likelihood-based identification is developed, with three working points (`Loose`, `Medium` and `Tight`)[43]. Figure 4.1 shows the efficiency of these three working points as a function of η and number of primary vertices. In the region of $\eta = 0$ and $1.37 < |\eta| < 1.52$, the efficiencies are low. Due to pile-up, the efficiencies decrease with the increasing number of primary vertices.

To further reduce the non-prompt background, electron isolation is defined which describes the activity level of other physics objects around the candidate in the region of $\Delta\eta \times \Delta\phi$. It is usually defined by summing the transverse energies of calorimeter clusters or the transverse energies of tracks, in a cone of radius $\Delta R = \sqrt{(\Delta\eta)^2 + (\Delta\phi)^2}$ around the candidate, with candidate itself excluded. Recently, a BDT-based isolation is developed, called prompt-lepton veto tagger (PLV)[44]. It has two working points: `Loose` and `Tight`. The PLV utilizes the information of the jet nearest to the candidate to identify non-prompt leptons. The selection requirement of PLV is in Equation (4.1) and the corresponding parameters are summarized in Table 4.1.

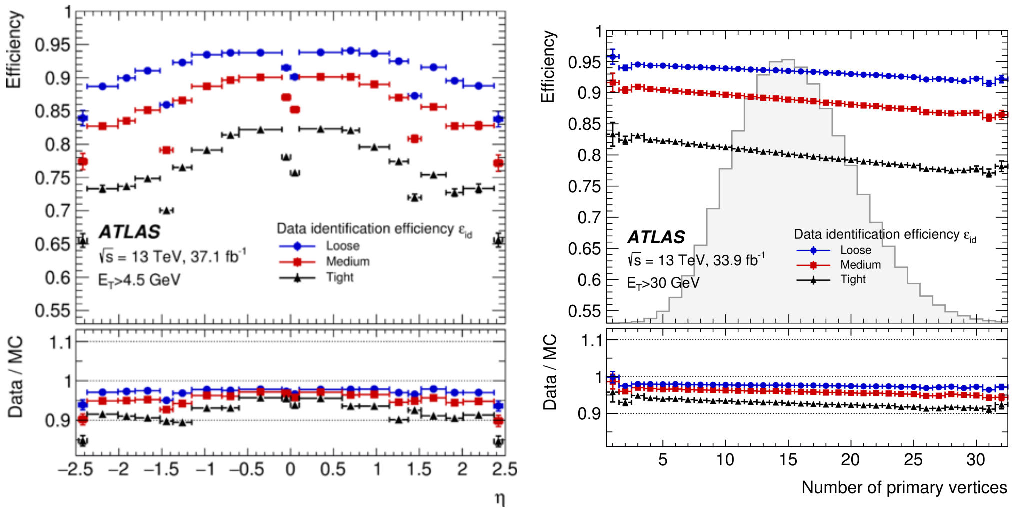

Figure 4.1 Electron identification efficiencies for `Loose`, `Medium` and `Tight` working points as a function of η (left) and number of primary vertices (right). The shaded histogram shows the distribution of the number of primary vertices for the 2016 data[43].

$$
\begin{aligned}
&\text{LowPtPLV} && < a' p_T^3 + b' p_T^2 + c' p_T + d' \quad (p_T < p_{T0}) \\
&\text{PLV} && < a p_T^3 + b p_T^2 + c p_T + d \quad (p_{T0} < p_T < p_{T1}) \\
&\text{PLV} && < max(-0.88, A + B e^{-\frac{p_T}{C}}) \quad (p_T > p_{T1})
\end{aligned}
\tag{4.1}
$$

In physics analysis, we need to selection suitable identification working point and isolation working point according to signal properties and main backgrounds.

4.3 Muon

A muon can leave hits in both the inner detector and muon spectrometer. The reconstruction of muons is, firstly, performed in the two detectors, respectively. The reconstruction in the muon spectrometer is similar to the inner detector. Next, the information in the two detectors are matched. There are five matching types[45]:

1. Stand-alone (SA) muons: only leave hits in the muon spectrometer.
2. Combined (CB) muons: reconstructed with a global refit using the hits from both the inner detector and muon spectrometer.
3. Segment-tagged (ST) muons: the track is reconstructed with the inner detector, and once extrapolated to the muon spectrometer, it's associated with at least one track segment in the muon spectrometer.
4. Calorimeter-tagged (CT) muons: the track is reconstructed with the inner detector and it can be matched to an energy deposit in the calorimeter compatible with a minimum-ionizing particle.

Table 4.1 Parameter values of PLV selection requirement shown in Equation (4.1).

		a'	b'	c'	d'
PLVLoose (e)		0.000345	−0.016259	0.243588	−1.133747
PLVTight (e)		0.000041	−0.002542	0.041502	0.152846
PLVLoose (μ)		0.000335	−0.014904	0.215737	−0.730525
PLVTight (μ)		0.000099	−0.004141	0.056019	0.207732
	p_{T0} [GeV]	a	b	c	d
PLVLoose (e)	12	0	−0.000106967	−0.0160896	0.960105
PLVTight (e)	12	0	−0.000722487	−0.0750674	1.13016
PLVLoose (μ)	12	−0.000186	0.0058481	−0.0788936	1.05942
PLVTight (μ)	12	0	−0.000992265	−0.0597252	0.998203
	p_{T1} [GeV]	A	B	C	
PLVLoose (e)	18.457	−0.94386	3.03257	28.0508	
PLVTight (e)	16.967	−0.881497	2.29469	11.5776	
PLVLoose (μ)	18.452	−0.958651	3.54785	19.6155	
PLVTight (μ)	18.703	−0.929774	2.9159	10.2339	

5. Extrapolated (ME) muons: the track is reconstructed with the muon spectrometer, satisfying loose compatibility requirement. They are mainly used to reconstruct muons in the region of $2.5 < |\eta| < 2.7$.

ATLAS provides three muon identification working points[45-46]:

1. `Loose` muons: maximize the reconstruction efficiency while providing good-quality muon tracks.
2. `Medium` muons: minimize the systematic uncertainties and commonly used in physics analysis.
3. `Tight` muons: maximize the purity of muons.

The efficiencies of three muon identification working points are shown in Figure 4.2. The `Loose` working point has the highest efficiency. At high p_T region, the efficiencies for prompt muons are almost flat.

Muons also have isolation working points as summarized in Table 4.1.

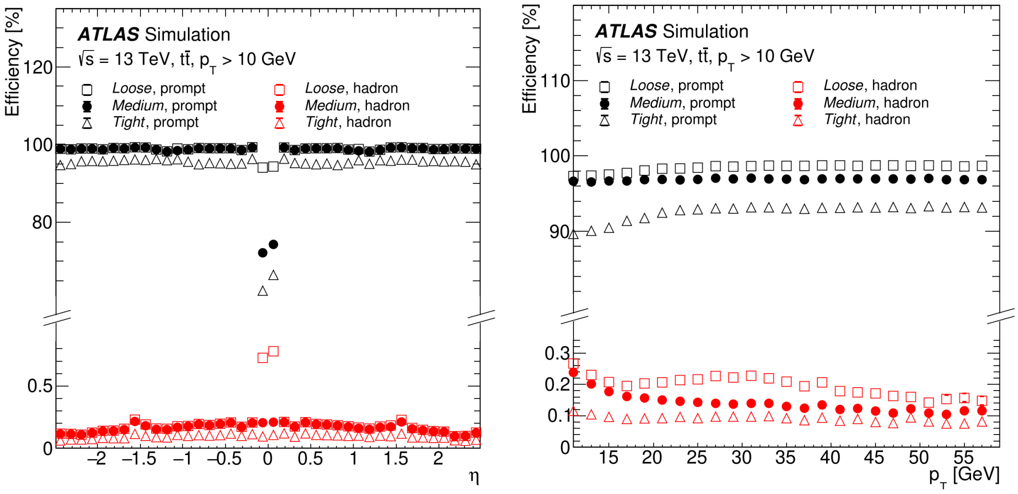

Figure 4.2 Muon identification efficiencies for `Loose`, `Medium` and `Tight` working points as a function of η (left) and p_T (right) for prompt muons and muons from light hadron decays, using simulated $t\bar{t}$ events[46].

4.4 Jet

4.4.1 Reconstruction method

Lots of quarks and gluons are produced in the high energy pp collision. Quarks are generated directly from collision or hadronic decays of particles, such as the Higgs boson and W/Z bosons. Due to the color confinement, quarks and gluons can not exist alone. After the production, they are hadronized to form jets immediately. In ATLAS, the charged particles in the jet can be measured by the inner detector just like other charged particles, and the neutral particles can interact with calorimeters to deposit energy. The jets can be reconstructed using topological clusters with anti-k_t algorithm[47]. It introduces distance d_{ij} between entities (particles, jets) i and j, and distance d_{iB} between entities i and the beam:

$$d_{ij} = min(k_{ti}^{2p}, k_{tj}^{2p})\frac{\Delta_{ij}^2}{R^2} \tag{4.2}$$

$$d_{iB} = k_{ti}^{2p} \tag{4.3}$$

where $\Delta_{ij}^2 = (y_i - y_j)^2 + (\phi_i - \phi_j)^2$, y and ϕ are the rapidity and azimuth, respectively. k_{ti} is the transverse momentum of particle i, and R is the radius parameter. p is a parameter used to goven the relative power of the energy versus geometrical scales and it's set to -1 in the anti-k_t algorithm. For k_t algorithm[48] and Cambridge/Aachen algorithm[49], p is set to 1 and 0, respectively. The anti-k_t algorithm utilizes information of entities to calculate d_{ij} and d_{iB} and compares their values. If d_{ij} is smaller, entities i and j are combined to form a new entity and the distances are re-calculated. If d_{iB} is smaller, the entity i is recognized as a jet. The above processes are repeated, until all the entities are reconstructed.

Due to the detector design, in the high energy region, the energy resolution of calorimeters is better than the momentum resolution of the inner detector, but in the low energy region, the momentum resolution of the inner detector is much better than the energy resolution of the calorimeter. And the inner detector has a better angular resolution. Therefore, using both information of the two detectors is optimal for the object reconstruction. The difficulty is how to avoid the reusing of the track momentum and the calorimeter energy. For this purpose, the particle flow algorithm[50] is developed to use both track and topological cluster information. It matches each track to a topological cluster and carefully removes the energy deposits from the tracks. The tracks and the corrected topological clusters are used as input to the anti-k_t algorithm to reconstruct jets. A jet energy scale (JES) correction is then applied to account for differences between data and MC simulations. The main JES uncertainties can be derived using a measurement of the calorimeter response to single hadrons, which is briefly introduced in Chapter 5.

In this thesis, two radius values are used, $R = 0.4$ and $R = 1.0$. $R = 0.4$ is used to reconstruct jets from single quark which is called small-R jet (j), while $R = 1.0$ is suitable for jets originating from hadronic decaying high-energy particles (such as the Higgs boson and W/Z bosons) which is called large-R jet (J)[51].

When reconstructing large-R jets, the sub-jets with $R = 0.2$ need to be reconstructed first. Then, they are used as input to reconstruct large-R jet. To reduce the effect of pile-up and underlying events, the trimming algorithm is applied which uses sub-jets as input and requires a minimum proportion ($f_{sub} = 0.05$) of sub-jet p_T.

4.4.2 b-jet tagger

Jets containing b-hadrons are called b-jets. The lifetime of b-hadron is about 1.5×10^{-12}s, so it has a long flight length and has at least one second vertex away from the primary vertex. The identification of b-jets against the large jet background is very important for many physics programmes, such as SM measurement, study of Higgs boson properties and search of new physics. ATLAS developed various algorithms to identify b-jets, referred to as b-tagging algorithms. To tag b-jet, there are two steps[52]; first, low-level b-tagging algorithms are used to reconstruct observables related to b-jet specific properties (impact parameter, second vertex and decay chain); second, results of low-level algorithm are combined as input of high-level algorithms (such as MV2c10 and DL1r). This thesis uses the DL1r b-tagger[53] which is based on the neural network.

4.4.3 W-boson tagger

With the high collision energy of LHC, it is important for searches of physics phenomena involving highly boosted massive particles, such as W and Z bosons, using dedicated tagging algorithms to improve identification efficiency. The algorithm aiming to identify the W boson is called W-boson tagger[54-55]. Due to the high W momentum, the decay products of W boson have basically the same direction as that of the parent particle and can be concentrated in a small area. They can be reconstructed with a large-R jet which has obvious substructure and is different from the jets originating from light quarks or gluons. Thesis uses LCTopo large-R jets whose input is LCW (Local hadronic Cell Weighting) calibrated topological clusters, so only the W-boson tagger based on LCTopo large-R jets is introduced. This W-boson tagger used the information of large-R jet mass (m_J), the jet substructure variables (D_2) and number of tracks ghost-associated to the jet (n_{trk}). Obviously, the m_J should be around 80 GeV. D_2 is defined by a set of energy correlation functions based on energies and pair-wise angles of the sub-constituents:

$$D_2 = E_{\mathrm{CF3}} \left(\frac{E_{\mathrm{CF1}}}{E_{\mathrm{CF2}}} \right)^3 \tag{4.4}$$

where the energy correlation functions (E_{CF}) are defined as:

$$E_{\mathrm{CF1}} = \sum_i p_{\mathrm{T},i} \tag{4.5}$$

$$E_{\mathrm{CF2}} = \sum_{ij} p_{\mathrm{T},i} p_{\mathrm{T},j} \Delta R_{ij} \tag{4.6}$$

$$E_{\mathrm{CF3}} = \sum_{ijk} p_{\mathrm{T},i} p_{\mathrm{T},j} p_{\mathrm{T},k} \Delta R_{ij} \Delta R_{jk} \Delta R_{ki}. \tag{4.7}$$

As can be seen, jets with real 2-prong substructure favor low D_2 while ones with single-prong (e.g. quark/gluon jets) or 3-prong (e.g. top jet) tend to have high D_2.

The use of n_{trk} is motivated by the fact that W bosons are color-singlet therefore the particle multiplicity is nearly constant over different p_T as opposed to quark or gluon jets where the multiplicity increases quickly against the jet p_T.

There are two working points for this W-boson tagger: smooth tagging 50% signal efficiency working point (50%WP) and smooth tagging 80% signal efficiency working point (80% WP).

The W tagger with 80% WP is considered in this thesis and the definition of the cuts is summarized in Equation (4.8) and Table 4.2. The background jet rejection and signal acceptance as a function of p_T are shown in Figure 4.3.

$$
\begin{aligned}
& f_{m,\text{low}} < m_J < f_{m,\text{high}} \\
& D_2 < f_{D2} \\
& n_{\text{trk}} \leq f_{n_{\text{trk}}}, \quad \text{where} \\
f_m(p_T) &= \sqrt{\left(\frac{a_m^0}{p_T} + a_m^1\right)^2 + (a_m^2 p_T + a_m^3)^2} \\
f_{D2}(p_T) &= b_{D2}^0 + b_{D2}^1 p_T + b_{D2}^2 p_T^2 + b_{D2}^3 p_T^3 \\
f_{n_{\text{trk}}}(p_T) &= c_{n_{\text{trk}}}^0 + e^{c_{n_{\text{trk}}}^1 p_T + c_{n_{\text{trk}}}^2}
\end{aligned} \tag{4.8}
$$

Table 4.2 Summary of coefficients of the W-tagging threshold functions defined in Equation (4.8).

	$a_{m,\text{low}}^0$	$a_{m,\text{low}}^1$	$a_{m,\text{low}}^2$	$a_{m,\text{low}}^3$
50%WP	-11.7489	63.4351	-23.9185	69.2862
80%WP	-11.0332	58.43021	-23.80421	63.7906
	$a_{m,\text{high}}^0$	$a_{m,\text{high}}^1$	$a_{m,\text{high}}^2$	$a_{m,\text{high}}^3$
50%WP	15.9377	-29.0870	4.92512	89.4082
80%WP	10.0101	22.5265	13.9768	81.1515
	b_{D2}^0	b_{D2}^1	b_{D2}^2	b_{D2}^3
50%WP	0.82475	1.55628	-0.77058	0.17714
80%WP	1.03877	2.16018	-1.35260	0.34697
	$c_{n_{\text{trk}}}^0$	$c_{n_{\text{trk}}}^1$	$c_{n_{\text{trk}}}^2$	
50%WP	25.8773	-0.31474	-3.94590	
80%WP	32.7780	-0.27049	-4.37904	

4.5 Missing E_T

Not all the particles can be detected by ATLAS. Those that hardly interact with detector materials, such as neutrinos and some new particles beyond the SM, can not be

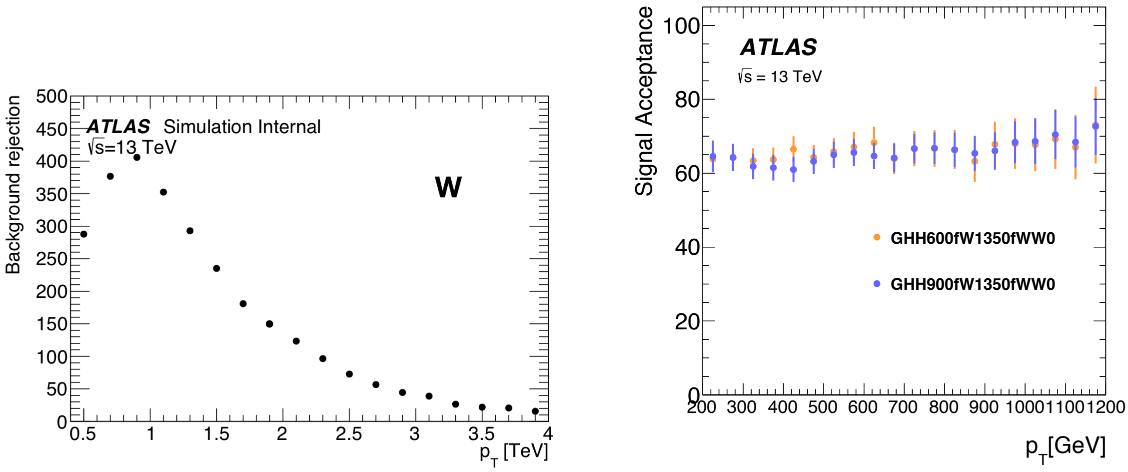

Figure 4.3 Background rejection by the W-tagging 80% efficiency working points as a function of large-R jet p_T (left). Rejection is defined as $1/\epsilon_{bkg}$ where ϵ_{bkg} is the background efficiency. Signal acceptance as a function of leading large-R jet p_T with two benchmark signal samples used in Section 8.2.2 (right) is retrieved after truth matching of truth W jets and leading large-R jet.

detected directly. The missing transverse momentum (E_T^{miss}) is an important observable measuring the transverse momentum carried by undetected particles. In the pp collision of the LHC, the transverse momentum of the proton is almost 0, so the initial total transverse momentum is close to 0. According to the conservation of transverse momentum, the reconstruction of the missing transverse momentum can be achieved using the information of all the detected particles in the final state. Since all sub-detectors are needed and it's strictly required that there is no overlap between the physical objects (a specific algorithm is required to remove overlaps), the reconstruction of the missing transverse momentum is challenging[56]. The reconstructed missing transverse momentum is characterized by two parts; the first one is from the hard objects (electrons, photons, τ-leptons, muons and jets); the second part is from the soft signals consisting of reconstructed tracks associated with the hard-scattering vertex but not with the hard objects. So the missing transverse momentum is expressed as:

$$E_T^{miss} = \sqrt{(E_x^{miss})^2 + (E_y^{miss})^2} \tag{4.9}$$

$$E_{x(y)}^{miss} = \underbrace{-\sum_{\text{electrons}} p_T^e - \sum_{\text{photons}} p_T^{\gamma} - \sum_{\tau} p_T^{\tau_{had}} - \sum_{\text{muons}} p_T^{\mu} - \sum_{\text{jets}} p_T^{jet}}_{\text{hard objects}} \underbrace{- \sum_{\text{unused tracks}} p_T^{track}}_{\text{soft signals}} \tag{4.10}$$

CHAPTER 5 E/P MEASUREMENT

The measurement of the calorimeter response to single charged hadrons provides an important validation of the modeling of hadronic showers in the calorimeters and of the detector geometry implemented in the ATLAS simulation. Such kind of measurement is known as E/p measurement. The calorimeter response to charged hadrons is studied using the ratio of the energy deposited by the isolated charged particle in the calorimeter which is grouped into topological clusters, E, to the momentum of its track, p, as measured by the ID. The ratio is denoted E/p, and the average ratio is denoted $< E/p >$. Since jet is reconstructed using topological clusters with EM scale clusters while hadronic decaying τ is reconstructed using topological clusters with local cluster weighting (LCW) scale, the E/p measurement with LCW scale clusters and with EM scale clusters are both studied in this chapter. EM and LCW scale are two topological cluster calibration schemes used in ATLAS[57-58]. For the EM scale, the EM component of energy deposits is used and it accounts correctly for the energy of photons and electrons. For the LCW scale, the lost energy in the clusters classified as hadronic is compensated. The LCW scale clusters are calibrated topological clusters consisting of three weights applied one after the other, hadronic response weight used for detector non-compensation correction, out of cluster weight correcting for energy lost out-of-cluster and dead material weight correcting for energy lost in dead material.

This chapter describes the E/p measurement using data with low average pile-up collected in 2017 at a center-of-mass energy of $\sqrt{s} = 13$ TeV, and MC events with single, double, and non diffractive. The minimum-bias track trigger is applied to the data. The total integrated luminosity is about $0.155 fb^{-1}$. For the MC events, the topological cluster seeding threshold is set at the nominal average pileup equal to 40.

5.1 Track selection

A loose-primary selection which can optimize the fake track rate is applied to the track[59]. The tracks selected for the measurement are required to have $p_T > 500$ MeV, as well as small longitudinal and transverse impact parameters $|z_0 \times \sin\theta| < 1.5$ mm and $|d_0| < 1.5$ mm with respect to the primary vertex. In order to get the isolated tracks, no other track extrapolated to the second longitudinal layer of the electromagnetic (EM) calorimeter is allowed within a cone of size $\Delta R = \sqrt{(\Delta\phi)^2 + (\Delta\eta)^2} < 0.4$ around the track of interest[60]. The track momentum considered in this chapter is within the range $0.5 < p/\text{GeV} < 30$.

5.2 E/p distributions

Figure 5.1 shows some E/p distributions from MC simulations and data. Due to the higher energy of LCW scale clusters, there is a larger fraction of tracks with a large E/p value in E/p distributions with LCW scale compared to E/p distributions with EM scale.

The large fraction of tracks with $E/p = 0$ corresponds to tracks without an associated topological cluster in the calorimeter. This can happen if either a particle interacts hadronically before reaching the calorimeter or no single energy deposit is large enough to seed a topological cluster[61]. The negative tail of these distributions is caused by noise in the calorimeter, which for data taking conditions with low $\langle\mu\rangle$ consists mostly of electronics noise, while the long positive tail is caused by the background of neutral particles, since these particles are added to the measured E but not to p.

Energy deposits from close-by neutral particles bias the calorimeter measurement of track energy, so neutral background subtraction is needed. Charged hadrons are selected that behave like minimum ionizing particles (MIP) in the EM calorimeter and start their shower in the hadronic calorimeter (late-showering hadrons). This kind of hadrons deposits most of their energy in the hadronic calorimeter in the cone of $\Delta R < 0.1$. Late-showering hadrons are selected by requiring a small amount of EM energy in a cone of $\Delta R < 0.1$ ($E^{0.1}_{\text{EM}} < 1.1$ GeV) and a large hadronic energy fraction ($E^{0.2}_{\text{HAD}}/E^{0.2} \geq 0.7$ GeV), and at least 20 TRT hits in the region $|\eta| < 2.0$ is required in order to suppress tracks from particles that undergo nuclear interactions before the calorimeter[60].

Fig. 5.2 shows some E/p distributions for MIP-like tracks with LCW scale and with EM scale. With the requirement of a large hadronic energy fraction, there is no track with $E/p = 0$ and negative tails in these distributions. The fraction of tracks with large E/p value in distributions with LCW scale is larger than the fraction of distributions with EM scale, since energy of the topological clusters with LCW scale is higher than the energy of topological clusters with EM scale.

The energy deposits in the EM calorimeter in the annulus of inner radius 0.1 and outer radius 0.2 are almost entirely from close-by neutral particles. A geometric factor of 4/3 is applied to estimate the energy deposits from the neutral-particle background in the

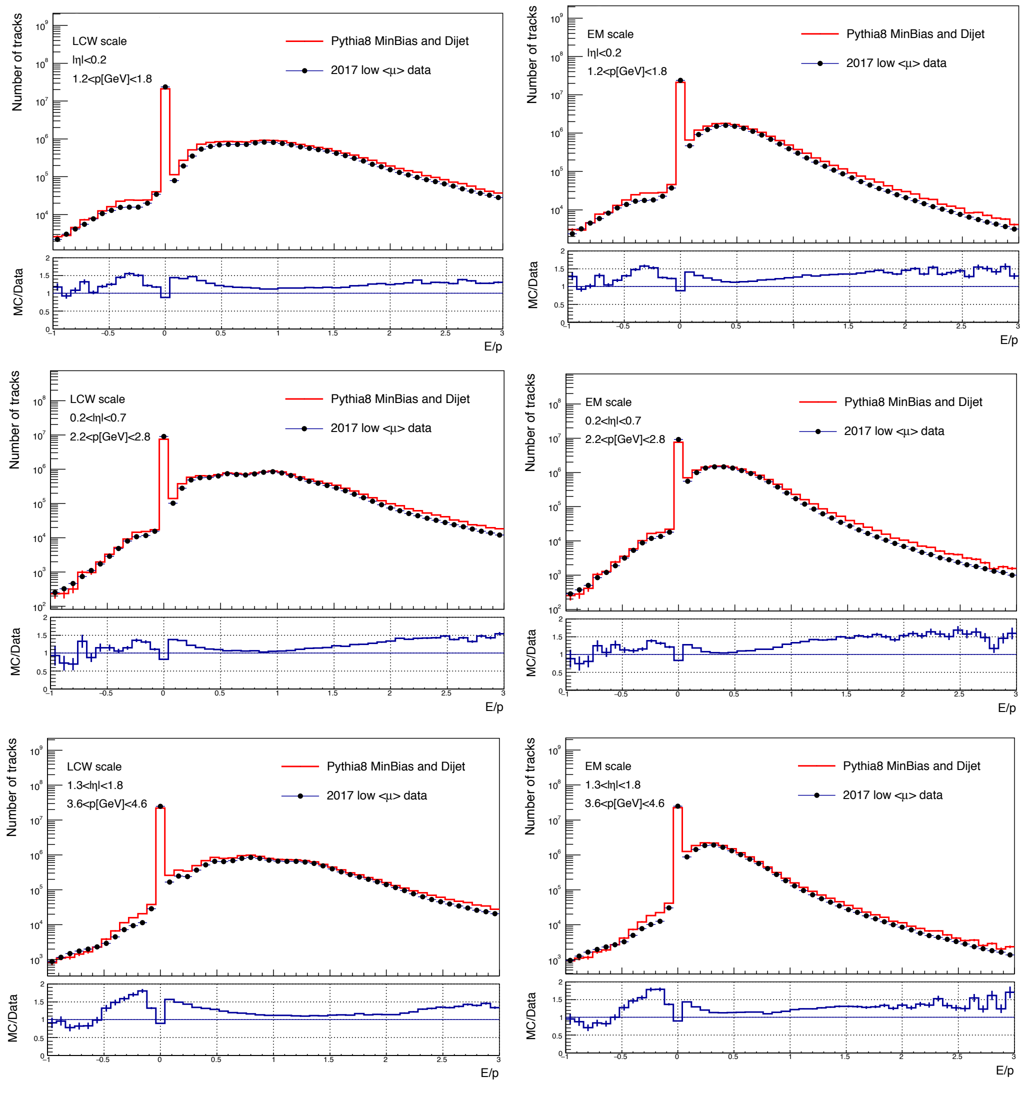

Figure 5.1 The E/p distributions with LCW scale (left) and EM scale (right) for isolated tracks with $|\eta| < 0.2$ and $1.2 < p/\text{GeV} < 1.8$, with $0.2 < |\eta| < 0.7$ and $2.2 < p/\text{GeV} < 2.8$, and with $1.3 < |\eta| < 1.8$ and $3.6 < p/\text{GeV} < 4.6$. The error bars represent statistical uncertainties.

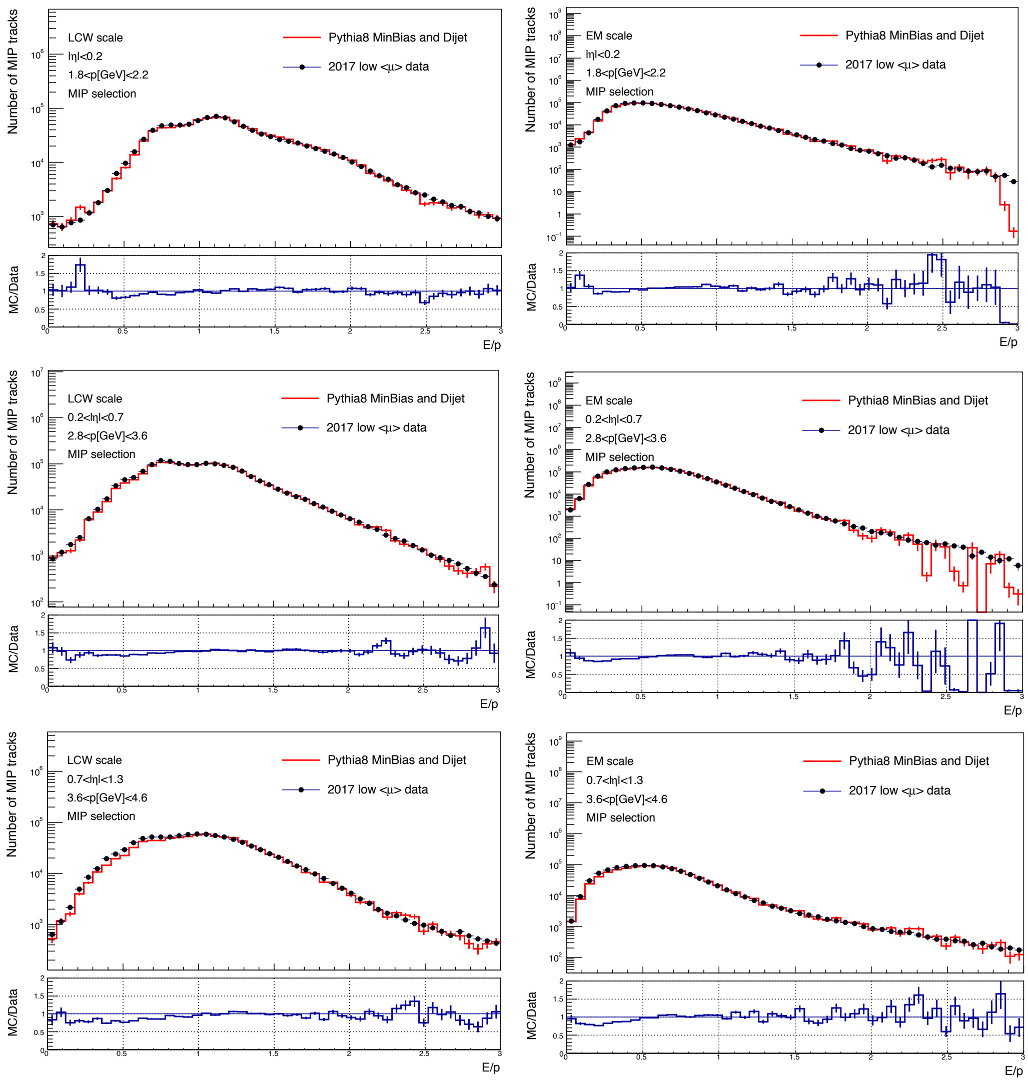

Figure 5.2 The E/p distributions for MIP-like tracks with LCW scale (left) and EM scale (right) for isolated MIP-like tracks with $|\eta| < 0.2$ and $1.8 < p/\text{GeV} < 2.2$, with $0.2 < |\eta| < 0.7$ and $2.8 < p/\text{GeV} < 3.6$, and with $0.7 < |\eta| < 1.3$ and $3.6 < p/\text{GeV} < 4.6$. The bottom portion of each panel shows the ratio of MC simulation to data. The error bars represent statistical uncertainties.

whole $\Delta R = 0.2$ cone. The energy deposits of close-by neutral particles can be estimated by the mean of the background distribution over many events in a given momentum and pseudo-rapidity bin:

$$< E/p >_{\mathrm{BG}} = \frac{4}{3} \times < \frac{E_{\mathrm{EM}}^{0.2} - E_{\mathrm{EM}}^{0.1}}{p} > \tag{5.1}$$

The corrected average response is[60]:

$$< E/p >_{\mathrm{COR}} = < E/p > - < E/p >_{\mathrm{BG}} \tag{5.2}$$

where $< E/p >$ is the mean value of the E/p distribution before background subtraction. This corrected response is the primary observable used in the studies.

Figure 5.3 shows the $< E/p >_{\mathrm{BG}}$ distributions as a function of the track momentum. The general shape of the background is well modeled by the simulations. But some discrepancies exist between the two at high track momentum, and there is an overall offset in the energy of the neutral background over the whole momentum range. The discrepancies may be caused by the overestimation of the simulation of the background at high track momentum in the central ($|\eta| < 0.2$) region of the detector. The overall offset means the MC predicts more energy of neutral background than what detected in data. That might have to do with the hadronization model in the event generator or with the Geant4 Physics List. Figure 5.4 shows the $< E/p >_{\mathrm{COR}}$ as a function of the track momentum. Due to the high seeding threshold, the influence from background energy deposits is very small. The $< E/p >_{\mathrm{COR}}$ in data and MC simulation are matched well except some discrepancies at the very low (p/GeV < 0.75) and high (p/GeV > 20) track momentum in the $0.7 < |\eta| < 1.3$ region of the detector. Comparing the $< E/p >_{\mathrm{BG}}$ and $< E/p >_{\mathrm{COR}}$ distributions with LCW scale and with EM scale separately, a higher $< E/p >_{\mathrm{BG}}$ and $< E/p >_{\mathrm{COR}}$ value is observed in distributions with LCW scale, due to a higher energy of clusters with LCW scale.

5.3 E/p uncertainties

Several assumptions are made in the measurement of the E/p corrections. Systematic uncertainties need to be considered and are estimated in the following.

5.3.1 E/p acceptance

The probability to find $E/p = 0$ is correlated to the amount of upstream material and influenced by the seeding threshold setting. Figure 5.5 shows the probability $P(E = 0)$

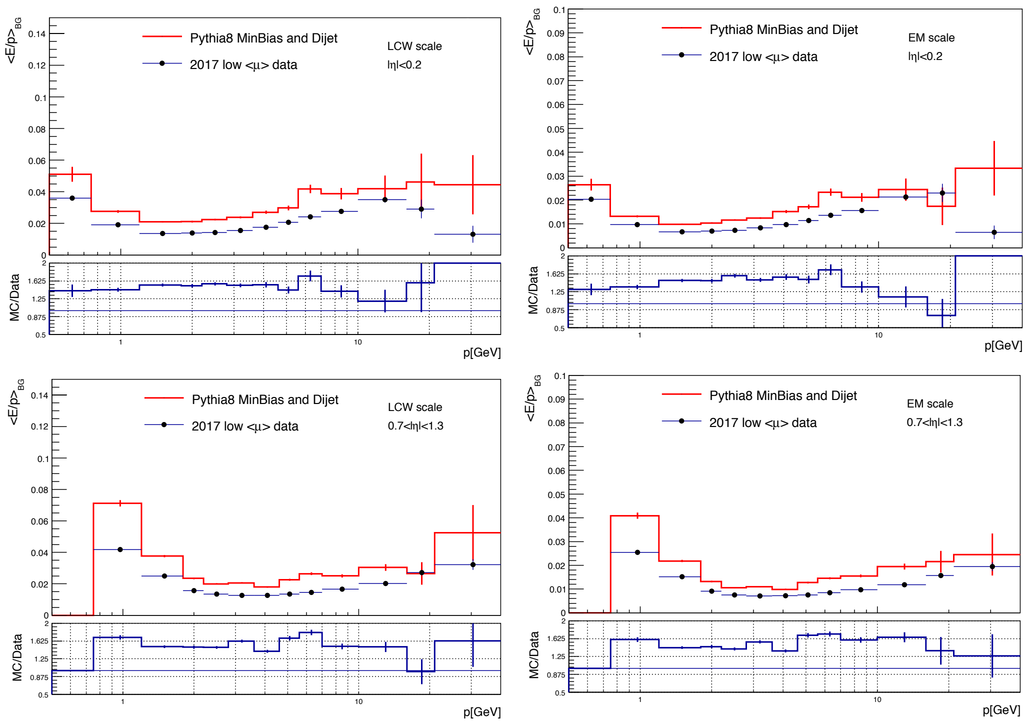

Figure 5.3 $< E/p >_{\mathrm{BG}}$ distributions as a function of the track momentum with LCW scale (left) and EM scale (right) for isolated MIP-like tracks with $|\eta| < 0.2$, and with $0.7 < |\eta| < 1.3$. The bottom portion of each panel shows the ratio of MC simulation to data. The error bars represent statistical uncertainties.

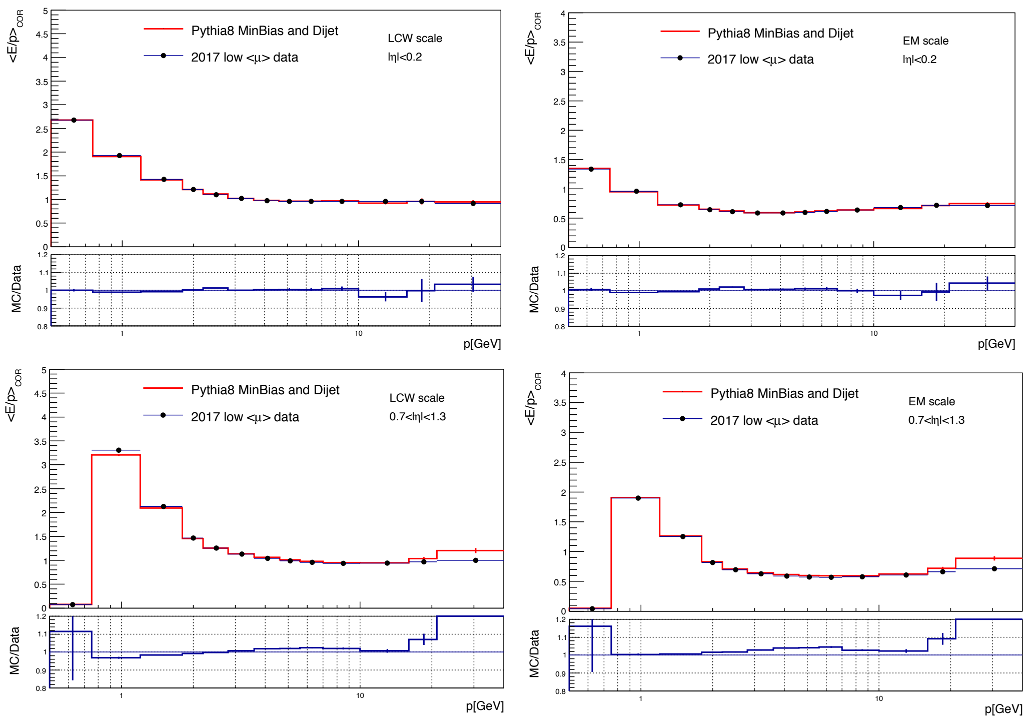

Figure 5.4 The $< E/p >_{\mathrm{COR}}$ as a function of the track momentum with LCW scale and EM scale for isolated MIP-like tracks with $|\eta| < 0.2$, and with $0.7 < |\eta| < 1.3$. The bottom portion of each panel shows the ratio of MC simulation to data. The error bars represent statistical uncertainties.

decreases when track momentum increases in the central calorimeter region, since the dead material in front of the calorimeter is approximately constant. Compared to the $P(E = 0)$ measured with 2009 data [61], the $P(E = 0)$ is much higher because of a higher seeding threshold setting. The data and MC simulation aren't matched well. The correlated uncertainty is derived from the maximal observed difference between data and MC simulation in the probability $P(E = 0)$. The uncertainty can reach 22% for p/GeV < 3 and increase to 34% for p/GeV > 3.

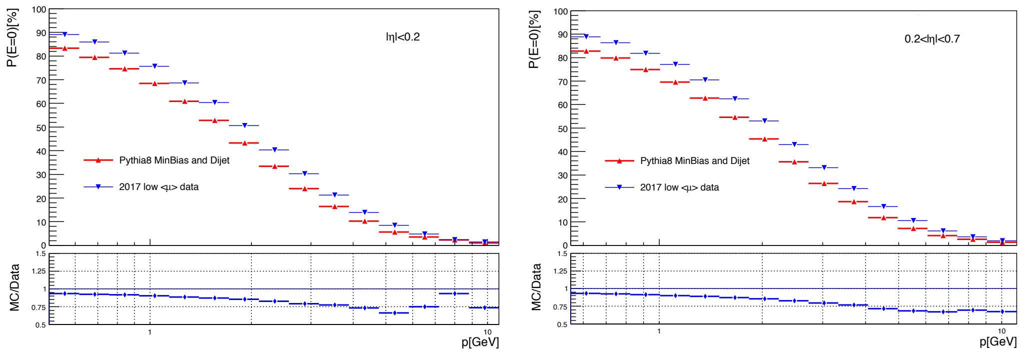

Figure 5.5 The probability to find a calorimeter response consistent with zero P(E = 0) as a function of track momentum p for $|\eta| < 0.2$ and $0.2 < |\eta| < 0.7$. The error bars represent statistical uncertainties.

5.3.2 Topological clustering effect

The energy collected in the topological clusters may be different from the energy released in the calorimeter, depending on how isolated the energy deposits are. This kind of uncertainty can be computed by comparing the results of the $< E/p >_{COR}$ measurement with topological clusters to the results obtained by re-calculating the measurement with all calorimeter cells in a cone of $\Delta R < 0.2$.

The ratio of MC/data of cluster response to MC/data of cell response is used to obtain the uncertainty. Figure 5.6 shows the relevant results calculated with LCW clusters and EM clusters in the central calorimeter region. The measured $< E/p_{\text{cluster}}/E/p_{\text{cell}} >$ value of topological clusters with LCW scale is apparently higher. In the central calorimeter region, the discrepancy between cluster response and cell response is about 2% at low p with LCW scale and is around 3% with EM scale at low p, while a discrepancy of 5% is obtained using 2010 data [61].

5.3.3 Validation of the background subtraction

A different background subtraction procedure is developed to validate the nominal background estimation method.

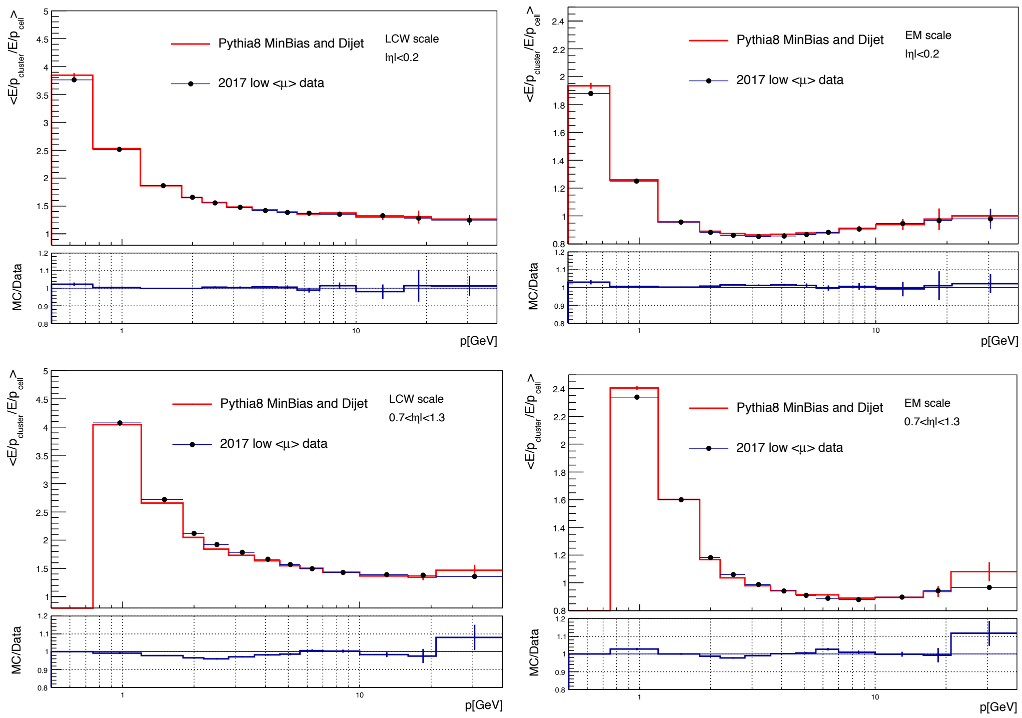

Figure 5.6 The ratio of $< E/p >_{\mathrm{COR}}$ measurement of topological clusters with LCW scale (left) and EM scale (right) to that with all calorimeter cells with $|\eta| < 0.2$ and $0.7 < |\eta| < 1.3$. The error bars represent statistical uncertainties.

In the validation method, the background is still measured with late showering hadrons. However, the energy of background is estimated by linearly extrapolating the energy density of background in a small annuli between a cone of radius 0.1 and 0.2 to the cone of $\Delta R < 0.1$. The energy density ρ_i for a small annulus of inner radius $R_i = i \times 0.025$ and outer radius $R_{i+1} = (i+1) \times 0.025$ is expressed as[60]:

$$\rho_i = \frac{E_{i+1} - E_i}{A_{i+1} - A_i}, \tag{5.3}$$

where $A_i = \pi R_i^2$.

As shown in Figure 5.7, the background energy density is approximately constant in the cone of $R \leq 0.2$, being consistent with the assumption of constant background energy density used in the nominal method .

In the validation method, the background estimation is calculated by fitting the background energy density with a linear function between $R_i = 0.1$ and $R_i = 0.2$ and integrating the function between $R_i = 0.1$ and $R_i = 0.2$:

$$f(R_i) = a + bR_i \tag{5.4}$$

The estimation of background with nominal method and the estimation with validation method are shown in Figure 5.7. The obtained background estimation with LCW scale gives a total of 1.1% (5.0%) more background with respect to the nominal background subtraction method for MC simulation (data), while the obtained background estimation with EM scale gives a total of 4.2% (6.9%) more background with respect to the nominal background subtraction method for MC simulation (data).

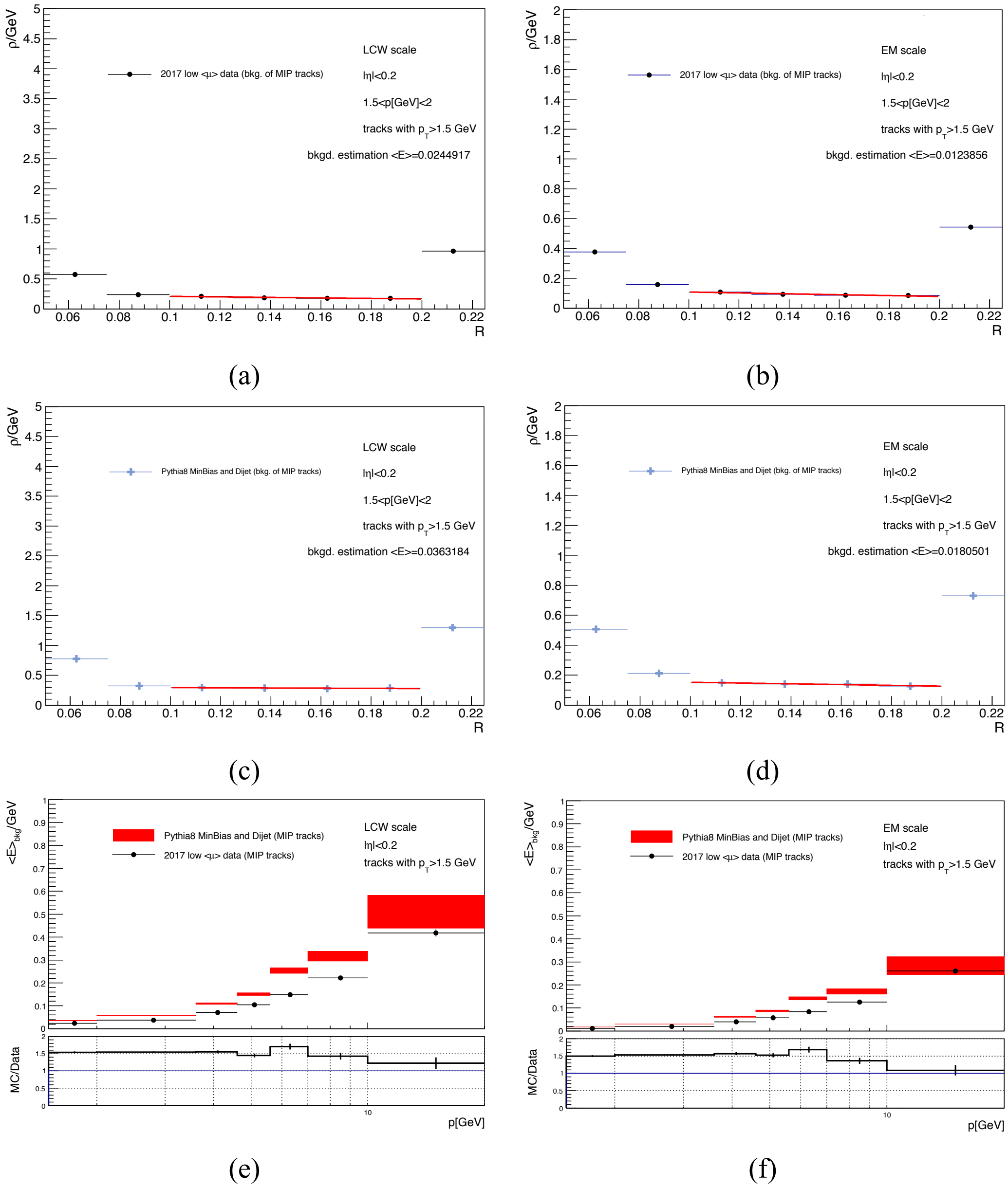

Figure 5.7 The background energy density fitted with a linear function (red line) between R_i = 0.1 and R_i = 0.2 in $|\eta| < 0.2$ for tracks with $1.5 < p/\text{GeV} < 2$, with LCW scale (left) and EM scale (right) for data ((a) and (b)) and MC simulation ((c) and (d)). Background estimation with nominal method, (e) LCW scale, the estimated background is $0.0359097 \pm 0.000588591$ ($0.0233328 \pm 0.0001115054$) for tracks with $1.5 < p/\text{GeV} < 2$ for MC simulation (data). (f) EM scale, the estimated background is $0.0173264 \pm 0.000315096$ ($0.0115826 \pm 0.000060702$) for tracks with $1.5 < p/\text{GeV} < 2$ for MC simulation (data). The error bars represent statistical uncertainties.

CHAPTER 6 EXPERIMENT: LOW MASS RESONANCES

The purpose of this chapter is to introduce the analysis that is aimed at searching for low-mass resonances in the four-muon final state[62]. The low-mass resonances can be new exotic hadrons or known bottomonia such as η_b and χ_{b0}. The search of new structures in the di-J/ψ and $J/\psi + \psi(2S)$ channel is presented in this chapter and the search of $\eta_b/\chi_{b0} \to J/\psi J/\psi$ decay is also introduced.

6.1 Motivation

The quark model of conventional hadrons successfully describes mesons and baryons as being composed of two or three valence quarks. At the same time, theorists also predicted the existence of exotic hadrons with more than three quarks, such as the tetraquark (TQ) containing four quarks, whose properties would not fit the standard picture of the quark model. The study of exotic hadrons can provide a unique insight into the nature of strong interaction[63]. In 2003, the first exotic hadron $X(3872)$ was discovered by the Belle experiment, which is a tetraquark candidate[64]. A series of further candidates was discovered successively, designated as “X”, “Y” and “Z” states. Most of the observed exotic hadrons contain up to two charm or bottom quarks. Some phenomenology models based on QCD predict the existence of full-heavy tetraquark $T_{Q_1Q_2\bar{Q}_3\bar{Q}_4}$, where Q_i represents charm or bottom quark[65-66]. The advantage of fully-heavy tetraquarks is the non-relativistic treatments which largely simplify the calculations, and make theory-experiment comparison easier. Such calculations include lattice QCD, QCD sum rules and potential models. In 2020, LHCb experiment claimed evidence for a narrow resonance $X(6900)$ in the di-J/ψ to 4 muons channel, presumably coming from a full-charm tetraquark with $cc\bar{c}\bar{c}$[67]. If there is narrow resonance in the di-J/ψ channel, a structure in the $J/\psi + \psi(2S)$ channel is also possible. For a deeper understanding of the structure, analyses from other experiments are needed.

The final state with four muons is clean with small contributions from SM background. So it’s also a golden channel to search for the rare decay of bottomonia η_b and χ_{b0} ($\eta_b/\chi_{b0} \to J/\psi J/\psi$). η_b and χ_{b0} was detected in the radiation decays of $\Upsilon(3S)$ and $\Upsilon(2S)$, and many studies have been done on their decay modes[68-70]. However, $\eta_b/\chi_{b0} \to J/\psi J/\psi$ decay channel hasn’t been observed yet.

6.2 Data and Monte Carlo samples

The data used in this analysis were collected by the ATLAS detector at the LHC pp collisions in Run2 with a center-of-mass energy of $\sqrt{s} = 13$ TeV, corresponding to an integrated luminosity of 139 fb^{-1}.

MC simulated events are used to understand the detector performance for signals and backgrounds. For all the signal and background MC samples, Pythia 8.244 is used for parton shower and hadronization with A14 parameter set[71] and NNPDF23LO PDF[72]. PHOTOS 3.61[73] is applied to simulate the final state radiation in the decays. The signal and background samples used in this analysis are summarized in Table 6.1.

The signal events are generated by JHU event generator[74] with CTEQ6L1 PDF[75], assuming it's a spin zero and CP even resonance with a natural width of 100 MeV. Background samples are generated with Pythia 8.244, including processes of the single parton scattering (SPS), double parton scattering (DPS) and heavy flavor pair. In the SPS process, the two J/ψ mesons are produced in a single parton-parton interaction, while in the DPS process, the two J/ψ mesons are produced in two parton-parton interactions of a single pp collision, separately. Events from heavy flavor pair processes contain at least 4 muons from the decays of a pair of B mesons. The heavy flavor background is referred to as the non-prompt background. The muons from DPS and heavy flavor processes usually have small p_T and fail the trigger thresholds. To improve the generation efficiency, a cut on the phase space parameter (Pythia) is applied on the DPS and heavy flavor events with the principle that the cut doesn't introduce any bias with respect to the analysis cuts listed in Table 6.5.

Table 6.1 Summary of background and signal MC samples used in this analysis.

Di-charmonium Process	Generator	PDF	Parton shower	Process
SPS	Pythia 8.244	NNPDF23LO	Pythia 8.244+NNPDF23LO	di-charmonium
DPS	Pythia 8.244	NNPDF23LO		di-charmonium
Non-prompt	Pythia 8.244	NNPDF23LO		$b\bar{b} \to$ di-charmonium $+ X$
X(6900)	JHU	CTEQ6L1		$X(6900) \to J/\psi J/\psi$
η_b	JHU	CTEQ6L1		$\eta_b \to J/\psi J/\psi$
χ_{b0}	JHU	CTEQ6L1		$\chi_{b0} \to J/\psi J/\psi$

6.3 Triggers

This analysis uses dedicated multi-muon triggers, which are developed for the ATLAS B-physics and Light States programme (BLS). BLS replies on events of low-p_T leptons, typically muons. Due to high instantaneous luminosity, the p_T thresholds of standard single muon and di-muon triggers are larger than 20 GeV and are too high to provide useful data for BLS. Therefore, dedicated triggers are developed. To keep the trigger rates low enough for online record, some additional requirements, such as requirements on invariant mass and vertex, are included in these multi-muon triggers[76].

6.3.1 BLS triggers

Due to higher instantaneous luminosity in Run 2, the usage of low threshold multi-muon triggers became challenging. However, the installation of the L1 Topological Trigger (L1Topo) processor made it possible. L1Topo combines the information from calorimeters and muon trigger objects into topological information, thus it can reduce the rate while keeping the thresholds unchanged. Three typical L1Topo items are listed below:

- L1_BPH-2M9-2MU6_BPH-2DR15-2MU6: requires 2 muons with $p_T > 6$ GeV and 2 GeV $< m_{\mu\mu} <$ 9 GeV, and 2 muons with $p_T >$ 6 GeV and $0.2 < \Delta R_{\mu\mu} < 1.5$.
- L1_BPH-8M15-MU6MU4_BPH-0DR22-MU6MU4-BO: requires 2 muons with $p_T >$ 6 (4) GeV and 8 GeV $< m_{\mu\mu} <$ 15 GeV, and 2 "barrel-only" muons with $p_T >$ 6 (4) and $0 < \Delta R_{\mu\mu} < 2.5$.
- L1_BPH-2M9-2MU4_BPH-0DR15-2MU4: requires 2 muons with $p_T >$ 4 GeV and 2 GeV $< m_{\mu\mu} <$ 9 GeV, and 2 muons with $p_T >$ 4 GeV and $\Delta R_{\mu\mu} < 1.5$.

where $m_{\mu\mu}$ is the di-muon invariant mass and is calculated as $m_{\mu\mu} = 2p_T^1 p_T^2(cosh\Delta\eta - cos\Delta\phi)$. $\Delta R_{\mu\mu}$ is the opening angle of two muons and is expressed as $\Delta R_{\mu\mu} = \sqrt{(\Delta\eta)^2 + (\Delta\phi)^2}$. The "barrel-only" muons means muons with $|\eta| < 1.05$. As shown in Figure 6.1, comparing 2MU6 trigger with and without the L1Topo requirement, L1Topo reduces the rate by a factor of 4.

To further reduce the background and the rate of BLS trigger chains, additional selections are applied at the HLT. The general flow of a BLS trigger chain is illustrated in Figure 6.2. The first step is the fast muon reconstruction (L2) step, after which a first vertex reconstruction is performed with the ID tracks. If the reconstructed vertex satisfies the requirements on χ^2 and mass, the second step, precision reconstruction (EF)

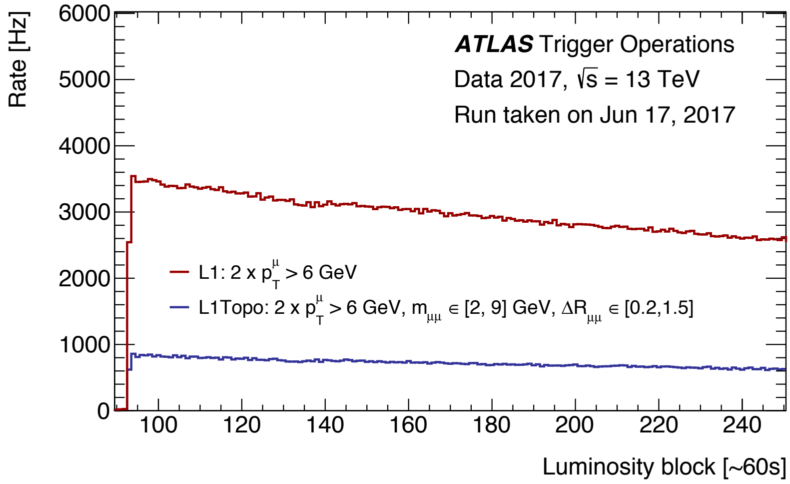

Figure 6.1 The rate of L1 triggers requiring two muons with $p_T > 6$ GeV, with (blue) and without (red) the L1Topo requirement, as a function of luminosity block[76].

step, proceeds. Most of the chains start with a multi-track vertex reconstruction algorithm in the L2 step, followed by vertex hypothesis testing, which is also used in the EF step for many BLS topologies. The multi-track vertex reconstruction algorithm applies cuts on p_T, multiplicity and total charge of selected high-p_T tracks, sets mass hypothesis, and passes tracks to a Kalman vertex fitter[77]. The vertex hypothesis testing algorithm selects vertices satisfying predefined mass and vertex fit χ^2 requirements.

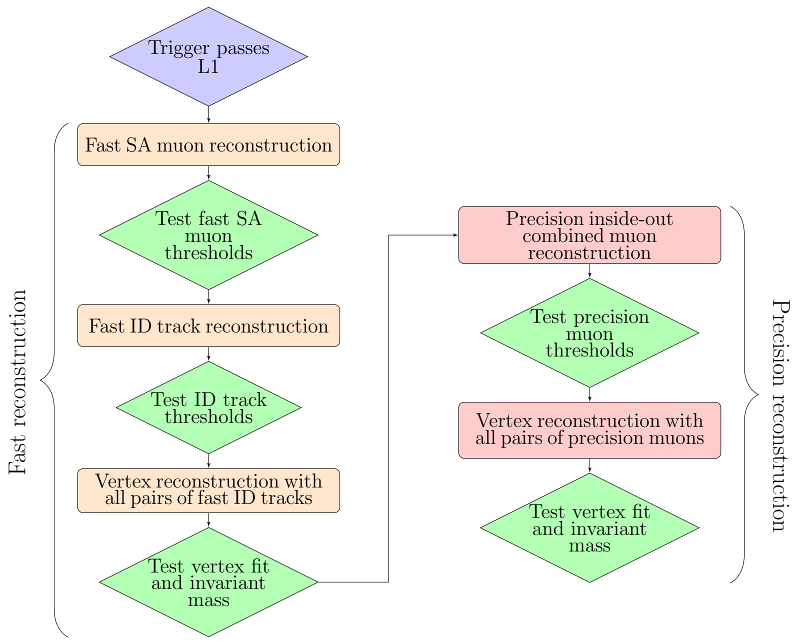

Figure 6.2 General construction of a BLS trigger[76].

At the EF step, a more complicated topological selection is applied; dimuon vertex reconstruction and hypothesis testing algorithms are used for $J/\psi/\Upsilon/B \to \mu\mu$ topologies;

multi-muon + track vertex reconstruction and hypothesis testing algorithms are applied for $\mu\mu + X$ topologies (di-muon + one track or di-muon + two tracks), such as $B^{\pm} \to J/\psi K^{\pm}$ and $B_s^0 \to J/\psi\phi$; multi-muon vertex reconstruction and hypothesis testing algorithms reconstruct vertex with two to four muons, and apply mass and χ^2 cuts; muon+track vertex reconstruction and hypothesis testing algorithms reconstruct vertex with one muon and one ID track.

Table 6.2 lists the BLS topologies used at HLT and the corresponding selections. Figure 6.3 shows the invariant mass of muon pairs for events passing the triggers. Thanks to the low-threshold BLS triggers, many events containing charmonium, b-hadron and bottomonium can be saved, which are the backbone of BLS.

Table 6.2 BLS topologies selected at the HLT with their fast and precision hypotheses[76].

HLT name	Description	L2 cuts	EF cuts
bDimu	$2 \times \mu$, broad mass	$1.5 < m_{\mu\mu} < 14$ GeV, $\chi^2 < 20$	
bDimu6000	$2 \times \mu$, low mass	$m_{\mu\mu} < 6$ GeV, $\chi^2 < 50$	$0.1 < m_{\mu\mu} < 6$ GeV, $\chi^2 < 20$
bDimu2700	$2 \times \mu$, very low mass	$m_{\mu\mu} < 2.7$ GeV, $\chi^2 < 50$	$0.1 < m_{\mu\mu} < 2.7$ GeV, $\chi^2 < 20$
bJpsi(mumu)	$J/\psi \to \mu\mu$	$2.5 < m_{\mu\mu} < 4.3$ GeV, $\chi^2 < 20$	
bUpsi(mumu)	$\Upsilon \to \mu\mu$	$8 < m_{\mu\mu} < 12$ GeV, $\chi^2 < 20$	
bBmumu	$B \to \mu\mu$	$4 < m_{\mu\mu} < 8.5$ GeV, $\chi^2 < 60$	$4 < m_{\mu\mu} < 8.5$ GeV, $\chi^2 < 20$
bBmumuxv2	$B \to \mu\mu + X$	$0.1 < m_{\mu\mu} < 6.5$ GeV, $\chi^2 < 20$	Depends on channel
bTau	$\tau \to 3\mu$	2-μ triggers: $m_{\mu\mu} < 2.7$ GeV, $\chi^2 < 50$ 3-μ triggers: $m_{\mu\mu\mu} < 2.7$ GeV, $\chi^2 < 50$	
bPhi	$\phi \to \mu\mu$	$0.94 < m_{\mu\mu} < 1.1$ GeV, $\chi^2 < 10$	

6.3.2 Trigger study

This analysis looks at the final state with at least four muons. To save events as much as possible, combinations of di-muon and tri-muon triggers are used as listed in Table 6.3. Since the trigger chains in different years or sub-periods are a bit different, different triggers are selected for different years or sub-periods.

For a certain data-taking sub-period, different triggers can have different prescales. This effect is not considered in the MC simulation, so additional weights should be applied to MC events in order to account for the difference in muon kinematic variables in the

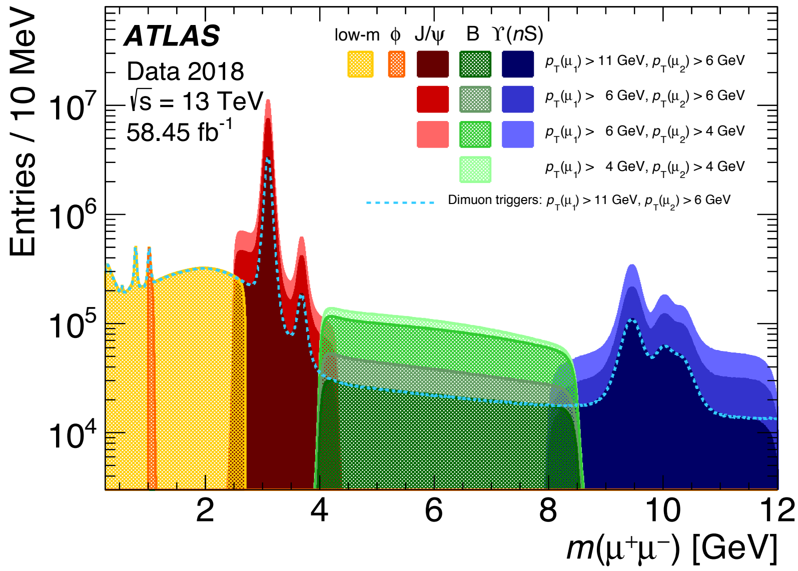

Figure 6.3 Di-muon invariant mass for events passing BLS triggers. The dashed line represents the events collected by the lowest unprescaled di-muon trigger, which is inclusive for the full mass range.

event collected by different triggers. The weight is calculated for each event based on lumiblock-by-lumiblock prescales taken from data:

$$w = \frac{1}{L}\sum_j L_j \left[1 - \prod_i^n \left(1 - \frac{1}{p_i^j}\right)\right] \tag{6.1}$$

where p_i^j is the prescale factor of trigger i in lumiblock j. L_j is the luminosity of lumiblock j and L is the total luminosity of the considered lumiblocks. The trigger weights for individual triggers used in different data sub-periods are in Table 6.3.

To check the influence of each trigger in each year and sub-period, Table 6.4 shows the percentage loss of event yields for TQ signal, SPS and DPS after removing the corresponding trigger in each sub-period, with the prescales of triggers taken into account. Due to low threshold, the HLT_3mu4_bJpsi trigger has the largest impact on event yields.

Table 6.3 The high level triggers used in the low-mass resonances analysis for different years or sub-periods, and the corresponding prescale weights.

year	run/period	trigger	prescale 因子
2015	266904-284484 (A-H)	HLT_2mu4_bJpsimumu_noL2	0.799429
		HLT_mu6_mu4_bJpsimumu_noL2	0.999928
2016	296939-302393 (A-C)	HLT_mu6_mu4_bJpsimumu	0.368008
		HLT_2mu6_bJpsimumu	0.668316
		HLT_mu10_mu6_bJpsimumu	0.999670
		HLT_3mu4	0.285545
		HLT_mu6_2mu4_bJpsi	0.642683
		HLT_3mu6_bJpsi	0.999823
	302737-303560 (D)	HLT_mu6_mu4_bJpsimumu_Lxy0_delayed	0.367026
		HLT_2mu6_bJpsimumu_delayed	0.751667
		HLT_mu10_mu6_bJpsimumu_delayed	0.754030
		HLT_3mu4	0.141156
		HLT_mu6_nomucomb_2mu4_nomucomb_delayed_L1MU6_3MU4	0.260818
		HLT_3mu6_bJpsi	0.999700
	303638-311481 (E-L)	HLT_mu6_mu4_bJpsimumu_Lxy0_delayed	0.343048
		HLT_2mu6_bJpsimumu_delayed	0.996833
		HLT_3mu4_nomucomb_delayed	0.534698
		HLT_mu6_nomucomb_2mu4_nomucomb_delayed_L1MU6_3MU4	0.997986
2017	325713-328393 (A-B)	HLT_2mu6_bJpsimumu	0.987310
		HLT_mu11_mu6_bDimu	0.999065
		HLT_3mu4_bJpsi	1.0
	329385-340453 (C-K)	HLT_mu11_mu6_bDimu	1.0
		HLT_3mu4_bJpsi	1.0
		HLT_mu6_mu4_bJpsimumu_Lxy0_L1BPH-2M9-MU6MU4_BPH-0DR15-MU6MU4	0.031653
		HLT_2mu6_bJpsimumu_L1BPH-2M9-2MU6_BPH-2DR15-2MU6	0.978623
2018	348197-364485 (A-R)	HLT_mu11_mu6_bDimu	1.0
		HLT_3mu4_bJpsi	1.0
		HLT_mu6_mu4_bJpsimumu_Lxy0_L1BPH-2M9-MU6MU4_BPH-0DR15-MU6MU4	0.431211
		HLT_2mu6_bJpsimumu_L1BPH-2M9-2MU6_BPH-2DR15-2MU6	1.0
		HLT_2mu4_bJpsimumu_Lxy0_L1BPH-2M9-2MU4_BPH-0DR15-2MU4	0.084496

Table 6.4 Trigger study to check the influence of each trigger in each year and sub-period. The percentage numbers mean the changes of event yields for signal, SPS and DPS after removing the corresponding trigger in each sub-period.

year	run/period	trigger	Signal	SPS	DPS
2015	266904-284484 (A-H)	HLT_2mu4_bJpsimumu_noL2	-0.25%	-0.28%	-2.45%
		HLT_mu6_mu4_bJpsimumu_noL2	-2.02%	-2.02%	-2.00%
2016	296939-302393 (A-C)	HLT_mu6_mu4_bJpsimumu	-0.62%	-0.52%	-1.61%
		HLT_2mu6_bJpsimumu	-0.19%	-0.15%	-0.56%
		HLT_mu10_mu6_bJpsimumu	-1.16%	-1.04%	-0.54%
		HLT_3mu4	-0.10%	-0.10%	-0.63%
		HLT_mu6_2mu4_bJpsi	-1.02%	-1.02%	-2.61%
		HLT_3mu6_bJpsi	-0.11%	-0.11%	-0.14%
	302737-303560 (D)	HLT_mu6_mu4_bJpsimumu_Lxy0_delayed	-0.56%	-0.46%	-1.09%
		HLT_2mu6_bJpsimumu_delayed	-0.29%	-0.24%	-0.89%
		HLT_mu10_mu6_bJpsimumu_delayed	-0.01%	-0.01%	0.00%
		HLT_3mu4	-0.32%	-0.33%	-0.90%
		HLT_mu6_nomucomb_2mu4_nomucomb_delayed_L1MU6_3MU4	-0.50%	-0.54%	-1.23%
		HLT_3mu6_bJpsi	-1.07%	-1.16%	-0.31%
	303638-311481 (E-L)	HLT_mu6_mu4_bJpsimumu_Lxy0_delayed	-1.03%	-0.83%	-2.77%
		HLT_2mu6_bJpsimumu_delayed	-7.81%	-6.77%	-8.69%
		HLT_3mu4_nomucomb_delayed	-0.53%	-0.47%	-4.43%
		HLT_mu6_nomucomb_2mu4_nomucomb_delayed_L1MU6_3MU4	-5.68%	-5.90%	-13.19%
2017	325713-328393 (A-B)	HLT_2mu6_bJpsimumu	-0.36%	-0.28%	-1.24%
		HLT_mu11_mu6_bDimu	-0.19%	-0.24%	-0.12%
		HLT_3mu4_bJpsi	-2.28%	-2.10%	-6.97%
	329385-340453 (C-K)	HLT_mu11_mu6_bDimu	-8.93%	-8.40%	-2.48%
		HLT_3mu4_bJpsi	-17.58%	-15.92%	-51.35%
		HLT_mu6_mu4_bJpsimumu_Lxy0_L1BPH-2M9-MU6MU4_BPH-0DR15-MU6MU4	-0.10%	-0.09%	-0.33%
		HLT_2mu6_bJpsimumu_L1BPH-2M9-2MU6_BPH-2DR15-2MU6	-2.01%	-1.66%	-7.47%
2018	348197-364485 (A-R)	HLT_mu11_mu6_bDimu	-9.96%	-9.44%	-2.45%
		HLT_3mu4_bJpsi	-15.92%	-14.32%	-47.36%
		HLT_mu6_mu4_bJpsimumu_Lxy0_L1BPH-2M9-MU6MU4_BPH-0DR15-MU6MU4	-1.26%	-1.10%	-3.82%
		HLT_2mu6_bJpsimumu_L1BPH-2M9-2MU6_BPH-2DR15-2MU6	-1.82%	-1.48%	-6.49%
		HLT_2mu4_bJpsimumu_Lxy0_L1BPH-2M9-2MU4_BPH-0DR15-2MU4	-0.06%	-0.05%	-0.49%

6.4 Event selections

During Run2, due to the increased collision energy, the effect of pile-up is enhanced and amounts of hadrons are produced, mainly pions and kaons, with hundreds of tracks. The reconstruction of vertices is challenging. Dedicated ATLAS offline software[78] is used to reconstruct the charmonium and 4μ candidates. Events should contain at least two opposite-charge muon pairs. The TQ vertex is reconstructed by fitting the four muon tracks in the inner detector. Then, each muon pair is revertexed with a J/ψ or $\psi(2S)$ mass constraint to achieve the best TQ mass resolution. With the mass constraint, the mass resolution is 23 MeV for TQ mass around 6.9 GeV. The TQ mass obtained with mass constraints ($m_{4\mu}^{\text{con}}$) and the one without mass constraints ($m_{4\mu}$) are both used in the analysis.

Combinations of di-muon and tri-muon triggers with J/ψ or $\psi(2S)$ mass window requirements are applied for the largest acceptance with details in Section 6.3.2. The lowest p_T thresholds are used and different triggers are combined together. To reduce backgrounds, muons and J/ψ need to satisfy some additional kinematic requirements. The four selected muons must pass the `Loose` identification working point and satisfy $p_T > 4, 4, 3, 3$ GeV from the leading to the fourth sub-leading muon. If there are more than one 4μ candidates in an event, the candidate with the least value of the requirement defined in Equation 6.2 is chosen as the best candidate and used in the analysis.

$$\chi^2_{4\mu}/N_{4\mu} + \chi^2_{J/\psi_1}/N_{J/\psi_1} + \chi^2_{J/\psi_2}/N_{J/\psi_2}, \text{ di-}J/\psi \text{ channel} \tag{6.2}$$

$$\chi^2_{4\mu}/N_{4\mu} + \chi^2_{J/\psi}/N_{J/\psi} + \chi^2_{J/\psi}/N_{J/\psi}, \ J/\psi + \psi(2S) \text{ channel} \tag{6.3}$$

where χ^2 and N are the vertex fit quality and number of degrees of freedom. To suppress the background without J/ψ or $\psi(2S)$, a mass window requirement is applied on J/ψ or $\psi(2S)$. The requirements on transverse decay length (L_{xy}) are also applied on 4μ candidate and J/ψ or $\psi(2S)$ in order to reduce the non-prompt background. The detailed selection criteria for signal regions is summarized in Table 6.5. The SR1 is used to search for di-J/ψ and J/ψ+$\psi(2S)$ resonances, while the SR2 is used to search for the $\eta_b \to 2J/\psi$ and $\chi_{b0} \to 2J/\psi$ decays. Events with $\Delta R > 0.25$ are used to validate the shape of the 4μ mass spectrum in the SPS background, thus they are not used in the SR1. To validate the background estimation, a nominal region is defined, which is composed of the SPS and DPS CRs.

Table 6.5 Summary of event selection requirements for SRs and CRs[?].

Conditions	SR1	SR2	SPS CR	DPS CR
Baseline	Di-muon or tri-muon triggers, Opposite charged muons from the same J/ψ or ψ(2S) vertex, `Loose` muon ID $p_{\mathrm{T}}^{1,2,3,4} > 4,4,3,3$ GeV and $\lvert\eta_{1,2,3,4}\rvert < 2.5$ for four muons $m_{J/\psi} \in \{2.94, 3.25\}$ GeV, or $m_{\psi(2S)} \in \{3.56, 3.80\}$ GeV, Loose vertex cuts $\chi^2_{4\mu}/N < 40$ and $\chi^2_{\text{di-}\mu}/N < 100$, Vertex $\chi^2_{4\mu}/N < 3$, $L_{xy}^{4\mu} < 0.2$ mm, $\lvert L_{xy}^{\text{di-}\mu}\rvert < 0.3$ mm,				
$m_{4\mu}$	<7.5 GeV,	(9, 10) GeV	(7.5, 12.0) GeV	(14.0, 25.0) GeV
ΔR between charmonia	<0.25	–	–	–

6.5 Background estimation

The backgrounds in this analysis can be divided into four categories:

1. SPS background: the SPS process produces two prompt charmonia and is modeled by MC simulation with kinematic and normalization corrections derived in SPS CR, which is defined in Table 6.5.
2. DPS background: the DPS process produces two prompt charmonia and is modeled by MC simulation with kinematic and normalization corrections derived in DPS CR, which is defined in Table 6.5.
3. Non-prompt background (labeled as "$b\bar{b} \to J/\psi J/\psi + X$"): the processes contain two non-prompt J/ψ or $\psi(2S)$ originating from b-hadron decays. The estimation is based on MC samples, but it's normalized and validated in dedicated regions.
4. "Others" background: processes contain at least one charmonium candidate and fake muons. It's estimated with a data-driven method.

SPS dominates the di-J/ψ channel, while in the J/ψ+$\psi(2S)$ channel, SPS and "Others" are the main backgrounds.

6.5.1 SPS background

SPS background is the main background. Since the two charmonia in the SPS background are close by, the SPS background mainly contributes to low mass region. Pythia can not model the SPS process well, especially the kinematic variables. A SPS CR is defined to correct the discrepancies in various kinematic distributions. These discrepancies are mainly reflected in the following variables for the di-J/ψ channel: $p_{\mathrm{T}}^{\mathrm{di}-J/\psi}$, $\left|p_{z}^{\mathrm{di}-J/\psi}\right|$, $\Delta\phi(J/\psi_1, J/\psi_2)$ and $p_{\mathrm{T}}^{\mu_4}$. To correct these variables, correction weights are derived with polynomial functions up to third order. The correction weights of the above variables are sequentially derived and applied on each event. In the $J/\psi + \psi(2S)$ channel, the corrections derived in the di-J/ψ channel are applied, except for the $p_{T}^{\mu_4}$ and normalisation which are rederived. After the corrections, there is a good agreement between data and predicted backgrounds as shown in Figure 6.4-6.5.

6.5.2 DPS background

The estimation of the DPS background uses the similar method as used for the SPS background. The two charmonia in the DPS background are far apart, so its control region is defined in high mass region. The discrepancies between data and backgrounds in the DPS CR are resolved by correcting the following variables in the di-J/ψ channel: $\Delta\phi(J/\psi, J/\psi)$, $\Delta\eta(J/\psi, J/\psi)$, $p_{\mathrm{T}}^{\mu_4}$, $p_{\mathrm{T}}^{\mu_1}$ and $p_{\mathrm{T}}^{\mathrm{di}-J/\psi}$. Correction weights are derived with polynomial functions up to third order. The correction weights of the above variables are sequentially derived and applied on each event. In the $J/\psi + \psi(2S)$ channel, the corrections derived in the di-J/ψ channel are applied, except for the normalisation which is rederived. After the corrections, predicted backgrounds and data are in good agreement as shown in Figure 6.6-6.7.

6.5.3 Non-prompt and “Others” backgrounds

As can be seen in Figure 6.8-6.9, the events of non-prompt background tend to have large values of L_{xy} for charmonium and worse vertex qualities. So a non-prompt region can be defined, in which the non-prompt background is rich. The definition of the non-prompt region is the same as the baseline selection defined in Table 6.5, except reversing the vertex quality requirements:

$$L_{xy} > 0.4 \text{ mm for either } J/\psi \text{ or } \psi(2S), \text{ or } \chi^2_{4\mu}/N_{4\mu} > 6 \tag{6.4}$$

The normalization of the non-prompt background is obtained in the non-prompt region and applied to the nominal and signal regions to estimate the contribution of the non-prompt background. Figure 6.10-6.11 show the charmonia mass spectra in the non-prompt region. In the J/ψ+$\psi(2S)$ channel, the “Others” component has a much larger contribution than the non-prompt background in the non-prompt region. Thus, the MC samples are used to estimate the non-prompt contribution in the nominal and signal re-

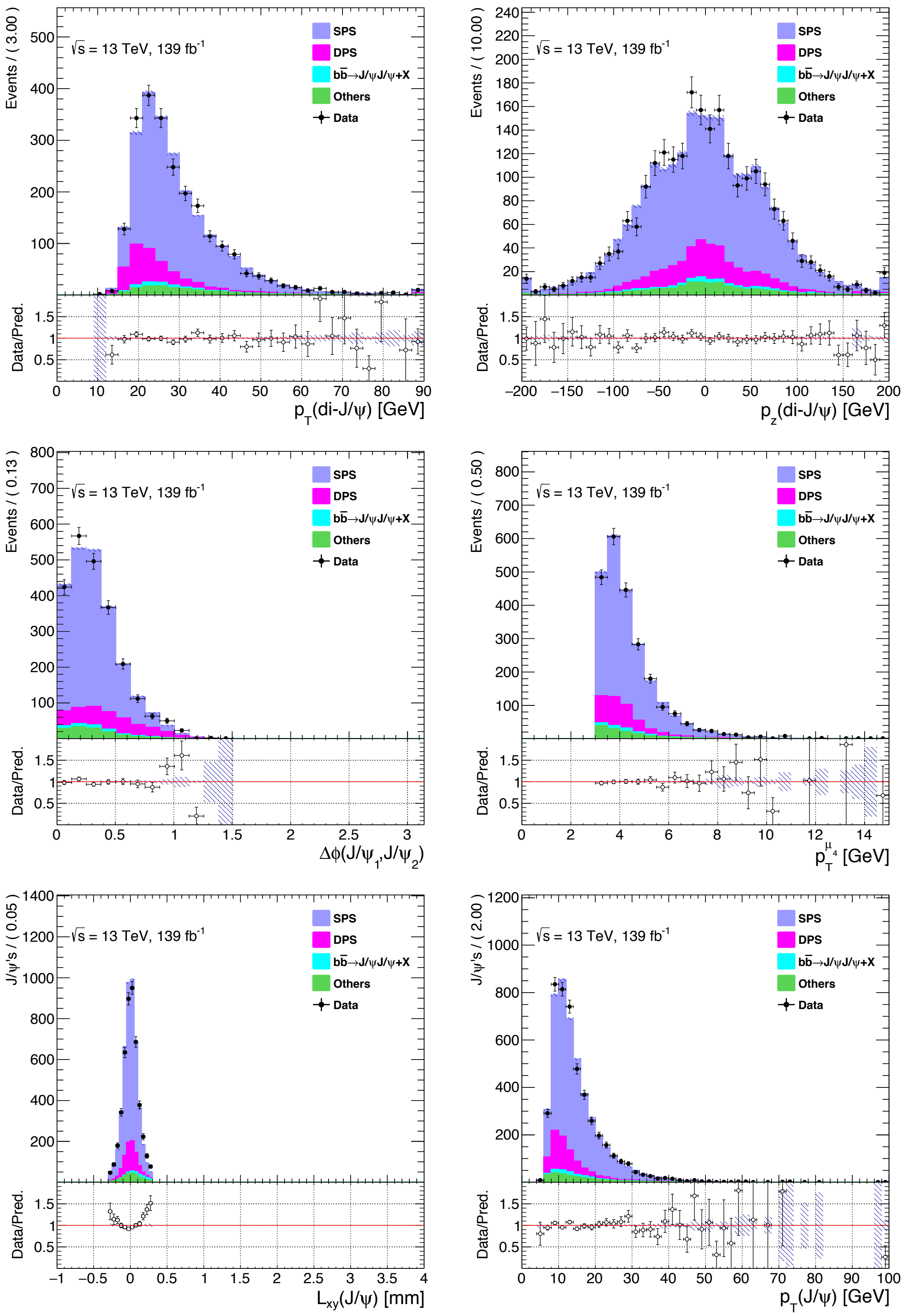

Figure 6.4 The distributions of kinematic variables after correction weights applied in the SPS CR in the di-J/ψ channel. The error bars represent statistical uncertainties.

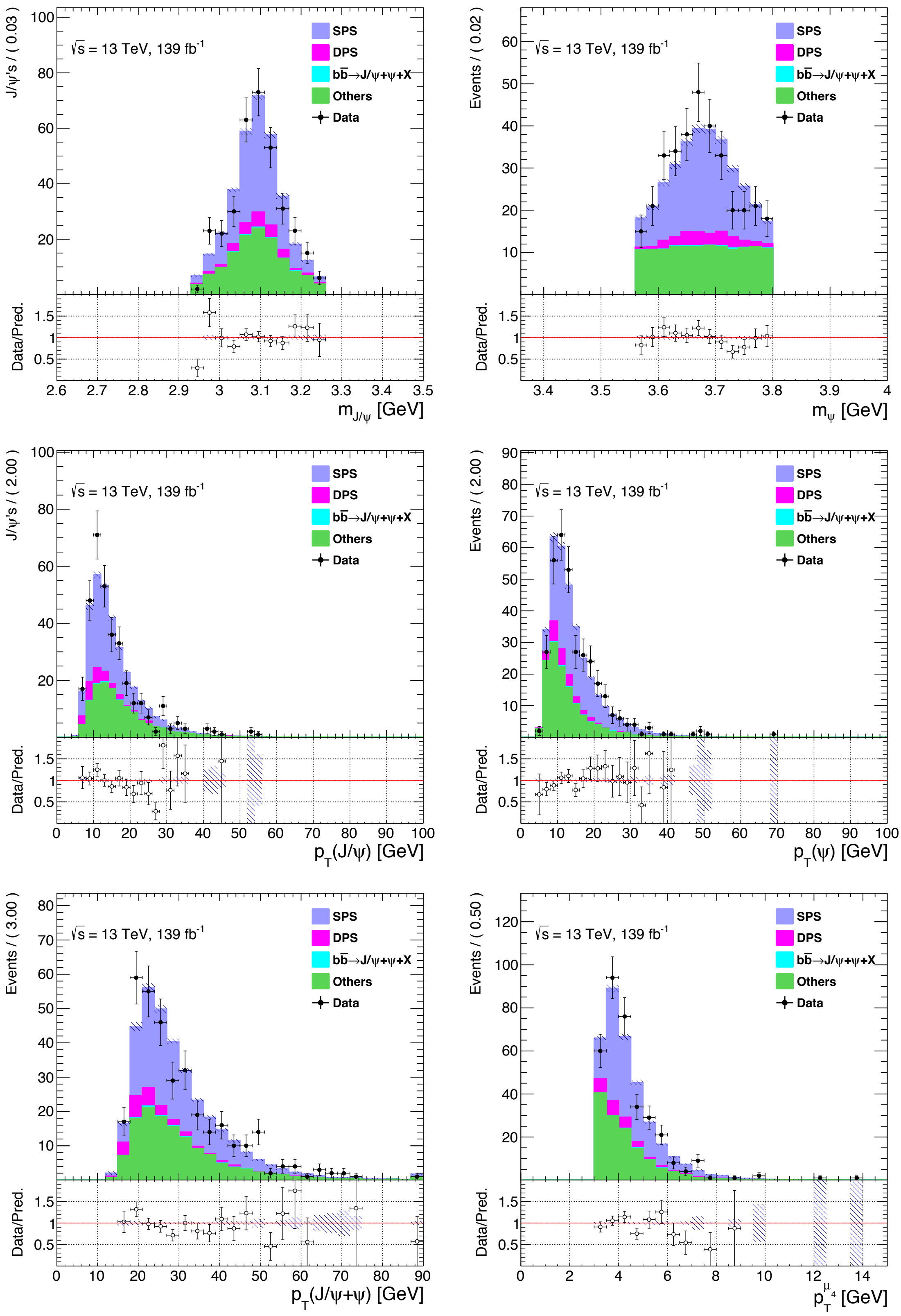

Figure 6.5 The distributions of kinematic variables after correction weights applied in the SPS CR in the J/ψ+ψ(2S) channel. The error bars represent statistical uncertainties.

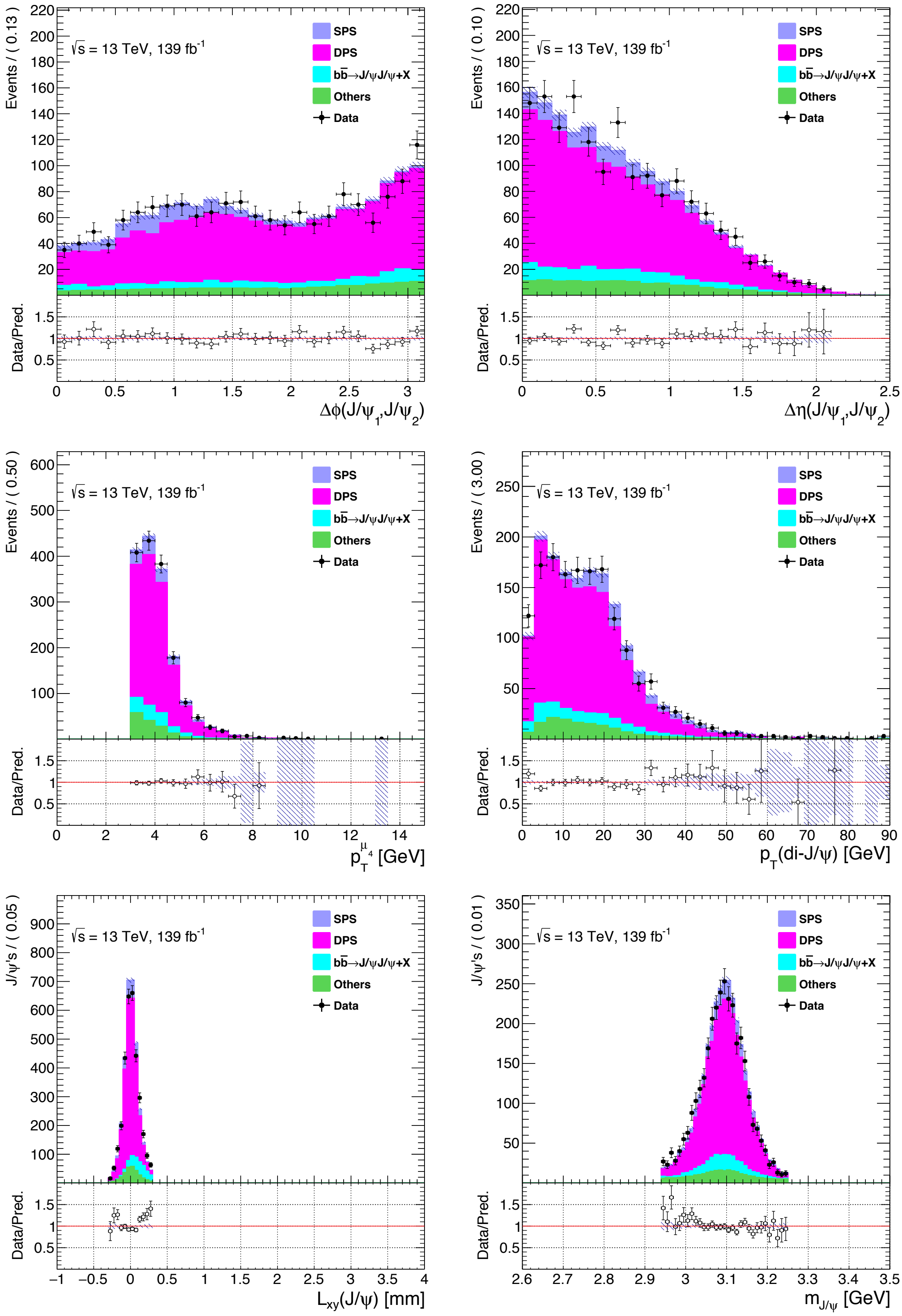

Figure 6.6 The distributions of kinematic variables after correction weights applied in the DPS CR in the di-J/ψ channel. The error bars represent statistical uncertainties.

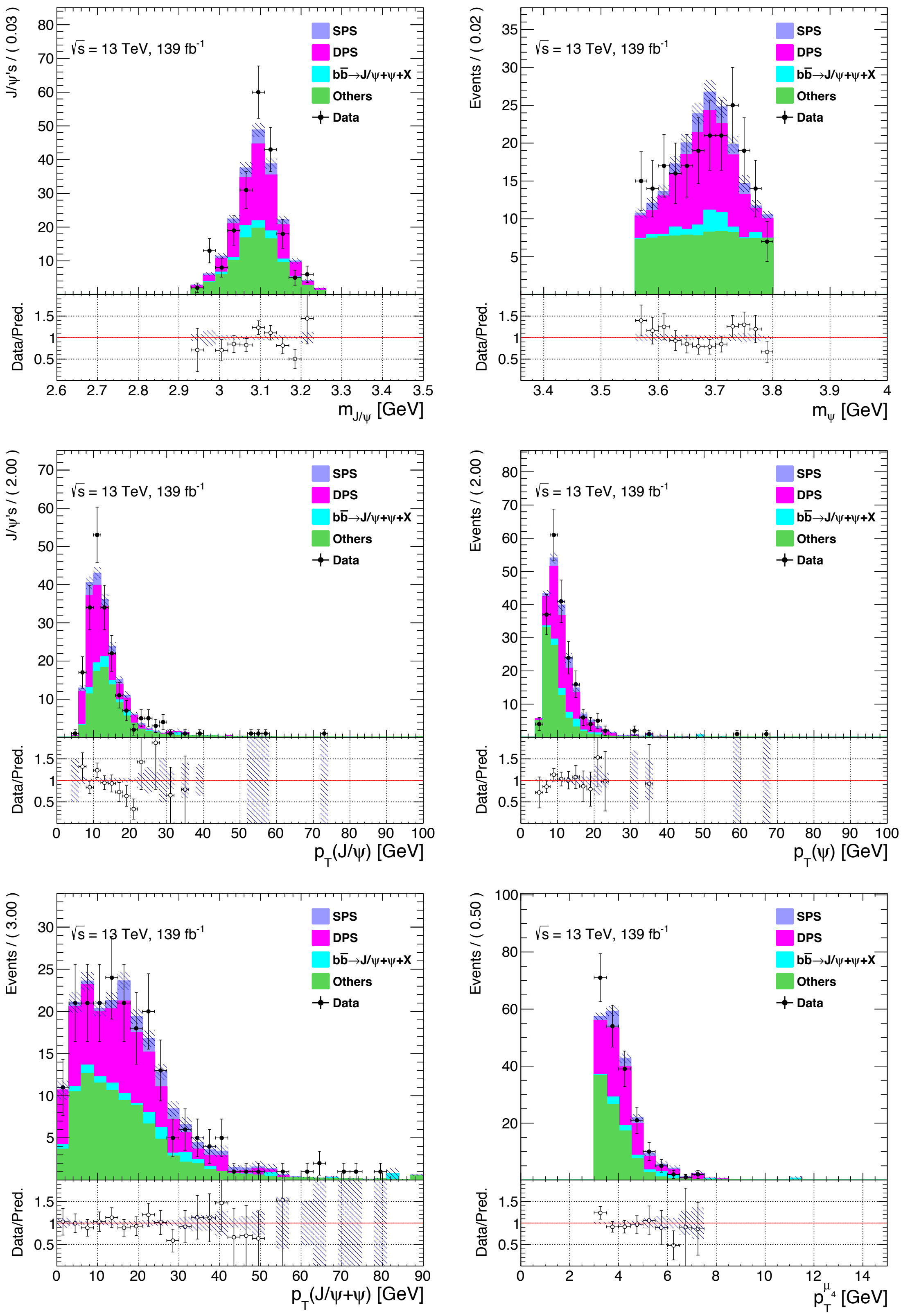

Figure 6.7 The distributions of kinematic variables after correction weights applied in the DPS CR in the J/ψ+ψ(2S) channel. The error bars represent statistical uncertainties.

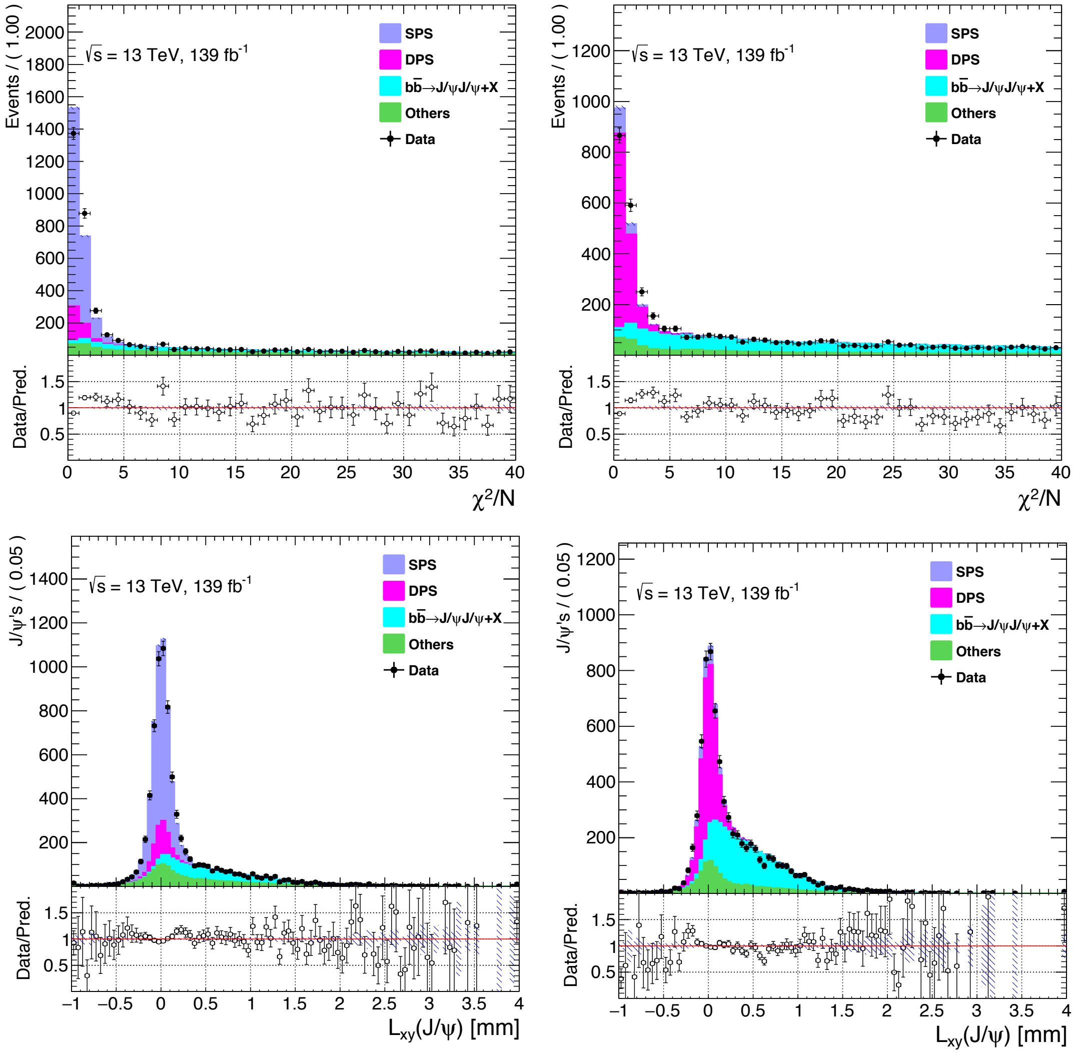

Figure 6.8 The distributions of vertex related variables before the vertex cuts in the SPS CR (left) and DPS CR (right) in the di-J/ψ channel. The $b\bar{b} \to J/\psi J/\psi + X$ MC is used. The error bars represents the statistical uncertainty.

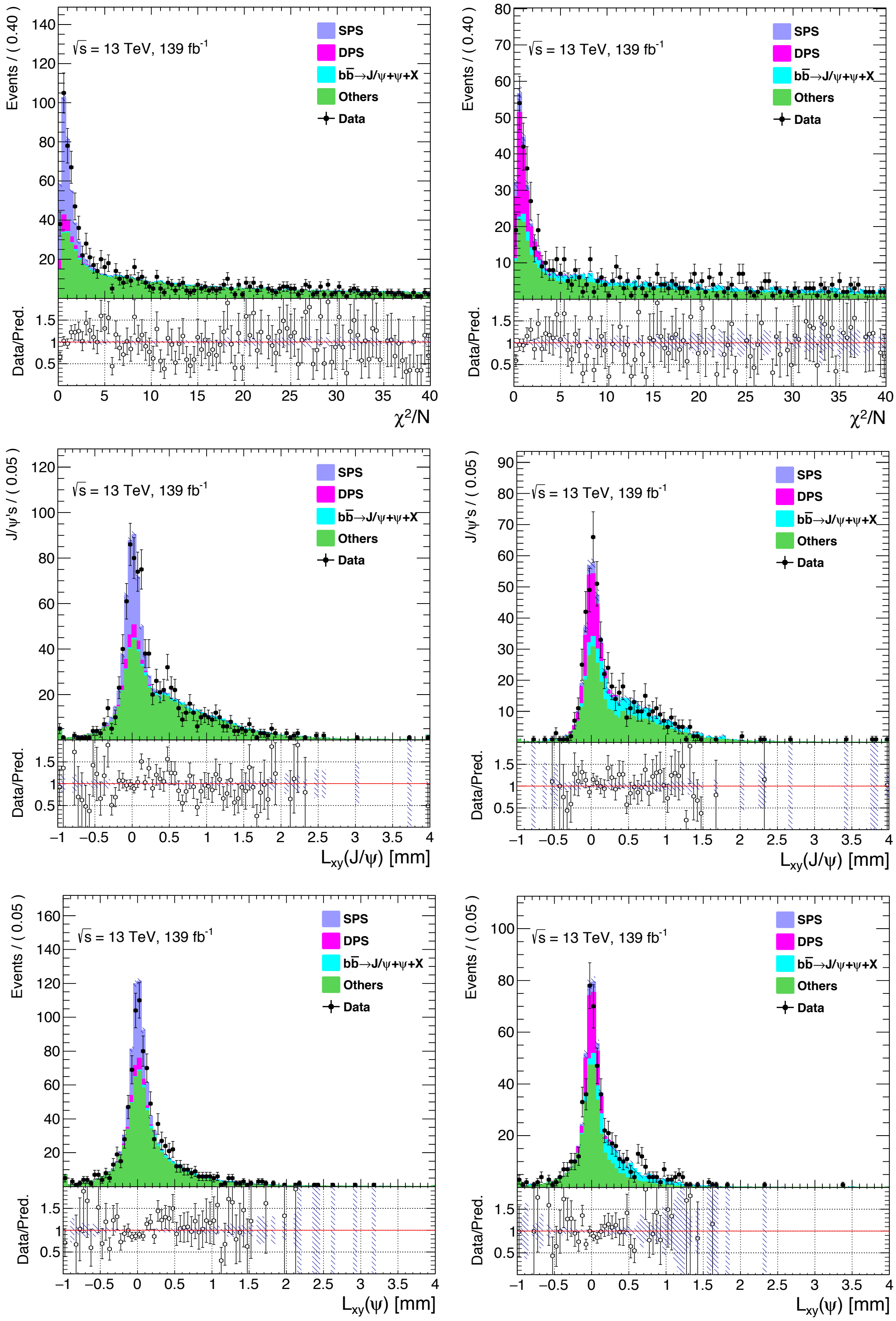

Figure 6.9 The distributions of vertex related variables before the vertex cuts in the SPS CR (left) and DPS CR (right) in the J/ψ+$\psi(2S)$ channel. The $b\bar{b} \rightarrow J/\psi J/\psi + X$ MC is used. The error bars represents the statistical uncertainty.

gions.

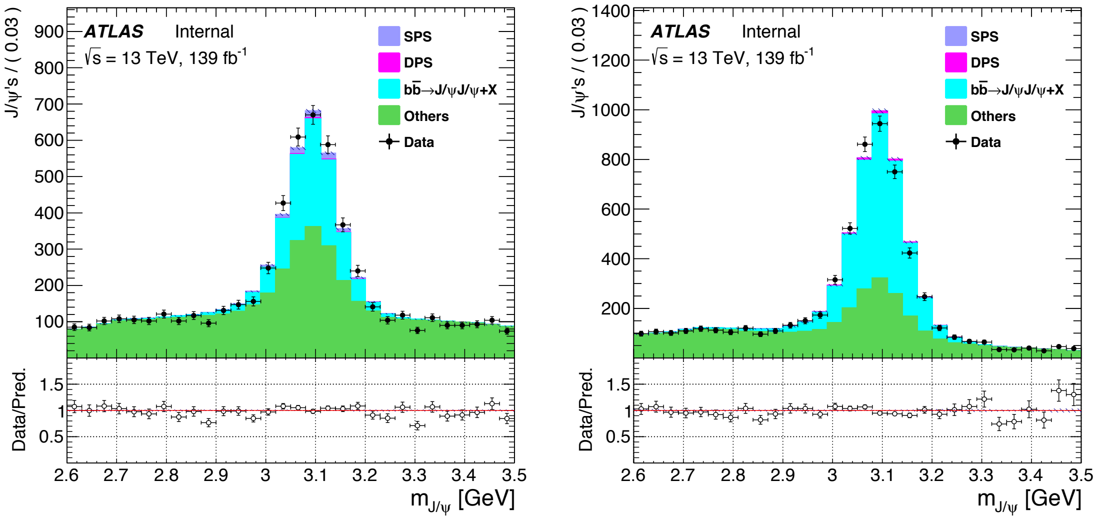

Figure 6.10 The distributions of the J/ψ mass in the di-J/ψ channel in the non-prompt region, with the SPS CR (left) and DPS CR (right) cuts. The corrections are applied. The $b\bar{b} \to J/\psi J/\psi +$ X MC is used. The error bars represent statistical uncertainties.

The "Others" background can not be accurately estimated by MC simulation, so it's estimated by the data-driven method with the fake muon control region, events in which are required to have one charmonium candidate containing a track that is not reconstructed as a muon, with other requirements unchanged. When estimating the contribution of the "Others" background in the nominal and signal regions with fake muon control region, corrections to p_{T,μ_4} and $m_{J/\psi}$, and transfer factor are applied. The corrections and transfer factor are derived in the J/ψ or $\psi(2S)$ mass sideband region. The mass sideband region is defined with the baseline selections except inversing the J/ψ or $\psi(2S)$ mass window cut:

- di-J/ψ channel: 2.60 GeV$< m_{J/\psi} <$ 2.80 GeV, or 3.34 GeV$< m_{J/\psi} <$ 3.50 GeV.
- J/ψ+ψ(2S) channel: 2.60 GeV$< m_{J/\psi} <$ 2.94 GeV, or 3.25 GeV$< m_{J/\psi} <$ 3.50 GeV, or 3.36 GeV$< m_{\psi(2S)} <$ 3.52 GeV, or 3.84 GeV$< m_{\psi(2S)} <$ 4.00 GeV.

Figure 6.12-6.15 show the distributions of kinematic variables in the mass sideband region with corrections applied. Overall good agreement between data and estimated background is seen.

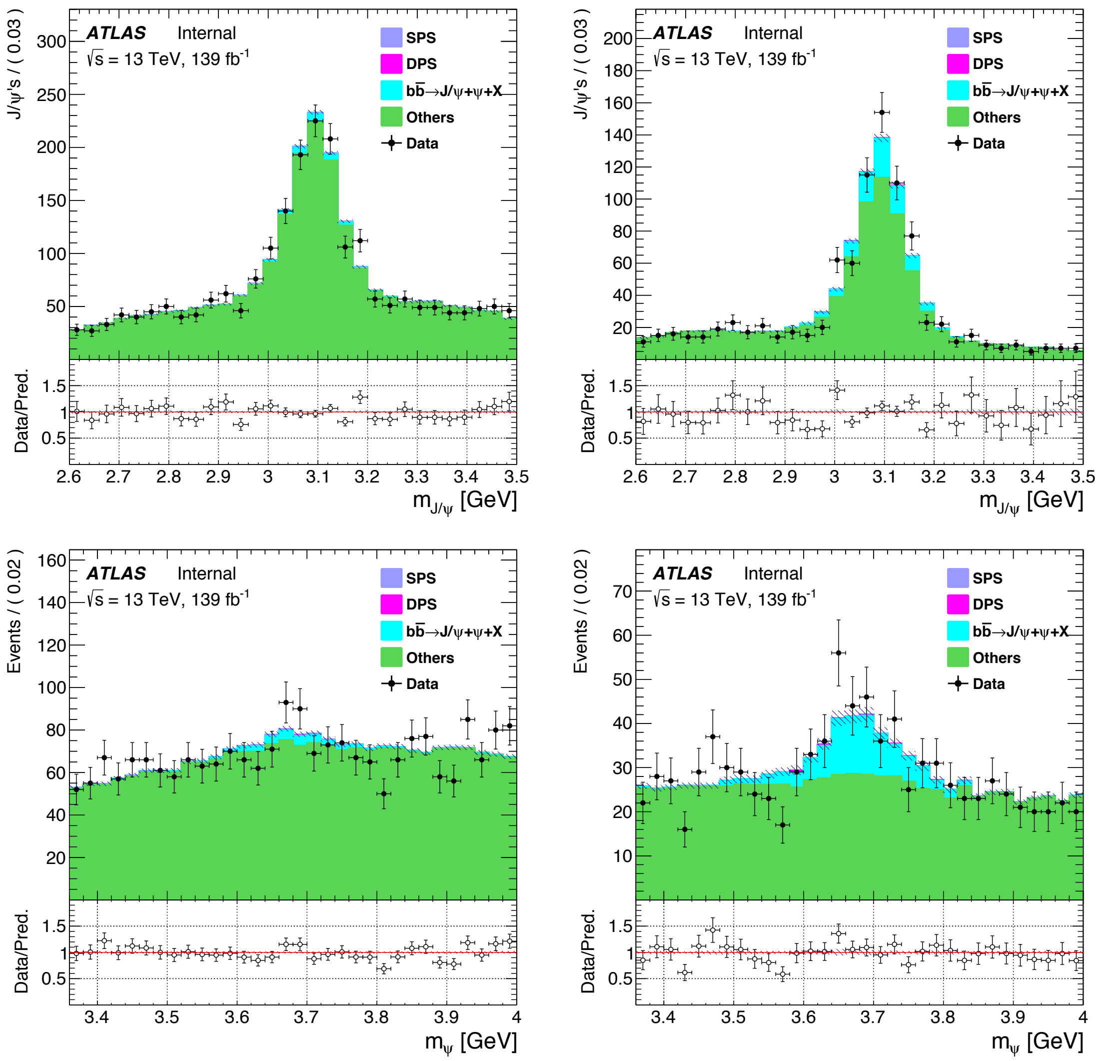

Figure 6.11 The distributions of the J/ψ mass and the $\psi(2S)$ mass in the J/ψ+$\psi(2S)$ channel in the non-prompt region, with the SPS CR (left) and DPS CR (right) cuts. The corrections are applied. The $b\bar{b} \to J/\psi J/\psi + X$ MC is used. The error bars represent statistical uncertainties.

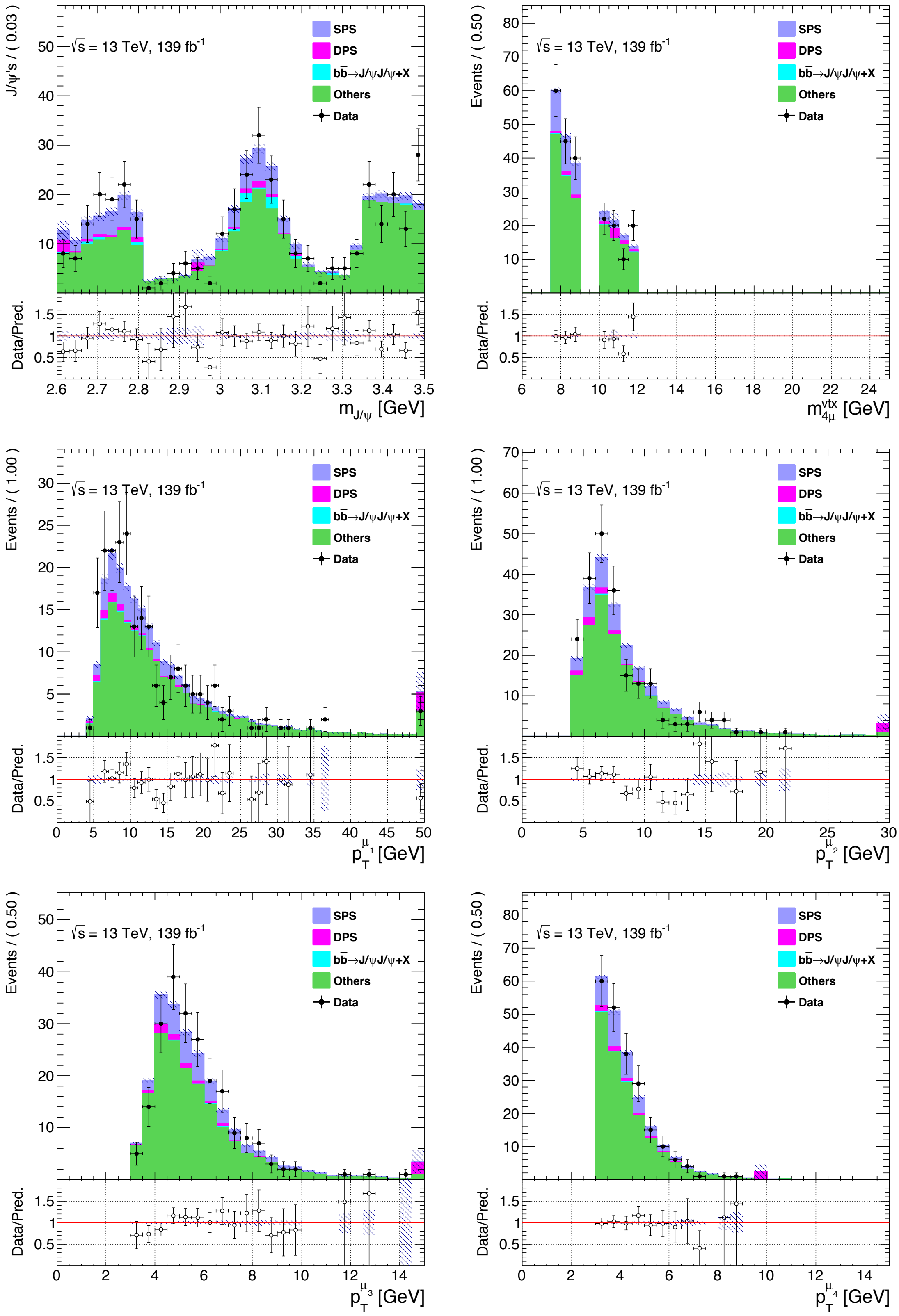

Figure 6.12 The distributions of kinematic variables in the di-J/ψ channel in the mass sideband region, with the SPS CR cuts and corrections applied. The error bars represent statistical uncertainties.

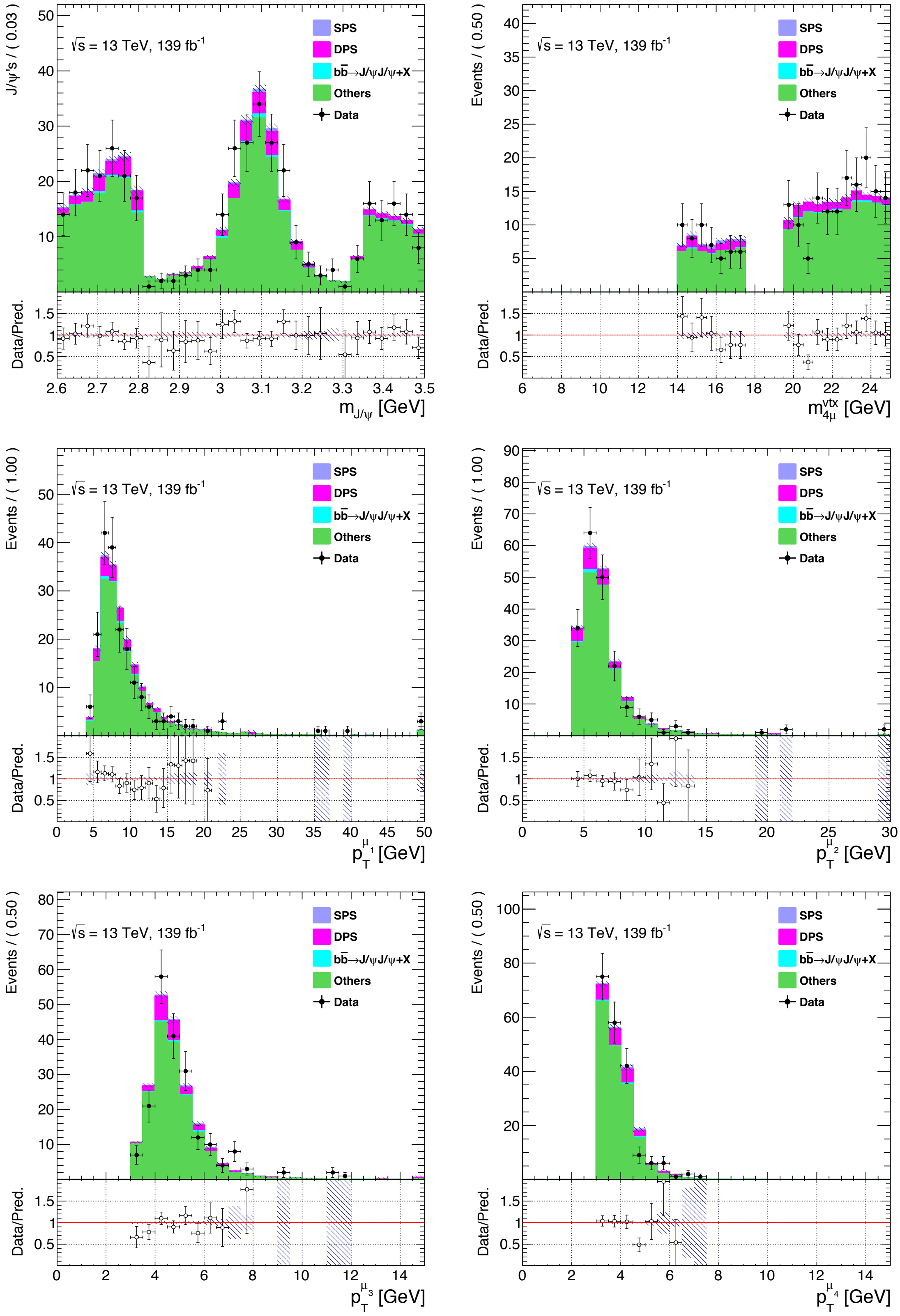

Figure 6.13 The distributions of kinematic variables in the di-J/ψ channel in the mass sideband region, with the DPS CR cuts and corrections applied. The error bars represent statistical uncertainties.

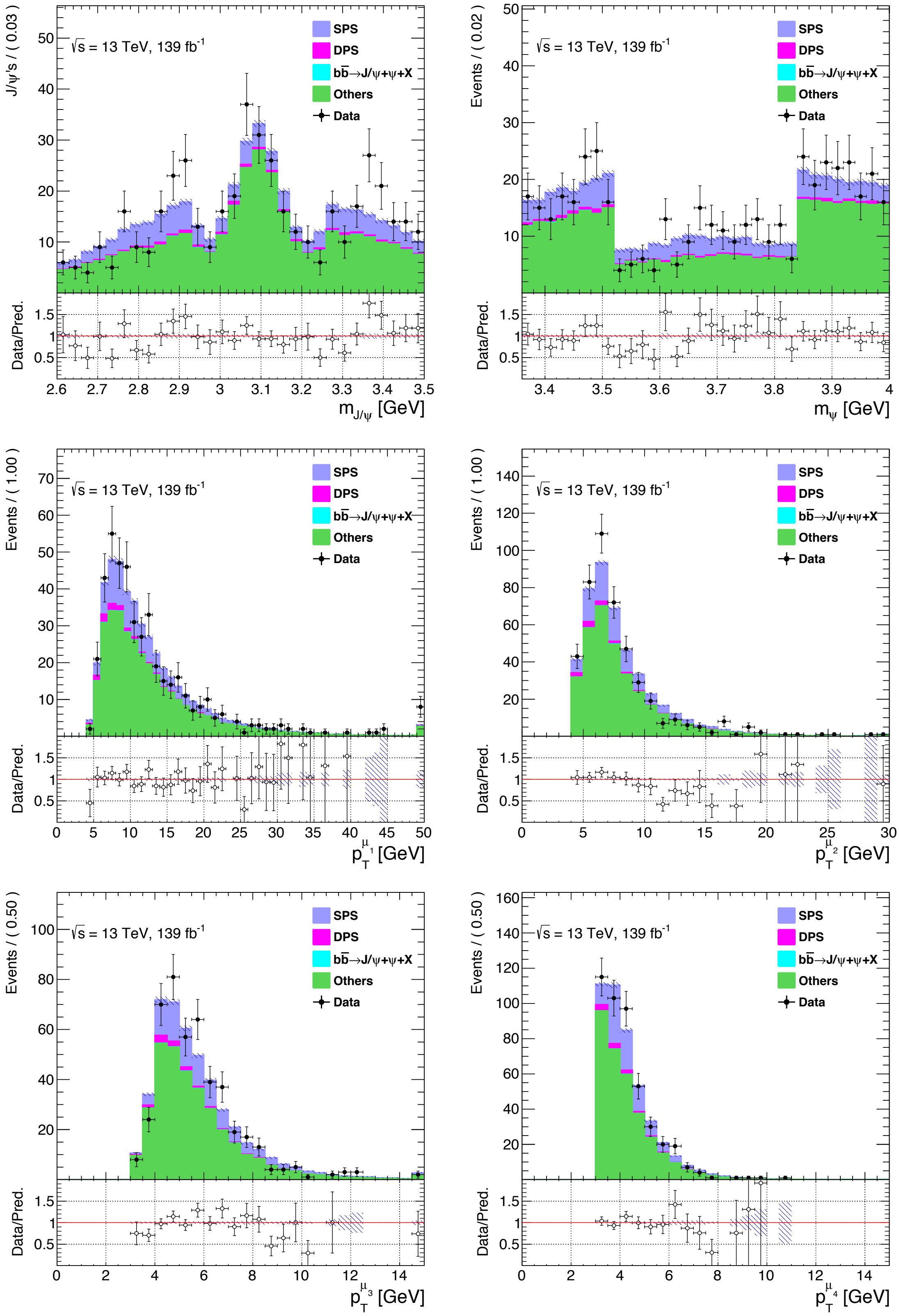

Figure 6.14 The distributions of kinematic variables in the J/ψ+$\psi(2S)$ channel in the mass sideband region, with the SPS CR cuts and corrections applied. The error bars represent statistical uncertainties.

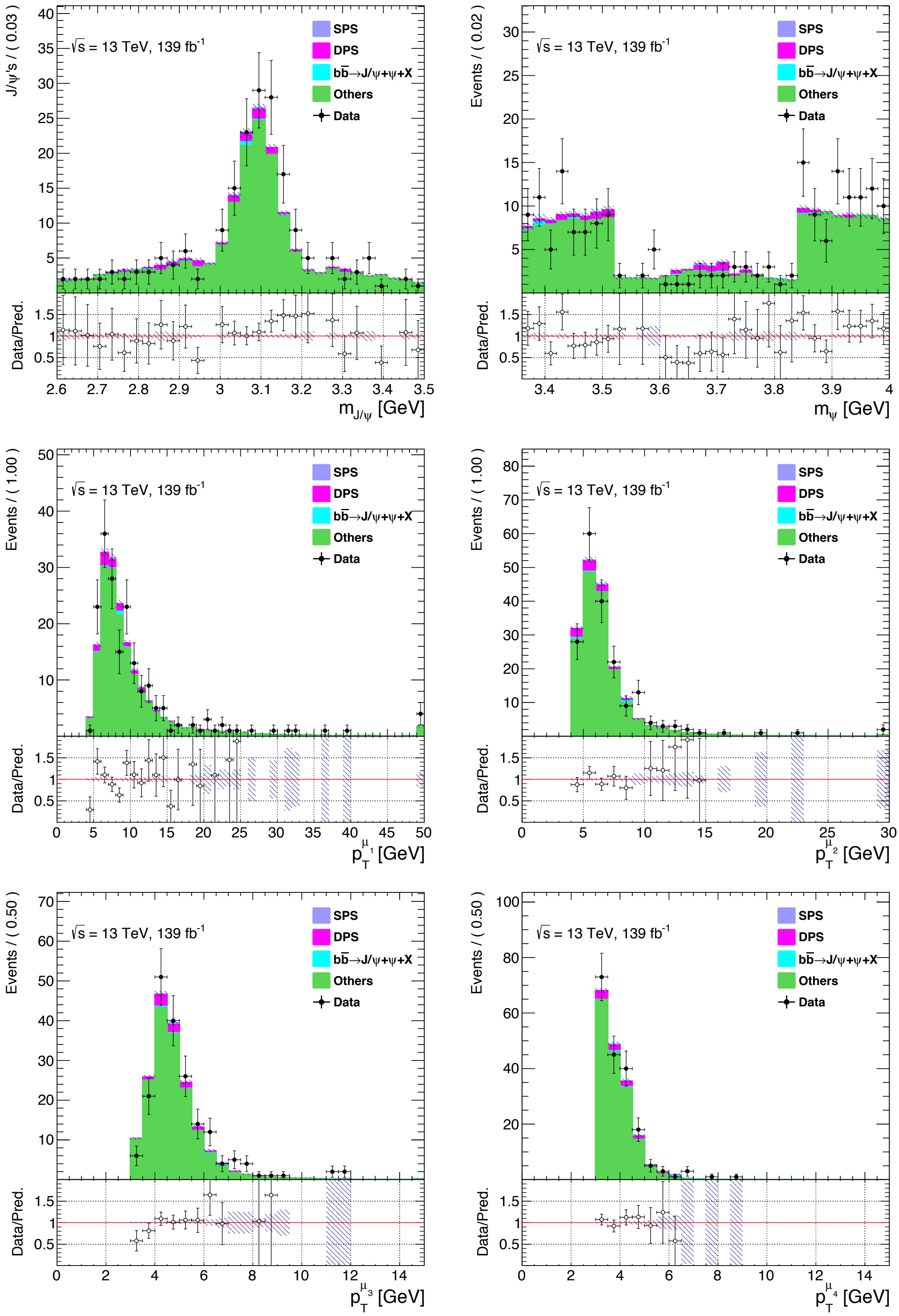

Figure 6.15 The distributions of kinematic variables in the J/ψ+$\psi(2S)$ channel in the mass sideband region, with the DPS CR cuts and corrections applied. The error bars represent statistical uncertainties.

6.5.4 Distributions in the nominal region

To validate the background estimation, the data and predicted distributions are compared in the nominal region as shown in Figure 6.16-6.17. An overall good agreement is seen.

6.6 p_T correction of bottomonium

The η_b signal is generated by JHU interfaced to Pythia. To correct the potential mismodelling of p_T spectrum, the p_T distribution of η_b is compared to the measurement of Υ production from LHCb[79] using 13 TeV pp collisions and from ATLAS[80] using 7 TeV pp collisions. The masses of η_b, χ_{b0} and $\Upsilon(1S)$ are similar which are 9.388 GeV, 9.858 GeV and 9.460 GeV respectively, so their p_T spectrum should also be similar. The correction weight extracted for η_b can be used for χ_{b0}. For comparison, truth events are generated with center-of-mass energy of $\sqrt{s} = 7$ pp and center-of-mass energy of $\sqrt{s} =$ 13 pp individually, without any event and object selections.

The p_T distributions with center-of-mass energy of $\sqrt{s} = 13$ TeV are compared to LHCb measurement as shown in Figure 6.18, with range of $p_T(\eta_b) < 3$ GeV scaled to the same area. There is a good agreement in the low p_T range, but the high p_T events from JHU and Pythia are obviously overestimated. The distributions in different rapidity (y) bins have similar shape, indicating that the correction weights should be y independent.

The p_T distributions with center-of-mass energy of $\sqrt{s} = 7$ TeV are compared to ATLAS measurement as shown in Figure 6.19, with range of $p_T(\eta_b) < 10$ GeV scaled to the same area. Similar y independent ratio is observed.

To retrieve the correction on η_b p_T, firstly, ATLAS measurement result is scaled by multiplying the ratio of p_T distributions from JHU with center-of-mass energies of $\sqrt{s} =$ 13 TeV and $\sqrt{s} = 7$ TeV as shown in Figure 6.20(a). The ratio is fitted with a third-order polynomial. Then, the correction weight in range of $p_T < 20$ GeV is retrived by comparing the result of LHCb measurement and JHU with center-of-mass energy of $\sqrt{s} = 13$ TeV, while the correction weight in range of $20 < p_T < 70$ GeV is retrieved by comparing the result of ATLAS measurement after scaling to 13 TeV case and JHU with center-of-mass energy of $\sqrt{s} = 13$ TeV. To keep the smoothness of correction weight, the result of ATLAS measurement in the range of $20 < p_T < 30$ GeV is scaled to the result of LHCb measurement as shown in Figure 6.20(b).

The uncertainties of the p_T correction consists of statistical, PDF and scale uncer-

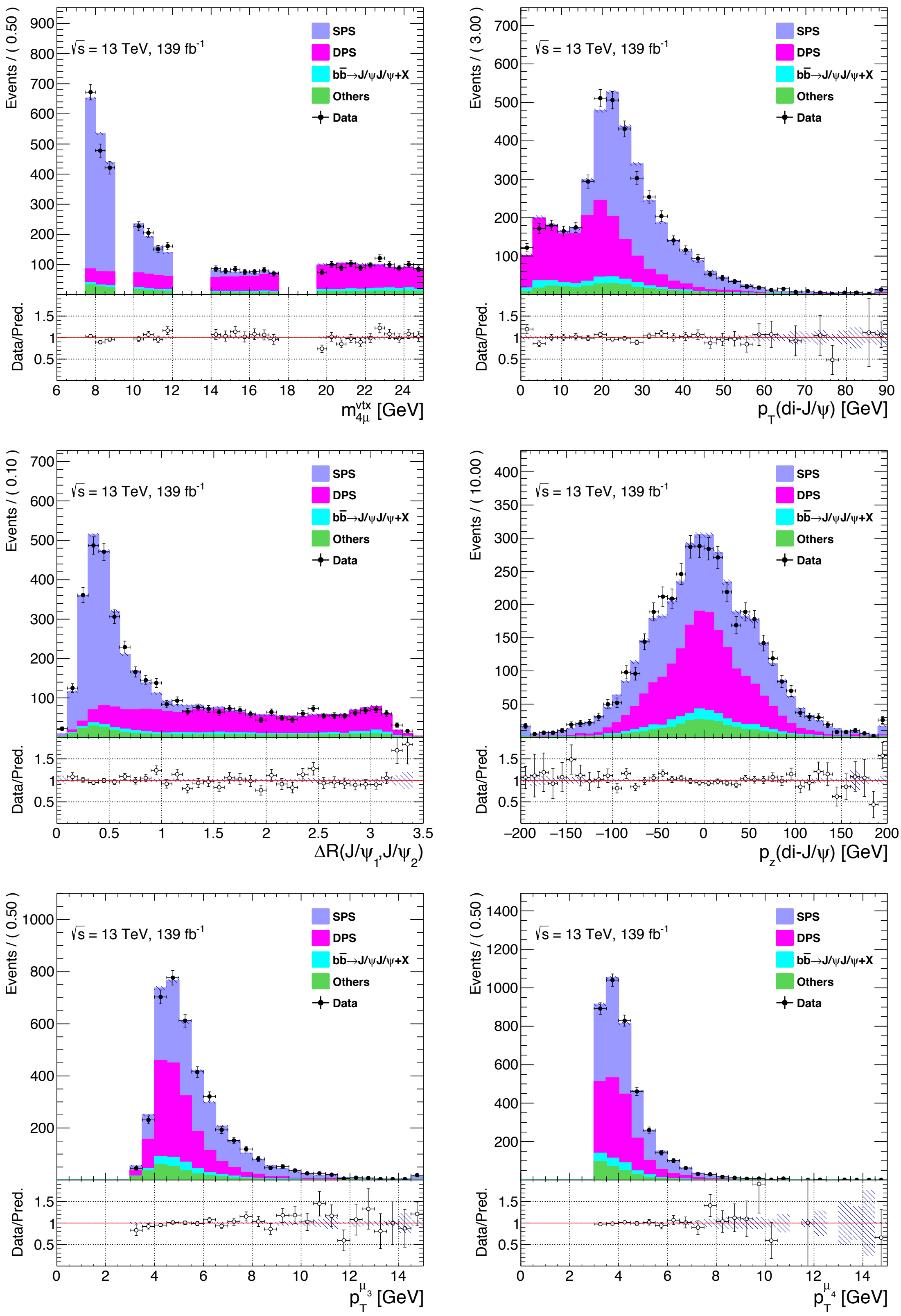

Figure 6.16 The distributions of kinematic variables in the nominal region with estimated backgrounds in the di-J/ψ channel. The error bars represent statistical uncertainties.

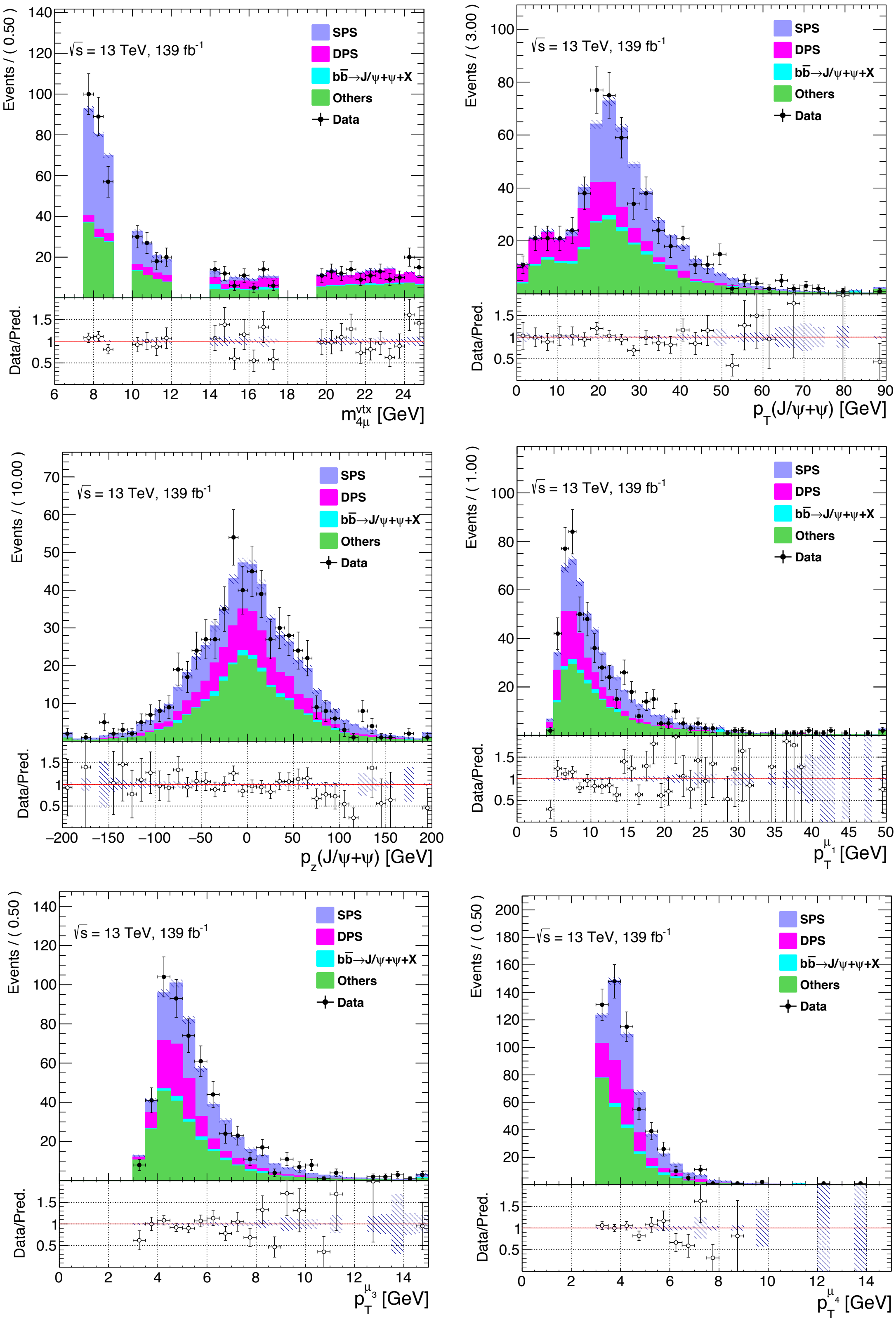

Figure 6.17 The distributions of kinematic variables in the nominal region with estimated backgrounds in the J/ψ+ψ(2S) channel. The error bars represent statistical uncertainties.

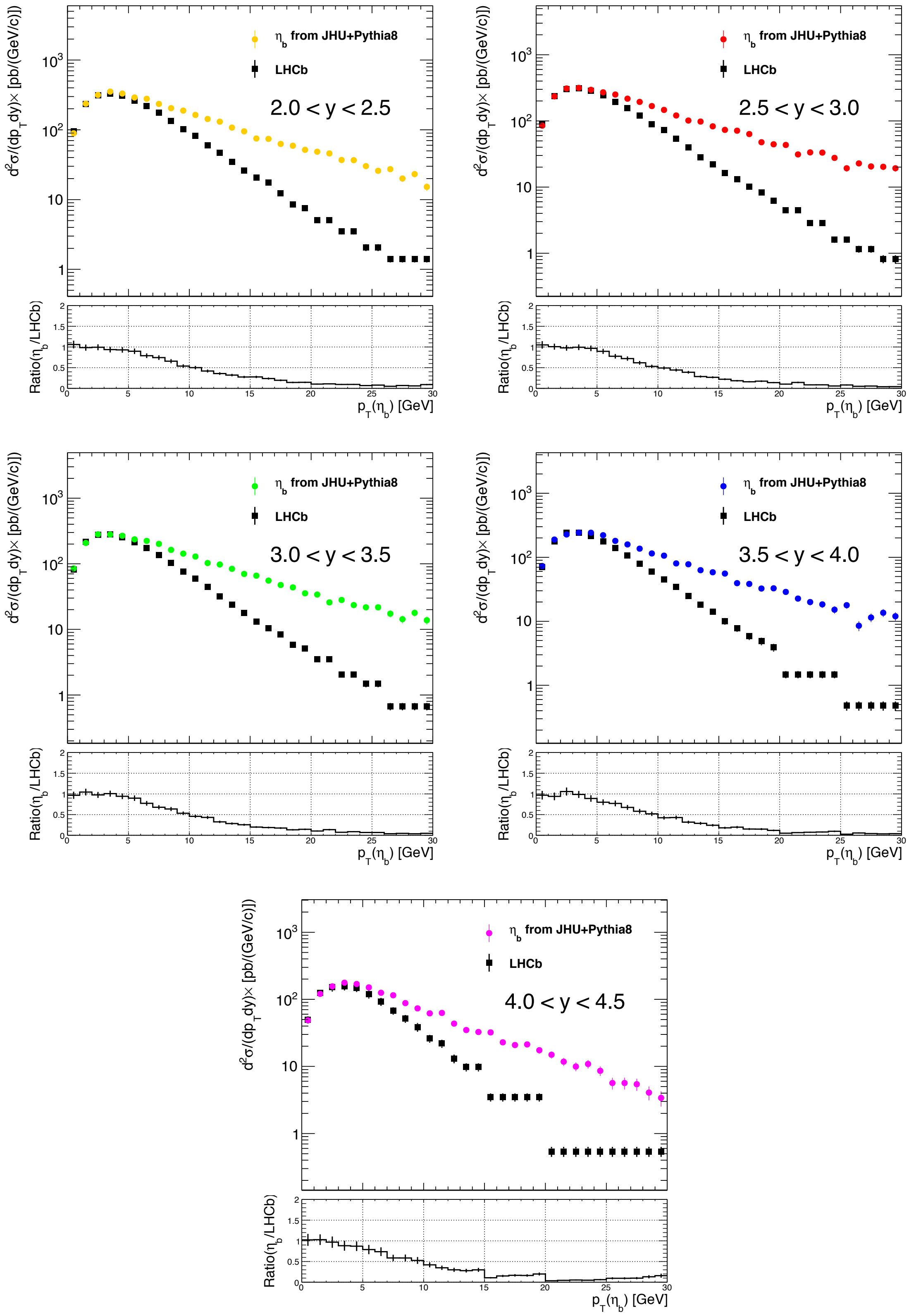

Figure 6.18 p_T distributions with center-of-mass energy of $\sqrt{s}$ = 13 TeV in different y bins compared to LHCb measurement. Range of $p_T(\eta_b)$ < 3 GeV is scaled to the same area for two distributions in each plot.

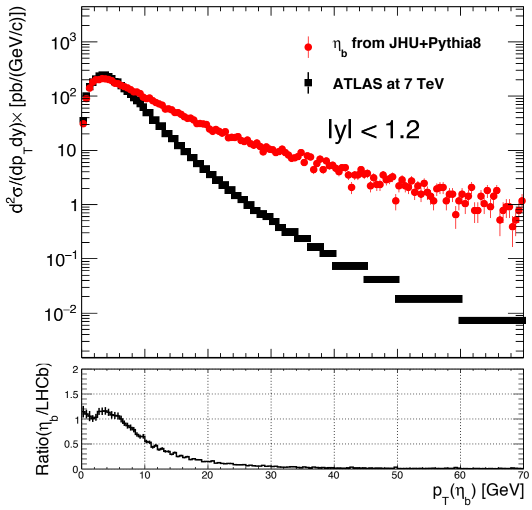

Figure 6.19 p_T distributions with center-of-mass energy of $\sqrt{s} = 7$ TeV in different y bins compared to ATLAS measurement. Range of $p_T(\eta_b) < 10$ GeV is scaled to the same area for two distributions in each plot.

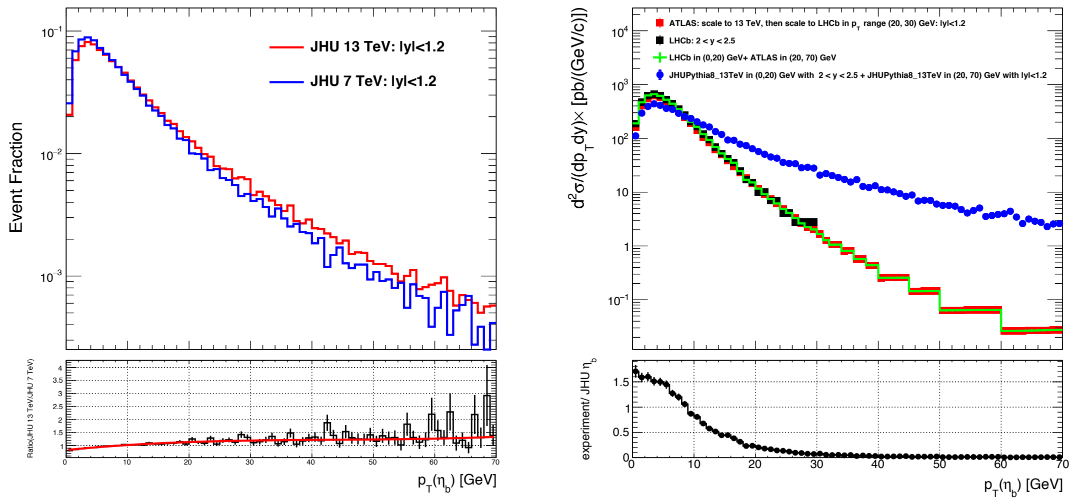

(a) (b)

Figure 6.20 (a) p_T distributions from JHU with center-of-mass energies of $\sqrt{s} = 13$ TeV and $\sqrt{s} = 7$ TeV in range $|y| < 1.2$, scaled to the same area for comparison. (b) Differential cross sections multiplied by the dimuon branching fraction from LHCb and ATLAS measurement. The result of ATLAS measurement in the range of $20 < p_T < 30$ GeV is scaled to the result of LHCb measurement and also for results from JHU. The ratio shows the correction weight (green over blue) tainties. The total uncertainties on η_b and χ_{b0} p_T correction are $+13.1\%/-12.4\%$ and $+12.4\%/-12.3\%$ respectively.

6.7 Systematic uncertainties

Various systematic uncertainties are considered and applied on signal and background components.

1. Experimental uncertainties:
   (a) Muon ID efficiency scale factors:
      - `MUON_EFF_RECO_STAT`
      - `MUON_EFF_RECO_SYS`
      - `MUON_EFF_RECO_SYS_LOWPT`
      - `MUON_EFF_RECO_STAT_LOWPT`

   (b) Muon momentum scales:
      - `MUON_ID`
      - `MUON_MS`
      - `MUON_SCALE`
      - `MUON_SAGITTA_RESBIAS`
      - `MUON_SAGITTA_RHO`

   (c) Modeling of pile-up effect

   (d) Modeling of vertex variable
2. Theoretical uncertainties:
   (a) Modeling of kinematic variables, such as di-J/ψ p_{T}

   (b) Choice of `Pythia` parameter `pT0timesMPI`
3. Systematic uncertainties on data-driven background estimation

The modeling of 4μ and J/ψ vertex variables can be different in data and MC. The vertex variables in MC samples are smeared. The difference in the final results with and without smearing is taken as the systematic uncertainty of vertex modeling. The smearing of L_{xy} is done with a Gaussian term and is applied to each charmonium candidate. The smearing of χ^2/N is achieved by multiplying a constant factor of 1.2 to this variable for each 4μ candidate. The comparison of vertex variables before and after smearing is shown in Figure 6.21.

The choice of Pythia parameter `pT0timesMPI` in the production of SPS events can affect kinematic shape and fit results. The `pT0timesMPI` parameter controls how much the soft di-J/ψ production is suppressed and can be tuned to data in the SPS CR. According to the study on change of negative logarithmic likelihood with different values of `pT0timesMPI`, as shown in Figure 6.22(a), it's found that the SPS events gener-

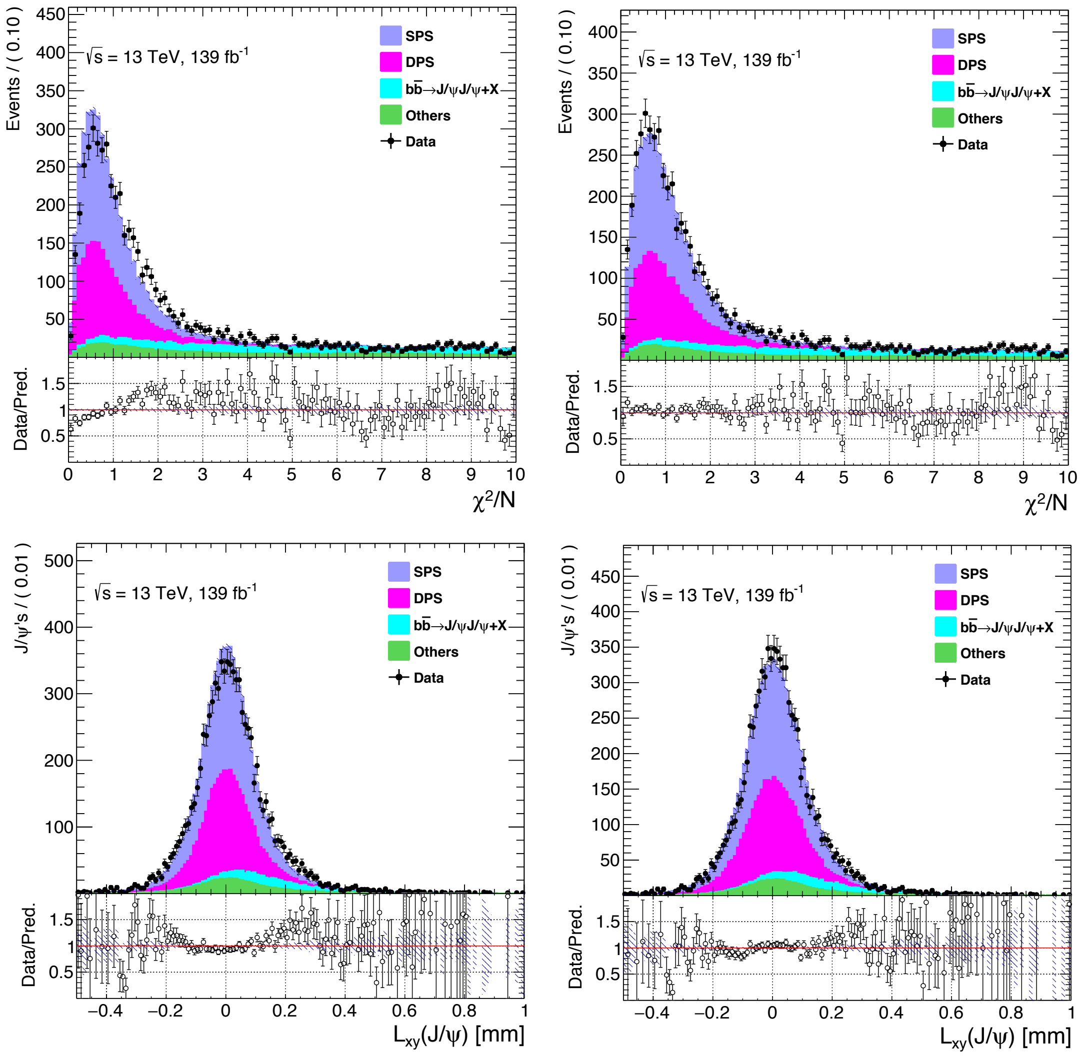

Figure 6.21 The distributions of 4μ vertex χ^2/N and J/ψ candidate's L_{xy} before (left) and after (right) smearing applied on the MC samples, in the nominal region in the di-J/ψ channel. For the χ^2/N distributions, no cuts on χ^2/N or J/ψ L_{xy} are applied. For the L_{xy} distributions, the $\chi^2/N < 3$ cut is applied. The $b\bar{b} \to J/\psi J/\psi + X$ MC is used.

ated with pT0timesMPI=0.61 fit best with data. The effects of 1σ variations (± 0.05) of pT0timesMPI are taken as the theoretical uncertainties of SPS. The distributions of variations are shown in Figure 6.22(b).

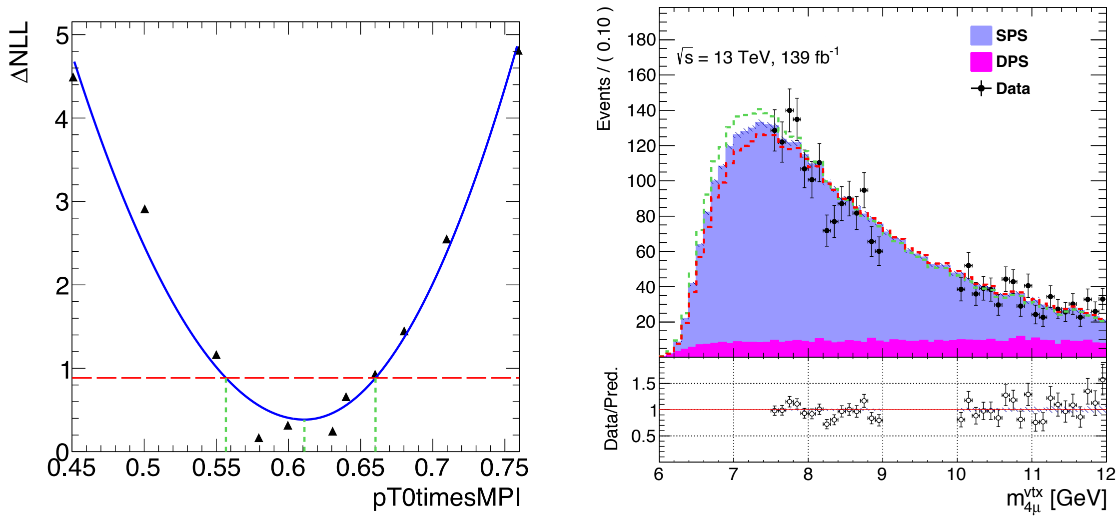

(a) ΔNLL for different values of pT0timesMPI (b) $m_{4\mu}^{\mathrm{vtx}}$ with pT0timesMPI variations

Figure 6.22 (a): the ΔNLL distribution for different values of pT0timesMPI parameter. (b): distributions of the $m_{4\mu}$ with 1 σ variations (green and red dashed lines). The $b\bar{b} \rightarrow J/\psi J/\psi + X$ and "Others" backgrounds have been subtracted from the data.

The systematic uncertainty of "Others" background estimation is estimated by comparing the data-driven prediction and the data in the non-prompt region (so-called "Others" nonclosure). The systematic uncertainty on the transfer factor of the non-prompt background is also evaluated in the non-prompt region by comparing the factors obtained from prediction and data.

The variations on the SPS and DPS normalizations in the nominal region due to different systematics are summarized in Table 6.6-6.7. The recommendations of systematic variations are provided by the corresponding performance groups, and implemented in the analysis framework. In each column, the two numbers correspond to the largest and smallest variations obtained. Some systematic sources (e.g., the muon momentum scale systematics) give rise to variations on the same side of the nominal values (i.e., the up and down variations have the same signs), which can cause problems in the fits. Therefore, they are manually symmetrized. For illustrations, the impact of pileup reweighting, muon momentum scale and 4μ vertex mass are shown in Figure 6.23, where the shaded error bands include the systematics considered.

Table 6.6 The relative variations on the SPS and DPS normalizations in the nominal region due to different systematics in the di-J/ψ channel.

Systematics	SPS	DPS
Luminosity	+1.7%/ − 1.7%	+1.7%/ − 1.7%
Pileup	+0.13%/ − 0.20%	+0.20%/ − 0.33%
`MUON_EFF_RECO_STAT`	+0.01%/ − 0.01%	+0.00%/ − 0.00%
`MUON_EFF_RECO_STAT_LOWPT`	+2.96%/ − 3.10%	+3.62%/ − 3.69%
`MUON_EFF_RECO_SYS`	+0.03%/ − 0.03%	+0.01%/ − 0.01%
`MUON_EFF_RECO_SYS_LOWPT`	+4.74%/ − 4.56%	+5.86%/ − 5.61%
`MUON_ID`	−0.95%/ − 1.47%	−0.74%/ − 0.97%
`MUON_MS`	−0.64%/ − 1.33%	−0.51%/ − 1.17%
`MUON_SCALE`	−0.32%/ − 3.37%	−0.24%/ − 2.96%
`MUON_SAGITTA_RESBIAS`	−1.04%	−0.77%
`MUON_SAGITTA_RHO`	−1.05%	−0.78%
Vertex smearing	−2.55%	−2.46%

Table 6.7 The relative variations on the SPS and DPS normalizations in the nominal region due to different systematics in the J/ψ+$\psi(2S)$ channel.

Systematics	SPS	DPS
Luminosity	+1.7%/ − 1.7%	+1.7%/ − 1.7%
Pileup	+0.15%/ − 0.12%	+0.25%/ + 0.17%
`MUON_EFF_RECO_STAT`	+0.01%/ − 0.01%	+0.00%/ − 0.00%
`MUON_EFF_RECO_STAT_LOWPT`	+2.54%/ − 2.65%	+3.58%/ − 3.63%
`MUON_EFF_RECO_SYS`	+0.03%/ − 0.03%	+0.01%/ − 0.01%
`MUON_EFF_RECO_SYS_LOWPT`	+4.31%/ − 4.14%	+5.84%/ − 5.60%
`MUON_ID`	−1.55%/ − 2.73%	−0.57%/ − 1.11%
`MUON_MS`	−1.43%/ − 2.77%	+0.55%/ − 1.05%
`MUON_SCALE`	−1.51%/ − 4.34%	−0.43%/ − 3.85%
`MUON_SAGITTA_RESBIAS`	−2.34%	−0.61%
`MUON_SAGITTA_RHO`	−2.34%	−0.54%
Vertex smearing	−2.53%	−1.83%

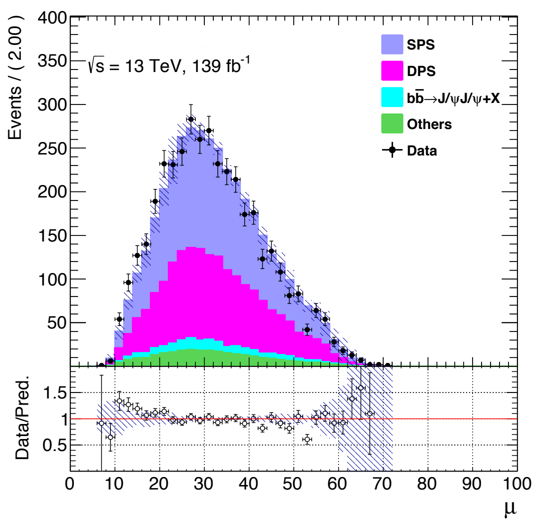

(a) Pileup μ

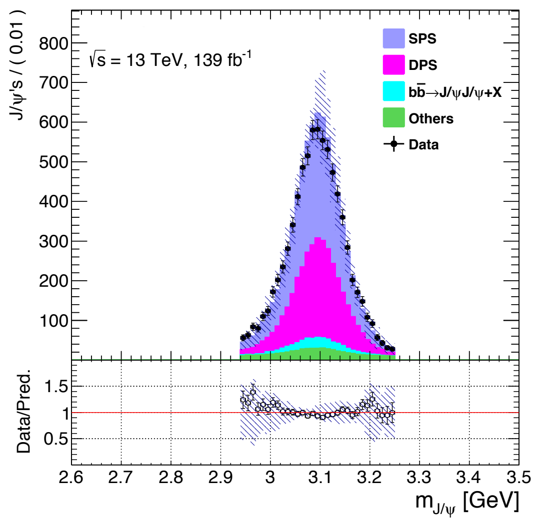

(b) J/ψ candidate mass

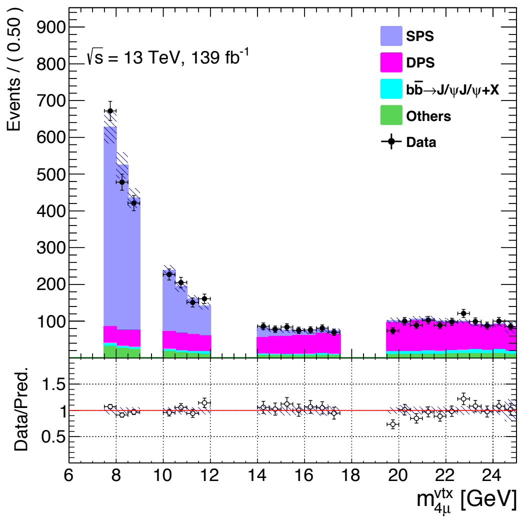

(c) Unconstrained 4μ vertex mass

Figure 6.23 Effects of systematics in the di-J/ψ channel. (a): pileup μ distribution with pileup systematics included in the shaded band.For 2015-2016 (2017-2018) data, average (actual) interactions per bunch crossing are plotted. (b): J/ψ mass distribution with muon momentum scale systematics (`MUON_ID`, `MUON_MS`, `MUON_SCALE`, `MUON_SAGITTA_RESBIAS`, `MUON_SAGITTA_RHO`) included in the shaded band. (c): unconstrained 4μ vertex mass distribution with all systematics included.

6.8 Fit results

The fit results in SR1 and SR2 are described in this section.

Unbinned maximum likelihood fits are conducted to extract signal yields (N_{sig}), mass and width. The likelihood function is

$$\mathcal{L} = \mathcal{L}_{SR}\left(\vec{\alpha}, \vec{\beta}\right) \cdot \mathcal{L}_{CR}\left(\vec{\alpha}\right) \cdot \prod_{j=1}^{K} G\left(\alpha'_j; \alpha_j, \sigma_j\right), \quad (6.5)$$

$$\mathcal{L}_{SR} = \frac{(s+b)^N}{N!} e^{-(s+b)} \prod_{i=1}^{N} \left[\frac{s}{s+b} f_s(x_i; \vec{\alpha}, \vec{\beta}) + \frac{b}{s+b} f_b(x_i; \vec{\alpha})\right], \quad (6.6)$$

$$\mathcal{L}_{CR} = \frac{b_{CR}^{N_{CR}}}{N_{CR}!} e^{-b_{CR}}, \; b_{CR} = b \cdot t(\alpha_t) \quad (6.7)$$

where $\mathcal{L}_{SR}$ and $\mathcal{L}_{CR}$ are the likelihood functions in the signal region and control region respectively, $\vec{\beta}$ are POIs (such as N_{sig}, mass and width), α_j are NPs. Each NP is contrained by a Gaussian with mean α_j and width σ_j ($\sigma_j = 1$ by construction). In the $\mathcal{L}_{SR}$, s, b, N, f_s and f_b are the signal yields, background yields, number of data events, signal and background PDFs. The t in $\mathcal{L}_{CR}$ is a transfer factor relating the background yields in signal region (b) and control region (b_{CR}) that depends on systematic NPs. All systematic uncertainties described in Section 6.7 are considered. Since the normalization of signals and backgrounds are freely floating in the fit, only systematic uncertainties affecting shape are considered.

6.8.1 Fit results in SR2

The SR2 with 4μ mass region of $9 < m_{4\mu} < 10$ GeV is defined to search for the $\eta_b \to J/\psi J/\psi \to 4\mu$ and $\chi_{b0} \to J/\psi J/\psi \to 4\mu$ decays. The signal is modeled by a three-component Gaussian with a common mean. The SPS and DPS backgrounds are modeled by a second order polynomial. The systematic uncertainties with impact larger than 1% are included in the fit and listed in Table 6.8. Five of the six shape NPs affect the signal, and the rest one affects the backgrounds. The corresponding distributions of variations are shown in Figure 6.24.

The pre-fit and post-fit $m_{4\mu}^{con}$ distributions are shown in Figure 6.25-6.26. No obvious excess is observed.

The signal yield N_{sig} and the product of production cross section times branching

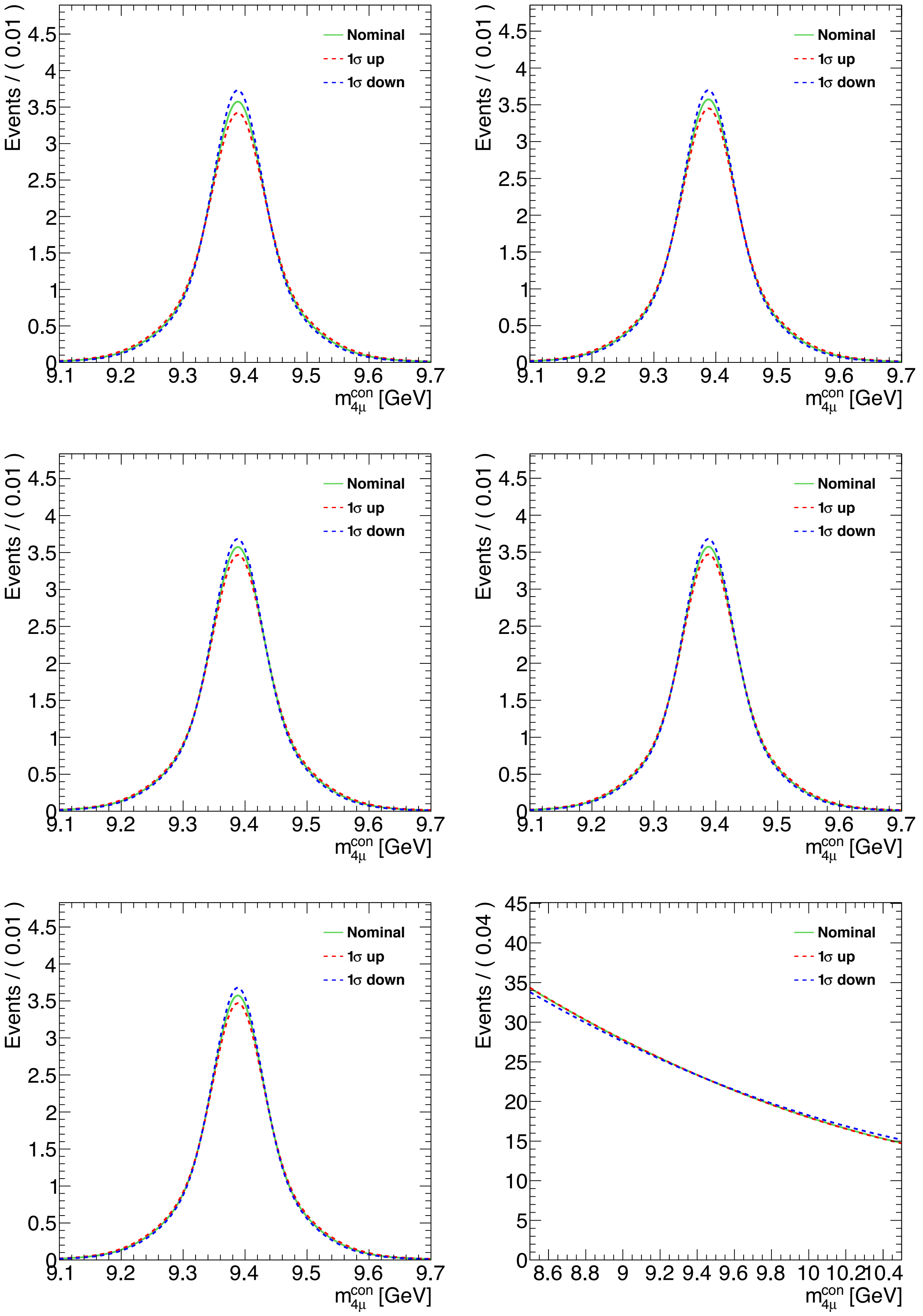

Figure 6.24 Distributions of nominal and systematic variations for $\eta_b \to J/\psi J/\psi \to 4\mu$ signal and backgrounds. The distributions for $\chi_{b0} \to J/\psi J/\psi \to 4\mu$ signal are very similar.

Table 6.8 The effect of systematic uncertainties on signal and background predictions in the fit region $m_{4\mu}^{con} \in [8.5, 10.5]$ GeV, in the rare bottomonium decay search. Only systematic uncertainties with impact larger than 1% are considered.

Systematics		η_b	χ_{b0}	background
Normalization	Luminosity	$\pm1.7\%$	$\pm1.7\%$	–
	`MUON_EFF_RECO_STAT_LOWPT`	$+2.8\%/-3.0\%$	$+2.9\%/-3.0\%$	–
	`MUON_EFF_RECO_SYS_LOWPT`	$+4.7\%/-4.5\%$	$+4.8\%/-4.6\%$	–
	Vertex smearing	$\pm2.4\%$	$\pm2.5\%$	–
	Bottomonium p_T correction	$+13.1\%/-12.4\%$	$+12.4\%/-12.3\%$	–
Shape & Normalization	`MUON_ID`	$\pm1.4\%$	$\pm1.0\%$	–
	`MUON_MS`	$\pm1.3\%$	$\pm1.0\%$	–
	`MUON_SCALE`	$\pm2.5\%$	$\pm2.2\%$	–
	`MUON_SAGITTA_RESBIAS`	$\pm1.1\%$	$\pm1.0\%$	–
	`MUON_SAGITTA_RHO`	$\pm1.1\%$	$\pm1.0\%$	–
	SPS theory	–	–	$\pm1.0\%$
	MC stat.	–	–	$\pm1.0\%$

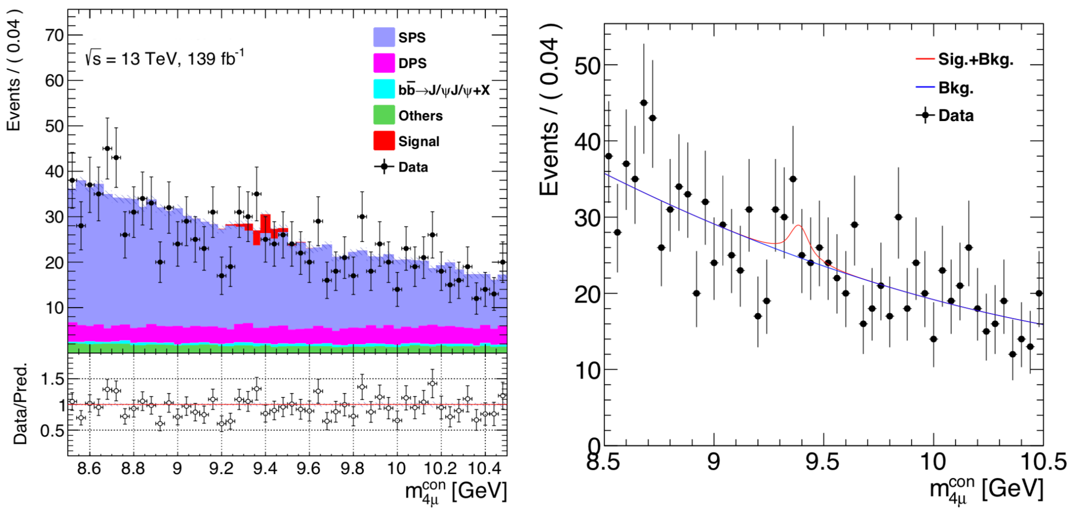

Figure 6.25 The pre-fit (left) and post-fit (right) $m_{4\mu}^{con}$ distributions in the $\eta_b \to 2J/\psi$ search.

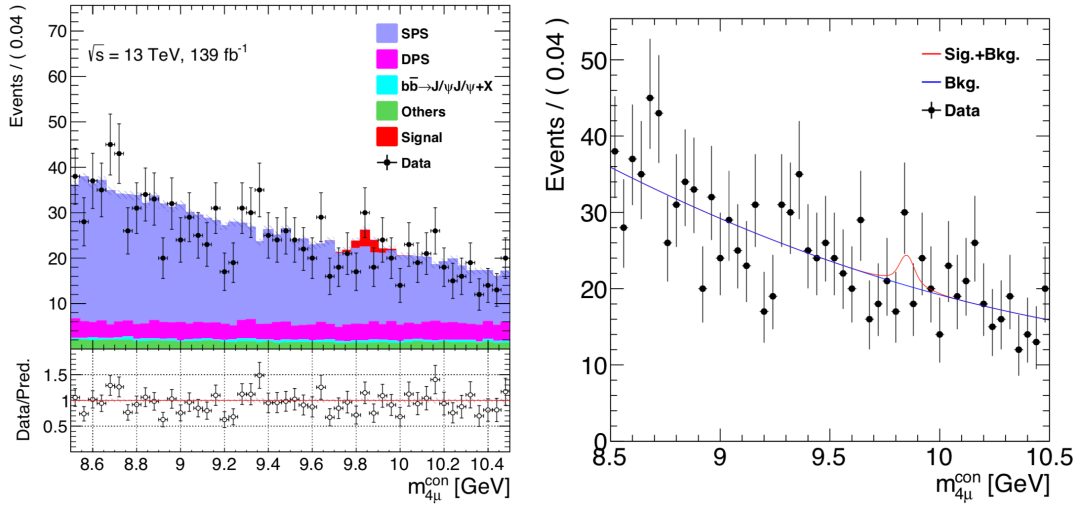

Figure 6.26 The pre-fit (left) and post-fit (right) $m_{4\mu}^{con}$ distributions in the $\chi_{b0} \to 2J/\psi$ search.

ratio of rare bottomonium decays ($\sigma \times \mathrm{BR}$) satisfy the relation:

$$N_{sig} = \sigma(pp \to \eta_b/\chi_{b0}+X)\times\mathrm{BR}(\eta_b/\chi_{b0} \to 2J/\psi)\times\mathrm{BR}^2(J/\psi \to \mu\mu)\times\left(\sum_i \mathcal{L}_i\epsilon_i\right) \quad (6.8)$$

where $\mathcal{L}_i$ is the luminosity in each period and ϵ_i is the corresponding signal efficiency.

The 95% confidence level upper limits on $\sigma \times \mathrm{BR}$ are set with the CL_s method described in Section 8.8.1, and summarized in Table 8.8.1.

Table 6.9 The observed and expected upper limits at 95% confidence level on $\sigma \times \mathrm{BR}$ of η_b and χ_{b0}. Both statistical and systematic uncertainties are included.

$\sigma(pp \to \eta_b + X) \times \mathrm{BR}(\eta_b \to 2J/\psi)$		$\sigma(pp \to \chi_{b0} + X) \times \mathrm{BR}(\chi_{b0} \to 2J/\psi)$	
best fit	obs. (exp.) limit	best fit	obs. (exp.) limit
64.1 ± 61.5 pb	177 (126) pb	35.2 ± 34.1 pb	103 (76) pb

6.8.2 Fit results in SR1

The SR1 is defined to search for new resonances in the di-J/ψ channel and $J/\psi + \psi(2S)$ channel. Since there is no obvious data excess in the SR2, the SR2 is included in the fit of SR1 to constrain backgrounds better.

Unbinned maximum likelihood fits are used to extract signal masses and widths in the 4μ mass spectra of fit regions. Two fit regions are defined based on the baseline conditions:

- Fit SR: $m_{4\mu}^{\mathrm{con}} < 11$ GeV and $\Delta R < 0.25$
- Fit CR: $m_{4\mu}^{\mathrm{con}} < 11$ GeV and $\Delta R \geq 0.25$

The SPS background is constrained in the fit CR, in which the SPS background dominates as shown in Figure 6.27.

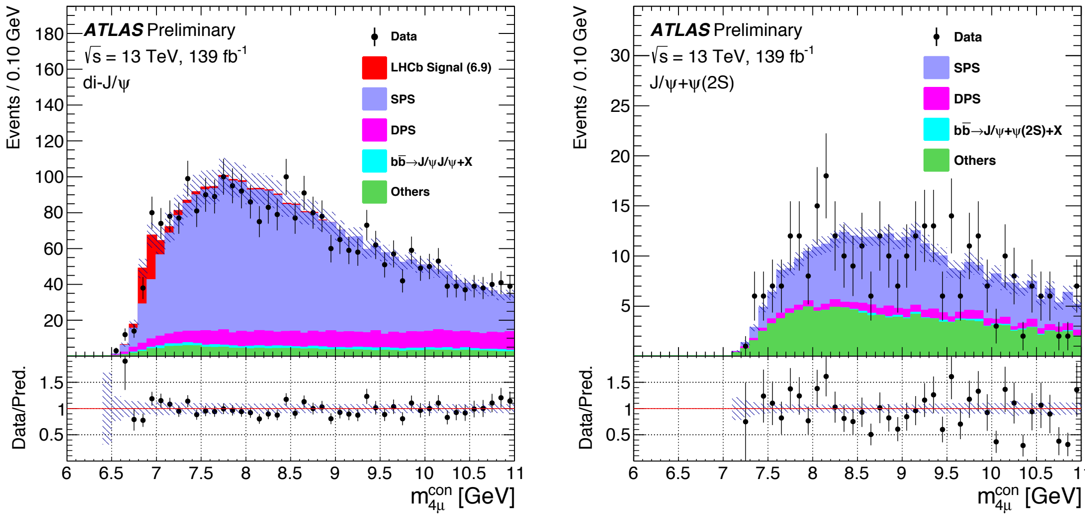

Figure 6.27 The pre-fit 4μ mass spectra of fit CR in the di-J/ψ (left) and $J/\psi + \psi(2S)$ (right) channels.

The pre-fit 4μ mass spectra in the fit SR with $m_{4\mu}^{\text{con}} < 11$ GeV are shown in Figure 6.28. The signal $X(6900)$ is scaled to data in excess of the total predicted background. There are obvious excesses in both channels. Additional kinematics distributions are shown in Appendix A.

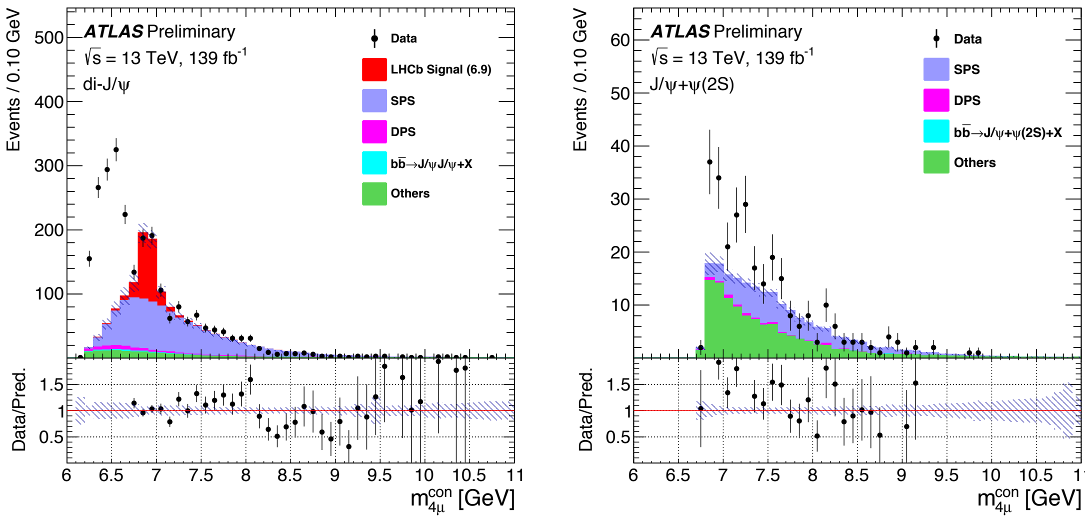

Figure 6.28 The pre-fit 4μ mass spectra of fit SR in the di-J/ψ (left) and $J/\psi + \psi(2S)$ (right) channels.

In the di-J/ψ channel, a three-resonance signal model with interferences among signal resonances is applied. The signal model reads

$$f_s(x) = \left| \sum_{i=0}^{2} \frac{z_i}{x^2 - m_i^2 + i m_i \Gamma_i} \right|^2 \sqrt{1 - \frac{4m_{J/\psi}^2}{x^2}} \otimes R(\alpha), \tag{6.9}$$

where m_i and Γ_i are the masses and widths of each resonance, z_i is a complex number representing the amplitude of $i-$th resonance (z_1 is fixed to unity with zero phase), the square root factor is the phase space factor, and $R(\alpha)$ is a resolution function. The resolution function $R(\alpha)$ is modeled with a triple Gaussian, as shown in Figure 6.29(a). Although the standard muons are used in the reconstruction and selection, only their ID tracks are used in the vertex reconstruction. So only `MUON_ID` and `MUON_SCALE` are relevant. Since applying muon calibrations on the ID tracks can improve the agreement between MC events and data. Tracks with muon calibration are used as nominal, and with `MUON_ID` and `MUON_SCALE` variations are used for systematic uncertainties. After applying muon calibration factors on the muons' tracks, the resultant $m_{4\mu}^{\mathrm{con}}$ will change. To rescue, an additional calibration factor is multiplied to the tracks such that the J/ψ mass is restored to the value recorded in PDG. In this case, impacts of `MUON_ID` and `MUON_SCALE` are negligible. The difference between resolutions with and without muon calibrations is treated as the systematic uncertainty, as shown in Figure 6.29(b). Since the J/ψ momentum entering $m_{4\mu}^{\mathrm{con}}$ calculation depends on the opening angle between the two J/ψ's, there is a correlation between $m_{4\mu}^{\mathrm{con}}$ and its resoltuion. The resolution derived in 6.5 GeV< $m_{4\mu}^{\mathrm{con}}$ <6.7 GeV is used as the nominal, and the ones in the other two regions ($m_{4\mu}^{\mathrm{con}}$ <6.5 GeV and 6.7 GeV< $m_{4\mu}^{\mathrm{con}}$ <7.1 GeV) are used as systematic variations, as shown in Figure 6.29(c). The nominal mass resolution is 23 MeV for mass around 6.9 GeV, and 29 MeV for mass around 7.1 GeV. The region of resolutions is 18-29 MeV.

Figure 6.30(a)(b) shows the fitted 4μ mass spectra in the di-J/ψ channel. The obtained masses and widths of resonances are summarized in Table 6.11. For the signal model with N interfering resonances, there are 2^{N-1} solutions with equal fit quality (same masses and widths, but different z_i)[81]. In the di-J/ψ channel, there are 3 interfering resonances, thus there are four solutions. The other two solutions are very similar to the solutions shown in Figure 6.30. The absolute values and complex phases of z_i of the four solutions are given in Table 6.10.

The significance of a resonance is calculated with the asymptotic formula[82] $Z = \sqrt{2 \ln \frac{L(\hat{z}_3,\hat{\theta})}{L(z_3=0,\hat{\hat{\theta}})}}$, where $\hat{z}_3$ and $\hat{\theta}$ are the values for z_3 and nuisance parameters that maximize the likelihood L, while $\hat{\hat{\theta}}$ denotes the values of θ that conditionally maximize L for

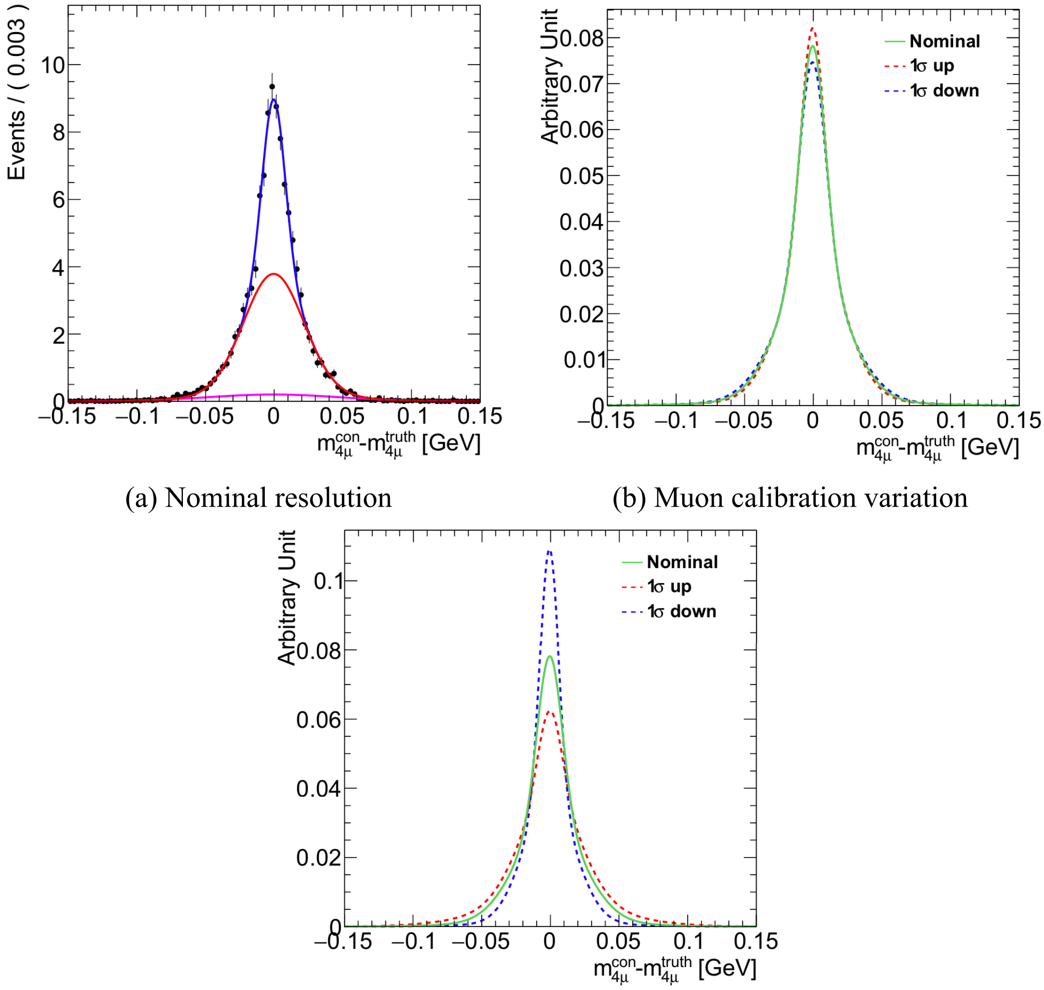

(a) Nominal resolution

(b) Muon calibration variation

(c) 4μ mass resolution

Figure 6.29 The nominal (a) and systematic variations (b) of the 4μ mass resolution in the di-J/ψ channel. (c) The μ mass resolutions in different mass ranges.

Table 6.10 The absolute values and complex phases of z_i of the four solutions shown in the di-J/ψ channel. Note that z_1 is normalized to unity with zero phase. (a) and (b) correspond to Figure 6.30(a) and (b).

	$\|z_0\|$	$\|z_1\|$	$\|z_2\|$	ϕ_0	ϕ_1	ϕ_2
(a)	1.145585	1.0	0.272531	2.925018	0.0	-1.127907
(b)	0.969260	1.0	0.315454	2.821472	0.0	-1.832527
(c)	1.145566	1.0	0.272467	2.923983	0.0	-1.127250
(d)	0.969244	1.0	0.315380	2.820436	0.0	-1.831870

the case of $z_3 = 0$, with all other shape parameters of the three resonances fixed. Note that the normalization s of all signal structures belongs to θ.

The third resonance which is consistent with the $X(6900)$ observed by LHCb[67] is observed with a significance of 10σ. A broad structure at threshold is also observed with a significance far above 5σ. Although the near threshold structure is explained by two interfering resonances, it could result from other physical processes e.g. feed down from di-charmonium resonances with higher masses. A fit model of two interfering resonances is also checked, but the fit quality is much worse than the fit quality of the signal model with three interfering resonances. The details are in Appendix B.

In the $J/\psi + \psi(2S)$ channel, due to lower statistics, two models (model A and model B) are used. Model A considers the same resonances in the di-J/ψ channel which can also contribute to the $J/\psi + \psi(2S)$ channel, plus a standalone resonance. It reads

$$f_s(x) = \left(\left| \sum_{i=0}^{2} \frac{z_i}{x^2 - m_i^2 + im_i\Gamma_i} \right|^2 + \left| \frac{z_3}{x^2 - m_3^2 + im_3\Gamma_3} \right|^2 \right) \sqrt{1 - \left(\frac{m_{J/\psi} + m_{\psi(2S)}}{x} \right)^2} \otimes R(\alpha), \tag{6.10}$$

Where the first three resonances are fixed to the results obtained in the di-J/ψ channel. Model B only assumes a standalone resonance. The modeling method of the resolution function is the same as the method used in the di-J/ψ channel. The region of resolutions is 26-46 MeV.

Figure 6.30(c)(d) shows the fitted 4μ mass spectra in the J/ψ+ψ(2S) channel. The obtained masses and widths of resonances are summarized in Table 6.11. In the $J/\psi + \psi(2S)$ channel, model A describes data better than model B, with a global significance of 4.6σ. The global significance of the signal is estimated by fixing its shape parameters (z_i, ϕ_i, m_i and Γ_i of each peak) to their best fit values, and using the asymptotic formula $Z = \sqrt{2 \ln \frac{L(\hat{s},\hat{\theta})}{L(s=0,\hat{\hat{\theta}})}}$, where $\hat{s}$ is the value of the global signal yield. The second resonance around 7.2 GeV with significance of 3.2σ is also hinted by the LHCb[67].

The effect of systematic uncertainties for both channels on the extracted masses and widths are summarized in Table 6.12. In the di-J/ψ channel, the influence of a fourth standalone resonance is considered, whose parameters are fixed to the values obtained for the standalone fourth resonance in the J/ψ+ψ(2S) channel. The changes in fitted masses and widths of the other three resonances are treated as systematic uncertainties in the di-J/ψ channel. The transfer factor uncertainties in the di-J/ψ channel is largely dominated

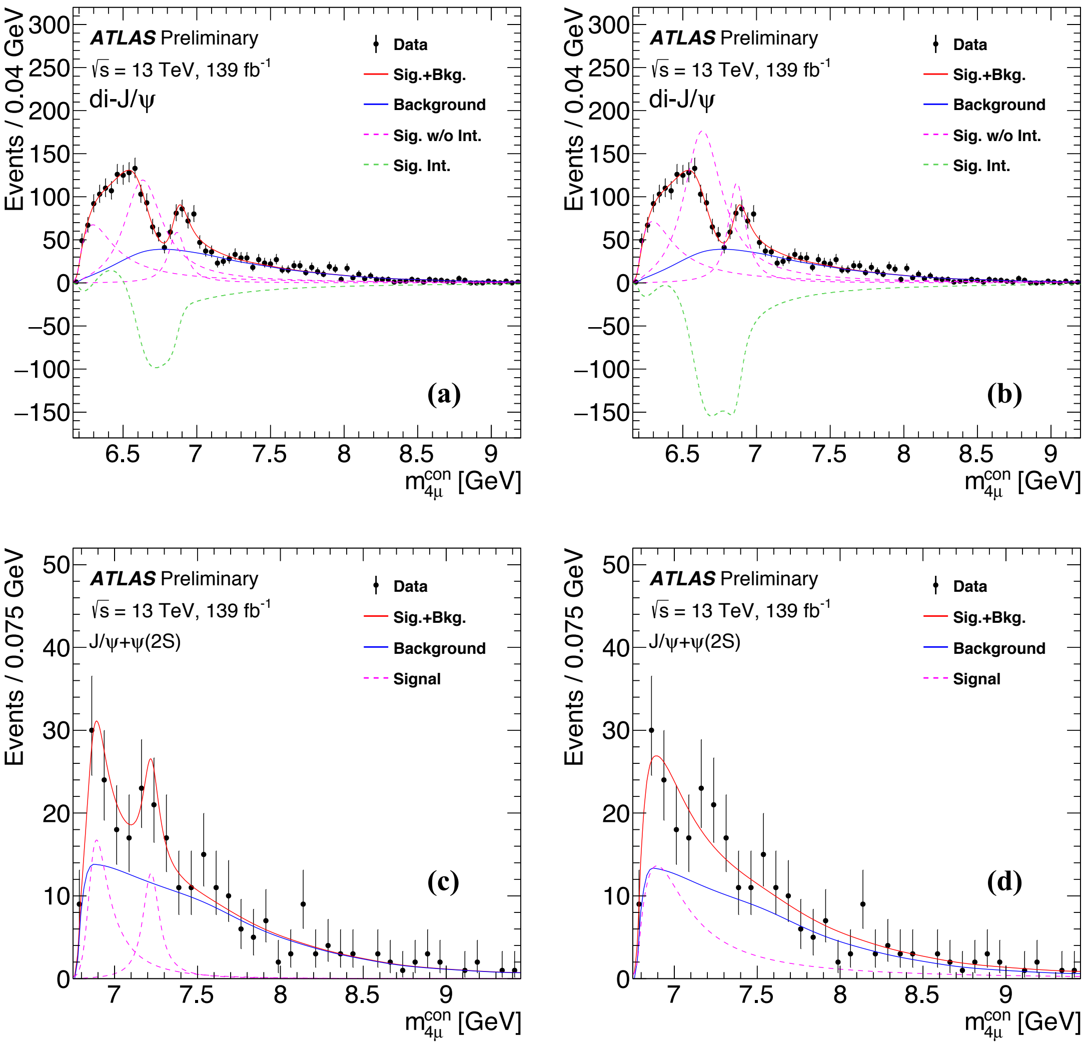

Figure 6.30 The post-fit 4μ mass spectra in the di-J/ψ (a,b) and J/ψ+ψ(2S) (c,d) channels.

Table 6.11 The extracted masses and widths of the resonances in the di-J/ψ and J/ψ+ψ(2S) channels. The first errors in each value are statistical while the second ones are systematic.

(GeV)	m_0	Γ_0	m_1	Γ_1
di-J/ψ	$6.22 \pm 0.05^{+0.04}_{-0.05}$	$0.31 \pm 0.12^{+0.07}_{-0.08}$	$6.62 \pm 0.03^{+0.02}_{-0.01}$	$0.31 \pm 0.09^{+0.06}_{-0.11}$
	m_2	Γ_2	—	
	$6.87 \pm 0.03^{+0.06}_{-0.01}$	$0.12 \pm 0.04^{+0.03}_{-0.01}$	—	
(GeV)		m_3	Γ_3	
J/ψ+ψ(2S)	model A	$7.22 \pm 0.03^{+0.02}_{-0.03}$	$0.10^{+0.13+0.06}_{-0.07-0.05}$	—
	model B	$6.78 \pm 0.36^{+0.35}_{-0.54}$	$0.39 \pm 0.11^{+0.11}_{-0.07}$	—

by the SPS theory uncertainty, so it is not treated as a separate NP. In the J/ψ+ψ(2S) channel, the interference between the fourth resonance and the other three resonances are considered. The changes in the fitted mass and width of the fourth resonance are also treated as systematic uncertainties.

Table 6.12 The effect of systematic and statistical uncertainties on the masses and widths in the di-J/ψ channel and model A of the J/ψ+ψ(2S) channel.

Systematic	di-J/ψ						J/ψ+ψ(2S)	
Uncertainties (MeV)	m_0	Γ_0	m_1	Γ_1	m_2	Γ_2	m_3	Γ_3
SPS theory	7	15	4	20	5	6	<1	
SPS di-charmonium p_T	<1	8	4	14	5	7	<1	
Background MC statistics	<1	8	4	14	5	7	<1	
Mass resolution	19	34	3	21	4	9	<1	4
Fit bias	43	58	10	56	11	16	13	41
Nonclosure	<1						<1	
Transfer factor	—						<1	16
Presence of fourth resonance	29	49	11	108	60	18	—	
Interference of fourth resonance	—						29	11
Data statistics	50	119	34	88	30	39	28	130

CHAPTER 7 PHENOMENOLOGY: GENERIC HEAVY HIGGS BOSONS

This chapter introduces the phenomenology study of the generic heavy Higgs bosons which have dimension-six effective interactions with the SM particles. The expected exclusion regions of parameter space (dimension-six coupling parameters f_W and f_{WW}) with 139 fb^{-1}, 300 fb^{-1} and 3 ab^{-1} LHC data are shown[83].

7.1 Motivation

In the SM, there is only one Higgs boson, but it may not be the case in nature. The Higgs boson with mass of 125 GeV discovered by the LHC is probably the lightest one, and the other heavier Higgs bosons just haven't been found yet. Many BSM predict more than one Higgs boson, such as 2HDM and MSSM. Searching heavy Higgs bosons in each phase space according to the properties predicted by each model is not a very efficient solution. Fortunately, there are theory studies about generic heavy Higgs bosons[84-85], where generic means model-independent. In this theory, the heavy Higgs boson have both dimension-four (dim-4) and dimension-six (dim-6) interactions with the SM particles with the expression of the Lagrangian given under the framework of effective field theory (EFT), and the ggF, VBF and VH production channels of the heavy Higgs boson are all studied. The dim-6 effective operators can significantly enhance the momentum of the heavy Higgs boson, so that it can be better distinguished from the SM background. The theory study finds that in the VH production channel, the effect of the dim-6 operators is the largest and the signal significance is the most significant. However, this theory study only focuses on the final state of $pp \to VH \to \ell\nu jjjj$ which is always accompanied by large backgrounds and has low sensitivity. In this thesis, we propose a more significant search method in the VH production channel based on the theory study mentioned above and only the decays of heavy Higgs bosons to vector bosons (W and Z bosons) are considered.

7.2 Effective couplings

In a multi-Higgs field theory, the original Higgs fields are expressed as $\Phi_1, \Phi_2, ...$. Due to the multi-Higgs potential, they are mixed to form the mass eigenstates. We use Φ_h and Φ_H to represent the doublets containing the lightest (h) and the next-to lightest (H) neutral Higgs bosons, respectively. The vacuum expectation values of h and H are v_h and v_H, not the same as the SM value $v = 246$. In the framework of EFT, the leading-order (LO) dim-4 gauge couplings of the h and H are:

$$\begin{aligned}
\mathcal{L}^{(4)}_{hWW} &= \rho_h g m_W h W^\mu W_\mu, \\
\mathcal{L}^{(4)}_{hZZ} &= \rho_h \frac{g m_W}{2\cos^2\theta_W} h Z^\mu Z_\mu, \\
\mathcal{L}^{(4)}_{HWW} &= \rho_H g m_W H W^\mu W_\mu, \\
\mathcal{L}^{(4)}_{HZZ} &= \rho_H \frac{g m_W}{2\cos^2\theta_W} H Z^\mu Z_\mu,
\end{aligned} \tag{7.1}$$

where θ_W and θ_W are the weak mixing angle and the W boson mass respectively. ρ_h and ρ_H are the scaling factors. In the example of the simplest 2HDM, ρ_h and ρ_H are expressed as $\rho_h = \cos(\beta - \alpha)$ and $\rho_H = \sin(\beta - \alpha)$.

In the BSM physics with high energy scale, the heavy Higgs boson H could also have dim-6 effective operators[84]:

$$\mathcal{L}^{(6)}_{HVV} = \sum_n \frac{f_n}{\Lambda^2}\mathcal{O}_n, \tag{7.2}$$

where Λ is the scale and set to 5 TeV in this thesis. The light Higgs boson h also has similar operators. Since its contribution is small and we mainly study the dim-6 operators of the heavy Higgs boson, it's not considered. There are many dim-6 operators, but there are only four dim-6 operators that are not constrained by precision EW data and relevant for the heavy Higgs boson[84]:

$$\begin{aligned}
\mathcal{O}_{WW} &= \Phi^\dagger_H \hat{W}_{\mu\nu}\hat{W}^{\mu\nu}\Phi_H, \\
\mathcal{O}_{BB} &= \Phi^\dagger_H \hat{B}_{\mu\nu}\hat{B}^{\mu\nu}\Phi_H, \\
\mathcal{O}_{W} &= \left(D_\mu\Phi_H\right)^\dagger \hat{W}^{\mu\nu}\left(D_\nu\Phi_H\right), \\
\mathcal{O}_{B} &= \left(D_\mu\Phi_H\right)^\dagger \hat{B}^{\mu\nu}\left(D_\nu\Phi_H\right),
\end{aligned} \tag{7.3}$$

where $\hat{B}_{\mu\nu} = i\frac{g'}{2}B_{\mu\nu}$ and $\hat{W}_{\mu\nu} = i\frac{g}{2}\sigma^a W^a_{\mu\nu}$. After the symmetry breaking, the effective couplings are:

$$\begin{aligned}
\mathcal{L}^{(6)}_{HWW} &= \rho_H g m_W \frac{f_W}{2\Lambda^2}\left(W^+_{\mu\nu}W^{-\mu}\partial^\nu H + h.c.\right) \\
&\quad - \rho_H g m_W \frac{f_{WW}}{\Lambda^2} W^+_{\mu\nu}W^{-\mu\nu}H, \\
\mathcal{L}^{(6)}_{HZZ} &= \rho_H g m_W \frac{c^2 f_W + s^2 f_B}{2c^2\Lambda^2} Z_{\mu\nu}Z^\mu\partial^\nu H \\
&\quad - \rho_H g m_W \frac{c^4 f_{WW} + s^4 f_{BB}}{2c^2\Lambda^2} Z_{\mu\nu}Z^{\mu\nu}H,
\end{aligned} \tag{7.4}$$

where $s = \sin\theta_W$ and $c = \cos\theta_W$. To simplify the parameter space, we set f_B and f_{BB} to 0 to neglect higher order terms $O(s^2)$ and $O(s^4)$. In Equation (7.4), the dim-6 operators with ∂ term can significantly enhance the momentum of the Higgs boson and the associated W/Z boson. The m_W should be the same as the SM value $m_W = gv/2$, we obtain the constraint[84]:

$$\rho_h \frac{v_h}{v} + \rho_H \frac{v_H}{v} + ... = 1. \tag{7.5}$$

Since h is SM-like, ρ_h is close to 1, then ρ_H should be a small value. We take $\rho_H = 0.05$ as the benchmark value. Therefore, there are only 3 free parameters: m_H, f_W and f_{WW}.

In theory, there are also unitarity constraint $|S^\dagger S| = |1-iT|^2 = 1$[84], which requires:

$$\begin{aligned}
&(Re\langle a|T|a\rangle)^2 + (Im\langle a|T|a\rangle - 1)^2 + \sum_{|b\rangle\neq|a\rangle} |\langle b|T|a\rangle|^2 = 1 \qquad (7.6)\\
&\Rightarrow (Re\langle a|T|a\rangle)^2 + \sum_{|b\rangle\neq|a\rangle} |\langle b|T|a\rangle|^2 \leq 1
\end{aligned}$$

7.3 Search channels

Heavy Higgs bosons have been searched for many years in various final states at the LHC. These searches mainly focus on the $H \to ZZ \to 4\ell$ process[86-87] and di-boson final state[88-89] in the ggF production channel. In this thesis, we assume the YUKAWA coupling between the heavy Higgs boson and fermions is small, so that it can escape the direct detection in the ggF and $t\bar{t}H$ production channels. The interactions between the heavy Higgs boson and the W/Z boson dominate. Then, the remaining production channels are VH and VBF.

With dim-4 operators only, in the large mass region, the production cross section of VBF is an order of magnitude larger than that of VH. However, when introducing dim-6 operators, the production cross section of VH is larger than that of VBF as shown in Figure 7.1(a). Thus, VH is the best channel to search for heavy Higgs bosons.

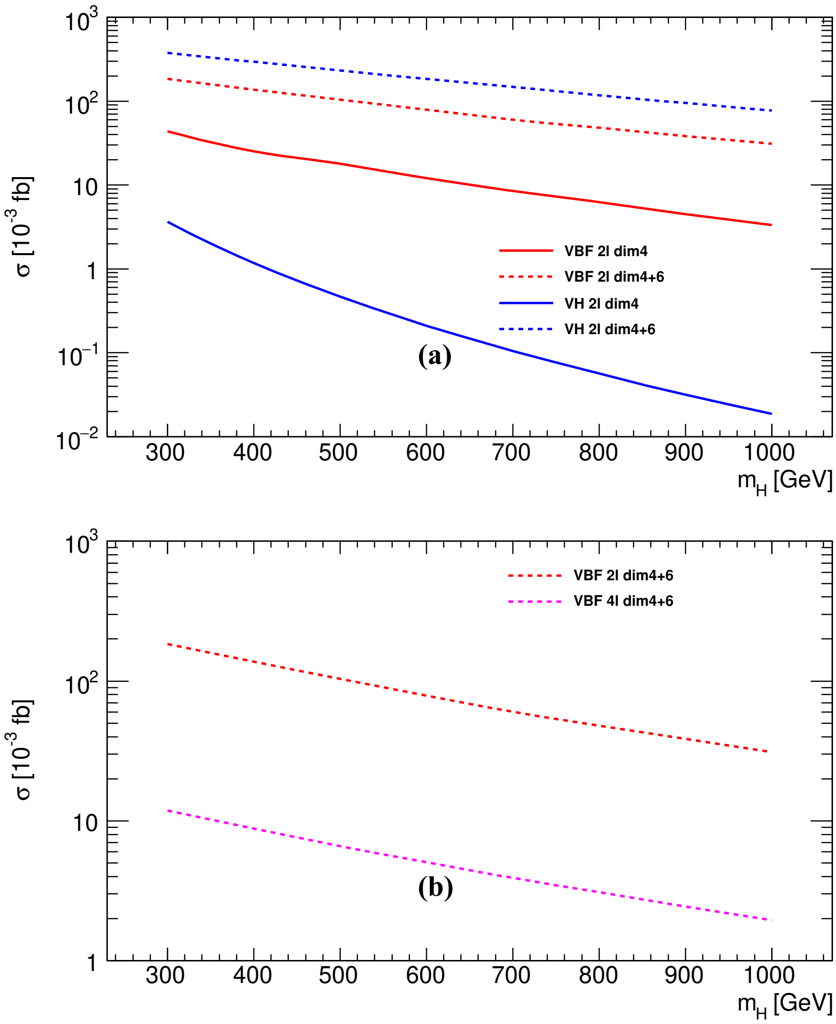

Figure 7.1 In the two-lepton and four-lepton final states, the LO cross section as a function of the heavy Higgs mass (m_H). Dim4: $\rho_H = 0.05$, $f_W = f_{WW} = 0$; Dim4+6: $\rho_H = 0.05$, $f_W = f_{WW} = 1000$. In (a), the VBF and VH processes are $pp \to Hjj \to \ell\ell + 4j$ and $pp \to VH \to \ell\ell + 4j$ respectively; in (b), the VBF 4ℓprocess is $pp \to Hjj, H \to 4\ell$.

Although this thesis only focuses on the VH production channel, the VBF production channel is briefly discussed below. The VBF 2ℓ ($H \to ZZ \to \ell\ell jj$) and 4ℓ ($H \to ZZ \to 4\ell$) final states are compared. Figure 7.1(b) shows the production cross section of the two final states. The cross section of the VBF 4ℓ final state is very small, in the order of $\mathcal{O}(10^{-3} - 10^{-2})$ fb, so it's difficult to detect it. The cross section of VBF 2ℓ final state is large enough. Due to the dim-6 operators, the Higgs boson momentum is enhanced, but some traditional VBF variables (such as $\Delta\eta_{jj}$) become more background-like, as shown in Figure 7.2. After event selections listed in Table 7.2, for the VBF 2ℓ final state, the signal yields are only about 2, while the background yields are about 6000, as shown in Table 7.1.

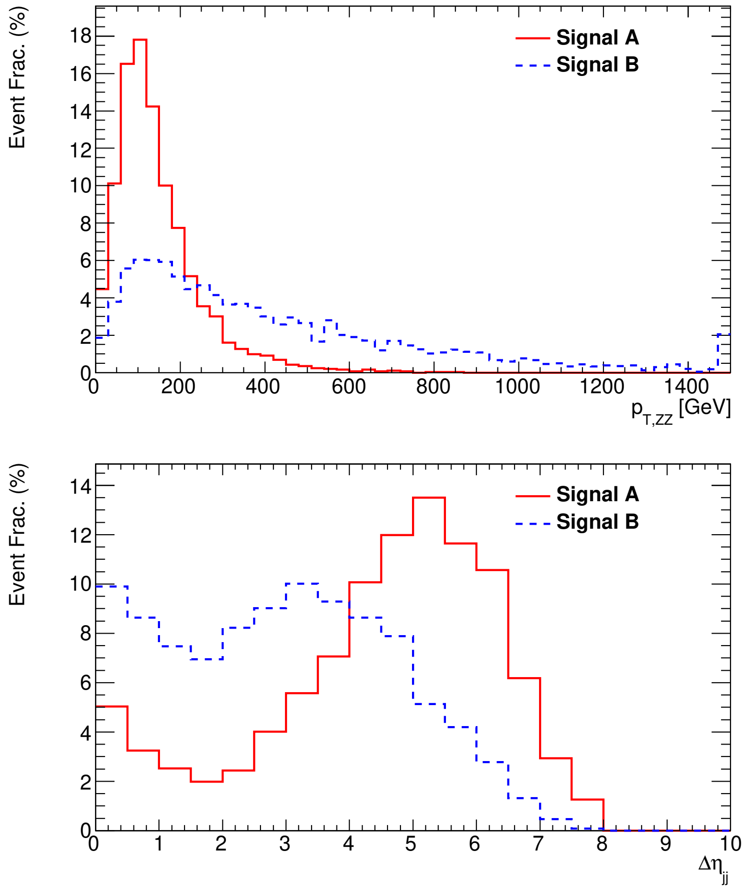

Figure 7.2 The distributions of the heavy Higgs boson p_T ($P_{T,ZZ}$) (top) and $\Delta\eta_{jj}$ of two leading jets (bottom). Signal A: $m_H = 600$ GeV, $\rho_H = 0.1$, $f_W = f_{WW} = 0$, with $\sigma = 3.1 \times 10^{-3}$ fb; Signal B: $m_H = 600$ GeV, $\rho_H = 0.05$, $f_W = f_{WW} = 1000$, with $\sigma = 5.1 \times 10^{-3}$ fb.

Table 7.1 The event yields of signals (dim-4 only and dim-4+dim-6) and backgrounds (Z+QCD Jets, ZV+QCD jets and ZVV) in the VBF 2ℓ final sate, with an integrated luminosity of $139 fb^{-1}$. The event selections are listed in Table 7.2. dim-4 only: $m_H = 600$ GeV, $\rho_H = 0.1$ and $f_W = f_{WW} = 0$; dim-4+dim-6: $m_H = 600$ GeV, $\rho_H = 0.05$ and $f_W = f_{WW} = 1000$。

Signal: dim-4 only	Signal: dim-4+dim-6	Z+QCD Jets	ZV+QCD jets	ZVV
2.0	1.8	5705	207	97

Table 7.2 Event selections for the VBF 2ℓ final state, based on the ATLAS VBF analysis[90]. τ_1 and τ_2 are substructure variables.

<table>
<tr><th>Event selection</th><th>$ZV \to ll + J$</th><th>$ZV \to ll + jj$</th></tr>
<tr><td>$Z \to ll$</td><td colspan="2">$p_T(e) > 15$ GeV, $p_T(\mu) > 10$ GeV
80 GeV $< m_{ll} <$ 100 GeV</td></tr>
<tr><td>VBF tag-jets</td><td colspan="2">Two small-R jets with
$\eta_1\dot{\eta}_2 < 0$, $|\Delta\eta_{jj}^{tag}| > 4.7$, $m_{jj}^{tag} > 770$ GeV
If more than one tag-jet pair, the one with the highest m_{jj}^{tag} is chosen</td></tr>
<tr><td>Jet requirement</td><td>≥ 1 large-R jet with
$p_T > 200$ GeV</td><td>≥ 2 small-R jets with
$p_T >$ (60)30 GeV</td></tr>
<tr><td>Kinematic criteria</td><td>$\min(p_T^{ll}, p_T^{J})/m_{llJ} > 0.3$</td><td>$\sqrt{(p_T^{ll})^2 + (p_T^{jj})^2}/m_{lljj} > 0.4$</td></tr>
<tr><td>V boson tagging</td><td>70 GeV $< m_J <$ 120 GeV,
$\tau_2/\tau_1 < 0.55$</td><td>70 GeV $< m_{jj} <$ 120 GeV</td></tr>
</table>

In the VH production channel, final states with at least two leptons are interested:

- $VH \to VVV \to \ell^+\ell^- jjjj$: the two leptons are of opposite sign (OS) and same flavor, originating from Z boson decay. This is the 2ℓ OS channel.
- $VH \to VVV \to \ell\nu\ell^+\ell^- jj$: one pair of lepton originates from Z boson decay. This is the 3ℓ channel.
- $VH \to VVV \to \ell^\pm\nu\ell^\pm\nu jj$: the two leptons have the same sign (SS). This is the 2ℓ SS channel.

where $\ell = e$ or μ, and jet is denoted by j. In the 2ℓ OS and 3ℓ channels, the heavy Higgs boson can be reconstructed with decay products, while it can not be reconstructed in the 2ℓ SS channel due to two neutrinos. But in the 2ℓ SS channel, the backgrounds are the least and the signal sensitivity is the largest.

7.4 Monte Carlo samples

Signal and background events are all generated by MadGraph5[91] at LO with center-of-mass energy $\sqrt{s} = 13$ TeV and Pythia8[92] is used for the parton shower and hadronization. The generated partons are matched to the parton showers with the MLM method[93].

For signal samples, UFO model with effective interactions in Equation (7.1) and (7.4) is built by FeynFules[94] and passed to MadGraph5 for the production and decays of heavy Higgs boson. The partons are showered and hadronized by Pythia8. There are four parameters (m_H, ρ_H, f_W and f_{WW}) in the model.

In the 2ℓ OS and 2ℓ SS channels, the main backgrounds are the processes containing two leptons:

1. Z+jets: two leptons from Z boson decay plus up to four QCD partons.
2. Diboson: two leptons plus two EW partons and up to two QCD partons.
3. Triboson: two leptons plus four EW partons.
4. $t\bar{t}$: $t \to \ell\nu b$.
5. $t\bar{t}V$: two leptons from t or vector boson decays.

In the 3ℓ channel, the main backgrounds are the processes with three leptons:

1. WZ+jets: three leptons, one neutrino and up to two QCD partons.
2. Triboson: three leptons, one neutrino and two EW partons, including the SM VBF process.
3. $t\bar{t}V$: three leptons.

Afterwards, the produced events are passed to DELPHES[95] for the ATLAS detector response simulation. The small-R jet and large-R jet are clustered with the anti-k_t algorithm[47] with the cone parameter set to 0.4 and 1.0 respectively. If the small-R jet (large-R jet) overlaps with a lepton in the region $\Delta R < 0.4$ ($\Delta R < 1.0$), the small-R jet (large-R jet) is removed. We also require the ΔR of small-R jet and large-R larger than 1.4. Electrons (muons) should satisfy $p_T > 15$ GeV ($p_T > 10$ GeV) and $|\eta| < 2.5$. Small-R jet (large-R jet) should satisfy $p_T > 30$ GeV ($p_T > 50$ GeV) and $|\eta| < 4.0$.

7.5 Event selections

Event selections are optimized according to the signal properties for the 2ℓ OS, 2ℓ SS and 3ℓ channels. Due to the high momentum of signals, the decay products of the heavy Higgs boson and W/Z boson can be clustered with a small cone size, so that they can be reconstructed with a large-R jet or small-R jet. According to the reconstruction of bosons, the above three channels are further divided into several signal regions in the order of signal sensitivity. To avoid the reusing of events, the event selections are performed in the order of regions, that is, the event passing the previous region will not be considered in the next region.

7.5.1 $2\ell OS$ and $2\ell SS$ channels

In the $2\ell OS$ channel, there are two leptons from Z boson decays and four partons from hadronic decaying vector bosons. It's possible that both vector bosons from the heavy Higgs boson decays undergo hadronic decays, or one of them decays hadronicly and the associated vector boson decays hadronicly. Thus, the $2\ell OS$ channel is divided into four signal regions, as displayed in Figure 7.3. The upper plane shows the decay products and reconstruction of the associated vector boson, and the bottom plane shows the decay products and reconstructions of the vector bosons from the heavy Higgs boson. The event selections of the four regions are defined in Table 7.3.

- Region(1): the associated Z boson decays to two leptons ($\ell\ell$); due to the high p_T of the heavy Higgs boson, the hadronic decaying products are reconstructed with a large-R jet which has obvious substructure[96].
- Region(2): the associated Z boson decays to two leptons; one of the vector boson from the heavy Higgs boson forms a small-R jet j_1 (which is the leading jet in p_T), and the other is reconstructed with two small-R jets j_2 and j_3 (which are the next-to leading and next-next-to leading jets).

- Region(3): the associated vector boson decays hadronicly and is reconstructed with j_1; one of the vector boson from the heavy Higgs boson is reconstructed with two small-R jets, and the other decays to two leptons.
- Region(4): the associated vector boson reconstructed with j_1; one of the vector bosons from the heavy Higgs boson is reconstructed with j_2, and the other decays to two leptons.

Table 7.3 The definitions of signal regions in the 2ℓ OS channel, for $m_H = 600$ GeV.

Region(1)	Region(2)
80 GeV $< m_{\ell\ell} <$ 100 GeV	
$p_T^{\ell\ell} > 950$ GeV	$p_T^{\ell\ell} > 550$ GeV
$p_T^{J} > 750$ GeV	$p_T^{j_1} > 300$ GeV
$N_{sj} = 2$	70 GeV $< m_{j_1} <$ 150 GeV
70 GeV $< m_{sj_{1,2}} <$ 150 GeV	$\tau_2^{j_1}/\tau_1^{j_1} < 0.40$
$\tau_2^{J}/\tau_1^{J} < 0.45$	70 GeV $< m_{j_{23}} <$ 110 GeV
	$p_T^{j_{23}} > 150$ GeV
	$\Delta R(j_1, j_{23}) < \Delta R(\ell\ell, j_1)$
	$\Delta R(j_1, j_{23}) < \Delta R(\ell\ell, j_{23})$
	$p_T^{j_1+j_{23}} > 550$ GeV
Region(3)	**Region(4)**
80 GeV $< m_{\ell\ell} <$ 100 GeV, $p_T^{\ell\ell} > 300$ GeV	
$p_T^{j_1} > 700$ GeV, 70 GeV $< m_{j_1} <$ 150 GeV	
$\tau_2^{j_1}/\tau_1^{j_1} < 0.60$	$\tau_2^{j_1}/\tau_1^{j_1} < 0.52$
75 GeV $< m_{j_{23}} <$ 115 GeV	$p_T^{j_2} > 250$ GeV
$p_T^{j_{23}} > 50$ GeV	70 GeV $< m_{j_2} <$ 150 GeV
$\Delta R(\ell\ell, j_{23}) < \Delta R(j_1, \ell\ell)$	$\tau_2^{j_2}/\tau_1^{j_2} < 0.52$
$\Delta R(\ell\ell, j_{23}) < \Delta R(j_1, j_{23})$	$\Delta R(\ell\ell, j_2) < \Delta R(j_1, \ell\ell)$
$p_T^{\ell\ell+j_{23}} > 700$ GeV	$\Delta R(\ell\ell, j_2) < \Delta R(j_1, j_2)$
	$p_T^{\ell\ell+j_2} > 700$ GeV

In the 2ℓ SS channel, the SM backgrounds are largely suppressed, thanks to the requirement of two same-sign leptons. The channel is further divided into three signal regions as displayed in Figure 7.4, with the event selections listed in Table 7.4. Two of the three W bosons decay leptonicly, while the rest one decays hadronicly and can be reconstructed with a small-R jet, a large-R jet or two small-R jets. Compared to the 2ℓ OS

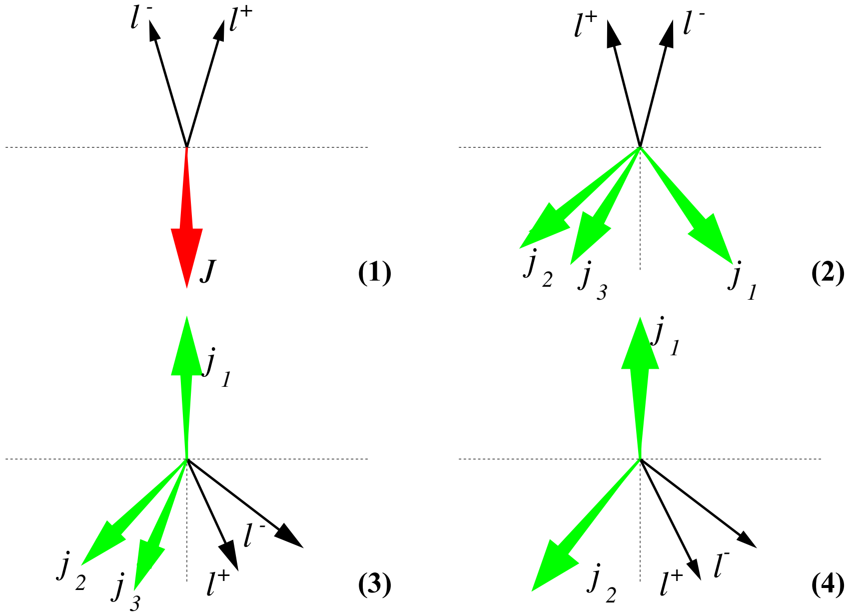

Figure 7.3 Illustrations of the four signal regions in the 2ℓ OS channel. The green (red) arrow represents a small-R (large-R) jet.

Table 7.4 The definitions of signal regions in the 2ℓ SS channel, for $m_H = 600$ GeV.

Region(1)	Region(2)
$m_{\ell\ell} > 300$ GeV, $p_T^{\ell\ell} > 100$ GeV	
$p_T^{\ell_1} > 300$ GeV, $p_T^{\ell_2} > 50$ GeV	
$\Delta\phi_{\ell\ell} > 2.0$, $E_T^{\text{miss}} > 100$ GeV	
no b-tagged jets	
$p_T^{j_1} > 400$ GeV	$p_T^J > 100$ GeV
	$\tau_2^J/\tau_1^J < 0.6$

Region(3)
$m_{\ell\ell} > 400$ GeV, $p_T^{\ell\ell} > 100$ GeV
$p_T^{\ell_1} > 450$ GeV, $p_T^{\ell_2} > 50$ GeV
$\Delta\phi_{\ell\ell} > 1.6$, $E_T^{\text{miss}} > 100$ GeV

channel, events in this channel are required to have larger missing transverse momentum, $p_T > 50$ GeV to reduce fake lepton background and no b-tagged small-R jet to suppress $t\bar{t}V$ background.

7.5.2 3ℓ channels

The 3ℓ channel consists of six signal regions as displayed in Figure 7.5. The definitions are summarized in Table 7.5.

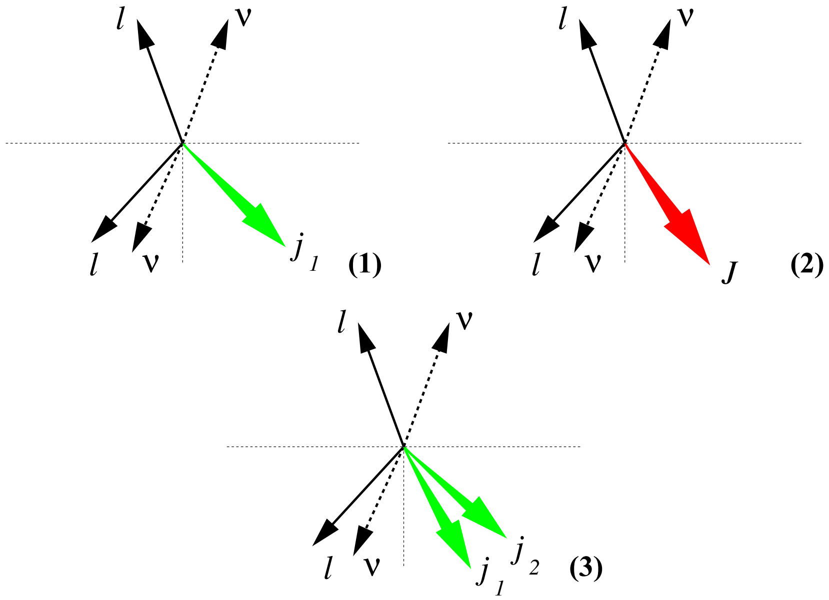

Figure 7.4 Illustrations of the three signal regions in the 2ℓ SS channel. The green (red) arrow represents a small-R (large-R) jet.

In the region (1) - (3), the associated vector boson is W boson undergoing leptonic decay ($W \to \ell\nu$), and the heavy Higgs boson has the decay $H \to ZZ \to \ell^+\ell^- jj$. The hadronic decaying Z boson can be reconstructed with a small-R jet, a large-R jet or two small-R jets. The region (4) - (6) are similar with the region (1) - (3), except exchanging the $W \to \ell\nu$ and $Z \to \ell^+\ell^-$ processes. The total charge of the three leptons must be ± 1. The two leptons from Z boson have the opposite charge and the same flavor. For the final state with two electrons and one muon, or two muons and one electron, the combination is obvious. For the final state with three electrons or three muons, the opposite-charge lepton pair with the least ΔR is regarded as the one from the Z boson decay. To reduce the fake lepton background, the lepton from W boson decay is required to satisfy $p_T > 50$ GeV.

Neutrinos can not be detected. But according to momentum conservation and the W boson mass condition, the longitudinal momentum (p_z^ν) of neutrinos can be obtained, so that the neutrino momentum is reconstructed. The transverse mass of W boson mass is expressed as

$$m_T = \sqrt{2p_T^\ell E_T^{\text{miss}}[1 - \cos\Delta\phi(\ell, E_T^{\text{miss}})]} \tag{7.7}$$

If $m_T \geq m_W$ (due to resolutions of missing transverse momentum and W boson mass), p_z^ν can be set to $E_T^{\text{miss}} \cdot p_z^\ell / p_T^\ell$. If $m_T < m_W$, the solution of Equation 7.7 with

Table 7.5 The definitions of signal regions in the 3ℓ channel, for $m_H = 600$ GeV.

<table>
<tr><th>Region(1)</th><th>Region(4)</th></tr>
<tr><td colspan="2">$80 \text{ GeV} < m_{\ell\ell} < 100 \text{ GeV}$</td></tr>
<tr><td colspan="2">$60 \text{ GeV} < m_{j_1} < 160 \text{ GeV},\ \tau_2^{j_1}/\tau_1^{j_1} < 0.60$</td></tr>
<tr><td>$p_T^{\ell\nu} > 600$ GeV</td><td>$p_T^{\ell\ell} > 600$ GeV</td></tr>
<tr><td>$\Delta R(\ell\ell, j_1) < \Delta R(\ell\nu, \ell\ell)$</td><td>$\Delta R(\ell\nu, j_1) < \Delta R(\ell\ell, \ell\nu)$</td></tr>
<tr><td>$\Delta R(\ell\ell, j_1) < \Delta R(\ell\nu, j_1)$</td><td>$\Delta R(\ell\nu, j_1) < \Delta R(\ell\ell, j_1)$</td></tr>
<tr><td>$p_T^{\ell\ell+j_1} > 600$ GeV</td><td>$p_T^{\ell\nu+j_1} > 600$ GeV</td></tr>
<tr><th>Region(2)</th><th>Region(5)</th></tr>
<tr><td colspan="2">$80 \text{ GeV} < m_{\ell\ell} < 100 \text{ GeV}$</td></tr>
<tr><td colspan="2">$70 \text{ GeV} < m_J < 140 \text{ GeV},\ \tau_2^J/\tau_1^J < 0.50$</td></tr>
<tr><td>$p_T^{\ell\nu} > 600$ GeV</td><td>$p_T^{\ell\ell} > 600$ GeV</td></tr>
<tr><td>$\Delta R(\ell\ell, J) < \Delta R(\ell\nu, \ell\ell)$</td><td>$\Delta R(\ell\nu, J) < \Delta R(\ell\ell, \ell\nu)$</td></tr>
<tr><td>$\Delta R(\ell\ell, J) < \Delta R(\ell\nu, J)$</td><td>$\Delta R(\ell\nu, J) < \Delta R(\ell\ell, J)$</td></tr>
<tr><td>$p_T^{\ell\ell+J} > 600$ GeV</td><td>$p_T^{\ell\nu+J} > 600$ GeV</td></tr>
<tr><th>Region(3)</th><th>Region(6)</th></tr>
<tr><td colspan="2">$80 \text{ GeV} < m_{\ell\ell} < 100 \text{ GeV}$</td></tr>
<tr><td colspan="2">$60 \text{ GeV} < m_{j_{12}} < 120 \text{ GeV}$</td></tr>
<tr><td>$p_T^{\ell\nu} > 600$ GeV</td><td>$p_T^{\ell\ell} > 600$ GeV</td></tr>
<tr><td>$\Delta R(\ell\ell, j_{12}) < \Delta R(\ell\nu, \ell\ell)$</td><td>$\Delta R(\ell\nu, j_{12}) < \Delta R(\ell\ell, \ell\nu)$</td></tr>
<tr><td>$\Delta R(\ell\ell, j_{12}) < \Delta R(\ell\nu, j_{12})$</td><td>$\Delta R(\ell\nu, j_{12}) < \Delta R(\ell\ell, j_{12})$</td></tr>
<tr><td>$p_T^{\ell\ell+j_{12}} > 600$ GeV</td><td>$p_T^{\ell\nu+j_{12}} > 600$ GeV</td></tr>
</table>

smaller $|p_z^\nu|$ is taken.

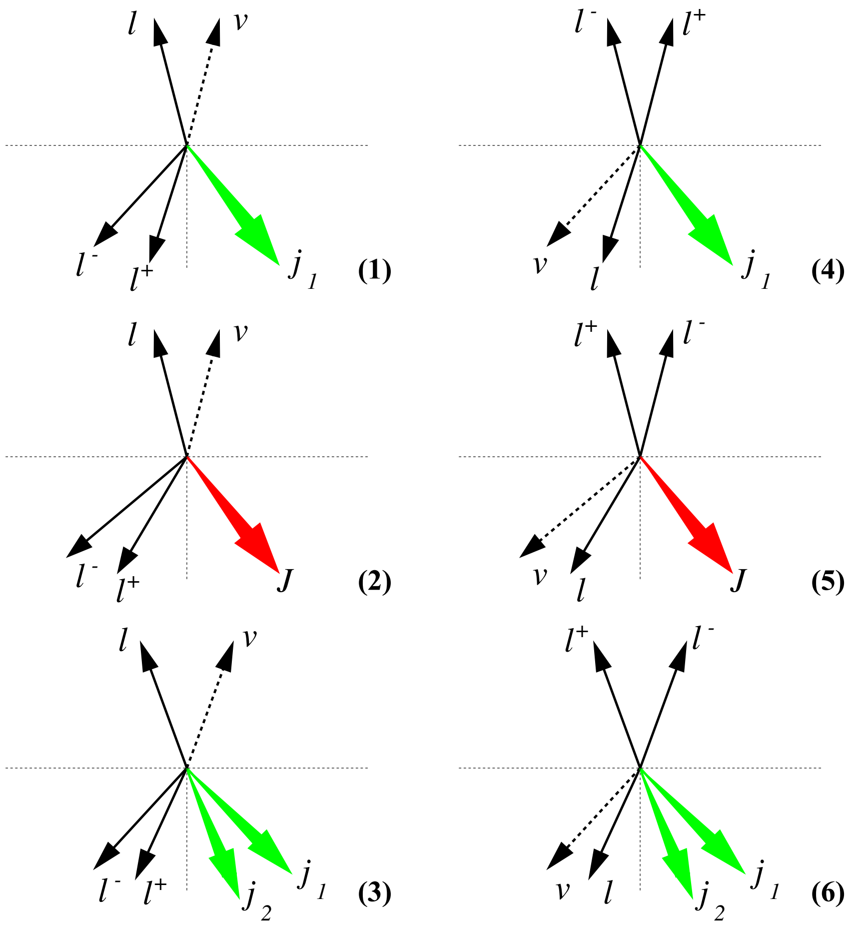

Figure 7.5 Illustrations of the six signal regions in the 3ℓ channel. The green (red) arrow represents a small-R (large-R) jet.

7.5.3 Event yields

Taking the signal of $m_H = 600$ GeV, $\rho_H = 0.05$ and $f_W = f_{WW} = 1000$ as example, the signal and background yields of three channels as summarize in Table 7.6, with corresponding observable distributions in Figure 7.6. In the 2ℓ OS and 3ℓ channels, the observable is the heavy Higgs mass (m_{VV}), while in the 2ℓ SS channel, the mass of the hadronic decaying W boson ($m_{V(jj)}$) is taken as the observable. It's obvious that the 2ℓ SS channel has the best sensitivity.

Table 7.6 At 300 fb^{-1} LHC data, the signal and backgrounds yields. In the 2ℓ OS and 2ℓ SS channel, "Other" includes diboson, triboson, $t\bar{t}$ and $t\bar{t}V$ backgrounds, while in the 3ℓ channel, "Other" consists of triboson and $t\bar{t}V$ backgrounds. Signal: $m_H = 600$ GeV, $\rho_H = 0.05$ and $f_W = f_{WW} = 1000$.

	Signal	Z+QCD jets	Other
2ℓ OS channel	4.0	41.6	3.5
	Signal	WZ+QCD jets	Other
3ℓ channel	3.6	7.2	1.3
	Signal	WZ+QCD jets	Other
2ℓ SS channel	11.4	4.1	3.1

7.6 Exclusion of the parameter space

To obtain the signal sensitivity, mass window cuts are applied to the observables shown in Figure 7.6, then the number counting is applied. We take $m_H = 300,\ 600,\ 900$ GeV as benchmark values and scan the f_W-f_{WW} parameter space. The exclusion regions at 95% Confidence Level (CL) of the parameter space for three benchmark mass values are shown in Figure 7.7- 7.12. A large part of parameter space allowed by theory can be excluded.

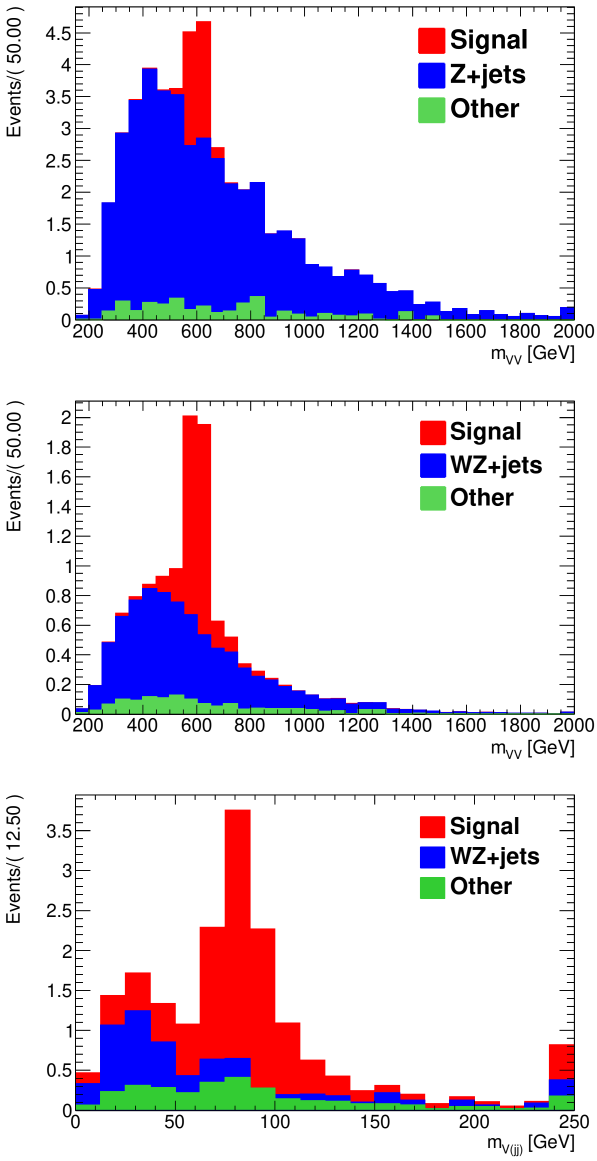

Figure 7.6 At 300 fb^{-1} LHC data, the observable distributions, defined as the heavy Higgs mass (m_{VV}) for the 2ℓ OS channel (top) and 3ℓchannel (middle), and defined as the hadronic decaying W boson mass ($m_{V(jj)}$) in the 2ℓ SS channel (bottom). Signal: $m_H = 600$ GeV, $\rho_H = 0.05$ and $f_W = f_{WW} = 1000$.

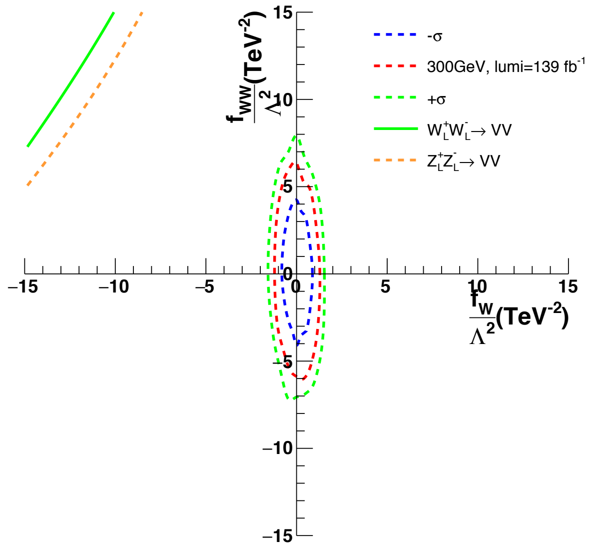

Figure 7.7 The exclusion regions at 95% CL of the f_W-f_{WW} parameter space, with $\rho_H = 0.05$ and $m_H = 300$ GeV, for the integrated luminosity of 139 fb^{-1}. The green solid line and the orange dashed line show the unitarity bounds from the gauge boson scattering.

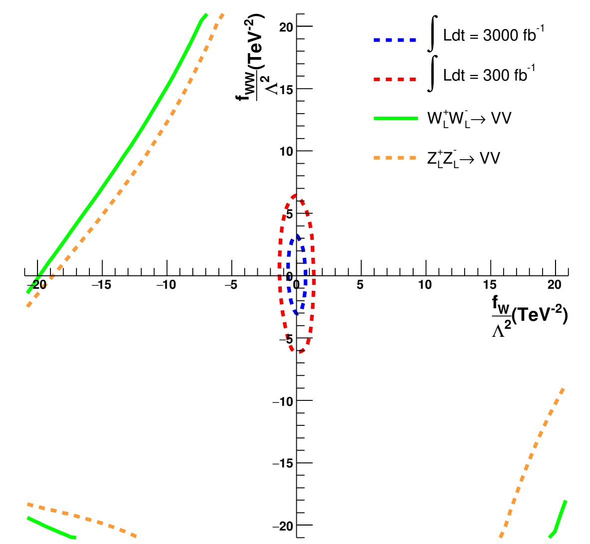

Figure 7.8 The exclusion regions at 95% CL of the f_W-f_{WW} parameter space, with $\rho_H = 0.05$ and $m_H = 300$ GeV, for the integrated luminosities of 300 fb^{-1} and 3 ab^{-1}. The green solid line and the orange dashed line show the unitarity bounds from the gauge boson scattering.

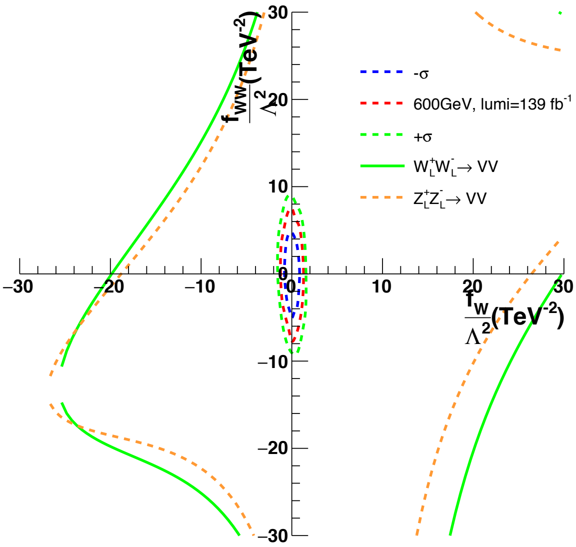

Figure 7.9 The exclusion regions at 95% CL of the f_W-f_{WW} parameter space, with $\rho_H = 0.05$ and $m_H = 600$ GeV, for the integrated luminosity of 139 fb^{-1}. The green solid line and the orange dashed line show the unitarity bounds from the gauge boson scattering.

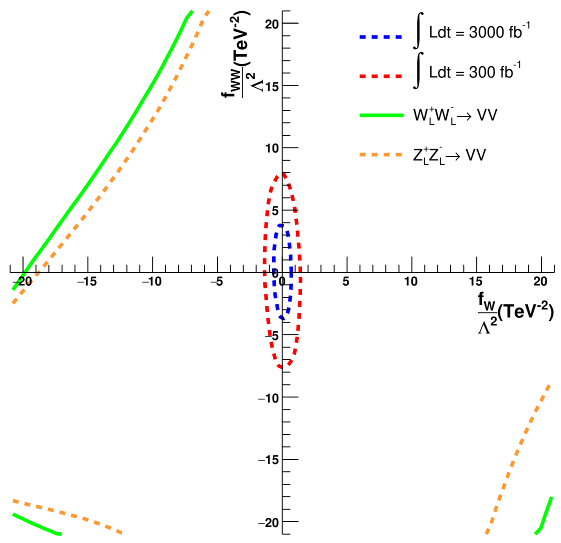

Figure 7.10 The exclusion regions at 95% CL of the f_W-f_{WW} parameter space, with $\rho_H = 0.05$ and $m_H = 600$ GeV, for the integrated luminosities of 300 fb^{-1} and 3 ab^{-1} . The green solid line and the orange dashed line show the unitarity bounds from the gauge boson scattering.

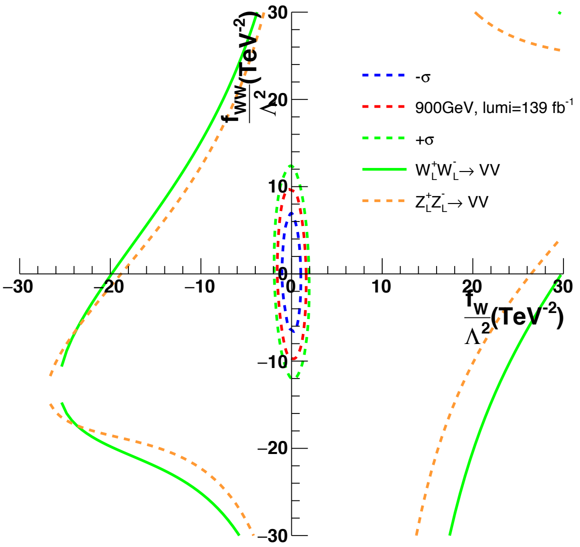

Figure 7.11 The exclusion regions at 95% CL of the f_W-f_{WW} parameter space, with $\rho_H = 0.05$ and $m_H = 900$ GeV, for the integrated luminosity of 139 fb^{-1}. The green solid line and the orange dashed line show the unitarity bounds from the gauge boson scattering.

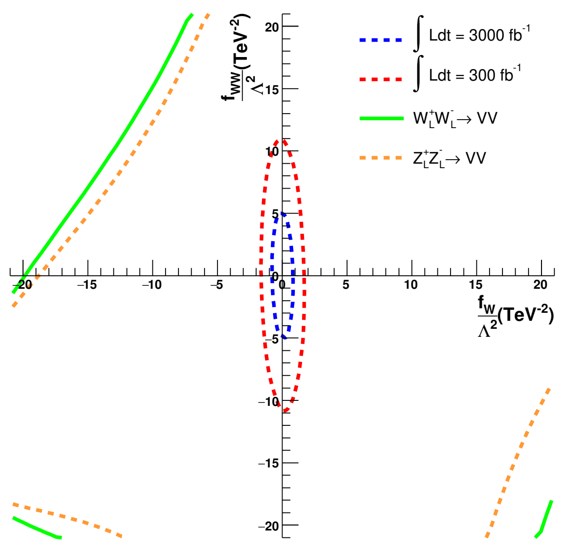

Figure 7.12 The exclusion regions at 95% CL of the f_W-f_{WW} parameter space, with $\rho_H = 0.05$ and $m_H = 900$ GeV, for the integrated luminosities of 300 fb^{-1} and 3 ab^{-1}. The green solid line and the orange dashed line show the unitarity bounds from the gauge boson scattering.

CHAPTER 8 EXPERIMENT: GENERIC HEAVY HIGGS BOSONS

Based on the phenomenology study of the generic heavy Higgs boson described in Chapter 7, we start to use the real data collected by the ATLAS detector to search for heavy Higgs bosons in the same-sign dilepton final state[97].

8.1 Analysis strategy

From the phenomenology study in Chapter 7, we learn that the final state with two same-sign leptons (SS2L) in the VH production channel, $pp \to W^{\pm}H \to W^{\pm}W^{\pm}W^{\mp} \to \ell^{\pm}\nu\ell^{\pm}\nu jj$, has the largest sensitivity. Therefore, the experimental analysis focuses on the SS2L final state to search for heavy Higgs bosons. The Feynman diagram of the SS2L process is shown in Figure 8.1. There are also some other analyses interested in the SS2L final state[98-102]. Why are experimentalists interested in this final state? It's because that the cross section of the SM background contributing to this final state is very small and it's a golden channel to search for new physics. At center-of-mass energy of $\sqrt{s} = 13$ LHC pp collisions, the production cross section of the SM SS2L states is of order 1 pb, a three order of magnitude suppression comparing to the process of opposite-sign leptons[33].

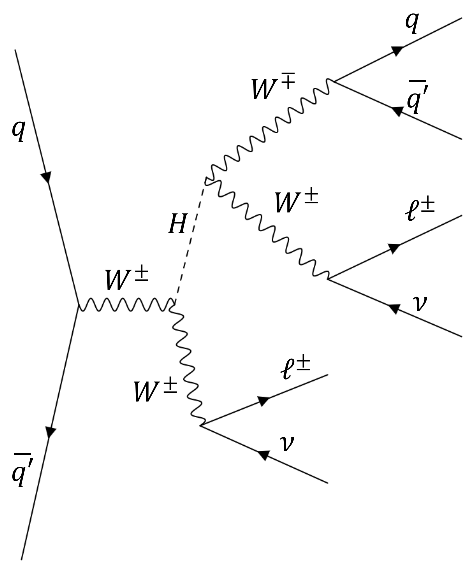

Figure 8.1 Feynman diagram of $W^{\pm}H \to W^{\pm}W^{\pm}W^{\mp} \to \ell^{\pm}\nu\ell^{\pm}\nu jj$ process.

Depending on the transverse momentum, the produced W boson could be boosted or resolved. To cover as much kinematic phase space as we can, both boosted and resolved categories are investigated. In the boosted category, the hadronic decaying W boson is reconstructed with one large-R jet, while in the resolved category, it's reconstructed with two small-R jets. Only events not passing the boosted category are considered in the resolved category. The definition of boosted category is that leading large-R jet satisfies $p_T > 200$ GeV, $|\eta| < 2$ and 50 GeV $< m_J <$ 200 GeV.

Due to two neutrinos, we can't reconstruct the mass of the heavy Higgs boson. This analysis uses the effective mass (m_{eff}) as observable:

$$\text{Boosted category:} \quad \sum_i p_T(\text{lepton}_i) + p_T(\text{leading J}) + E_T^{miss} \tag{8.1}$$

$$\text{Resolved category:} \quad \sum_i p_T(\text{lepton}_i) + p_T(\text{leading j}) + p_T(\text{sub-leading j}) + E_T^{miss} \tag{8.2}$$

The effective mass can reflect the boosted level and is expected to be larger for signals.

8.2 Data and Monte Carlo samples

This section describes the MC samples used in this analysis.

8.2.1 Data samples

The analysis uses the pp collision data collected between 2015 and 2018 by the ATLAS detector at center-of-mass energy of $\sqrt{s} = 13$ TeV, with an integrated luminosity of 139 fb^{-1}.

8.2.2 Monte Carlo samples

MC simulated events are used to model signals and estimate the SM backgrounds.

8.2.2.1 Signal Monte Carlo samples

The signal events are generated by MadGraph5_aMC@NLO[33] at LO with syntax:

$$pp > H > VVV \tag{8.3}$$

where H represents the heavy Higgs boson and V represents W or Z boson. The full decays of V are implemented in MadSpin[103].

The MadGraph5_aMC@NLO is then interfaced to Pythia for parton showering and hadronization with the NNPDF2.3LO PDF[72] and A14 parameter set[71]. Events are filtered with the requirement of at least one same-sign lepton pair. Each lepton is required to have $p_T > 18$ GeV and be within $|\eta| < 2.7$. The signal samples are produced with m_H from 300 GeV to 1.5 TeV, f_W from -2480 to 2510 and f_{WW} from -15000 to 15000.

The signal events are generated at LO, but they are normalized to the calculations at next-to-leading order (NLO) using a Higgs characterisation model[104]. Figure 8.3-8.4 compare the kinematic distributions obtained from NLO and LO calculations. All kinematic distributions are consistent. The ratio of NLO cross section to LO cross section is called K-factor. For our signals, the K-factor is about 1.3 as shown in Figure 8.2.

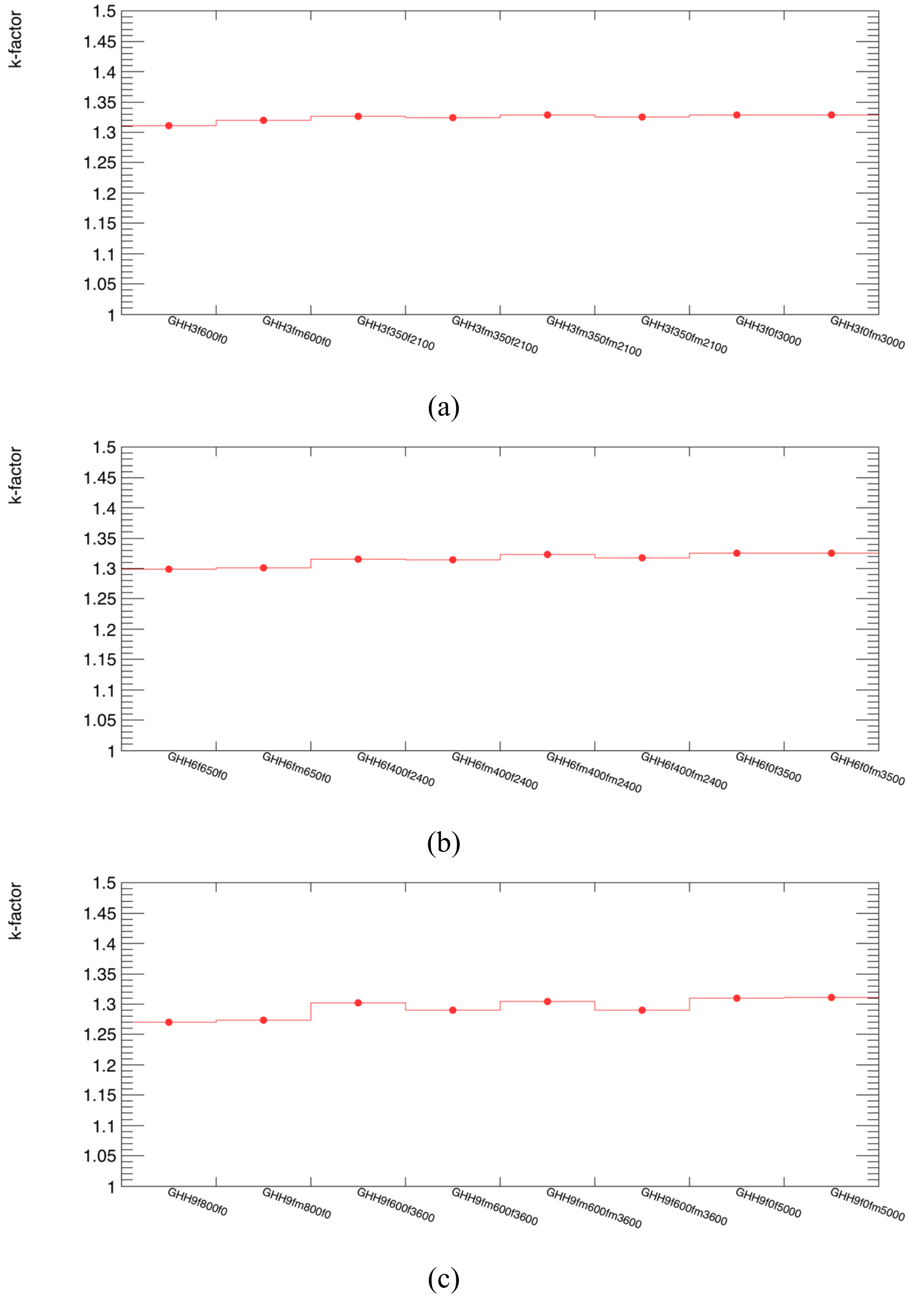

Figure 8.2 The distributions of K-factor with different signals. (a) $m_H = 300$ GeV; (b) $m_H = 600$ GeV; (c) $m_H = 900$ GeV. “GHH6f650f0” represents the signal with $m_H = 600$ GeV, $f_W/\rho_H = 650$ and $f_{WW}/\rho_H = 0$; “GHH6fm400f2400” represents the signal with $m_H = 600$ GeV, $f_W/\rho_H = -400$ and $f_{WW}/\rho_H = 2400$.

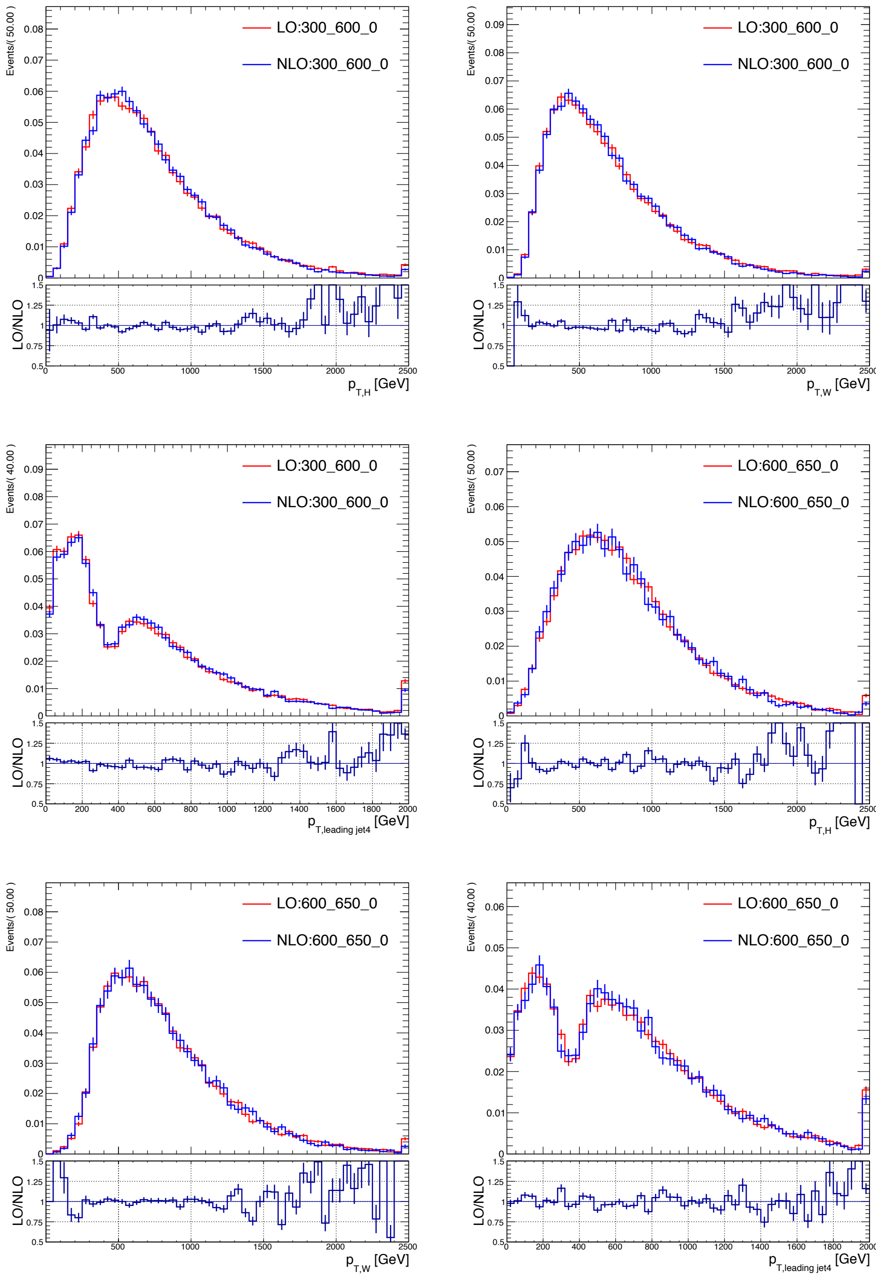

Figure 8.3 Kinematic distributions for NLO and LO calculations, normalized to the same area. 300_600_0: $m_H = 300$ GeV, $f_W/\rho_H = 600$, $f_{WW}/\rho_H = 0$.

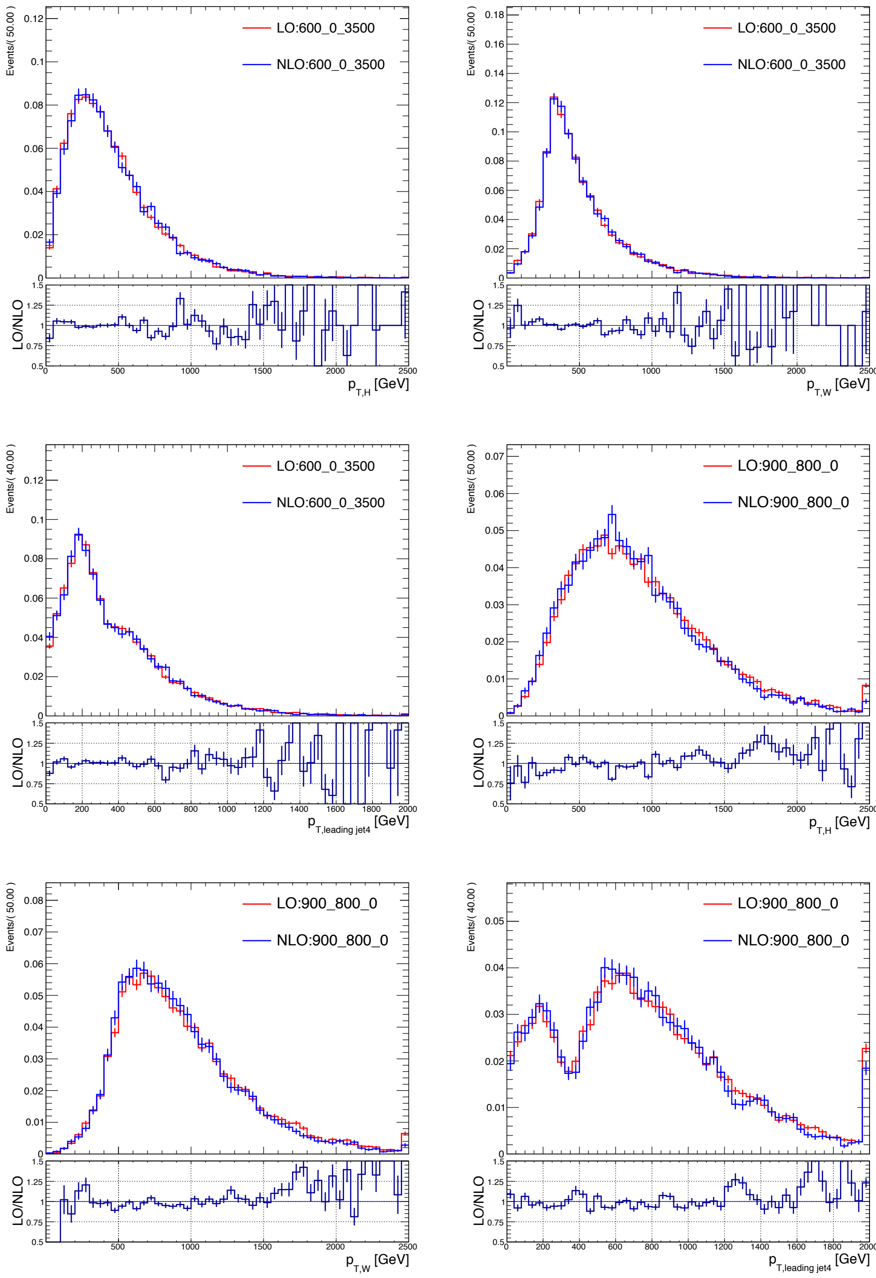

Figure 8.4 Kinematic distributions for NLO and LO calculations, normalized to the same area. 600_0_3500: $m_H = 600$ GeV, $f_W/\rho_H = 0$, $f_{WW}/\rho_H = 3500$.

8.2.2.2 Background Monte Carlo samples

The diboson ($W^{\pm}W^{\pm}$, WZ and ZZ) events are simulated by the SHERPA 2.2.2 [35], with NNPDF3.0NNLO PDF[72] and dedicated tuning parameters. Fully leptonic fianl states are generated at NLO accuracy in QCD for up to one additional parton and at LO accuracy for up to three additional parton emisions.

The on-shell $W^{\pm}W^{\mp}W^{\mp}$ process is simulated with SHERPA 2.2.2, including the $pp \to Wh^{*} \to WWW$, where the Higgs boson is off-shell and W bosons are on-shell. The off-shell process ($pp \to Wh \to WWW^{*}$) also has an important contribution and must be simulated separately. It's simulated to NLO accuracy in QCD with POWHEG[36-37] interfaced to Pythia for parton shower using NNPDF3.0NNLO PDF. The two processes are combined and called "WWW" background. Other triboson (VVV) processes are simulated with SHERPA 2.2.2 using factorised gauge-boson decays.

The productions of $t\bar{t}$ and single top events are both modeled by the POWHEG interfaced to Pythia. For the $t\bar{t}$ events, the h_{damp} parameter is set to $h_{\text{damp}} = 1.5m_{\text{top}}$, where $m_{\text{top}} = 175$ GeV. The $t\bar{t}V$ and tV processes are simulated with MadGraph5_aMC@NLO interfaced to Pythia, while the production of $t\bar{t}h$ events is modeled with POWHEG interfaced to Pythia. In this analysis, the contribution from $t\bar{t}V$, $t\bar{t}h$ and tV are small, so they are combined and called "TopX".

The $V\gamma$ processes are simulated with SHERPA 2.2.8 using NNPDF3.0NNLO PDF. Events are generated using matrix elements at NLO accuracy in QCD for up to one additional parton and at LO accuracy for up to three additional parton emissions.

The production of V+jets final states is modeled with SHERPA 2.2.1 using NNPDF3.0NNLO PDF. Events are generated using matrix elements at NLO accuracy in QCD for up to two additional partons and at LO accuracy for up to four additional parton emissions.

8.3 Event selections and optimization

This section describes the selection criteria for all objects used in this analysis and baseline event selections used for the optimisation procedure.

8.3.1 Triggers

The standard lowest unprescaled single muon and single electron triggers are used in this analysis as listed in Table 8.1. Each event is required to have at least one signal electron or muon matched to a trigger object with a p_T at least 1 GeV larger than that trigger's threshold. So the trigger matched lepton is required to satisfy $p_T > 27$ GeV.

Table 8.1 Single lepton triggers used in this analysis.

	Electron trigger	Muon trigger

2015	`HLT_e24_lhemedium_L1EM20VH`
	`HLT_e60_lhemedium`
	`HLT_e120_lhloose`
		`HLT_mu20_iloose_L1MU15`
		`HLT_mu50`

2016 - 2018	`HLT_e26_lhtight_nod0_ivarloose`
	`HLT_e60_lhmedium_nod0`
	`HLT_e140_lhloose_nod0`
	`HLT_e300_etcut`
		`HLT_mu26_ivarmedium`
		`HLT_mu50`

8.3.2 Object selections

There are two same-sign leptons, two neutrinos and one large-R jet or two small-R jets in the signal final state.

Muons used in this analysis must satisfy the `Medium` identification working point described in Section 4.3. Additional kinematic criteria are applied to further reject muons coming from pile-up collisions and non-prompt muons. Each muon's longitudinal impact parameter z_0 is required to satisfy $|z_0 \times \sin\theta| < 0.5$ mm, where θ is the polar angle of the track. The significance of the transverse impact parameter $|d_0/\sigma(d_0)|$ should be less than 3, where d_0 is the transverse impact parameter and $\sigma(d_0)$ is the corresponding uncertainty. Also, the muon is required to have $p_T > 20$ GeV and $|\eta| < 2.5$. For the isolation requirement, the PLV `Tight` working point is applied. The muons satisfying above requirements are used in signal, control and validation regions, called "Signal" muons. In addition to the "Signal" muons, "antiID" muons are defined for the fake background estimation. This selection has loosened impact parameter cuts and no isolation requirement. Only muons rejected by the "Signal" muon requirement are considered in the "antiID" muons' selection. So the two type of muons are orthogonal. When counting the number of muons, muons with $p_T < 4.5$ GeV and $|\eta| < 2.7$ are all rejected.

Electrons must satisfy the `Tight` identification working point. They are required to have $p_T > 20$ GeV and $|\eta| < 2.47$, with electrons in the transition region ($1.37 \leq |\eta| \leq 1.52$) excluded, and satisfy requirements on ambiguity. The ambiguity requirements are used to reject electrons from converted photons and mis-reconstructed photons. Similar to muons, electrons need to pass the PLV `Tight` working point. To reduce electrons with mis-reconstructed charge, another BDT based selector is applied to identify charge-flip events, called ECIDS (Electron Charge ID Selector)[42]. The electrons satisfying the above requirements are called "Signal" muons. Events rejected by "Signal" muons are considered in "antiID" and "antiBL" electrons; "antiID" electrons are defined to estimate the rate of jets mis-reconstructed as electrons, which requires `Medium` identification working point and no isolation requirement; "antiBL" electrons are defined to estimate background of photons mis-reconstructed as electrons, which like "Signal" electrons except that the track has no hit in the innermost layer of the pixel detector and ambiguity requirements. When counting the number of electrons, electrons with $p_T < 7$ GeV and $|\eta| < 2.47$ are rejected.

Unless otherwise specified, muons and electrons used in this analysis are "Signal" muons and "Signal" electrons.

All selected small-R jets are required to have $p_T > 20$ GeV and $|\eta| < 2.5$. For small-R jets with $|\eta| < 2.4$ and $20 < p_T < 60$, they are required to satisfy the `Medium` working point of jet vertex tagger (JVT)[105] to suppress pile-up jets. The 85% efficiency working point of the DL1r tagger is applied to tag b-jet. Since we are looking for W decays, the b-tagger is used to veto b-jets.

Only large-R jets with $p_T > 200$ GeV, $|\eta| < 2$ and 50 GeV $< m_J <$ 200 GeV are considered. The 80% efficiency working point of the W-tagger is applied to tag large-R jets as consistent with hadronic decaying W bosons.

The requirement on missing transverse momentum varies for different analysis regions.

8.3.3 Preliminary event selections

Based on the phenomenology study in Chapter 7. The preliminary event selections of signal regions are summarized in Table 8.2, where l_1, J_1, j_1, j_2, M_{ll} and M_{jj} represent leading lepton, leading large-R jet, leading small-R jet and next-to-leading small-R jet, invariant mass of two leading leptons and invariant mass of two leading small-R jets, respectively. Based on the preliminary selections, event selections are optimized as described below.

Table 8.2 Preliminary selection criteria before optimisation, not final selection criteria.

Boosted SR	Resolved SR
Boosted Category	!Boosted Category
$E_T^{\text{miss}} > 80$ GeV	$E_T^{miss} > 60$ GeV
$N_J \geq 1$	$N_j \geq 2$
$p_T(J_1) > 200$ GeV	$p_T(j_1) > 30,\ p_T(j_2) > 20$ GeV
J_1 @ 80% W-tagger	$M_{jj} \in (50, 120)$ GeV
Two same-sign leptons with $p_T > (27)20$ GeV	
3^{rd} lepton veto	
no b-jet @ 85% DL1r	
$p_T(l_1) > 100$ GeV	
$M_{ll} > 200$ GeV	

8.3.4 Optimization

The principle of optimization is to maximize the signal significance σ, which is defined as:

$$\sigma = \sqrt{\sum_{i \in bins} 2 \times ((S_i + B_i) \times ln(1 + \frac{S_i}{B_i}) - S_i)} \tag{8.4}$$

where S_i and B_i are the number of signal and background events in the i-th bin of the effective mass distribution. The effective mass distribution is estimated from MC simulations.

To optimize the selections, the choice of W-tagger working point, and cuts on leading lepton p_T ($p_T(\ell_1)$), invariant mass of two leading leptons, missing transverse momentum, leading small-R jet p_T ($p_T(j_1)$) and invariant mass of two leading small-R jets are studied by scanning these cuts.

8.3.4.1 Choice of W-tagger working point

The cuts applied on the leading large-R jet can be W-tagger with 80% efficiency working point, W-tagger with 50% efficiency working point and mass window cut ($60 < M_J < 110$ GeV), or no cut is applied. The signal significance with different cuts are compared in Figure 8.5. The W-tagger with 80% working point has a much better performance than others.

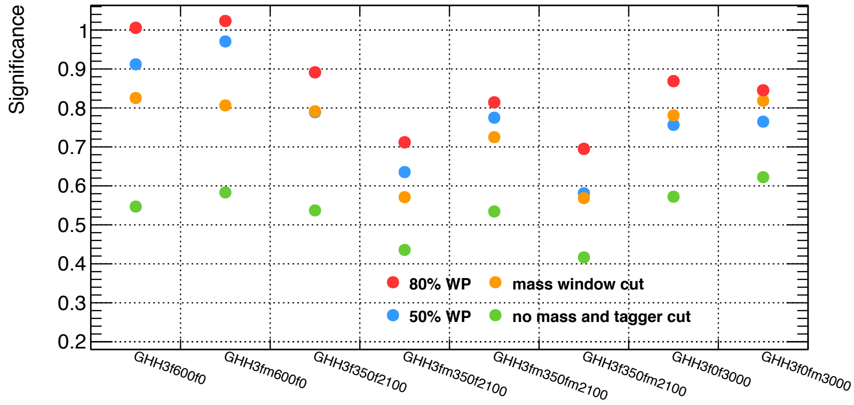

(a)

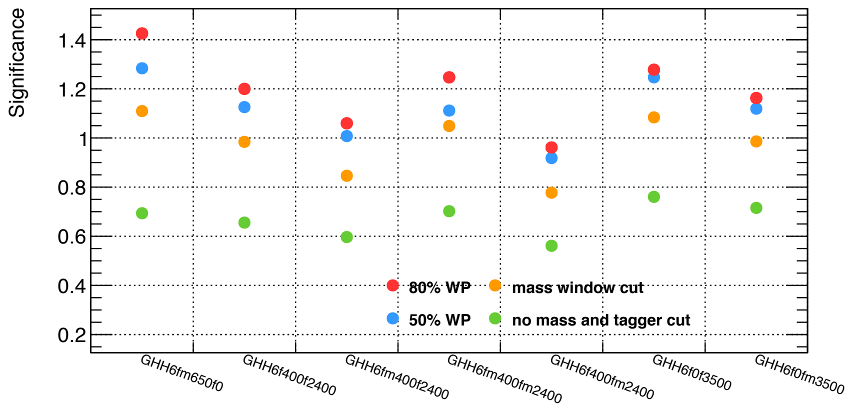

(b)

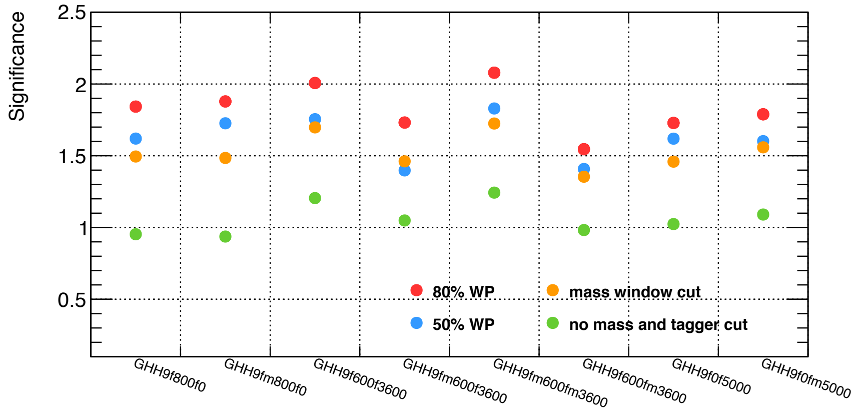

(c)

Figure 8.5 signal significance in boosted category with different cuts on leading large-R jet for signals with heavy Higgs mass of (a) 300 GeV, (b) 600 GeV and (c) 900 GeV.

8.3.4.2 Main variables

The main discriminant variables are $p_T(l_1)$, M_{ll}, E_T^{miss} and $p_T(j_1)$. They are scanned one by one. Since most of them are not correlated, the choice of optimization order will not influence the result. The correlation between $p_T(l_1)$ and M_{ll} is considered by re-scanning $p_T(l_1)$ based on the result of scanning M_{ll}.

Figure 8.6-8.7 show the scan of cut on $p_T(l_1)$ in the boosted and resolved signal regions. Due to the tight cut on $M_{\ell\ell}$, with the increasing of $p_T(l_1)$, no compelling increase in significance is observed. So cut $p_T(l_1) > 27$ GeV which is the loosest is preferred to reserve more signals with negligible change of significance.

The scan of cut on M_{ll} is based on $p_T(l_1) > 27$ GeV cut. As shown in Figure 8.8-8.9, the change of significance is negligible. So the $M_{ll} > 100$ GeV cut is kept to reserve more signals and suppress Z+jets background.

Due to correlation, the $p_T(l_1)$ is re-scanned based on $M_{ll} > 100$ GeV cut as shown in Figure 8.10-8.11. The $p_T(l_1) > 27$ GeV cut is still the best one.

Based on $p_T(l_1) > 27$ GeV and $M_{ll} > 100$ GeV cuts, the scan of cut on E_T^{miss} is shown in Figure 8.12-8.13. Considering the signal efficiency, the $E_T^{miss} > 80$ GeV is preferred in the boosted signal region, while the $E_T^{miss} > 60$ GeV cut is more suitable in the resolved region region.

The scan of the cut on $p_T(j_1)$ in the resolved signal region is shown in Figure 8.14. The $p_T(j_1) > 20$ GeV cut results in the largest significance and highest signal efficiency.

8.3.4.3 Variables in the resolved category

Based on the above optimization results, the jet assignment and M_{jj} cut in the resolved signal region are optimized. Besides the jet assignment with two leading small-R jets, the jet assignment using two jets with the closest mass to W mass is an alternative way. The invariant mass of these two jets ($W\ M_{jj}$) can also be constrained.

The scans of different jet assignments and different mass window cuts are shown in Figure 8.15-8.16. The jet assignment of choosing two leading small-R jets has better performance and the $M_{jj} \in (50, 110)$ GeV cut is preferred.

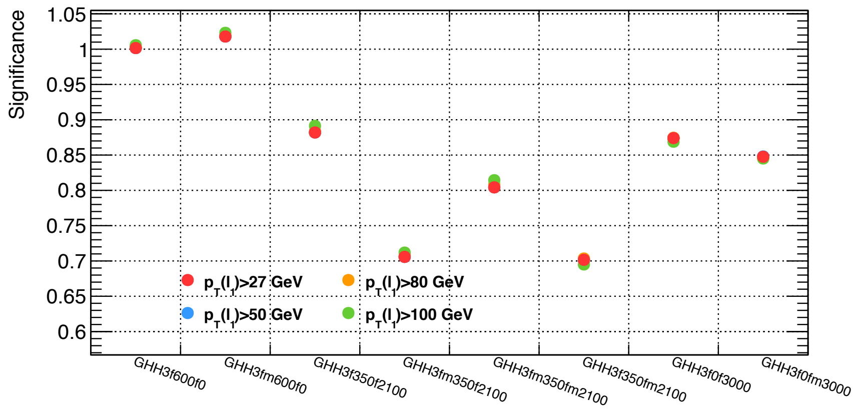

(a)

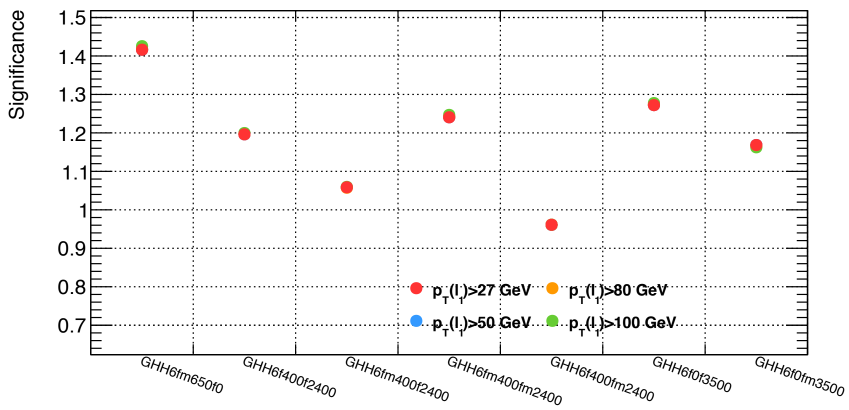

(b)

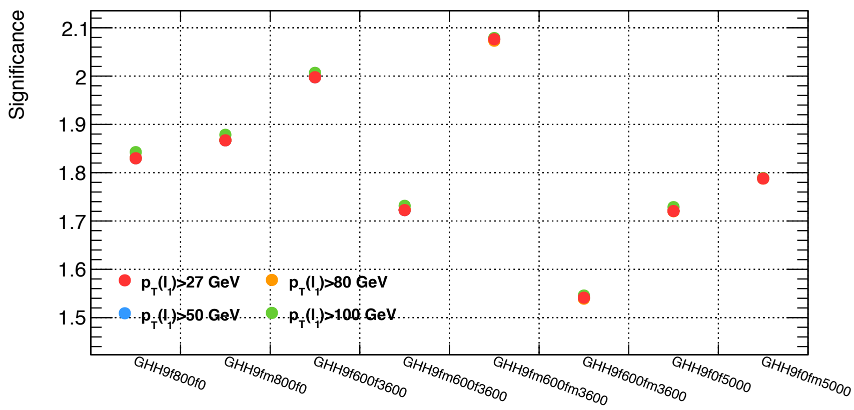

(c)

Figure 8.6 Signal significance in boosted signal region with different cut values on leading lepton p_T ($p_T(l_1)$) for signals with heavy Higgs mass of (a) 300 GeV, (b) 600 GeV and (c) 900 GeV.

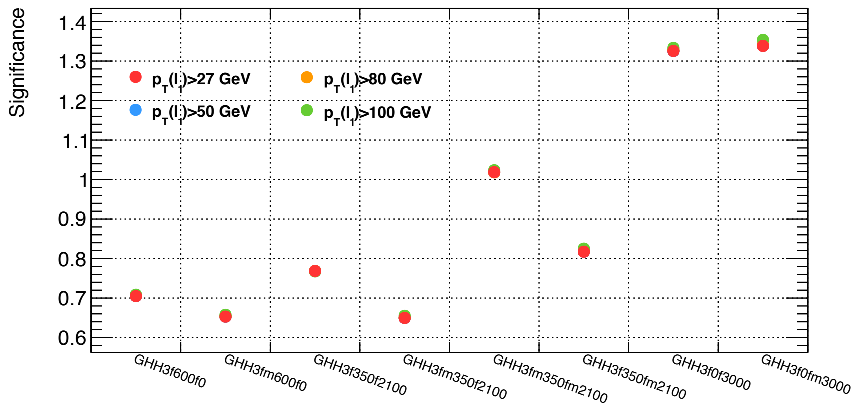

(a)

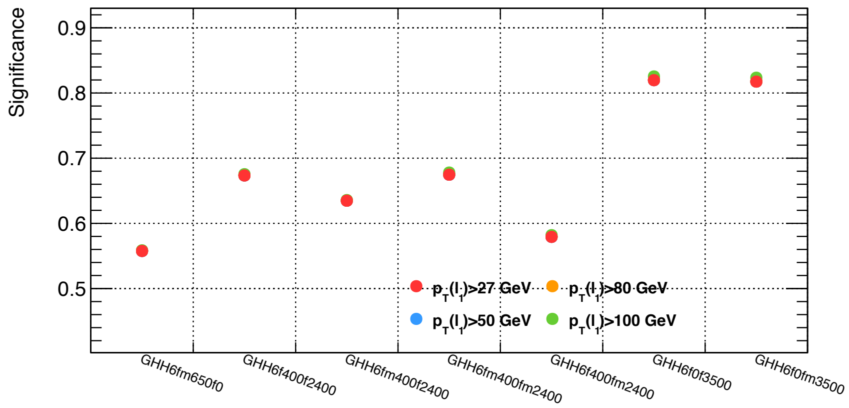

(b)

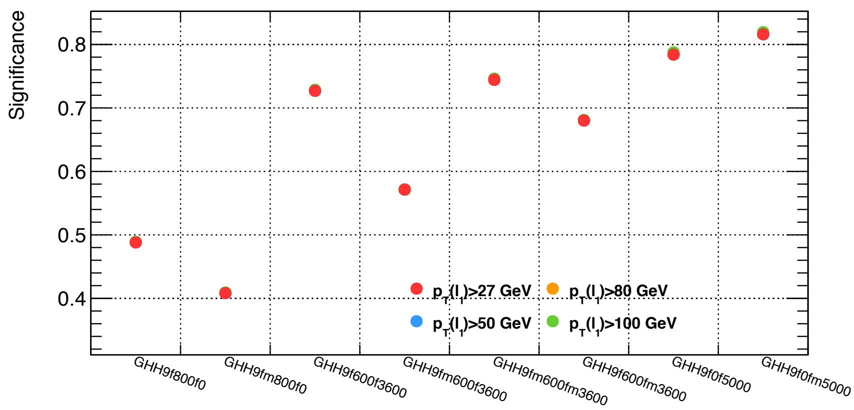

(c)

Figure 8.7 Signal significance in resolved signal region with different cut values on leading lepton p_T ($p_T(l_1)$) for signals with heavy Higgs mass of (a) 300 GeV, (b) 600 GeV and (c) 900 GeV.

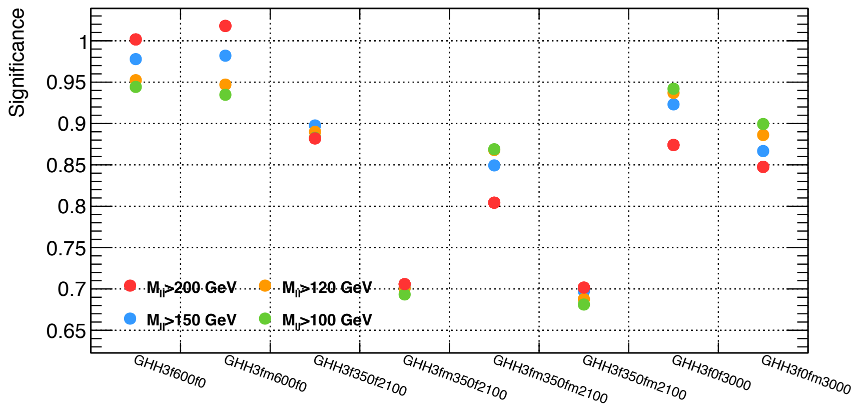

(a)

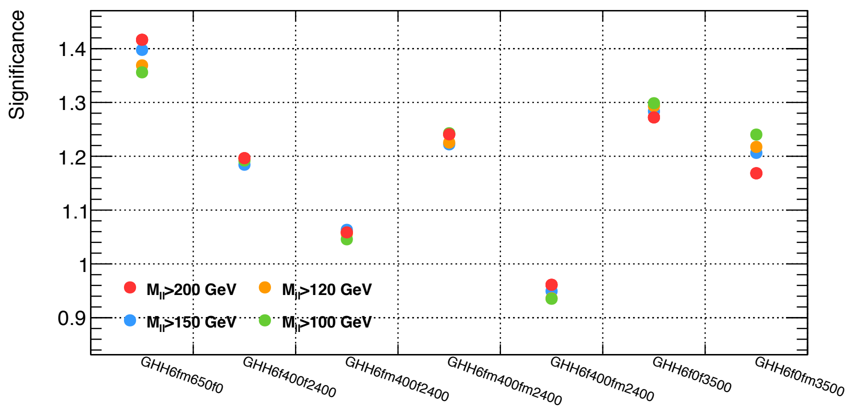

(b)

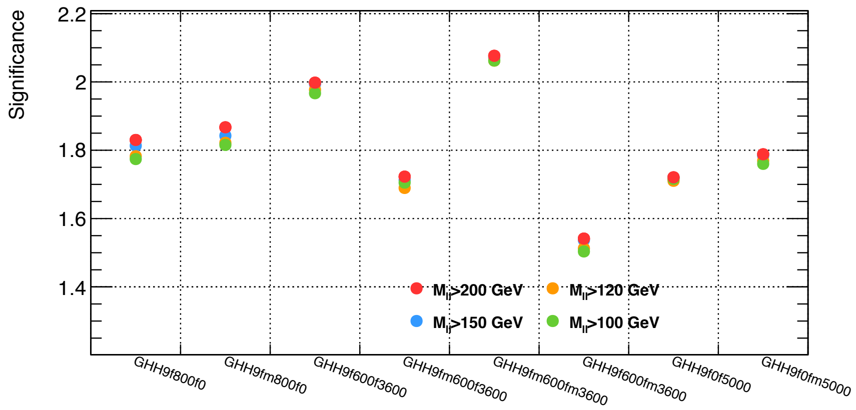

(c)

Figure 8.8 Signal significance in boosted signal region with different cut values on M_{ll} for signals with heavy Higgs mass of (a) 300 GeV, (b) 600 GeV and (c) 900 GeV.

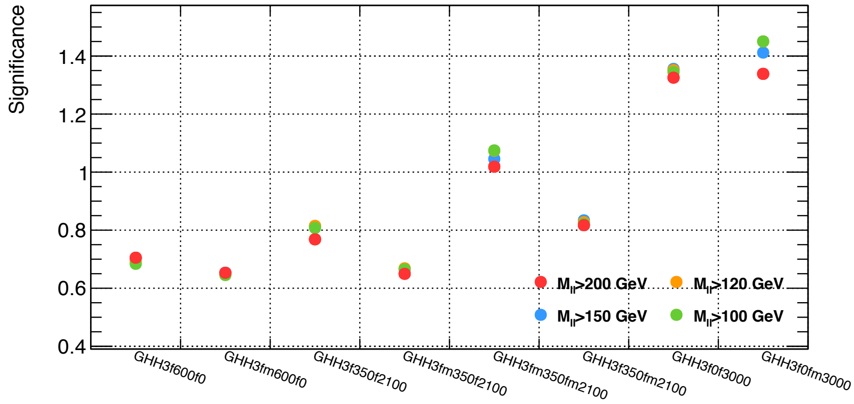

(a)

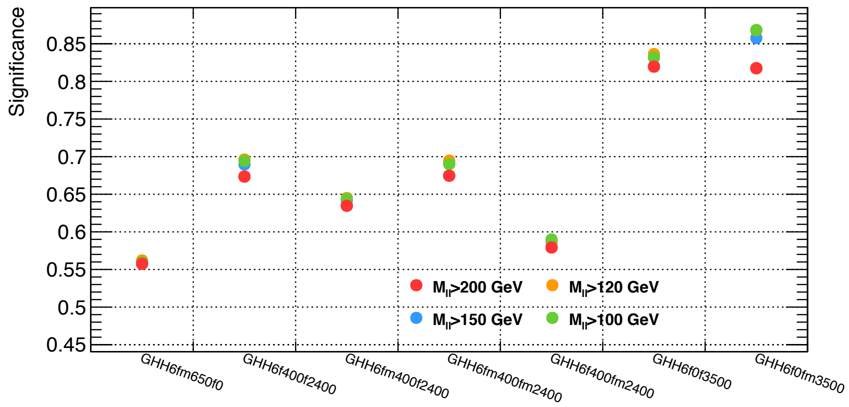

(b)

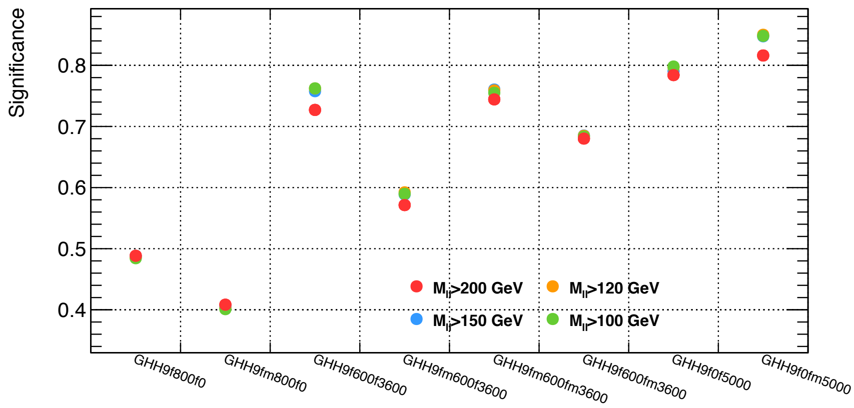

(c)

Figure 8.9 Signal significance in resolved signal region with different cut values on M_{ll} for signals with heavy Higgs mass of (a) 300 GeV, (b) 600 GeV and (c) 900 GeV.

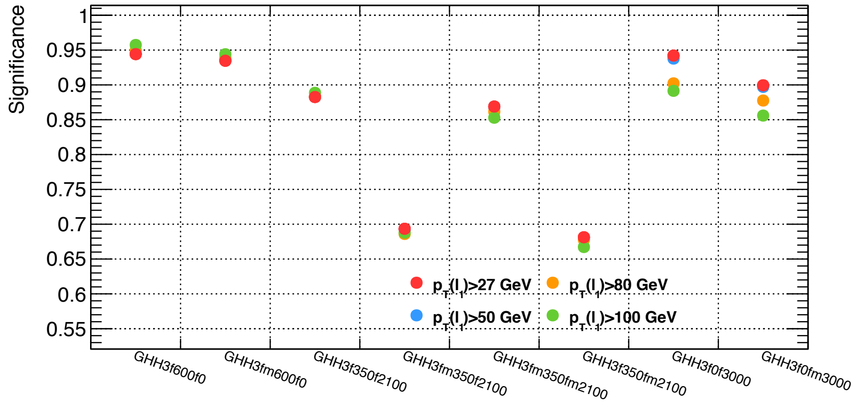

(a)

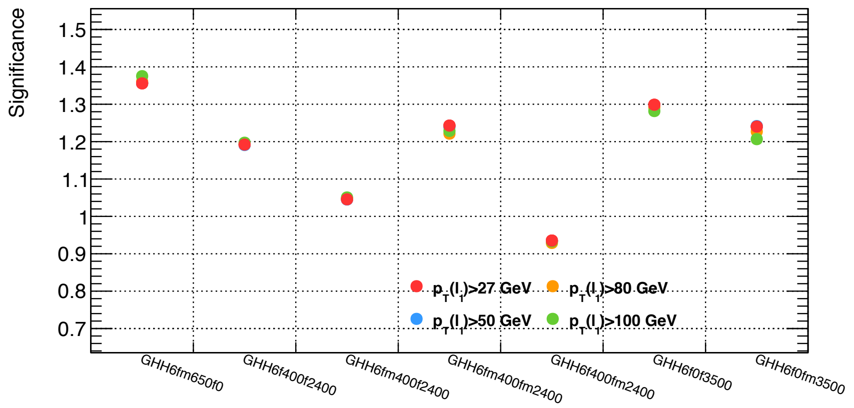

(b)

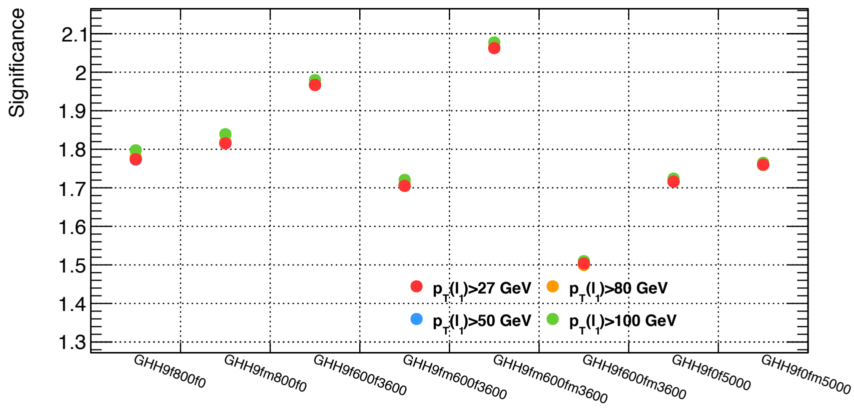

(c)

Figure 8.10 Signal significance in boosted signal region with different cut values on $p_T(l_1)$ for signals with heavy Higgs mass of (a) 300 GeV, (b) 600 GeV and (c) 900 GeV.

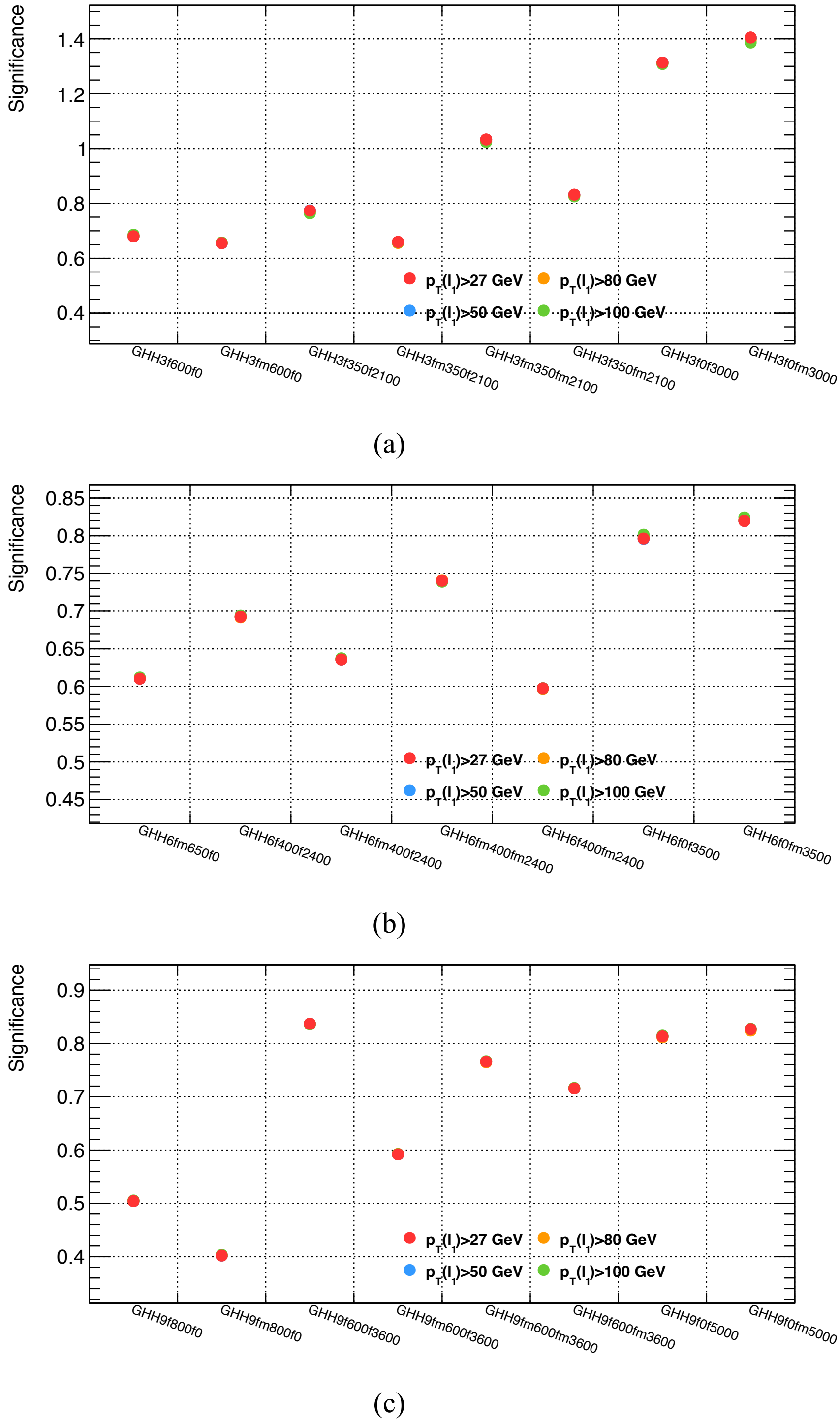

Figure 8.11 Signal significance in resolved signal region with different cut values on $p_T(l_1)$ for signals with heavy Higgs mass of (a) 300 GeV, (b) 600 GeV and (c) 900 GeV.

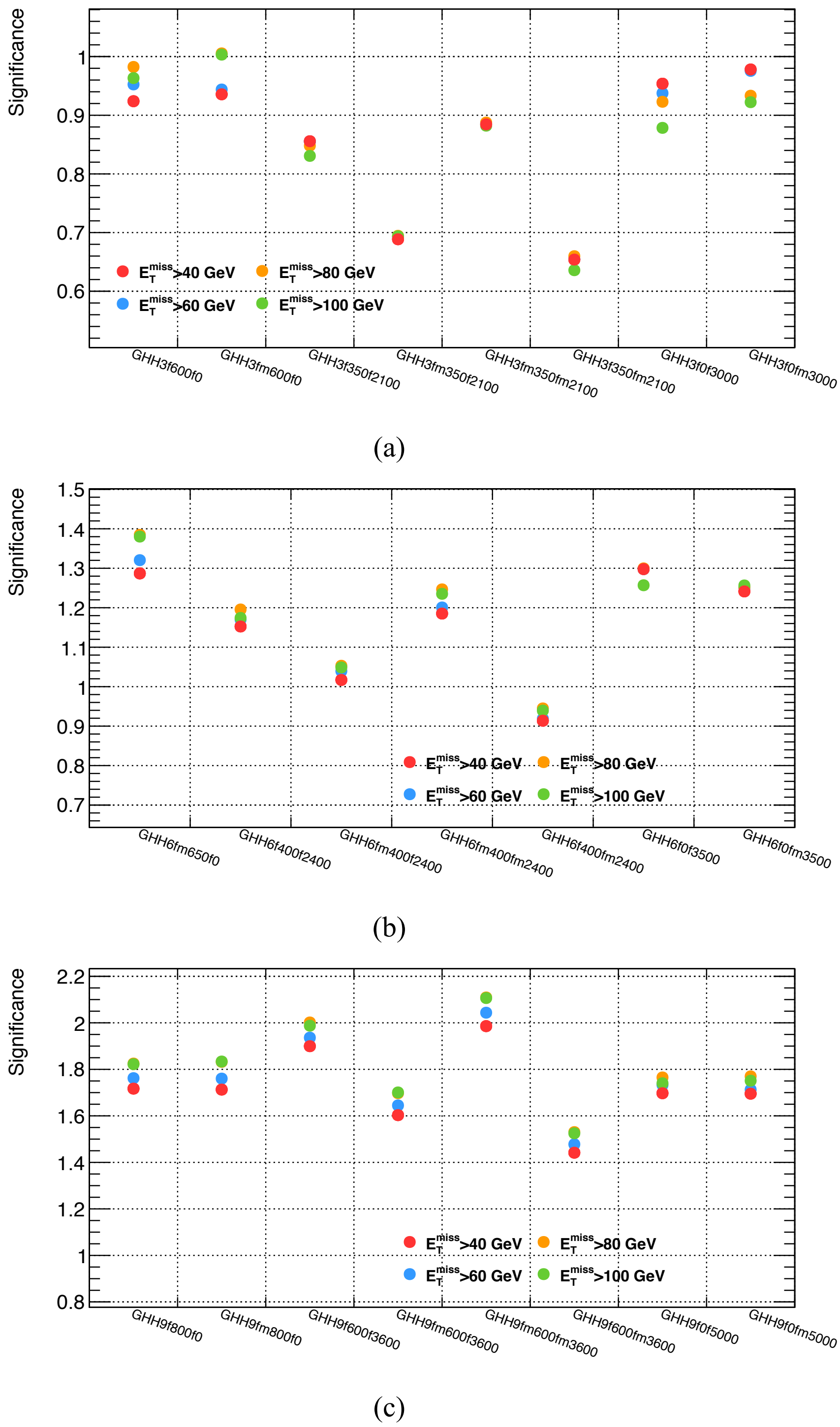

Figure 8.12　Signal significance in boosted signal region with different cut values on E_T^{miss} for signals with heavy Higgs mass of (a) 300 GeV, (b) 600 GeV and (c) 900 GeV.

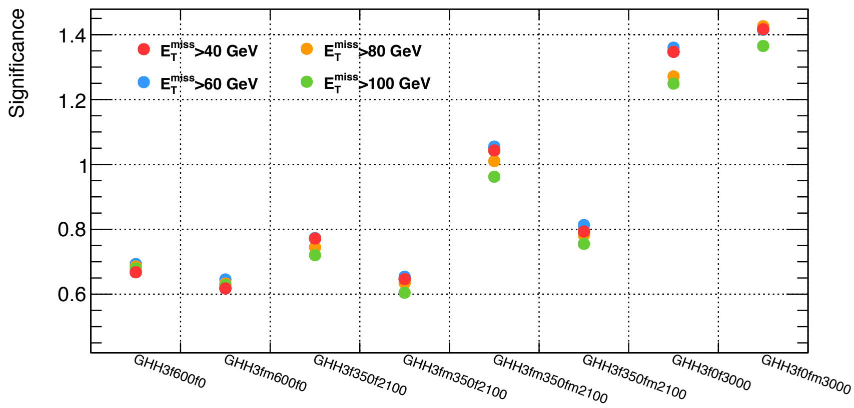

(a)

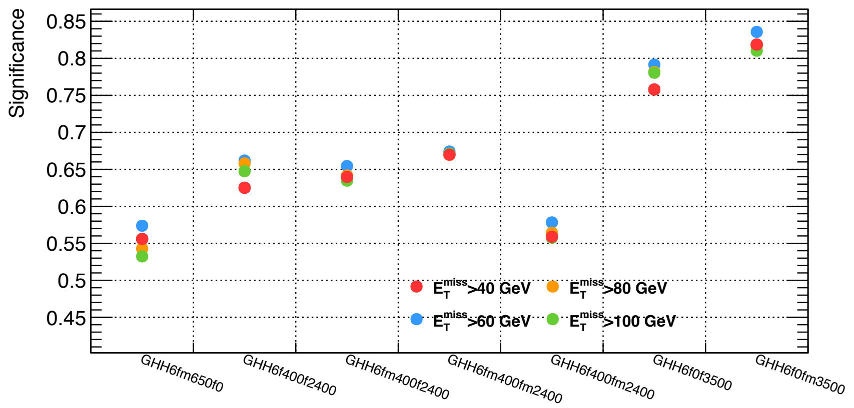

(b)

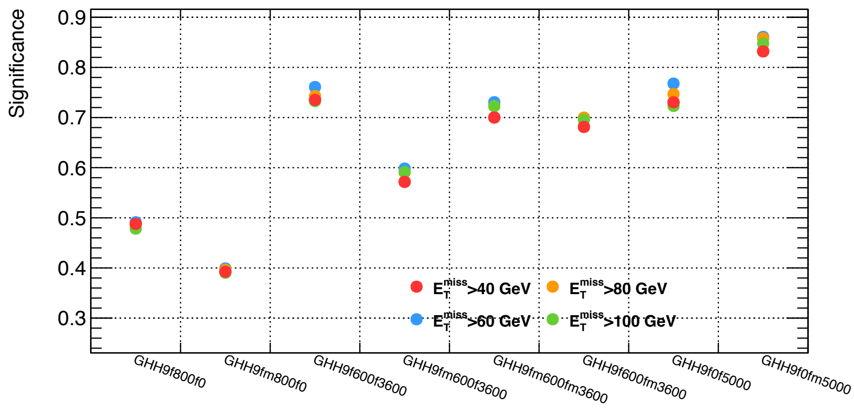

(c)

Figure 8.13 Signal significance in resolved signal region with different cut values on E_T^{miss} for signals with heavy Higgs mass of (a) 300 GeV, (b) 600 GeV and (c) 900 GeV.

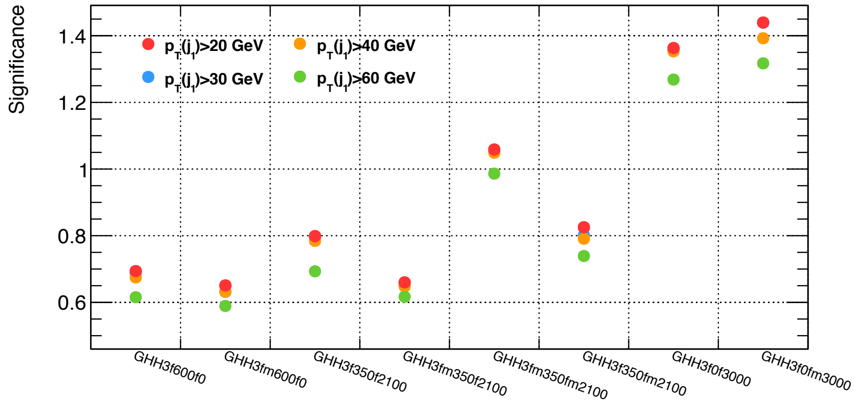

(a)

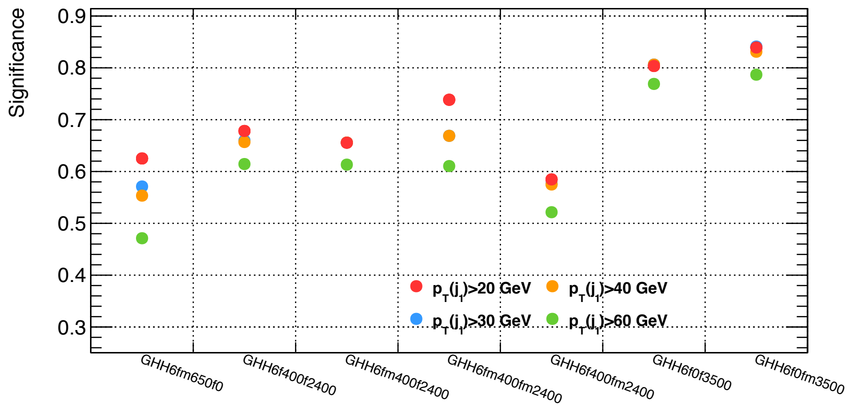

(b)

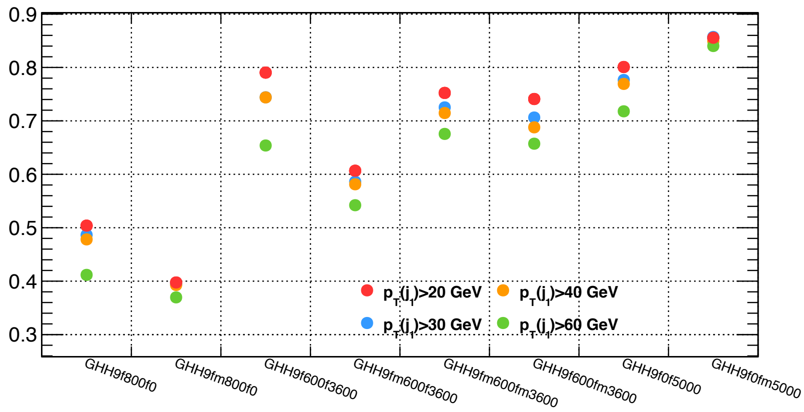

(c)

Figure 8.14 Signal significance in resolved signal region with different cut values on $p_T(j_1)$ for signals with heavy Higgs mass of (a) 300 GeV, (b) 600 GeV and (c) 900 GeV.

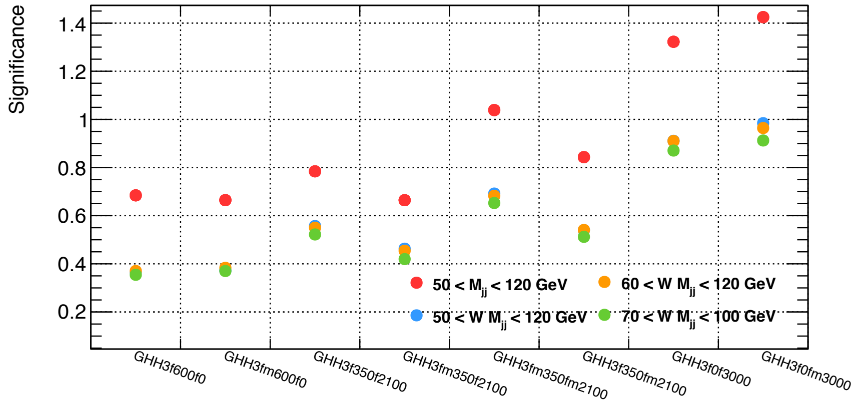

(a)

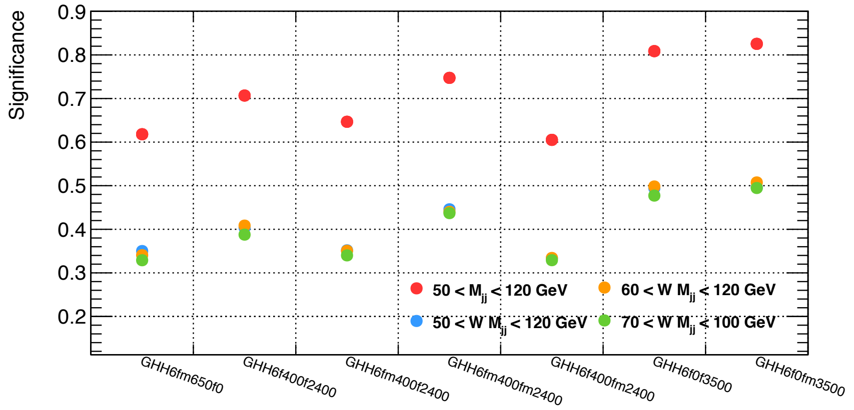

(b)

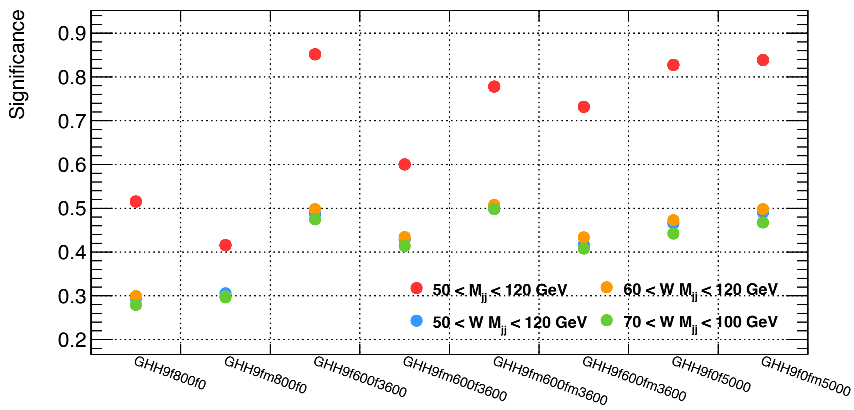

(c)

Figure 8.15 Signal significance in resolved signal region with different jet assignments for signals with heavy Higgs mass of (a) 300 GeV, (b) 600 GeV and (c) 900 GeV.

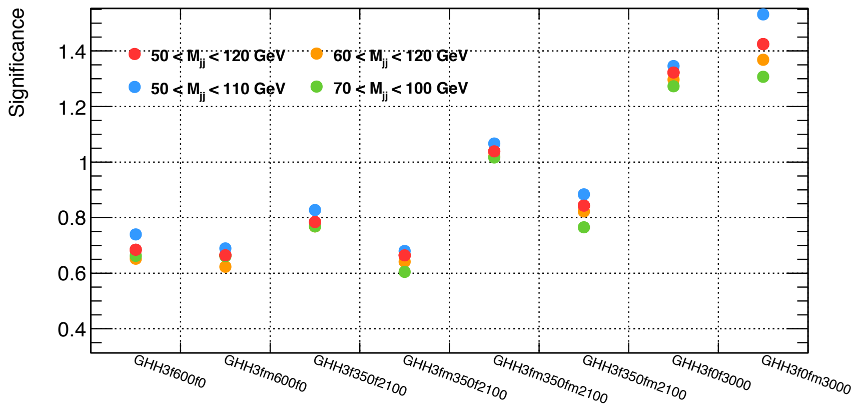

(a)

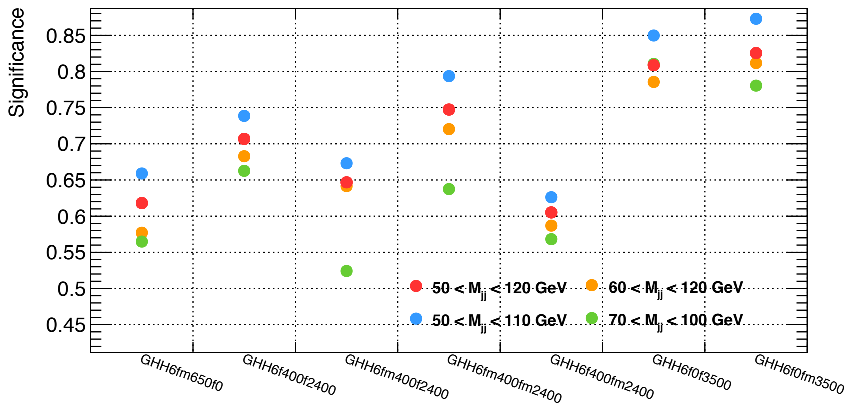

(b)

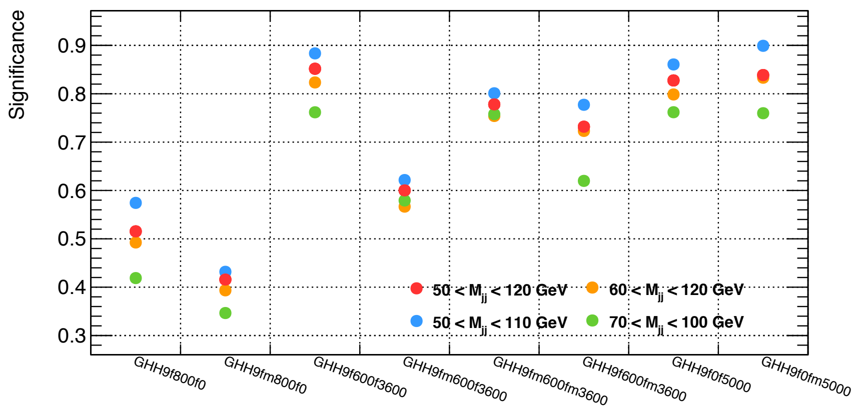

(c)

Figure 8.16 Signal significance in resolved signal region with different cuts on M_{jj} for signals with heavy Higgs mass of (a) 300 GeV, (b) 600 GeV and (c) 900 GeV.

8.4 Analysis regions

This analysis relies on the definition of different categories of events, fulfilling different sets of requirements, called analysis regions. Different regions have different purposes; signal region (SR) is used to compare data with the expected background + signal hypothesis in the fit; control region (CR) is defined to obtain the normalisations of backgrounds; validation region (VR) is aimed at validating the background estimation methods by comparing the background models with data.

8.4.1 Signal regions

According to the analysis strategy, there are two SRs: boosted SR and resolved SR. The event selections are defined in Table 8.3. In the boosted SR, the leading large-R jet passing the W-tagger 80% working point forms the hadronically decaying W boson, while in the resolved SR, two leading small-R jets are combined to form the hadronically decaying W candidate. A 3^{rd} lepton veto is applied to reduce the WZ background; a b-jet veto is used on small-R jets to suppress the SM backgrounds involving top quarks; A requirement of $M_{ll} > 100$ GeV is applied to reduce the Z+jets background.

Table 8.3 Selection criteria for the signal regions. The definition of boosted category is at least one large-R jet passing the object selection as described in Section 8.3.3.

Boosted SR	Resolved SR
Boosted Category	!Boosted Category
$E_T^{miss} > 80$ GeV	$E_T^{miss} > 60$ GeV
$N_J \geq 1$	$N_j \geq 2$
$p_T(J_1) > 200$ GeV	$p_T(j_1), p_T(j_2) > 20$ GeV
J_1 @ 80% W-tagger	$M_{jj} \in (50, 110)$ GeV
Two same-sign leptons with $p_T > (27)20$ GeV	
3^{rd} lepton veto	
no b-jet @ 85% DL1r	
$M_{ll} > 100$ GeV	

Figure 8.17-8.18 shows some representative plots for the boosted and resolved SRs. Obviously, signal has a larger value of effective mass.

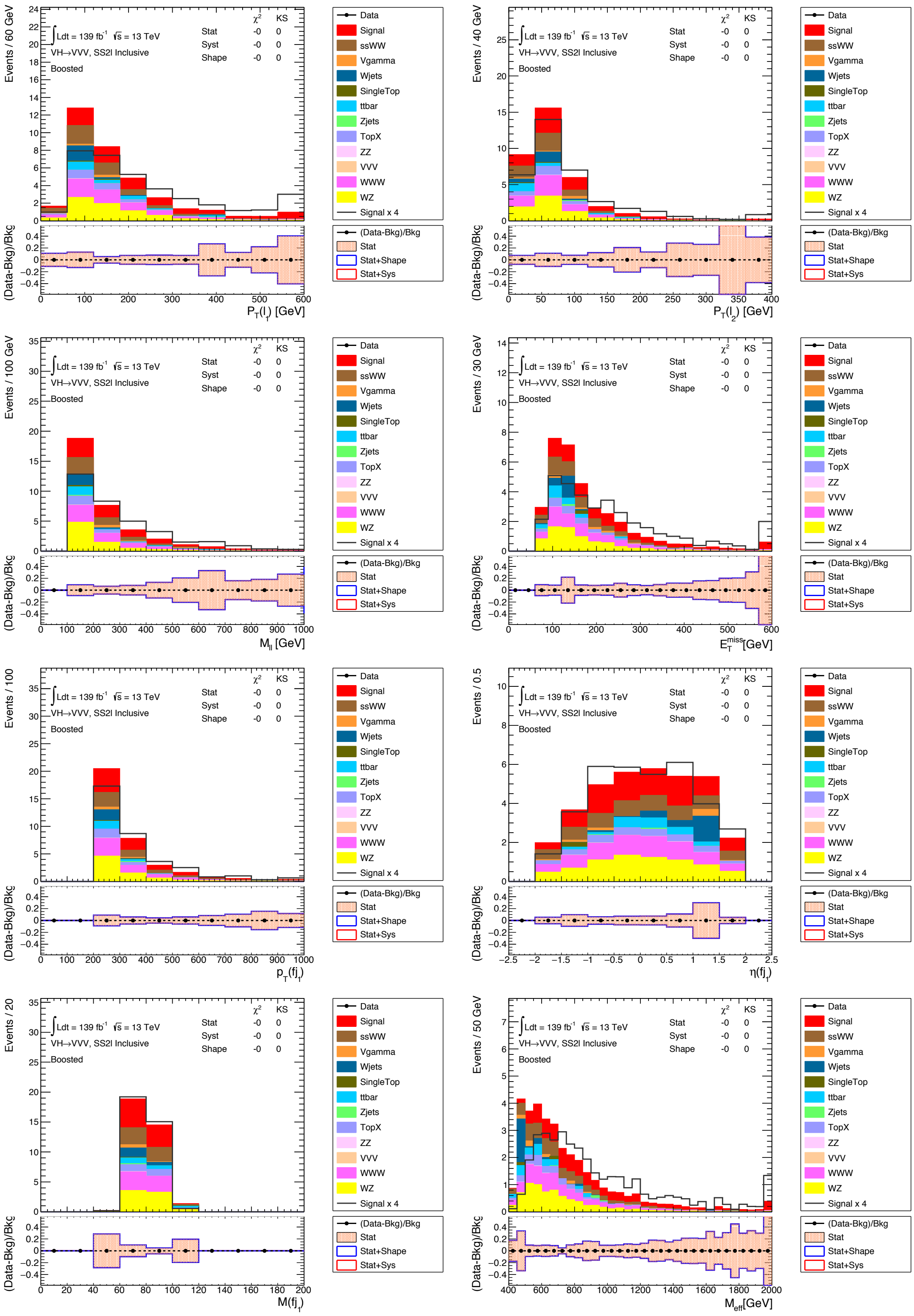

Figure 8.17 Kinematics' distributions in the boosted signal region. Only statistical uncertainty is included and backgrounds are directly from MC simulations. Signal: $m_H = 300$ GeV, $f_W = 0$ and $f_{WW} = 4600$.

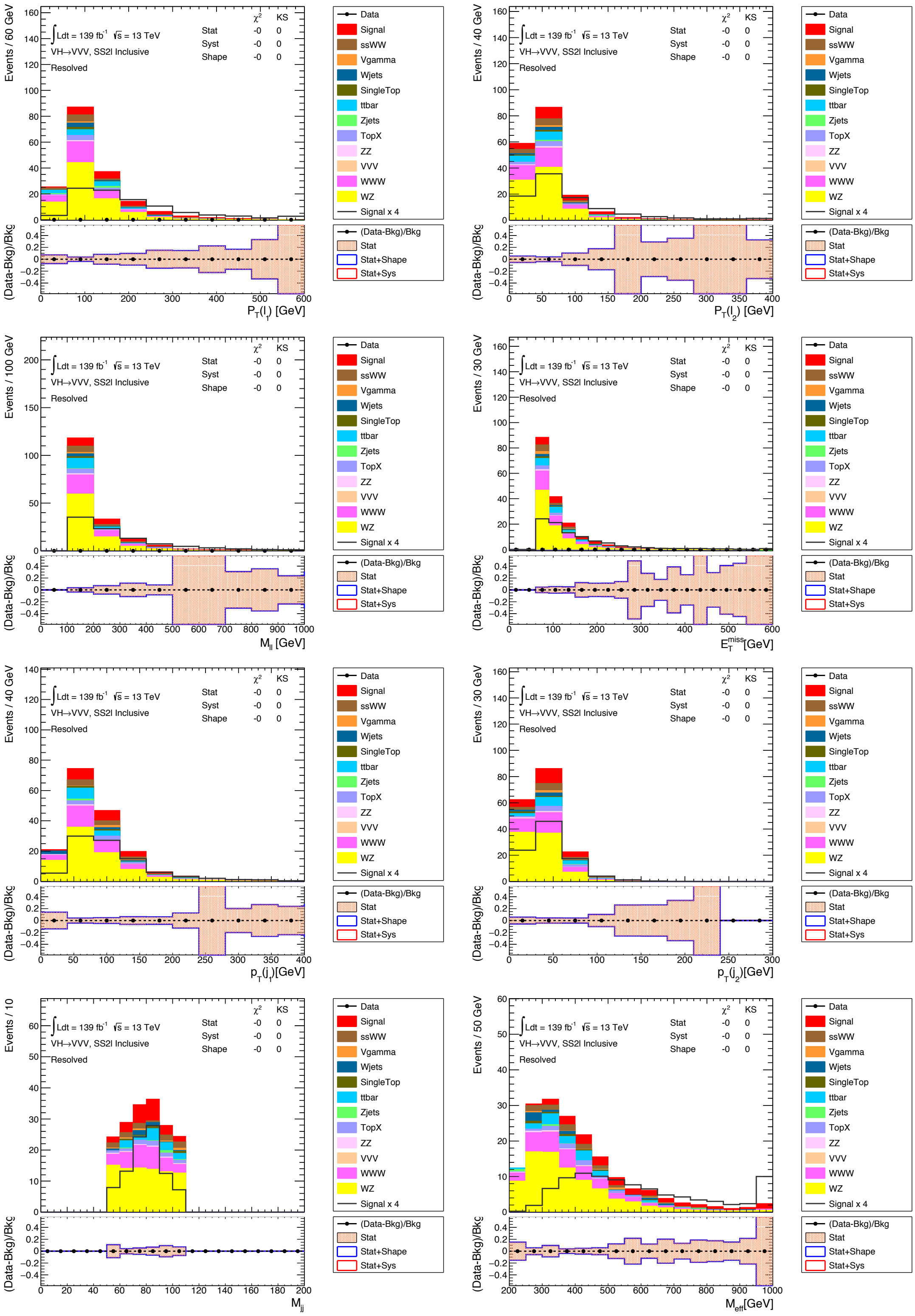

Figure 8.18 Kinematics' distributions in the resolved signal region. Only statistical uncertainty is included and backgrounds are directly from MC simulations. Signal: $m_H = 300$ GeV, $f_W = 0$ and $f_{WW} = 4600$.

8.4.2 Control regions

In this analysis, the dominant backgrounds are the SM WZ and same-sign WW ($ssWW$) processes, where the W and Z bosons decay leptonically. The corresponding MC samples can not model the backgrounds well, especially the yields in the signal regions. To estimate the contributions from WZ and $ssWW$ backgrounds, WZ and $ssWW$ control regions are defined, respectively.

Events in the WZ control regions must have exactly three leptons with invariant mass (M_{lll}) satisfying $M_{lll} > 110$ GeV. Among the three leptons, there should be at least one pair of same-flavor opposite-sign (SFOS) leptons. To gain additional statistics, the E_T^{miss} cut is loosened, and requirements of the W-tagger and M_{jj} are removed. The detailed event selections are described in Table 8.4.

Table 8.4 Selection criteria for the WZ control regions.

Boosted WZ CR	Resolved WZ CR
Boosted Category	!Boosted Category
≥ 1 large-R jet	≥ 2 small-R jets
$p_T > 200$ GeV	$p_T(j_1), p_T(j_2) > 20$ GeV
3 leptons with $p_T > 27, 20, 20$GeV	
4^{th} lepton veto	
at least one pair of same-flavor opposite-sign leptons	
$M_{lll} > 110$ GeV	
no b-jet @ 85% DL1r	
$E_T^{miss} > 40$ GeV	

Figure 8.19-8.20 show some kinematic distributions in the boosted and resolved WZ CRs. As can be seen, the total sum of MC yields is larger than the data yields, indicating that the WZ samples overestimate the data. But the shape from MC samples and from data are consistent. We can only correct the normalization of WZ.

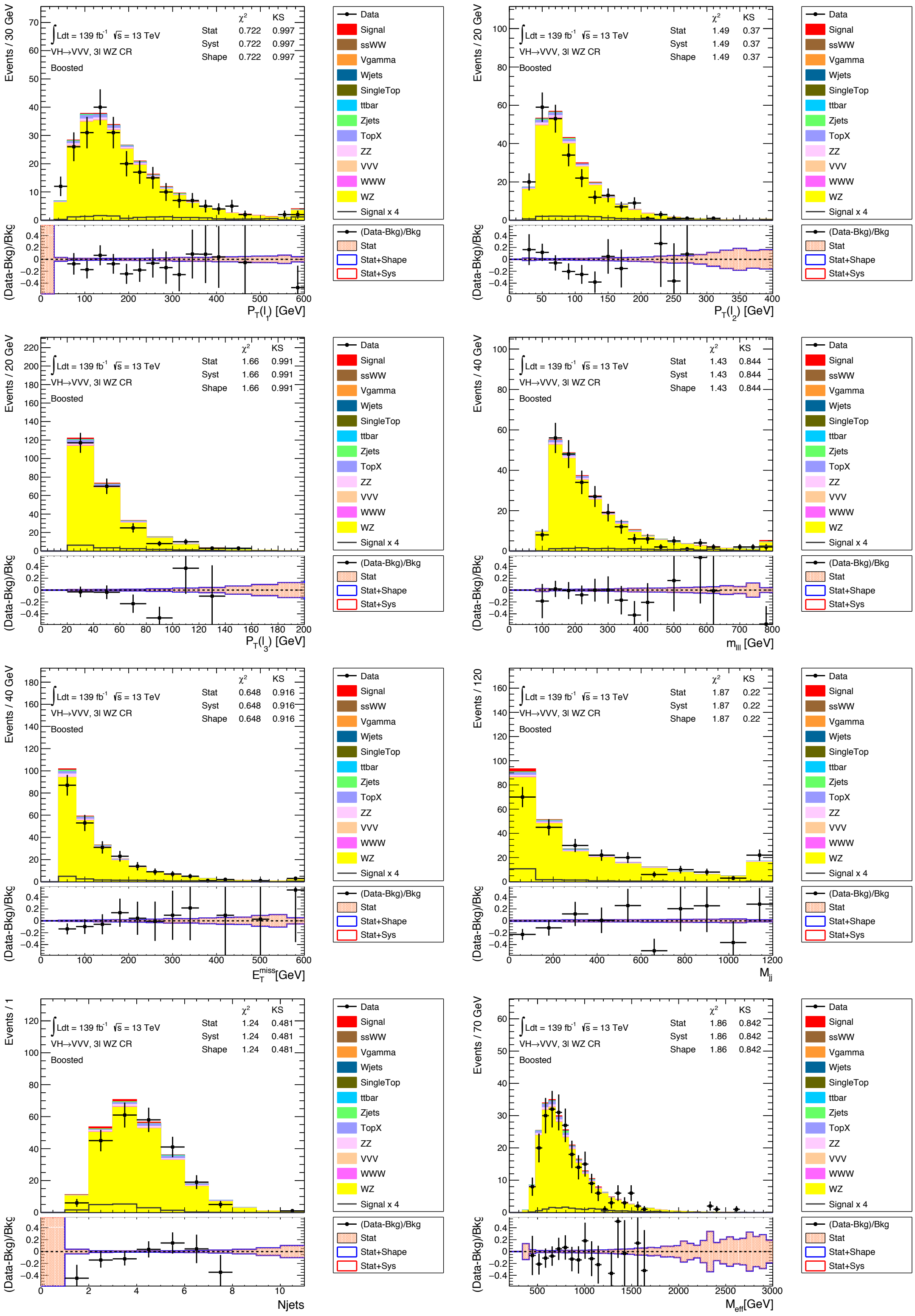

Figure 8.19 Kinematics' distributions in the boosted WZ CR. Only statistical uncertainty is included and backgrounds are directly from MC simulations. Signal: $m_H = 300$ GeV, $f_W = 0$ and $f_{WW} = 4600$.

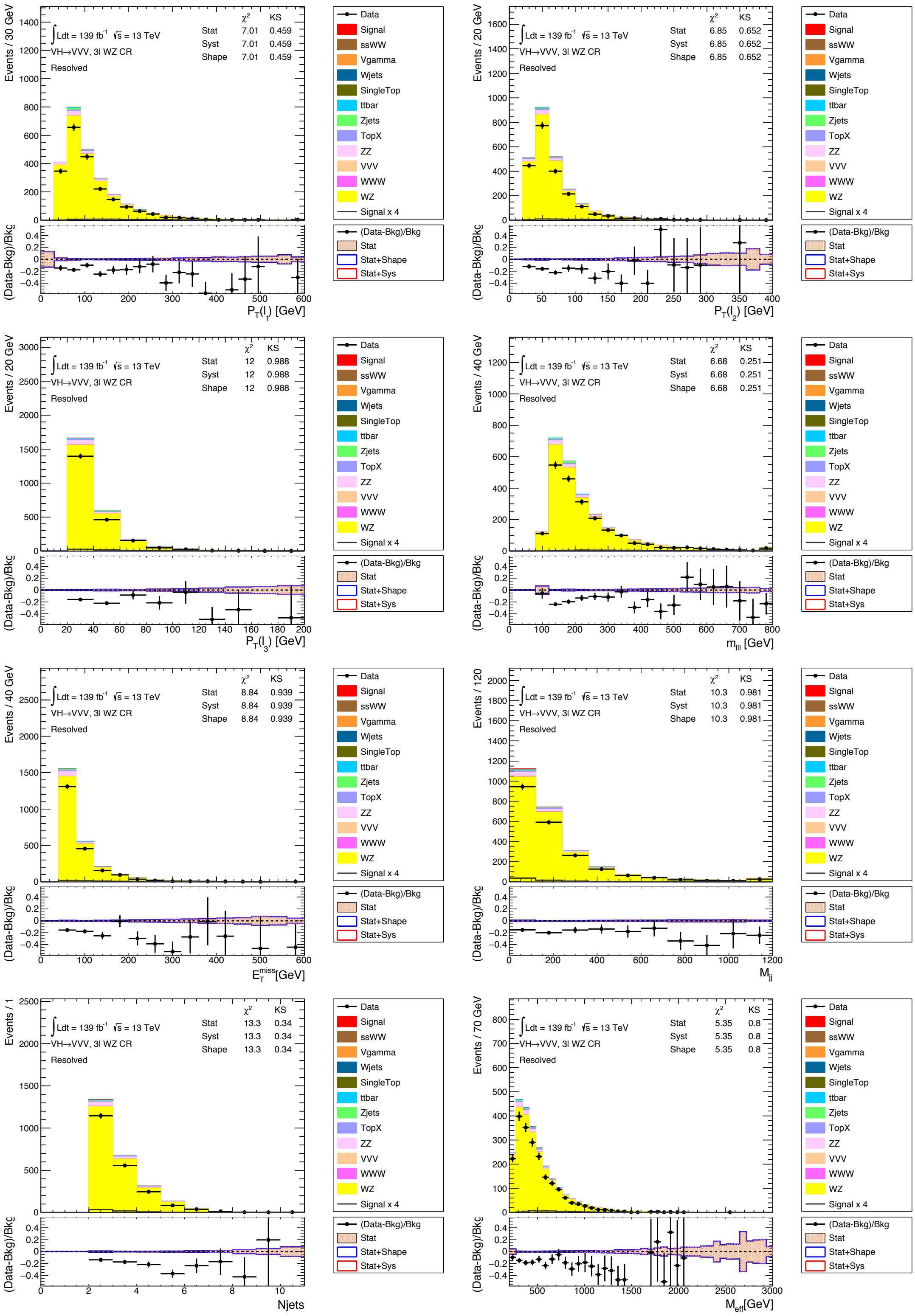

Figure 8.20 Kinematics' distributions in the resolved WZ CR. Only statistical uncertainty is included and backgrounds are directly from MC simulations. Signal: $m_H = 300$ GeV, $f_W = 0$ and $f_{WW} = 4600$.

To avoid overlap with SRs and VRs, the $ssWW$ CR is only defined in the resolved category as shown in Table 8.5. To improve the purity of the $ssWW$ component, the $M_{jj} > 200$ GeV cut is applied.

Table 8.5 Selection criteria for the $ssWW$ control region.

$ssWW$ **CR**
!Boosted Category
Two same-sign leptons with $p_T > 27(20)$ GeV
3^{rd} lepton veto
no b-jet @ 85% DL1r
$M_{ll} > 100$ GeV
$E_T^{miss} > 40$ GeV
$N_j \geq 2$
$p_T(j_1), p_T(j_2) > 20$ GeV
$M_{jj} > 200$ GeV

Figure 8.21 shows some kinematic plots in the $ssWW$ CR. It's obvious that the $ssWW$ samples underestimate the data, but shapes are consistent. So the $ssWW$ CR is also only used for normalization correction.

In the likelihood fit described in Section 8.8, normalization factors (NFs) of WZ and $ssWW$ backgrounds are free parameters. For the WZ background, there are two NFs corresponding to the boosted and resolved regions, respectively.

8.4.3 Validation regions

Validation regions are defined in Table 8.6. The event selections are similar with SRs' definitions, except failing the W-tagger and M_{jj} requirement.

Figure 8.22-8.23 show some representative plots for the boosted and resolved VRs.

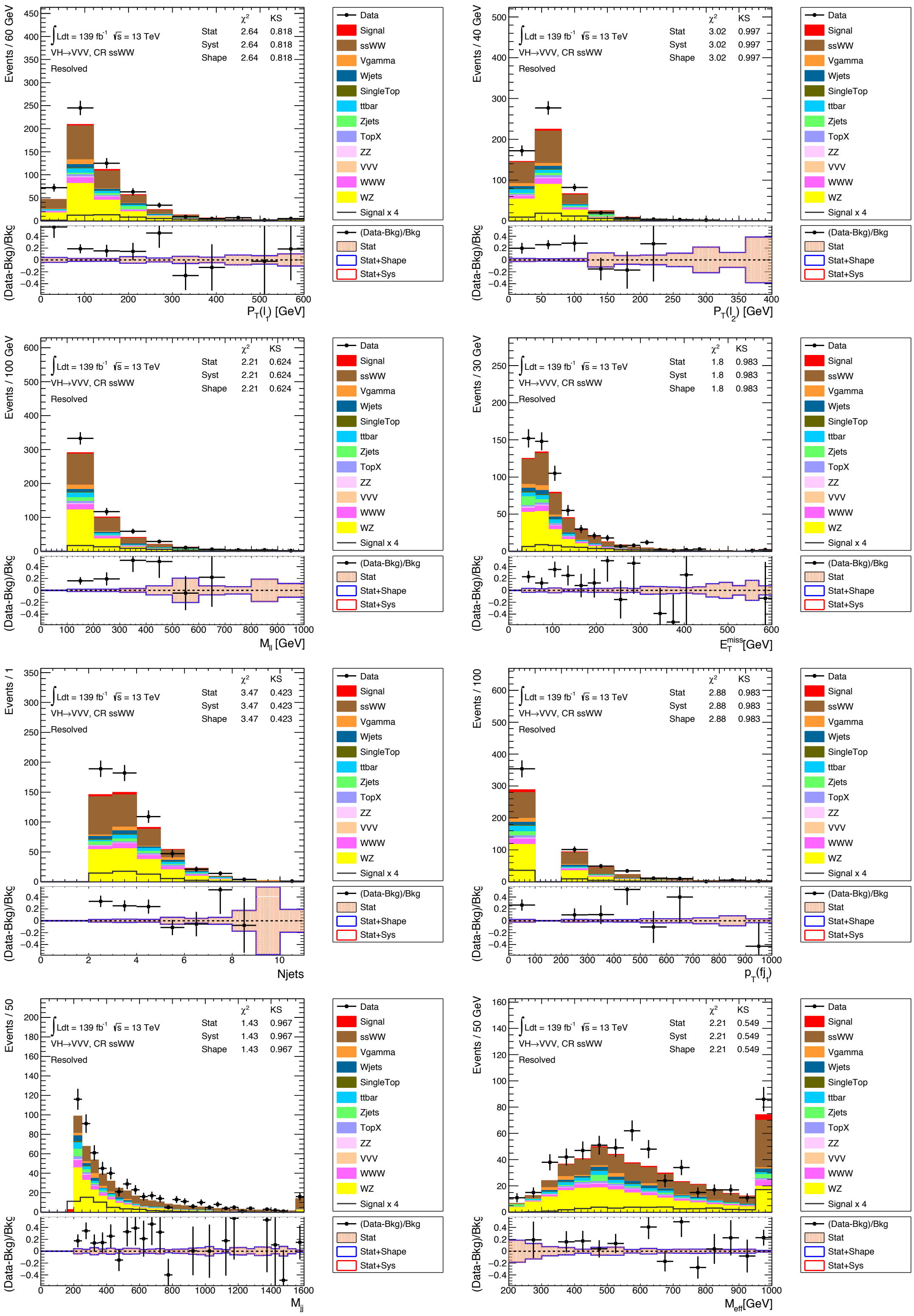

Figure 8.21 Kinematics' distributions in the $ssWW$ CR. Only statistical uncertainty is included and backgrounds are directly from MC simulations. Signal: $m_H = 300$ GeV, $f_W = 0$ and $f_{WW} = 4600$.

Table 8.6 Selection criteria for the validation regions.

Boosted VR	Resolved VR
Boosted Category	!Boosted Category
$E_T^{miss} > 80$ GeV	$E_T^{miss} > 60$ GeV
$N_J \geq 1$	$N_j \geq 2$
$p_T(J_1) > 200$ GeV	$p_T(j_1), p_T(j_2) > 20$ GeV
J_1 not @ 80% W tagger	$M_{jj} \leq 50$ GeV or
	110 GeV $\leq M_{jj} \leq 200$ GeV
Two same-sign leptons with $p_T >$ (27)20 GeV	
3^{rd} lepton veto	
no b-jet @ 85% DL1r	
$M_{ll} > 100$ GeV	

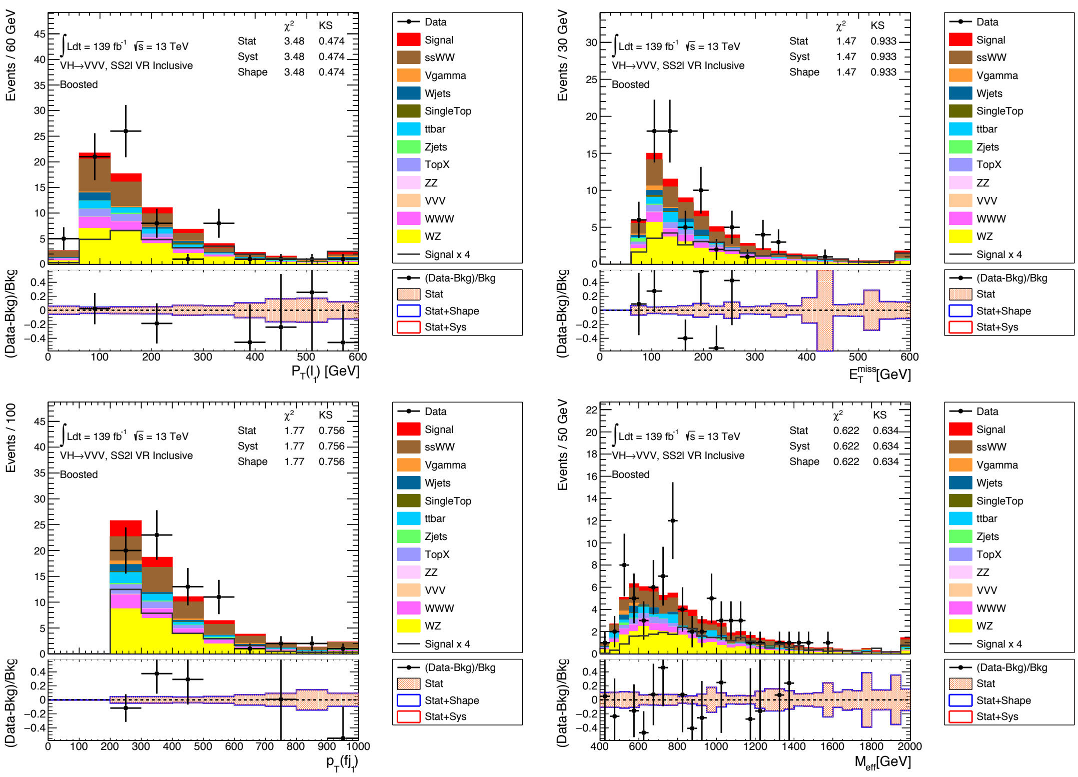

Figure 8.22 Kinematics' distributions in the boosted VR. Only statistical uncertainty is included and backgrounds are directly from MC simulations. Signal: $m_H = 300$ GeV, $f_W = 0$ and $f_{WW} = 4600$.

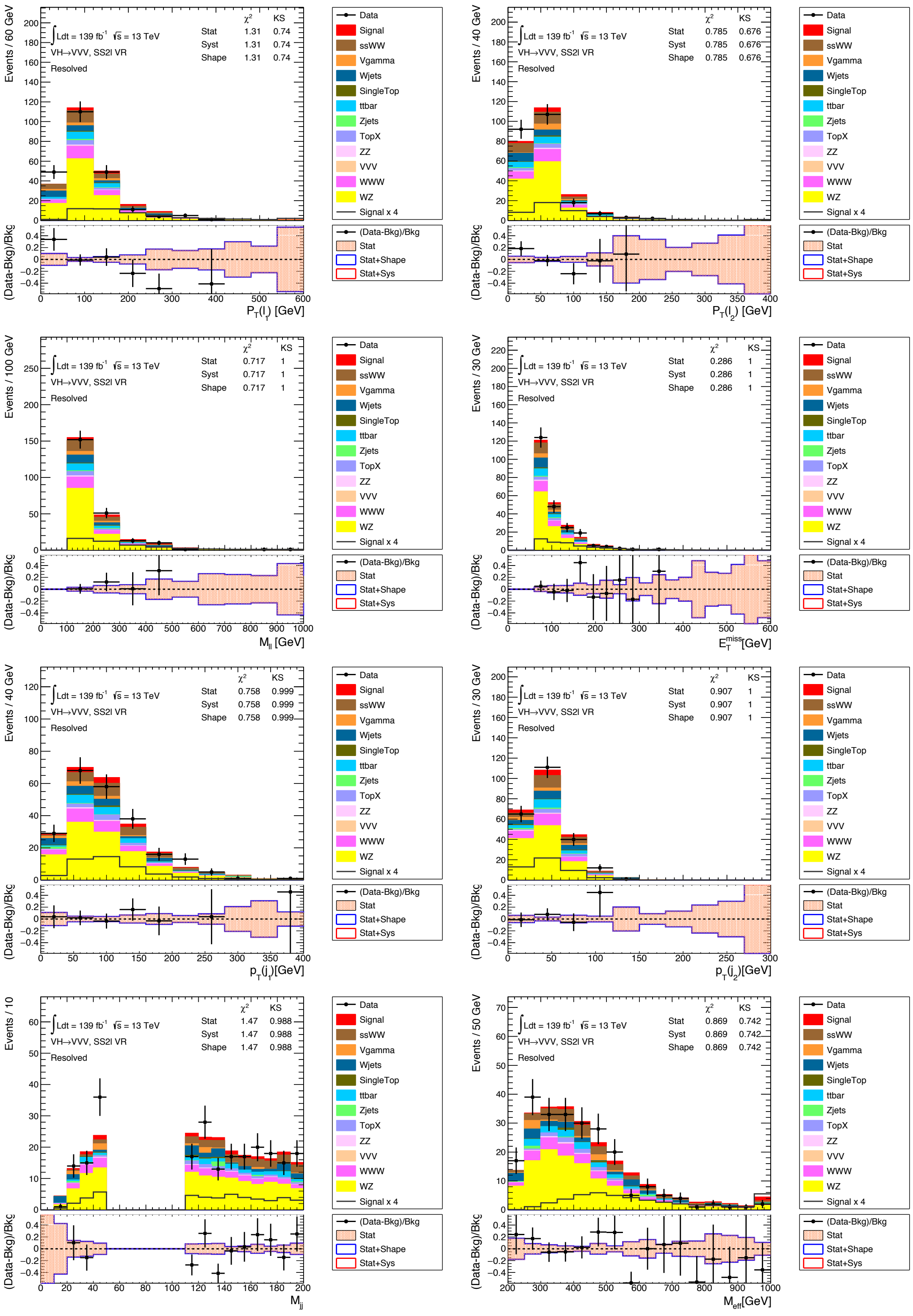

Figure 8.23 Kinematics' distributions in the resolved VR. Only statistical uncertainty is included and backgrounds are directly from MC simulations. Signal: $m_H = 300$ GeV, $f_W = 0$ and $f_{WW} = 4600$.

8.5 Signal acceptance × efficiency

This section shows the effect of m_H, f_W and f_{WW} on the effective mass distributions, and the acceptance × efficiency ($\mathcal{A} \times \varepsilon$) of signals.

Figure 8.24 shows M_{eff} distributions for some signal points used for (f_W, f_{WW}) parameter space scan with three fixed m_H values (300 GeV, 600 GeV and 900 GeV), indicating that f_W has larger impact on signal boosted level than f_{WW}. Figure 8.25 and Figure 8.26 show M_{eff} distributions for signal points used for m_H scan from 200 GeV to 2 TeV with two sets of the parameters (f_W, f_{WW}): (1350, 0) and (0, 6200), indicating that signal becomes more boosted and has smaller cross-section with higher m_H value.

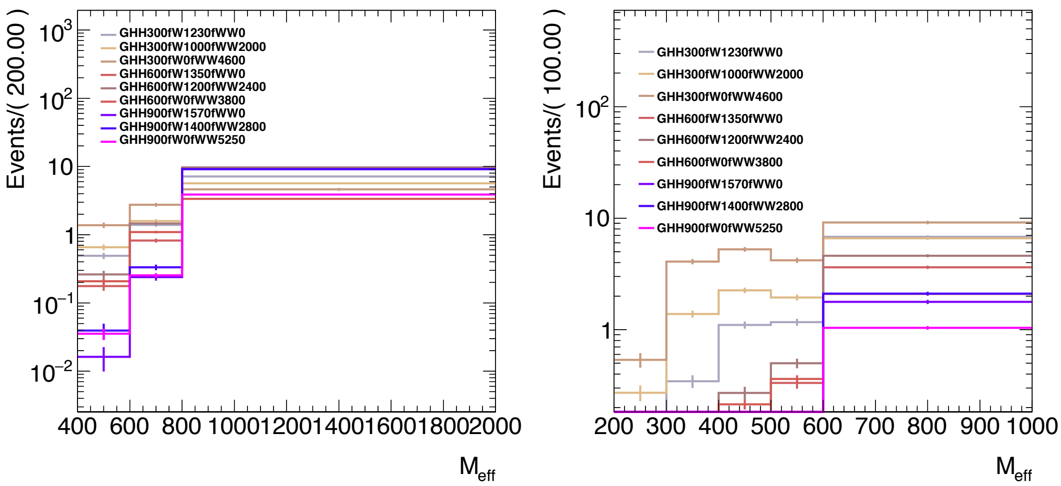

Figure 8.24 M_{eff} distributions in boosted (left) and resolved (right) signal regions for some signal points used for (f_W, f_{WW}) parameter space scan. For the naming convention of signal points, GHH600fW1350fWW0 represents m_H = 600 GeV, f_W = 1350 and f_{WW} = 0.

The product of acceptance × efficiency ($\mathcal{A}\times\varepsilon$) for signal events in region A is defined as the number of signal events satisfying the full set of selection criteria in region A, divided by the total number of generated signal events. So it's calculated with respect to all heavy Higgs boson signal decays filtered. Figure 8.27-8.30 show values of $\mathcal{A} \times \varepsilon$ in different analysis regions with $(f_W, f_{WW}) = (1350, 0)$ and $(f_W, f_{WW}) = (6200, 0)$, as a function of the mass of the heavy Higgs boson. With the increasing of m_H, the $\mathcal{A} \times \varepsilon$ in the boosted SR is increased.

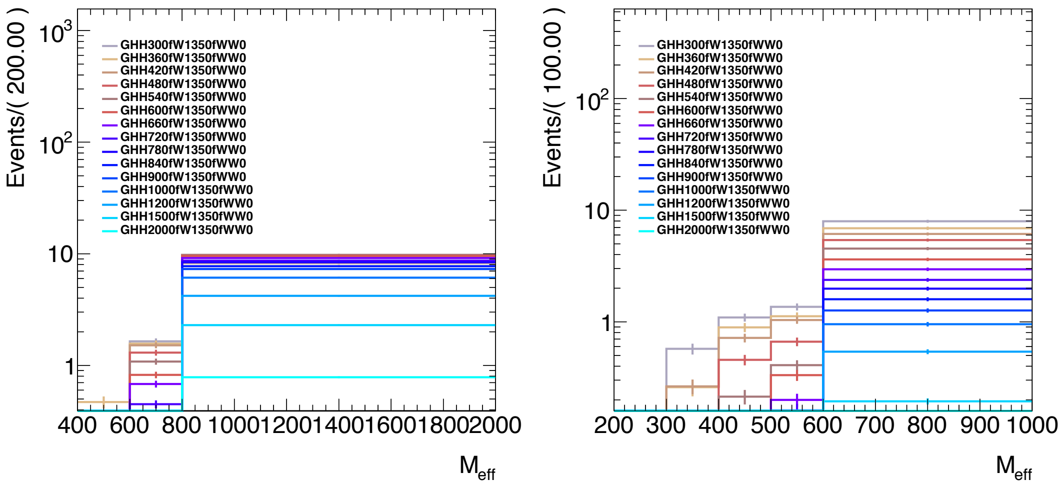

Figure 8.25 M_{eff} distributions in boosted (left) and resolved (right) signal regions for signal points used for m_H scan from 200 GeV to 2 TeV with $(f_W, f_{WW}) = (1350, 0)$. For the naming convention of signal points, GHH600fW1350fWW0 represents $m_H = 600$ GeV, $f_W = 1350$ and $f_{WW} = 0$.

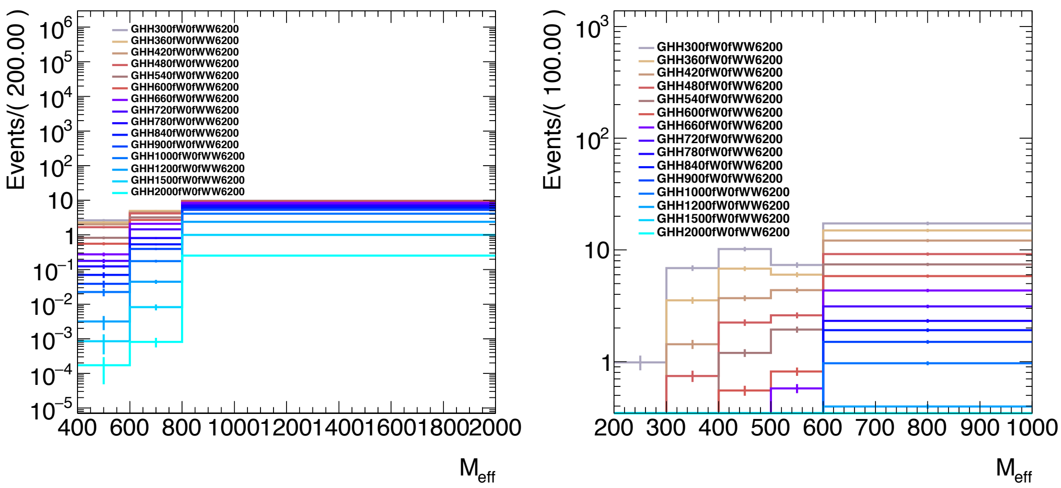

Figure 8.26 M_{eff} distributions in boosted (left) and resolved (right) signal regions for signal points used for m_H scan from 200 GeV to 2 TeV with $(f_W, f_{WW}) = (0, 6200)$. For the naming convention of signal points, GHH600fW0fWW6200 represents $m_H = 600$ GeV, $f_W = 0$ and $f_{WW} = 6200$.

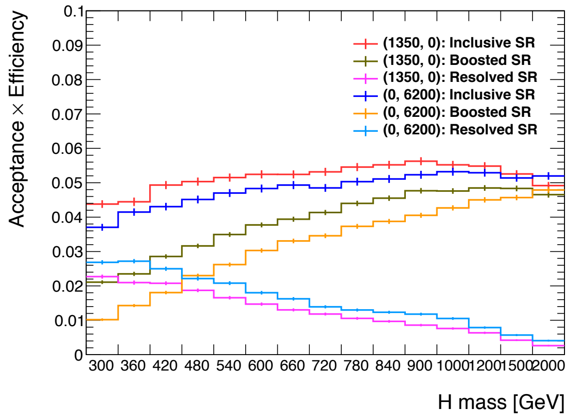

Figure 8.27 The product of acceptance × efficiency as a function of the mass of the heavy Higgs boson in the boosted, resolved and inclusive signal regions, with (f_W, f_{WW}) fixed to $(1350, 0)$ and $(0, 6200)$.

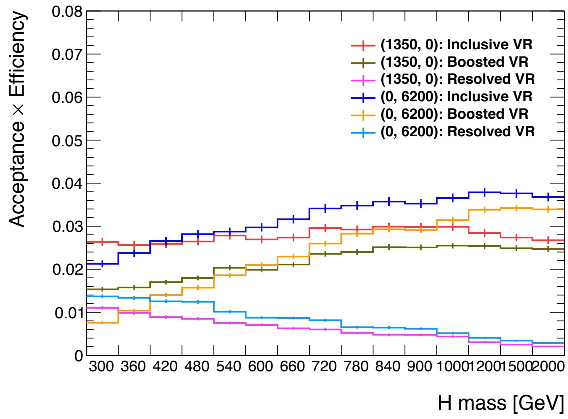

Figure 8.28 The product of acceptance × efficiency as a function of the mass of the heavy Higgs boson in the boosted, resolved and inclusive validations regions, with (f_W, f_{WW}) fixed to $(1350, 0)$ and $(0, 6200)$.

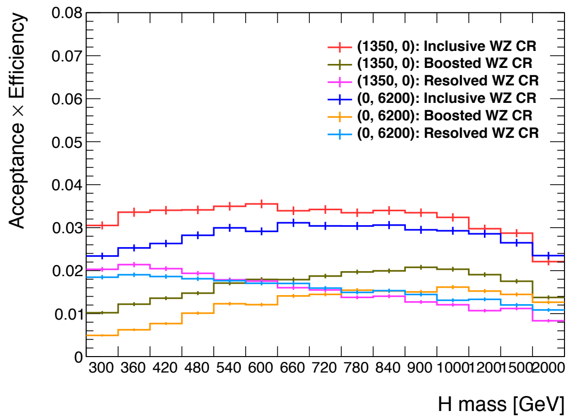

Figure 8.29 The product of acceptance × efficiency as a function of the mass of the heavy Higgs boson in the boosted, resolved and inclusive WZ control regions, with (f_W, f_{WW}) fixed to $(1350, 0)$ and $(0, 6200)$.

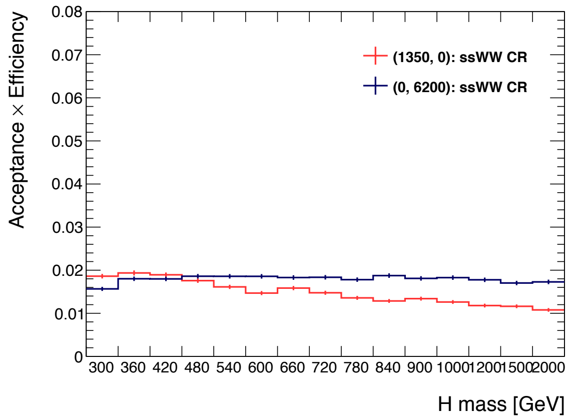

Figure 8.30 The product of acceptance × efficiency as a function of the mass of the heavy Higgs boson in the ssWW control region, with (f_W, f_{WW}) fixed to (1350, 0) and (0, 6200).

8.6 Background estimation and validation

The main SM backgrounds that mimic the $\ell^{\pm}\nu\ell^{\pm}\nu qq$ signature are charge-flip, non-prompt, photon conversion and prompt backgrounds. The first three are estimated with a data-driven method, while the prompt backgrounds are estimated with simulated MC samples, except for the WZ and $ssWW$ backgrounds which are estimated in dedicated CRs.

8.6.1 Charge-flip background

The charge-flip background originates from processes that produce two opposite-sign leptons, but the charge of one lepton is misidentified. It's only significant for electrons and is mainly due to the interactions of electrons and material of the inner detector. The main contribution comes from $t\bar{t}$, W+jets and Z+jets→ e^+e^- + jets processes and can be suppressed by requirements on ECIDS, E_T^{miss} and M_{ll}. The charge misidentification rate is determined in a data sample enriched in $Z \to e^+e^-$ events (referred to as Zee CR) with requirements:

- exactly two electrons with $p_T > 27(20)$ GeV
- at least one small-R jet or large-R jet
- Z mass window: $75 < m_{ee} < 105$ GeV

The Z boson mass reconstruted with two leptons always has good resolution. In the Zee CR, the processes not containing $Z \to e^+e^-$ decay are referred to as "non-Zee". We assume the non-Zee contribution in the Z mass window equals to the non-Zee contribution in the side-band regions ($60 < m_{ee} < 75$ GeV and $105 < m_{ee} < 120$ GeV), and it roughly equals to the data yields in the side-band regions. With this assumption, the Zee events in the Z mass window are obtained by subtracting the data in the side-band regions from the data in the Z mass window. In the Zee CR, most of the events have opposite-sign electron pair, and only a small part contains same-sign lepton pair. A likelihood fit is performed to extract the misidentification rate as a function of electron p_T and $|\eta|$ from the two parts of the events[106]. The rate ranges between 0.01% and 4% with statistical uncertainty varing between 1% and 10%, and increases with the increasing of p_T and $|\eta|$, as shown in Figure 8.31. The contribution of the charge-flip background is estimated by applying the rates to data events in a region satisfying all the selection criteria except that the two electrons are oppositely charged.

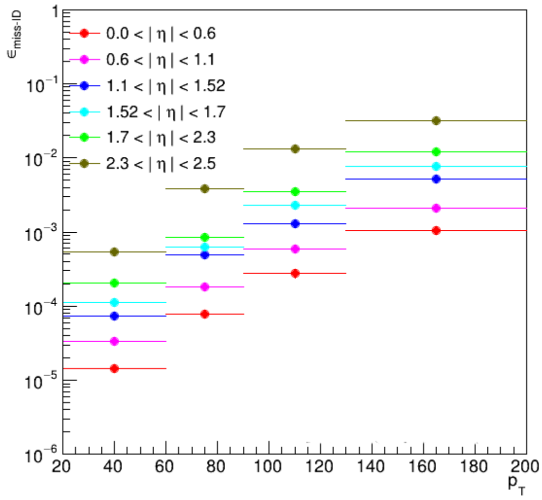

Figure 8.31 The electron misidentification rate as a function of electron p_T and $|\eta|$.

8.6.2 Non-prompt background

The processes that produce one or two non-prompt leptons are referred to as "non-prompt background". Since the MC simulation may not accurately model the details of the non-prompt leptons, a data-driven ABCD method is employed to extract the fake factor. The ABCD method defines four regions as shown in Figure 8.32 and assume that the ratio of non-prompt background yields in region A and non-prompt background yields in region C equals to the ratio of non-prompt background yields in region B and non-prompt background yields in region D. The ratio is known as the fake factor. Region A is the signal region. Region C is defined with exactly the same definition as signal region, but requiring one "Signal" lepton and one "antiID" lepton. Region B and region D are defined by requesting exactly one b-tagged jet and have large component of $t\bar{t}$ background. The fake factors derived from region B and region D are applied to region C to obtain the non-prompt background contribution in signal region. The fake factors are calculated separately for electrons and muons as a function of lepton p_T and $|\eta|$. The electron fake factor is strongly dependent on p_T, but the dependency on $|\eta|$ is negligible. In the region of $p_T \leq 30$ GeV, $30 < p_T \leq 40$ GeV and $p_T > 40$ GeV, the electron fake factors are found to be 0.03±0.005, 0.05±0.01 and 0.14±0.03 (the error corresponds to statistical uncertainty). For muon fake factors, the dependency is opposite. In the region of $0 < |\eta| \leq 0.5$, $0.5 < |\eta| \leq 1.5$ and $|\eta| > 1.5$, the corresponding muon fake factors are 0.024 ± 0.004, 0.016 ± 0.003 and 0.011 ± 0.003 (the error is statistical uncertainty).

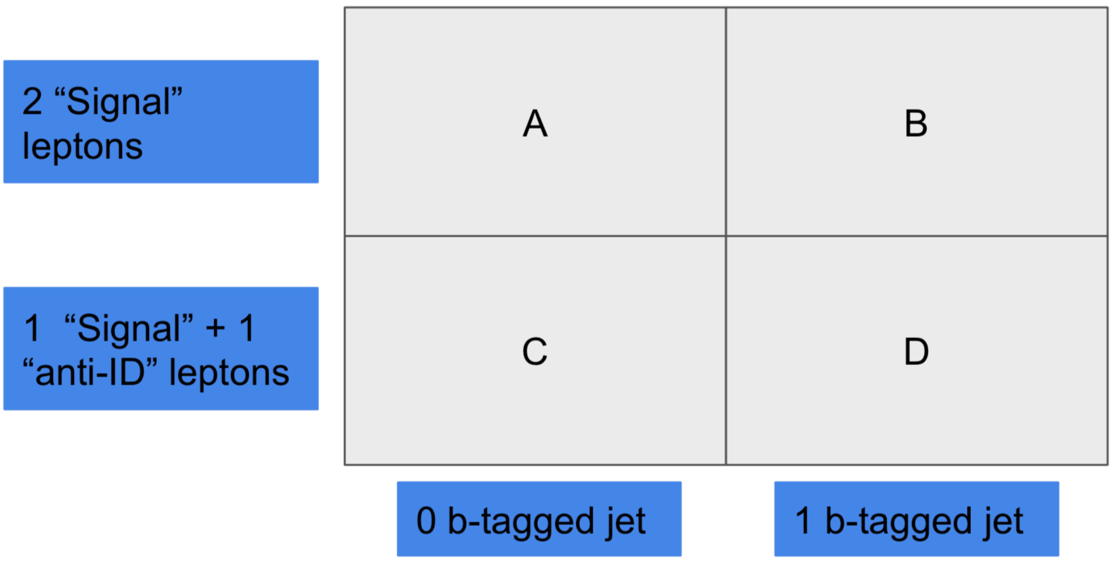

Figure 8.32 Illustration of the ABCD method.

8.6.3 Photon-conversion background

The photon-conversion background originates from the $W\gamma$+jets and $Z\gamma$+jets processes where the photon converts to electron and positron. The reconstructed electron is actually a mis-reconstructed photon. Similar to the non-prompt background, the data-driven ABCD method is used to estimate the photon conversion rate. Events in region C are required to have one "Signal" lepton and one "antiBL" electron. In region B and region D, events must contain three leptons $\mu^{\pm}\mu^{\mp}e$ satisfying $80 < m_{\mu\mu e} < 100$ GeV ; in region B, the three leptons are all "Signal" leptons; in region D, the electron is "antiBL" electron, while muons are "Signal" muons. The "antiBL" lepton is defined in Section 8.3.2. The photon conversion rates are measured to be 0.40 ± 0.05 and 0.45 ± 0.05 in two p_T bins: $p_T \leq 25$ GeV and $p_T > 25$ GeV, respectively. The error is statistical uncertainty.

8.6.4 Prompt backgrounds

Processes producing at least three prompt leptons or two same-sign charged leptons are prompt backgrounds. The main contributions come from WZ and $ssWW$ backgrounds, and the other small contributions come from TopX, ZZ, WWZ, WZZ and ZZZ processes (referred to as "Other background"). The WZ and $ssWW$ backgrounds are estimated in dedicated CRs which correct the normalisations.

If one of the leptons from the WZ+jets process is not reconstructed, this process could contribute to the signal regions. The boosted and resolved WZ CRs are defined in Section 8.4.2, among which the purity of WZ component reaches 95%. The contributions from charge-flip, non-prompt and photon-conversion backgrounds in the WZ CRs are found to be negligible by studying MC simulations. From the likelihood fit described in Section 8.8, the normalization factors of WZ in the boosted and resolved regions are found to be 0.93 ± 0.07 and 0.83 ± 0.03, respectively. Figure 8.33-8.34 show some kinematic distributions in boosted and resolved WZ CRs after applying normalization factors. In general, the estimated backgrounds agree with the data. The WZ samples simulated with SHERPA can not model the number of small-R jets (Njet) well, but the difference can be covered by systematic uncertainties.

The $ssWW$ process produces two same-sign leptons, which is the irreducible background. The $ssWW$ CR defined in Section 8.4.2 is used to correct the normalization of the $ssWW$ background. The normalization factor is extracted from the likelihood fit and is found to be 1.54 ± 0.17, which is consistent with the ATLAS measurement[107]. Some

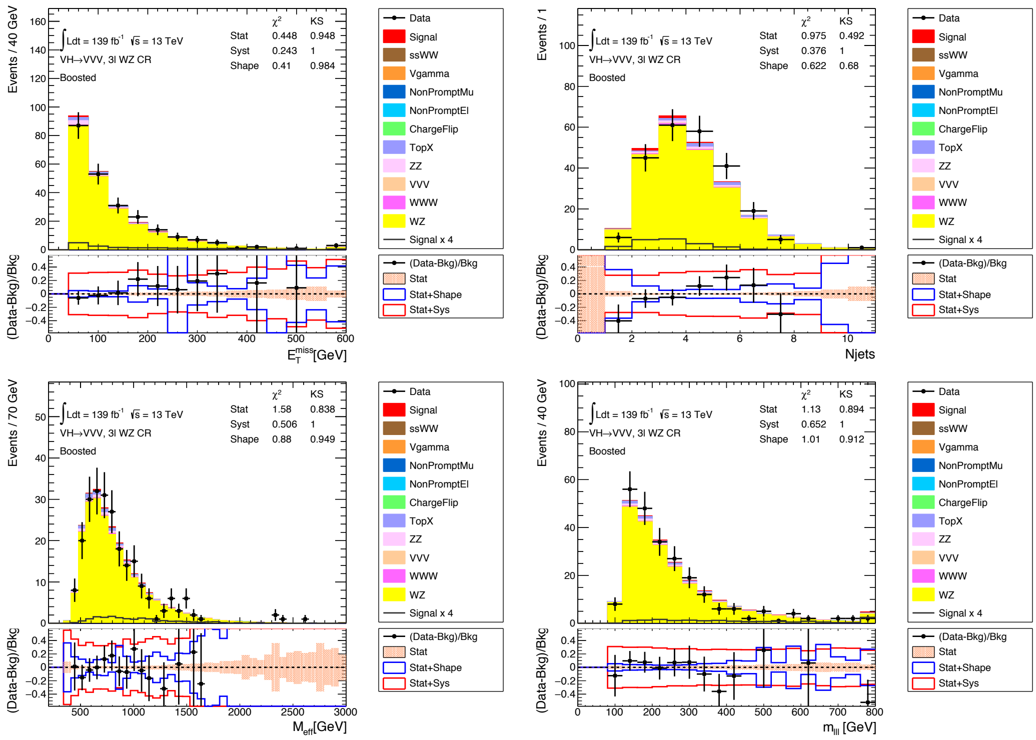

Figure 8.33 Distributions of E_T^{miss}, Njet, effective mass and $m_{\ell\ell\ell}$ in the boosted WZ CR. A normalization factor of 0.93 is applied to the WZ events. Both statistical and systematic uncertainties are included.

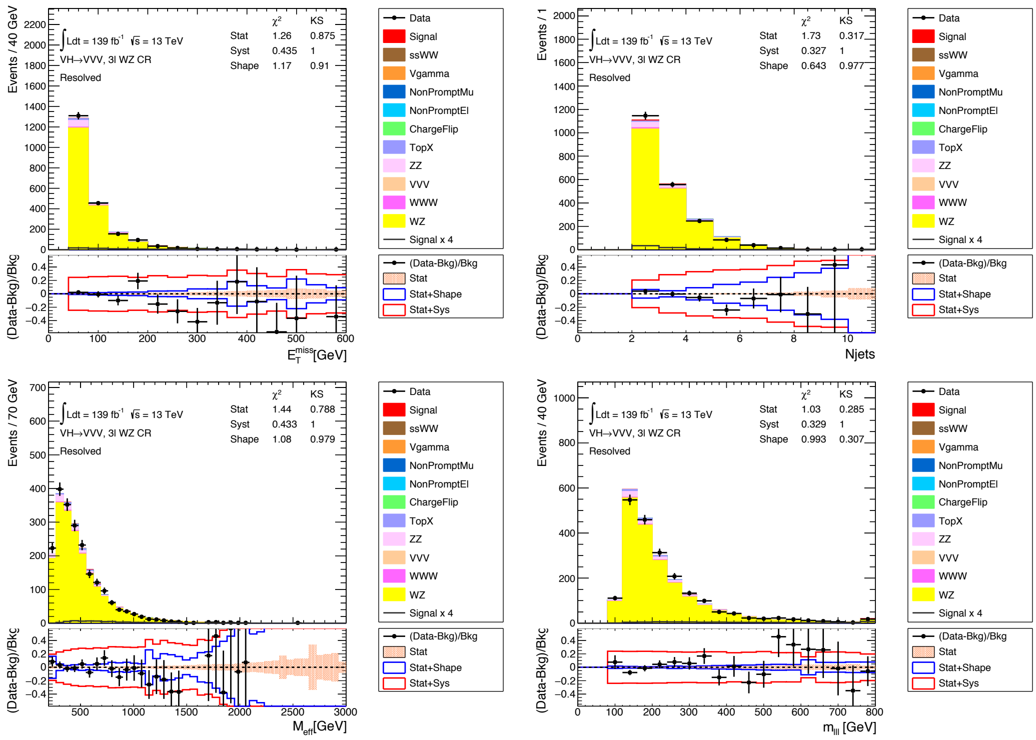

Figure 8.34 Distributions of E_T^{miss}, Njet, effective mass and $m_{\ell\ell\ell}$ in the resolved WZ CR. A normalization factor of 0.83 is applied to the WZ events. Both statistical and systematic uncertainties are included.

kinematic distributions after applying normalization factors of $ssWW$ and WZ backgrounds in this region are shown in Figure 8.35, indicating a good agreement between data and estimated backgrounds.

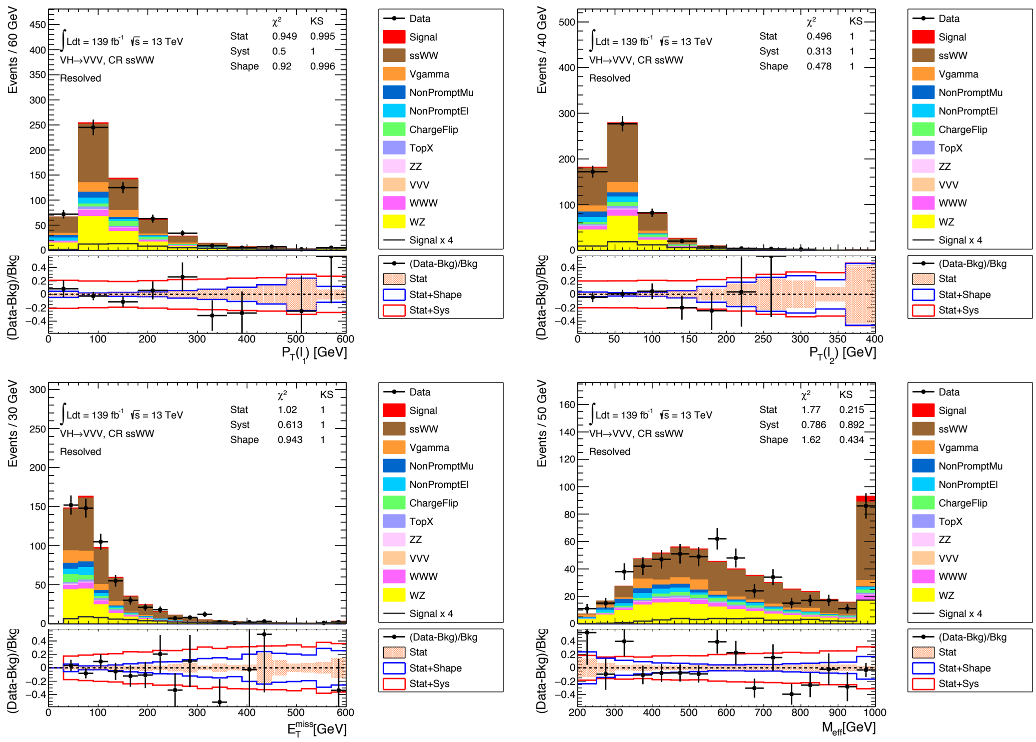

Figure 8.35 Distributions of E_T^{miss}, leading lepton p_T, effective mass and leading small-R jet p_T in the $ssWW$ CR. Normalization factors of $ssWW$ and WZ are applied. Both statistical and systematic uncertainties are included.

8.6.5 Validation of background estimates

Validation regions are used to validate the estimation of WZ, $ssWW$ and WWW backgrounds, defined in Section 8.4.3. The plots and tables shown in this section include the estimated non-prompt, charge-flip and photon-conversion backgrounds ,and WZ and $ssWW$ backgrounds with normalization factors applied. Figure 8.36-8.37 show some kinematic distributions in the boosted and resolved VRs, and the corresponding signal and background yields are summarized in Table 8.7-8.8. Within the statistical uncertainty, the data and the estimated backgrounds agree well.

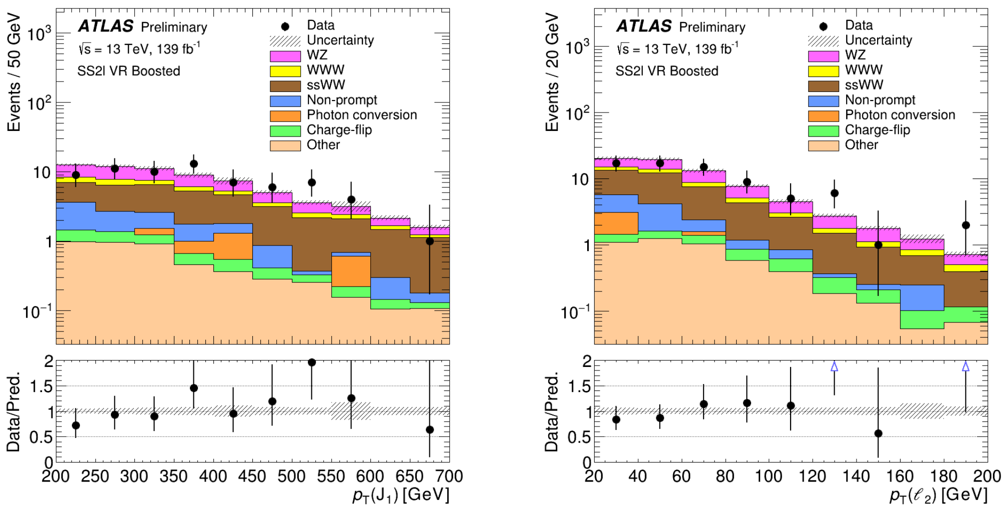

Figure 8.36 Distributions of $p_T(J_1)$ and $p_T(\ell_2)$ in the boosted VR. Only statistical uncertainty is included.

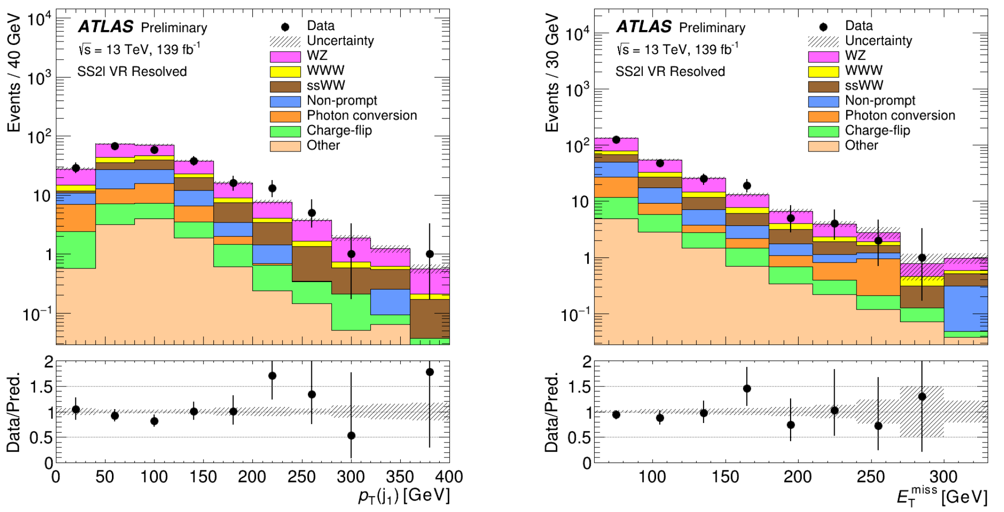

Figure 8.37 Distributions of $p_T(j_1)$ and E_T^{miss} in the resolved VR. Only statistical uncertainty is included.

Table 8.7 The data, signal and background yields in the boosted VR. GHH6f650f0, GHH300fW0fWW4600, GHH600fW1200fWW2400, GHH600fW1350fWW0 and GHH900fW1350fWW0 are benchmark signals. NonPromptEl and NonPromptMu are the non-prompt backgrounds originating from fake electrons and muons respectively. Only statistical uncertainty is included.

	$e^{\pm}e^{\pm}$	$e^{\pm}\mu^{\pm}$	$\mu^{\pm}e^{\pm}$	$\mu^{\pm}\mu^{\pm}$	$\ell\ell$
GHH6f650f0	0.19 ± 0.02	0.32 ± 0.03	0.31 ± 0.03	0.30 ± 0.03	1.12 ± 0.05
GHH300fW0fWW4600	0.83 ± 0.11	2.03 ± 0.17	1.82 ± 0.16	2.80 ± 0.20	7.48 ± 0.32
GHH600fW1200fWW2400	1.37 ± 0.09	1.99 ± 0.11	1.77 ± 0.10	2.14 ± 0.11	7.27 ± 0.20
GHH600fW1350fWW0	1.10 ± 0.07	1.58 ± 0.09	1.34 ± 0.08	1.56 ± 0.09	5.58 ± 0.17
GHH900fW1350fWW0	0.77 ± 0.05	1.03 ± 0.05	1.06 ± 0.05	1.09 ± 0.05	3.95 ± 0.11
TopX	0.89 ± 0.08	1.25 ± 0.10	1.03 ± 0.09	1.41 ± 0.11	4.57 ± 0.19
WWW	1.23 ± 0.08	1.94 ± 0.09	1.51 ± 0.08	2.27 ± 0.10	6.96 ± 0.18
ssWW	4.93 ± 0.10	7.16 ± 0.13	6.27 ± 0.12	8.69 ± 0.14	27.06 ± 0.25
VVV	0.03 ± 0.01	0.03 ± 0.00	0.03 ± 0.00	0.03 ± 0.01	0.11 ± 0.01
ZZ	0.04 ± 0.01	0.05 ± 0.01	0.05 ± 0.01	0.05 ± 0.01	0.19 ± 0.02
WZ	4.92 ± 0.17	5.89 ± 0.19	4.85 ± 0.18	5.99 ± 0.18	21.65 ± 0.36
NonPromptEl	1.42 ± 0.47	0.18 ± 0.20	0.97 ± 0.34	0.00 ± 0.00	2.57 ± 0.61
NonPromptMu	0.00 ± 0.00	2.16 ± 0.21	0.41 ± 0.09	2.15 ± 0.21	4.73 ± 0.31
Charge-flip	0.81 ± 0.08	0.99 ± 0.09	0.20 ± 0.03	0.00 ± 0.00	1.99 ± 0.12
Photon conversion	1.47 ± 0.86	0.08 ± 0.44	-0.00 ± 0.00	0.00 ± 0.00	1.55 ± 0.97
Total Bkg.	16.04 ± 1.01	20.16 ± 0.60	15.69 ± 0.43	21.12 ± 0.35	73.01 ± 1.30
Data	13.00	26.00	18.00	16.00	73.00

Table 8.8 The data, signal and background yields in the resolved VR. GHH6f650f0, GHH300fW0fWW4600, GHH600fW1200fWW2400, GHH600fW1350fWW0 and GHH900fW1350fWW0 are benchmark signals. NonPromptEl and NonPromptMu are the non-prompt backgrounds originating from fake electrons and muons respectively. Only statistical uncertainty is included.

	$e^{\pm}e^{\pm}$	$e^{\pm}\mu^{\pm}$	$\mu^{\pm}e^{\pm}$	$\mu^{\pm}\mu^{\pm}$	$\ell\ell$
GHH6f650f0	0.10 ± 0.01	0.07 ± 0.01	0.11 ± 0.01	0.09 ± 0.01	0.37 ± 0.03
GHH300fW0fWW4600	2.57 ± 0.18	2.90 ± 0.19	2.90 ± 0.19	3.37 ± 0.20	11.73 ± 0.38
GHH600fW1200fWW2400	0.60 ± 0.05	0.64 ± 0.06	0.77 ± 0.06	0.71 ± 0.06	2.73 ± 0.11
GHH600fW1350fWW0	0.47 ± 0.04	0.56 ± 0.05	0.45 ± 0.04	0.50 ± 0.04	1.98 ± 0.09
GHH900fW1350fWW0	0.19 ± 0.02	0.19 ± 0.02	0.20 ± 0.02	0.17 ± 0.02	0.75 ± 0.04
TopX	1.63 ± 0.11	2.28 ± 0.13	1.95 ± 0.12	2.27 ± 0.13	8.13 ± 0.25
WWW	4.39 ± 0.12	6.30 ± 0.14	5.54 ± 0.13	7.59 ± 0.15	23.81 ± 0.27
ssWW	6.46 ± 0.12	9.14 ± 0.15	8.51 ± 0.14	11.93 ± 0.17	36.05 ± 0.30
VVV	0.08 ± 0.01	0.10 ± 0.01	0.08 ± 0.01	0.08 ± 0.01	0.34 ± 0.02
ZZ	0.40 ± 0.05	0.81 ± 0.07	0.50 ± 0.05	0.60 ± 0.07	2.31 ± 0.12
WZ	21.17 ± 0.65	27.89 ± 0.92	20.35 ± 0.57	27.70 ± 0.68	97.12 ± 1.44
NonPromptEl	8.46 ± 1.05	4.06 ± 0.80	6.34 ± 0.81	0.00 ± 0.00	18.85 ± 1.55
NonPromptMu	0.00 ± 0.00	6.47 ± 0.34	1.35 ± 0.16	10.34 ± 0.44	18.17 ± 0.58
Charge-flip	6.70 ± 0.23	4.83 ± 0.19	0.93 ± 0.06	0.00 ± 0.00	12.46 ± 0.30
Photon conversion	9.97 ± 2.55	7.76 ± 2.16	4.44 ± 1.50	0.00 ± 0.00	22.17 ± 3.66
Total Bkg.	59.73 ± 2.85	70.27 ± 2.53	50.57 ± 1.82	61.30 ± 0.86	241.88 ± 4.31
Data	56.00	63.00	59.00	51.00	229.00

8.7 Systematic uncertainties

Various systematic uncertainties are included in the likelihood fit in Section 8.8. The sources of systematic uncertainty can be divided into three categories: experimental uncertainties related to the detector and reconstruction performance, theoretical uncertainties related to the modeling of the background and signal processes and background estimation uncertainties related to the data-driven background estimation.

8.7.1 Experimental uncertainties

The experimental uncertainties are composed of uncertainties of luminosity, trigger and identification, calibration and resolution of physics objects.

The systematic uncertainty for luminosity is about 1.7%[108] for the Run2 dataset. It's applied on the processes estimated from MC.

The systematic uncertainty for pile-up is estimated with PileupReweightingTool[109], which provides nominal and varied weights for pile-up reweighting of the MC events according to the pile-up of data.

Various systematic uncertainties for muons are considered. They are track uncertainty, isolation efficiency uncertainty, sagitta uncertainty, momentum scale uncertainty, reconstruction efficiency uncertainty, track to vertex association efficiency uncertainty and trigger efficiency uncertainty. These uncertainties are derived with the MuonCalibrationAndSmearingTool and the MuonEfficiencyScaleFactors tool[45].

For electrons, uncertainties of reconstruction efficiency, identification efficiency, isolation efficiency, trigger efficiency, momentum scale and resolution are considered and obtained with the AsgElectronEfficiencyCorrectionTool and the EgammaCalibrationAndSmearingTool[43].

The systematic uncertainties for small-R jets are provided by the JetUncertaintiesTool. The following uncertainties are considered:

1. Jet energy scale (JES): the CategoryReduction configuration is used, which has 30 JES uncertainty components.
2. Jet energy resolution (JER): since we only use small-R jets to form the W boson candidate and don't have tight selection on jets, the SimpleJER configuration is applied, which is composed of 8 components.
3. b-tagging: we only use b-tagging to veto events with b-jet. The loose reduction scheme is used to vary scale factors to obtain systematic uncertainties. There are

19 b-tagging uncertainties.

4. JVT efficiency: it's derived by comparing the performance of JVT on hard-scattering jets in $Z \to \mu\mu$ data and the performance in MC simulation.

The JetUncertaintiesTool is also used to derive the systematic uncertainties for large-R jets. The uncertainties are:

1. Jet energy scale and jet mass scale: the CategoryReduction configuration is used. There are 4 components.
2. Jet energy resolution: it's obtained by assigning an absolute p_T resolution uncertainty of 2%.
3. Jet mass resolution: it's obtained by assigning a relative mass resolution uncertainty of 20%.
4. W-tagging: the efficiency and inefficiency are considered[54-55], with totally 24 uncertainties.

We use the METUtitilties tool to get the systematics uncertainties for E_T^{miss}. Since the E_T^{miss} is calculated with all the detected objects, it's affected by uncertainties affecting the objects. In addition, the uncertainties of pile-up modeling, momentum of the soft term, momentum resolution and reconstruction efficiency are included. There are 4 components.

8.7.2 Theoretical uncertainties

Theoretical uncertainties arise from the settings affecting modelings, e.g. PDFs, parton shower models and choice of generators. They affect the selection efficiency and the shape of m_{eff} distributions. The parton shower, PDF and scale uncertainties are considered for signals, WZ, $ssWW$ and WWW backgrounds.

The scale and PDF uncertainties are extracted by constructing an envelope with internal weights stored in MC events. The internal weights from the normalization (μ_R) and factorization (μ_F) variations are used to quantify the scale uncertainty. According the recommendation of ATLAS, the envelope with seven point variations is considered for scale uncertainty: (μ_R, μ_F) = (0.5, 0.5), (0.5, 1.0), (0.5, 2.0), (1.0, 0.5), (1.0, 1.0), (2.0, 0.5), (2.0, 1.0), (1.0, 2.0), (2.0, 2.0), where (μ_R, μ_F) = (1.0, 1.0) is the nominal scale. The parton shower uncertainty is calculated at generator level by comparing nominal MC samples with alternative samples using different parton showers or corresponding scales.

For the signal samples, the scale uncertainty is estimated by varying the (μ_R, μ_F). The PDF uncertainty is derived by comparing NNPDF30, MMHT2014 and CTEQ14

PDF sets. The parton shower uncertainty is estimated by comparing the nominal samples generated by MadGraph5_aMC@NLO + Pythia with alternative samples generated by MadGraph5_aMC@NLO + HERWIG 7. The total theoretical uncertainty in signal yields of SRs from different signal samples varies between 10% and 40%.

The estimation of the scale and PDF uncertainties in the WZ background uses the same approach as for the signal samples. The parton shower uncertainty in the WZ background is estimated by comparing the nominal WZ sample generated by SHERPA with four alternative samples generated by SHERPA but varying CKKW merging scale from 30 GeV to 15 GeV and varying resummation scale by factors of 0.5 and 2. The total theoretical uncertainties in the WZ yields in the boosted SR and resolved SR are 29% and 20% respectively.

The same approach as used for the WZ background is also used to obtain the scale, PDF and parton shower uncertainties of the on-shell WWW background, and the scale, PDF uncertainties of the off-shell WWW background. The parton shower uncertainty of the off-shell WWW background is estimated by comparing the nominal sample (POWHEG + Pythia) with alternative sample (POWHEG + HERWIG 7). The total theoretical uncertainty in the WWW background yields in the boosted SR and resolved SR are 16% and 8% respectively.

The estimation of the scale and PDF uncertainties for the $ssWW$ background uses the same method as for the WZ background. The parton shower uncertainty is derived by comparing the nominal sample generated by SHERPA with the alternative sample generated by MadGraph5_aMC@NLO + Pythia. The total theoretical uncertainty in the $ssWW$ background yields in the boosted SR and resolved SR are 31% and 25% respectively.

The theoretical uncertainties of the WZ, $ssWW$ and WWW backgrounds are treated as decorrelated between the boosted and resolved regions to cover the potential differences of the two regions.

For the small contribution backgrounds estimated with MC modeling (ZZ, VVV and TopX), an overall theoretical uncertainty is applied as listed in Table 8.9.

8.7.3 Background estimation uncertainties

The systematic uncertainties for data-driven background estimation are derived by comparing the fake factor, charge misidentification rate and photon conversion rate obtained by additional methods with the nominal one. The impact of charge-flip background

Table 8.9 Overall theoretical uncertainties for ZZ, VVV and TopX backgrounds.

Process	Theoretical uncertainty (%)
TopX	15[110-111]
VVV	15[112]
ZZ	20[113]

systematic uncertainties on its yields is 10%. For the non-prompt background, the overall systematic uncertainties are 13% for electrons and 10% for muons respectively. The total systematic uncertainty for the photon-conversion background estimation is 8%.

8.8 Statistical result

The statistical analysis is based on the HistFitter framework[114] with histograms as input. A binned likelihood function is constructed as the product of Poisson probability terms over the bins of the input distributions involving the numbers of data events and the expected signal and background yields, taking into account the effects of the floating background normalisations and the systematic uncertainties. A profile-likelihood-ratio test statistic is used to test the background-only hypothesis, and the signal-plus-background hypothesis for the production of a heavy Higgs boson with signal strength (μ). Signal strength is the ratio of the extracted cross section to the injected signal cross section, and is the parameter of interest (POI). The maximum-likelihood fit is made to the observed binned m_{eff} distributions in SRs, and to the numbers of observed events in CRs (Boosted WZ CR, Resved WZ CR and $ssWW$ CR) simultaneously. The distributions used in the likelihood fit for SRs and CRs are summarized in Table 8.10. The m_{eff} distributions in the boosted SR and the resolved SR are divided into 3 and 5 bins respectively. The bin sizes are optimized according to the fit performance as described in Section 8.8.2. The normalization factors of the WZ and the $ssWW$ backgrounds are free parameters in the fits and constrained by the data in CRs and SRs. There are two normalization factors for the WZ background, separated into boosted and resolved regions, while there is one normalization factor for the $ssWW$ background. Each systematic uncertainty is described by a nuisance parameter (NP), which is constrained by Gaussian or log-normal probability density functions. If the systematic uncertainty in different regions are correlated, only one NP is considered for this systematic uncertainty; if it's uncorrelated, different NPs are assigned in different regions. For each NP, the prior is added as a penalty term to the likelihood, which decreases as soon as the NP is shifted away from its nominal value. The statistical uncertainties of background predictions from MC simulation are included with one NP per bin, using the Beeston-Barlow technique[115]. A signal injection test is performed to test the linearity of the extracted signal strength and the injected signal strength, with details in Appendix C.

Table 8.10 The distributions used in the likelihood fit for SRs and CRs.

Region	Distribution
Boosted SR	m_{eff}
Resolved SR	m_{eff}
Boosted WZ CR	Yield
Resolved WZ CR	Yield
$ssWW$ CR	Yield

8.8.1 Likelihood function and hypothesis test

8.8.1.1 Likelihood function

The binned likelihood function is defined with a Poissonian term ($\mathcal{L}_{\text{poiss}}$) describing the statistical fluctuations of the data, and a Gaussian term considering the constraint on systematic uncertainties ($\mathcal{L}_{\text{gauss}}$):

$$\mathcal{L}(\mu,\sigma) = \prod_{i}^{\text{bins}} \mathcal{L}_{\text{poiss}}(N^i_{\text{data}} \mid \mu s^i(\boldsymbol{\theta}) + b^i(\boldsymbol{\theta})) \times \mathcal{L}_{\text{gauss}}(\boldsymbol{\theta}), \tag{8.5}$$

where μ is the signal strength. We assume the signal hypothesis can only increase the number of events, thus μ is always larger than 0. $\boldsymbol{\theta}$ represents the NP. N^i_{data}, $s^i(\boldsymbol{\theta})$ and $b^i(\boldsymbol{\theta})$ are the number of data events, the expected signal yield and the expected background yield in the i-th bin, respectively.

8.8.1.2 Hypothesis test

If there is no obvious data excess in SRs, we need to set the 95% confidence level (CL) upper limits on the signal cross section. The test statistic q_μ provides separation power between background-only hypothesis (B) and signal-plus-background hypothesis (S+b), and is defined as:

$$q_\mu = -2 \ln \left(\frac{\mathcal{L}(\mu, \hat{\hat{\theta}}_\mu)}{\mathcal{L}(\hat{\mu}, \hat{\theta})} \right) \tag{8.6}$$

where μ is a given constant and $\hat{\hat{\theta}}_\mu$ is the θ which maximizes the likelihood for a constant μ. $\hat{\mu}$ and $\hat{\theta}$ are determined from the data.

The p-value is then defined to quantify the incompatibility of data and a given μ and derive the 95% CL limits. The p_{S+B} and p_B are defined as:

$$p_{\mathrm{B}} = \int_{-\infty}^{q_\mu^{\mathrm{obs}}} f(q_\mu \mid \mathrm{B})\ dq_\mu \tag{8.7}$$

$$p_{\mathrm{S+B}} = \int_{q_\mu^{\mathrm{obs}}}^{\infty} f(q_\mu \mid \mathrm{S+B})\ dq_\mu \tag{8.8}$$

where $f(q_\mu \mid \mathrm{B})$ and $f(q_\mu \mid \mathrm{S+B})$ are the probability density function of the test-statistic under B and S+B hypotheses. q_μ^{obs} is determined from data. The CL_s limit on μ at a CL of $1 - CL_s$ is defined as such a μ that $CL_s = p_{\mathrm{S+B}}/(1 - p_{\mathrm{B}})$. A 95% CL limit corresponds to $CL_s = 0.05$. The expected limit is obtained with asimov data, while the observed limit is extracted with data.

8.8.2 Binning study

In order to optimize the performance of the fit but also take into account the statistical limitations, a procedure was defined to determine the optimal binning of m_{eff} distributions in SRs. Since there are only about 26 background events in the boosted SR, two or three bins are enough. In the resolved SR, four or five bins are preferred with about 195 background events. m_{eff} histograms with 64 (32) bins for the boosted SR (resolved SR), with 25 GeV wide bins containing the sum of all considered backgrounds, with overflow (underflow) added to the last (first) bin are used as input. These histograms are rebinned according to two criterias:

1. The bin content of the merged bin is larger than a specified lower value `minBinContent`.
2. The relative bin error must be smaller than a certain `maxBinError`.

The `minBinContent` and `maxBinError` are separately defined for the boosted SR and resolved SR in Table 8.11. Once these conditions are met for both distributions, the merged bin is saved. So there can be many choices of binning. The binning with the best combined expected upper limit is chosen as the final binning.

Different binnings used for comparison are listed in Table 8.12, totally 9. The ex-

Table 8.11 The conditions of `minBinContent` and `maxBinError` in the boosted and resolved SRs.

设置	Boosted SR	Resolved SR
`minBinContent`	6	6
`maxBinError`	10%	10%

pected upper limits of various signal samples with different binnings are compared in Table 8.13.

Table 8.12 Different binnings used for comparison. “inf” means infinite.

Label	Boosted SR	Resolved SR
binning 1	(0, 600, 800, inf) GeV	(0, 300, 400, 600, inf) GeV
binning 2	(0, 600, 800, inf) GeV	(0, 250, 300, 400, 600, inf) GeV
binning 3	(0, 600, 800, inf) GeV	(0, 300, 400, 500, 600, inf) GeV
binning 4	(0 , 800, inf) GeV	(0, 300, 400, 600, inf) GeV
binning 5	(0 , 800, inf) GeV	(0, 250, 300, 400, 600, inf) GeV
binning 6	(0 , 800, inf) GeV	(0, 300, 400, 500, 600, inf) GeV
binning 7	(0 , 700, inf) GeV	(0, 300, 400, 600, inf) GeV
binning 8	(0 , 700, inf) GeV	(0, 250, 300, 400, 600, inf) GeV
binning 9	(0 , 700, inf) GeV	(0, 300, 400, 500, 600, inf) GeV

Although the influence of binning on the expected upper limit is small, the binning 3 has the best significance. Thus, the binnings of m_{eff} distributions used in the final fit are:

Boosted SR

(0, 600, 800, inf) GeV

Resolved SR

(0, 300, 400, 500, 600, inf) GeV

8.8.3 Fit results

8.8.3.1 Background-only fit

The background-only fit is used to test the compatibility of the data and the expected backgrounds. The SRs and CRs listed in Table 8.10 are fitted simultaneously with the background-only hypothesis. The extracted normalization factors of the WZ background in the boosted and resolved regions are 0.93 ± 0.07 and 0.83 ± 0.03. The normalization

Table 8.13 The expected upper limits at 95% confidence level for various signal samples with different binnings. "GHH6f650f0": $m_H = 600$ GeV, $f_W = 650$ and $f_{WW} = 0$. Only statistic uncertainty is included.

	GHH3f600f0	GHH3fm350fm2100	GHH3f0fm3000	GHH6f650f0	GHH6fm400fm2400	GHH6f0fm3500	GHH9f800f0	GHH9f0fm5000
binning 1	3.23837	2.00312	1.57942	3.08473	2.41975	2.22071	2.73532	2.07646
binning 2	3.23837	2.00298	1.57948	3.08474	2.4198	2.22063	2.73533	2.07646
binning 3	3.23408	1.99196	1.57159	3.08415	2.41611	2.21629	2.73528	2.07633
binning 4	3.24648	2.02208	1.58251	3.09114	2.4441	2.26247	2.73593	2.07745
binning 5	3.24648	2.02196	1.58273	3.09118	2.44414	2.26237	2.73594	2.07746
binning 6	3.24215	2.01062	1.57479	3.09054	2.44034	2.25782	2.73589	2.07732
binning 7	3.47062	2.00613	1.58242	3.42886	2.55727	2.30589	3.15226	2.36361
binning 8	3.47058	2.00601	1.58272	3.42876	2.55722	2.30587	3.15226	2.3636
binning 9	3.46603	1.99493	1.57481	3.42814	2.5537	2.30062	3.15219	2.36342

factor of the $ssWW$ background is 1.54 ± 0.17 and it's consistent with the ATLAS measurement[107]. To validate the estimation of the WZ, $ssWW$ and WWW backgrounds, the three normalization factors are applied in the VRs and various kinematic variables are checked as shown in Section 8.6.5. Also, post-fit plots in the boosted WZ, resolved WZ and $ssWW$ CRs are presented in Figure 8.38. Post-fit distributions in the boosted and resolved SRs are shown in Figure 8.39-8.40. Good overall agreement between data and estimated backgrounds is seen in Table 8.14. Table 8.15 summarizes the systematic uncertainties in background yields for the boosted and the resolved SRs.

Table 8.14 Data and fitted background yields in SRs and CRs with background-only fit. Both statistical and systematic uncertainties are included.

Yields	Boosted SR	Resolved SR	Boosted WZ CR	Resolved WZ CR	$ssWW$ CR
Observed events	24	191	236	2094	567
Fitted bkg events	26.8 ± 2.7	189.0 ± 7.8	235 ± 15	2095 ± 46	566 ± 24
WWW	5.8 ± 1.0	30.4 ± 2.9	1.30 ± 0.31	11.2 ± 2.1	28.5 ± 5.5
$ssWW$	7.5 ± 2.3	16.5 ± 1.9	–	–	254 ± 27
WZ	6.71 ± 0.76	68.7 ± 5.0	221 ± 15	1956 ± 50	150.6 ± 5.7
Non-prompt	3.20 ± 0.36	39.6 ± 6.3	–	–	48.6 ± 8.8
Charge-flip	0.43 ± 0.03	8.61 ± 0.57	–	–	22.8 ± 1.3
Photon conversion	0.73 ± 0.07	17.2 ± 1.7	–	–	46.7 ± 4.7
Other	2.50 ± 0.45	9.0 ± 1.5	12.3 ± 1.6	130 ± 20	14.3 ± 2.0

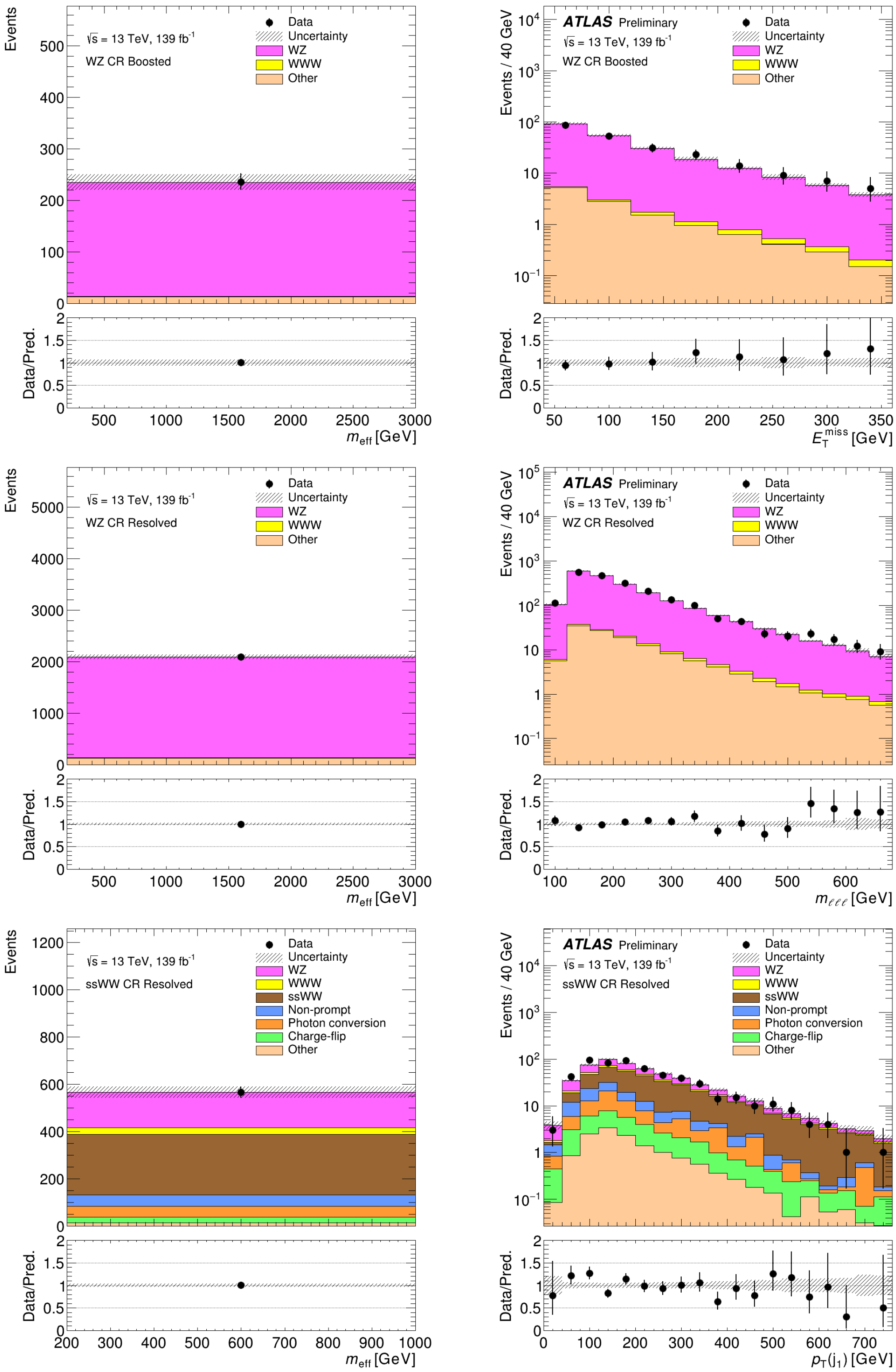

Figure 8.38 Post-fit distributions in the boosted WZ, resolved WZ and $ssWW$ CRs with background-only fit. Both statistical and systematic uncertainties are included.

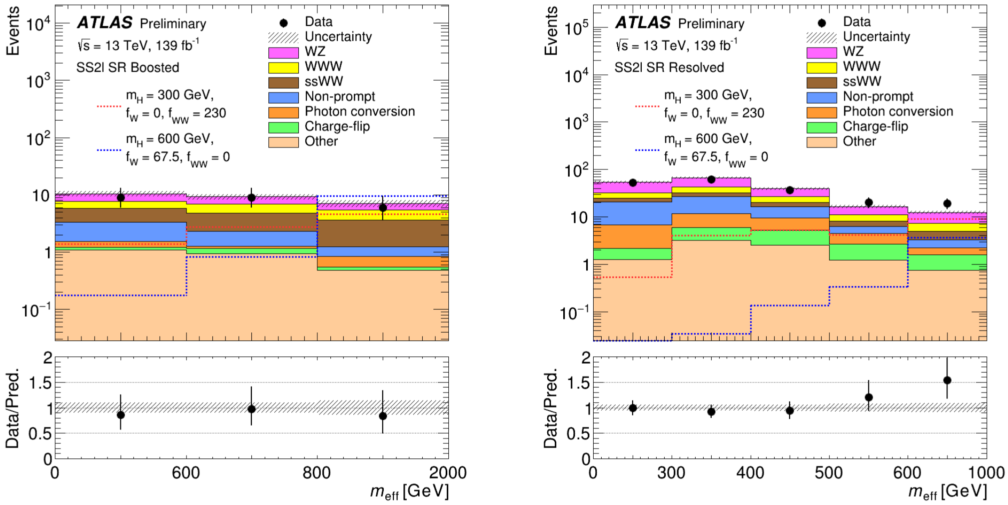

Figure 8.39 Post-fit m_{eff} distributions in the boosted and the resolved SRs with background-only fit. Two benchmark signals are also shown as unstacked unfilled histograms normalized to the expected cross section and 139fb^{-1} integrated luminosity. Both statistic and systematic uncertainties are included.

Table 8.15 Breakdown of systematic uncertainties in background yields in the boosted and the resolved SRs[97].

Uncertainty of channel	Boosted SR	Resolved SR
Total systematic uncertainties	10.0%	4.1%
Data driven non-prompt	1.3%	3.3%
Theoretical uncertainties	8.9%	2.6%
MC statistical uncertainties	3.0%	1.9%
Floating normalizations	3.5%	1.2%
Small-R jet	-	1.1%
Data driven photon conversion	0.2%	0.9%
E_T^{miss}	0.2%	0.7%
b-tagging	0.8%	0.5%
Data driven charge-flip	0.1%	0.3%
Electron	0.5%	0.2%
Muon	0.6%	0.2%
Pile-up reweighting	0.2%	0.2%
Large-R jet	1.1%	0.2%
W-tagger	3.7%	-

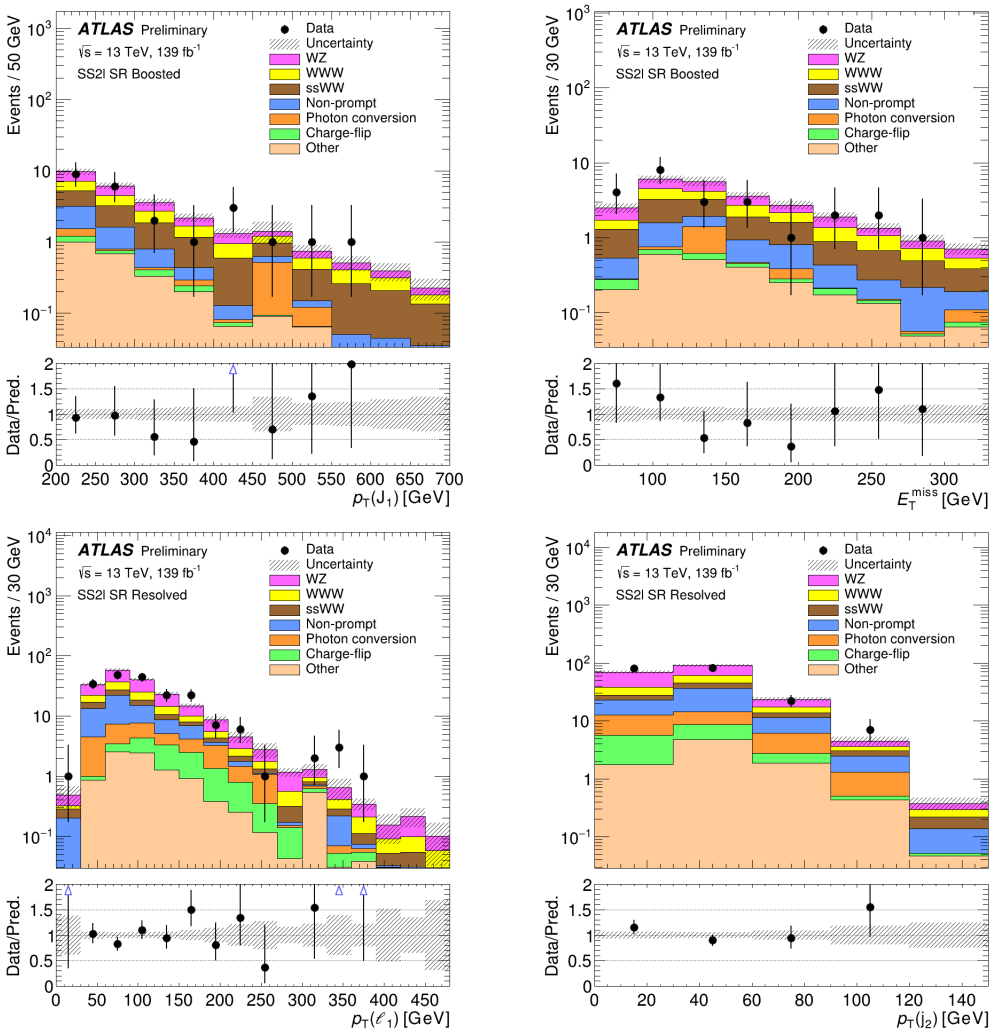

Figure 8.40 Post-fit distributions in the boosted and the resolved SRs with background-only fit. Both statistical and systematic uncertainties are included.

8.8.3.2 Exclusion fit

In the absence of a significant excess, upper limits on the production of heavy Higgs bosons are extracted by repeating the exclusion fit, which uses signal-plus-background hypothesis. All the SRs and CRs are fitted simultaneously. The obtained normalization factors are consistent with the background-only fit.

Taking GHH600fW1350fWW0 (m_H = 600 GeV, f_W = 1350 and f_{WW} = 0) as benchmark signal, the pre-fit and post-fit m_{eff} distributions in the boosted and the resolved SRs are shown in Figure 8.41. The observed (expected) upper limit on signal strength μ is 0.84 (0.75).

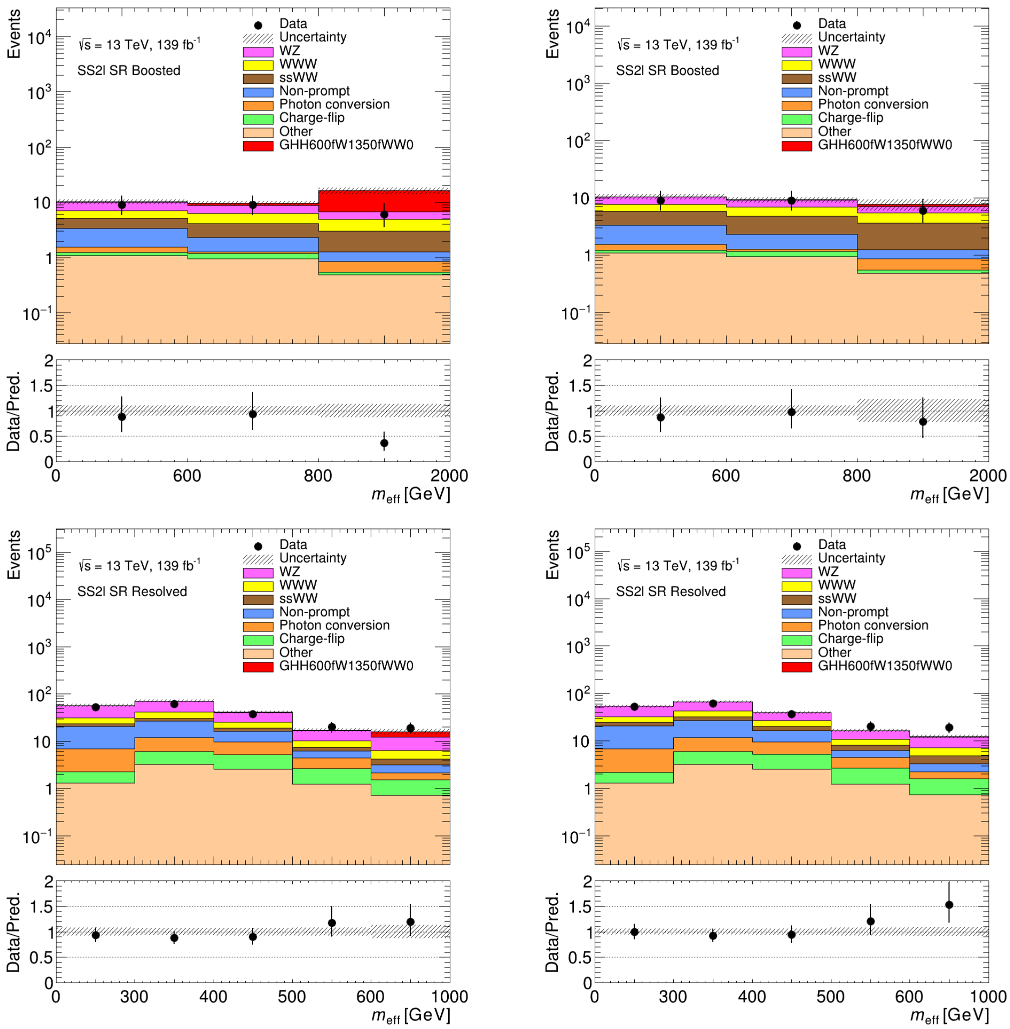

Figure 8.41 Pre-fit (left) and post-fit (right) m_{eff} distributions in the boosted and resolved signal regions with exclusion fit. GHH600fW1350fWW0 is the benchmark signal with m_H = 600 GeV, f_W = 1350 and f_{WW} = 0.

8.8.4 Upper limits

There is no significant excess in SRs, so the constraints on the production of heavy Higgs bosons are set by scanning the parameter space.

Figure 8.42 shows the observed and expected exclusion contours at 95% CL in the f_W-f_{WW} parameter space for heavy Higgs bosons with masses of 300 GeV, 600 GeV and 900 GeV. The parameter space outside the exclusion contours can be excluded. With $m_H = 300$ GeV, $|\rho_H f_W/\Lambda^2| > 2.7$ and $|\rho_H f_{WW}/\Lambda^2| > 10$ can be excluded; With $m_H = 600$ GeV, $|\rho_H f_W/\Lambda^2| > 2.5$ and $|\rho_H f_{WW}/\Lambda^2| > 12$ can be excluded; With $m_H = 900$ GeV, $|\rho_H f_W/\Lambda^2| > 2.9$ and $|\rho_H f_{WW}/\Lambda^2| > 15$ can be excluded;

Figure 8.43 shows the observed and expected 95% CL upper limits on the production cross section of the heavy Higgs boson as a function of its mass for two sets of $(\rho_H f_W \Lambda^2, \rho_H f_{WW} \Lambda^2)$ with values $(2.7\ \text{TeV}^{-2}, 0)$ and $(0, 12.4\ \text{TeV}^{-2})$. With $(\rho_H f_W \Lambda^2, \rho_H f_{WW} \Lambda^2) = (2.7\ \text{TeV}^{-2}, 0)$, a heavy Higgs boson with mass up to 900 GeV can be excluded; with $(\rho_H f_W \Lambda^2, \rho_H f_{WW} \Lambda^2) = (0, 12.4\ \text{TeV}^{-2})$, a heavy Higgs boson with mass up to 700 GeV can be excluded.

The excluded areas shown in Figure 8.42 are smaller than the excluded areas shown in Figure 7.7-7.11 from the phenomenology study. It's because that in the phenomenology study, the result includes three signal regions and well reconstructed boosted W/Z bosons (heavy Higgs bosons) with small-R jets (large-R jets).

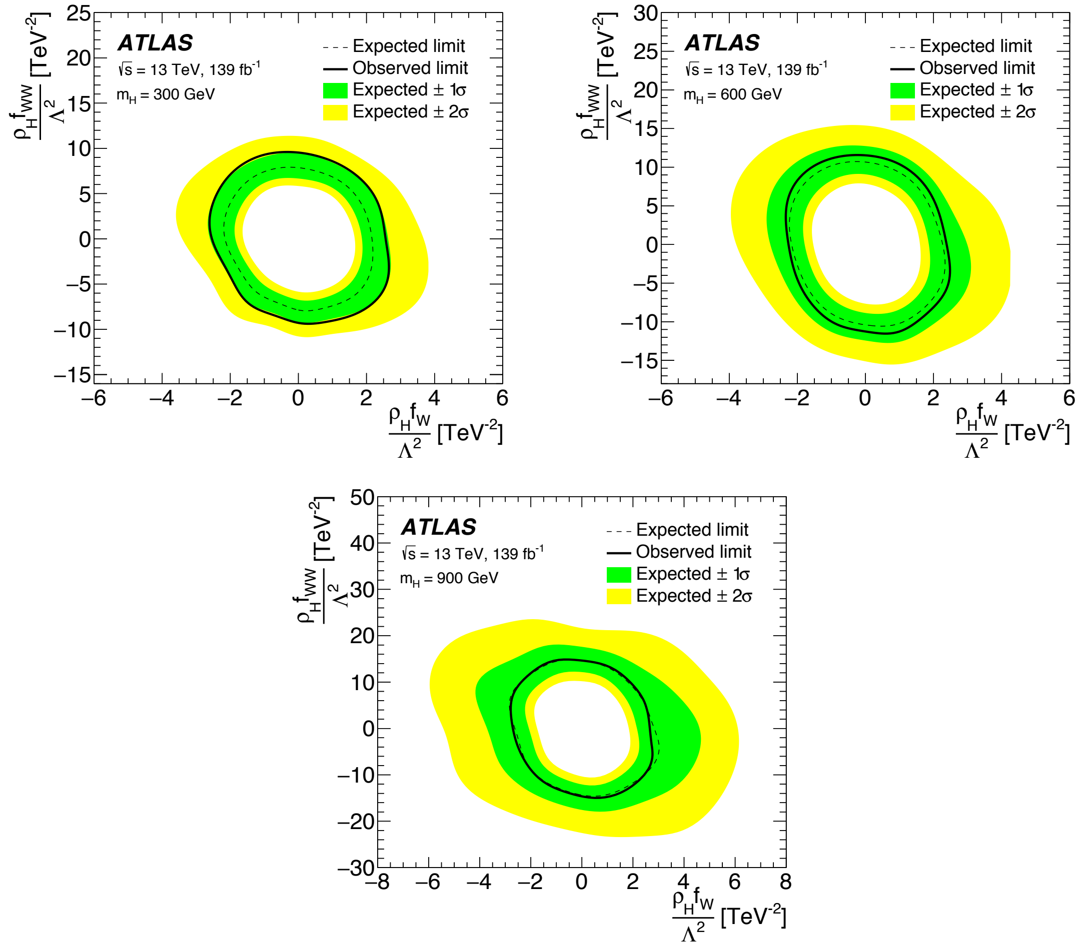

Figure 8.42 Observed and expected 95% CL exclusion contours in the $f_W - f_{WW}$ parameter space for heavy Higgs boson with masses of 300 GeV (top left), 600 GeV (top right) and 900 GeV (bottom).

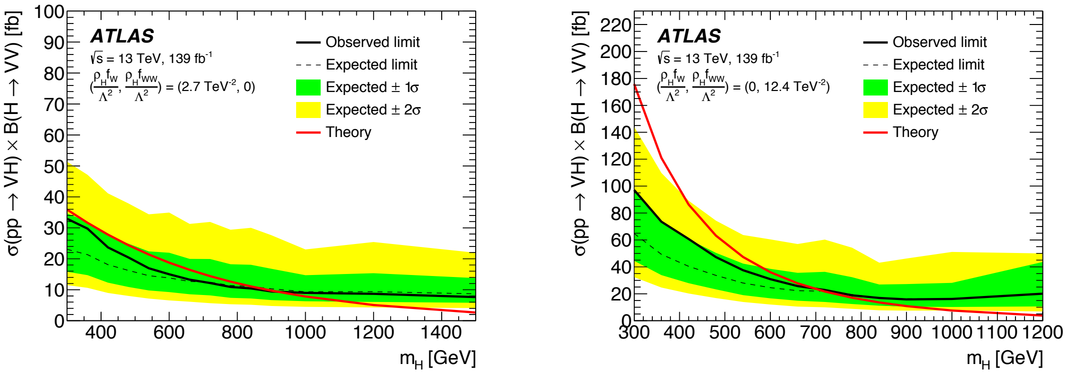

Figure 8.43 Observed and expected 95% CL upper limits on the production cross section of a heavy Higgs boson as a function of its mass with $(\rho_H f_W \Lambda^2, \rho_H f_{WW} \Lambda^2)$ fixed to (2.7 TeV^{-2}, 0) (left) and (0, 12.4 TeV^{-2}) (right).

CHAPTER 9 CONCLUSION

The SM includes electroweak gauge theory and quantum chromodynamics, and has been a great success in experiment. But there are still some issues that are not yet understood. New elementary or composite particles are our probes for understanding these issues. Chapter 6 describes the analysis aimed at searching for di-J/ψ and $J/\psi + \psi(2S)$ resonances in the four-muon final state, using ATLAS data collected during Run2. Prompt and non-prompt backgrounds are modeled by MC simulations with kinematic and normalization corrected in dedicated control regions, while the background containing fake muons is estimated with a data-driven method. A resonance around 6.9 GeV in the di-J/ψ channel is observed, which is consistent with the $X(6900)$ observed by LHCb. An excess with a significance of 4.6σ is also seen in the $J/\psi + \psi(2S)$ channel. In the search of rare decays of known bottomonia, the 95% CL upper limits are set on the product of production cross section times branching ratio of rare bottomonium decays. The analysis in Chapter 8 targets searching for generic heavy Higgs bosons produced in association with a W boson and decaying into a pair of W bosons, in the same-sign dilepton final state, based on the phenomenology study in Chapter 7. The heavy Higgs boson can have both dim-4 and dim-6 interactions with the SM particles. The introduction of dim-6 operators can significantly enhance the momentum of the heavy Higgs boson and the associated W boson. The 95% CL upper limits on the production of heavy Higgs bosons are derived using ATLAS Run2 data. LHC has started the Run3 data taking with an expected integrated luminosity of 300 fb^{-1}. The much larger dataset holds hope for the search of BSM particles and allows physicists to study more interesting properties of new resonances.

REFERENCES

[1] Weinberg S. A Model of Leptons[J/OL]. Phys. Rev. Lett., 1967, 19:1264-1266. DOI: 10.1103/PhysRevLett.19.1264.

[2] Weinberg S. The Making of the standard model[J/OL]. Eur. Phys. J. C, 2004, 34:5-13. DOI: 10.1140/epjc/s2004-01761-1.

[3] Yang C N, Mills R L. Conservation of Isotopic Spin and Isotopic Gauge Invariance[J/OL]. Phys. Rev., 1954, 96:191-195. DOI: 10.1103/PhysRev.96.191.

[4] Glashow S L. Partial-symmetries of weak interactions[J/OL]. Nuclear Physics, 1961, 22(4): 579-588. https://www.sciencedirect.com/science/article/pii/0029558261904692. DOI: https://doi.org/10.1016/0029-5582(61)90469-2.

[5] Glashow S L, Iliopoulos J, Maiani L. Weak Interactions with Lepton-Hadron Symmetry[J/OL]. Phys. Rev. D, 1970, 2:1285-1292. DOI: 10.1103/PhysRevD.2.1285.

[6] Gross D J, Wilczek F. Ultraviolet behavior of non-abelian gauge theories[J/OL]. Phys. Rev. Lett., 1973, 30:1343-1346. https://link.aps.org/doi/10.1103/PhysRevLett.30.1343.

[7] Politzer H D. Reliable Perturbative Results for Strong Interactions?[J/OL]. Phys. Rev. Lett., 1973, 30:1346-1349. DOI: 10.1103/PhysRevLett.30.1346.

[8] Aubert J J, Becker U, Biggs P J, et al. Experimental observation of a heavy particle j[J/OL]. Phys. Rev. Lett., 1974, 33:1404-1406. https://link.aps.org/doi/10.1103/PhysRevLett.33.1404.

[9] Augustin J E, Boyarski A M, Breidenbach M, et al. Discovery of a narrow resonance in e^+e^- annihilation[J/OL]. Phys. Rev. Lett., 1974, 33:1406-1408. https://link.aps.org/doi/10.1103/PhysRevLett.33.1406.

[10] Zyla P A, et al. Review of Particle Physics[J/OL]. PTEP, 2020, 2020(8):083C01. DOI: 10.1093/ptep/ptaa104.

[11] Branco G C, Ferreira P M, Lavoura L, et al. Theory and phenomenology of two-Higgs-doublet models[J/OL]. Phys. Rept., 2012, 516:1-102. DOI: 10.1016/j.physrep.2012.02.002.

[12] Martin S P. A Supersymmetry primer[J/OL]. Adv. Ser. Direct. High Energy Phys., 1998, 18: 1-98. DOI: 10.1142/9789812839657_0001.

[13] Binoth B C C P G E, T. Lhc physics[M/OL]. 1st ed. Boca Raton, 2012. DOI: 10.1201/b11865.

[14] Aad G, et al. The ATLAS Experiment at the CERN Large Hadron Collider[J/OL]. JINST, 2008, 3:S08003. DOI: 10.1088/1748-0221/3/08/S08003.

[15] Chatrchyan S, et al. The CMS Experiment at the CERN LHC[J/OL]. JINST, 2008, 3:S08004. DOI: 10.1088/1748-0221/3/08/S08004.

[16] Alves A A, Jr., et al. The LHCb Detector at the LHC[J/OL]. JINST, 2008, 3:S08005. DOI: 10.1088/1748-0221/3/08/S08005.

[17] Aamodt K, et al. The ALICE experiment at the CERN LHC[J/OL]. JINST, 2008, 3:S08002. DOI: 10.1088/1748-0221/3/08/S08002.

[18] Pinfold J L. The MoEDAL experiment at the LHC. Searching beyond the standard model[J/OL]. EPJ Web Conf., 2016, 126:02024. DOI: 10.1051/epjconf/201612602024.

[19] Anelli G, et al. The TOTEM experiment at the CERN Large Hadron Collider[J/OL]. JINST, 2008, 3:S08007. DOI: 10.1088/1748-0221/3/08/S08007.

[20] Ariga A, et al. FASER: ForwArd Search ExpeRiment at the LHC[J]. 2019.

[21] Airapetian A, et al. ATLAS: Detector and physics performance technical design report. Volume 1[J]. 1999.

[22] Airapetian A, et al. ATLAS: Detector and physics performance technical design report. Volume 2[J]. 1999.

[23] Schott M, Dunford M. Review of single vector boson production in pp collisions at $\sqrt{s} = 7$ TeV[J/OL]. Eur. Phys. J. C, 2014, 74:2916. DOI: 10.1140/epjc/s10052-014-2916-1.

[24] Capeans M, Darbo G, Einsweiler K, et al. ATLAS Insertable B-Layer Technical Design Report [R/OL]. 2010. https://cds.cern.ch/record/1291633.

[25] Fabbri L. Forward Detectors in ATLAS: LUCID, ZDC and ALFA[C]//17th International Workshop on Deep-Inelastic Scattering and Related Subjects. Berlin, Germany: Science Wise Publ., 2009:166.

[26] Erland P A. ATLAS Forward Proton detectors status and plans[J/OL]. PoS, 2019, VERTEX2018:007. DOI: 10.22323/1.348.0007.

[27] Collaboration A. ATLAS Forward Detectors[EB/OL]. 2018. https://cds.cern.ch/record/2627582.

[28] Aad G, et al. Technical Design Report for the Phase-I Upgrade of the ATLAS TDAQ System [J]. 2013.

[29] Aad G, et al. Operation of the ATLAS trigger system in Run 2[J/OL]. JINST, 2020, 15(10): P10004. DOI: 10.1088/1748-0221/15/10/P10004.

[30] Tricoli A. Underlying event studies at ATLAS[C]//1st International Workshop on Multiple Partonic Interactions at the LHC. 2009:117-123.

[31] Marshall Z. Simulation of Pile-up in the ATLAS Experiment[J/OL]. J. Phys. Conf. Ser., 2014, 513:022024. DOI: 10.1088/1742-6596/513/2/022024.

[32] Collaboration A. Luminosity public results run 2[EB/OL]. https://twiki.cern.ch/twiki/bin/view/AtlasPublic/LuminosityPublicResultsRun2.

[33] Alwall J, Frederix R, Frixione S, et al. The automated computation of tree-level and next-to-leading order differential cross sections, and their matching to parton shower simulations[J/OL]. JHEP, 2014, 07:079. DOI: 10.1007/JHEP07(2014)079.

[34] Sjostrand T, Mrenna S, Skands P Z. A Brief Introduction to PYTHIA 8.1[J/OL]. Comput. Phys. Commun., 2008, 178:852. DOI: 10.1016/j.cpc.2008.01.036.

[35] Bothmann E, et al. Event generation with Sherpa 2.2[J/OL]. SciPost Phys., 2019, 7(3):034. DOI: 10.21468/SciPostPhys.7.3.034.

[36] Frixione S, Nason P, Ridolfi G. A positive-weight next-to-leading-order Monte Carlo for heavy flavour hadroproduction[J/OL]. JHEP, 2007, 09:126. DOI: 10.1088/1126-6708/2007/09/126.

[37] Frixione S, Nason P, Oleari C. Matching NLO QCD computations with parton shower simulations: the POWHEG method[J/OL]. JHEP, 2007, 11:070. DOI: 10.1088/1126-6708/2007/11/070.

[38] GEANT4 Collaboration, Agostinelli S, et al. Geant4 – a simulation toolkit[J/OL]. Nucl. Instrum. Meth. A, 2003, 506:250. DOI: 10.1016/S0168-9002(03)01368-8.

[39] ATLAS Collaboration. The ATLAS Collaboration Software and Firmware[M/OL]. 2021. https://cds.cern.ch/record/2767187.

[40] Aaboud M, et al. Performance of the ATLAS Track Reconstruction Algorithms in Dense Environments in LHC Run 2[J/OL]. Eur. Phys. J. C, 2017, 77(10):673. DOI: 10.1140/epjc/s10052-017-5225-7.

[41] Boutle S, et al. Primary vertex reconstruction at the ATLAS experiment[J/OL]. J. Phys. Conf. Ser., 2017, 898(4):042056. DOI: 10.1088/1742-6596/898/4/042056.

[42] Aad G, et al. Electron and photon performance measurements with the ATLAS detector using the 2015–2017 LHC proton-proton collision data[J/OL]. JINST, 2019, 14(12):P12006. DOI: 10.1088/1748-0221/14/12/P12006.

[43] Aaboud M, et al. Electron reconstruction and identification in the ATLAS experiment using the 2015 and 2016 LHC proton-proton collision data at $\sqrt{s}$ = 13 TeV[J/OL]. Eur. Phys. J. C, 2019, 79(8):639. DOI: 10.1140/epjc/s10052-019-7140-6.

[44] Aad G, et al. Search for the Associated Production of a Higgs Boson and a Top Quark Pair in multilepton final states in 80 fb^{-1} pp Collisions at $\sqrt{s}$ = 13 TeV with the ATLAS Detector [R/OL]. Geneva: CERN, 2018. https://cds.cern.ch/record/2314122.

[45] Aad G, et al. Muon reconstruction performance of the ATLAS detector in proton–proton collision data at $\sqrt{s}$ =13 TeV[J/OL]. Eur. Phys. J. C, 2016, 76(5):292. DOI: 10.1140/epjc/s10052-016-4120-y.

[46] Aad G, et al. Muon reconstruction and identification efficiency in ATLAS using the full Run 2 pp collision data set at $\sqrt{s} = 13$ TeV[J/OL]. Eur. Phys. J. C, 2021, 81(7):578. DOI: 10.1140/epjc/s10052-021-09233-2.

[47] Cacciari M, Salam G P, Soyez G. The anti-k_t jet clustering algorithm[J/OL]. JHEP, 2008, 04:063. DOI: 10.1088/1126-6708/2008/04/063.

[48] Ellis S D, Soper D E. Successive combination jet algorithm for hadron collisions[J/OL]. Phys. Rev. D, 1993, 48:3160-3166. DOI: 10.1103/PhysRevD.48.3160.

[49] Dokshitzer Y L, Leder G D, Moretti S, et al. Better jet clustering algorithms[J/OL]. JHEP, 1997, 08:001. DOI: 10.1088/1126-6708/1997/08/001.

[50] Aaboud M, et al. Jet reconstruction and performance using particle flow with the ATLAS Detector[J/OL]. Eur. Phys. J. C, 2017, 77(7):466. DOI: 10.1140/epjc/s10052-017-5031-2.

[51] Aad G, et al. Optimisation of large-radius jet reconstruction for the ATLAS detector in 13 TeV proton–proton collisions[J/OL]. Eur. Phys. J. C, 2021, 81(4):334. DOI: 10.1140/epjc/s10052-021-09054-3.

[52] Aad G, et al. ATLAS b-jet identification performance and efficiency measurement with $t\bar{t}$ events in pp collisions at $\sqrt{s} = 13$ TeV[J/OL]. Eur. Phys. J. C, 2019, 79(11):970. DOI: 10.1140/epjc/s10052-019-7450-8.

[53] Collaboration A. Expected performance of the 2019 ATLAS btaggers: FTAG2019 005[R/OL]. Geneva: CERN, 2019. http://atlas.web.cern.ch/Atlas/GROUPS/PHYSICS/PLOTS/FTAG-2019-005/.

[54] Collaboration A. Boosted hadronic vector boson and top quark tagging with ATLAS using Run 2 data[R/OL]. Geneva: CERN, 2020. https://cds.cern.ch/record/2724149.

[55] Aaboud M, et al. Performance of top-quark and W-boson tagging with ATLAS in Run 2 of the LHC[J/OL]. Eur. Phys. J. C, 2019, 79(5):375. DOI: 10.1140/epjc/s10052-019-6847-8.

[56] Aaboud M, et al. Performance of missing transverse momentum reconstruction with the ATLAS detector using proton-proton collisions at $\sqrt{s}$ = 13 TeV[J/OL]. Eur. Phys. J. C, 2018, 78(11): 903. DOI: 10.1140/epjc/s10052-018-6288-9.

[57] Aad G, et al. Jet energy measurement and its systematic uncertainty in proton-proton collisions at $\sqrt{s} = 7$ TeV with the ATLAS detector[J/OL]. Eur. Phys. J. C, 2015, 75:17. DOI: 10.1140/epjc/s10052-014-3190-y.

[58] Barillari T, et al. Local hadronic calibration[R/OL]. 2009. https://cds.cern.ch/record/1112035.

[59] Track Reconstruction Performance of the ATLAS Inner Detector at $\sqrt{s} = 13$~TeV[R/OL]. 2015. https://cds.cern.ch/record/2037683/.

[60] Aaboud M, et al. A measurement of the calorimeter response to single hadrons and determination of the jet energy scale uncertainty using LHC Run-1 pp-collision data with the ATLAS detector[J/OL]. Eur. Phys. J. C, 2017, 77(1):26. DOI: 10.1140/epjc/s10052-016-4580-0.

[61] Aad G, et al. Single hadron response measurement and calorimeter jet energy scale uncertainty with the ATLAS detector at the LHC[J/OL]. Eur. Phys. J. C, 2013, 73(3):2305. DOI: 10.1140/epjc/s10052-013-2305-1.

[62] Aad G, et al. Observation of an excess of di-charmonium events in the four-muon final state with the ATLAS detector[R/OL]. 2022. https://cds.cern.ch/record/2815676.

[63] Brambilla N, et al. QCD and Strongly Coupled Gauge Theories: Challenges and Perspectives [J/OL]. Eur. Phys. J. C, 2014, 74(10):2981. DOI: 10.1140/epjc/s10052-014-2981-5.

[64] Choi S K, et al. Observation of a narrow charmonium-like state in exclusive $B^{\pm} \to K^{\pm}\pi^{+}\pi^{-}J/\psi$ decays[J/OL]. Phys. Rev. Lett., 2003, 91:262001. DOI: 10.1103/PhysRevLett.91.262001.

[65] Iwasaki Y. Is a state $c\bar{c}c\bar{c}$ found at 6.0 gev?[J/OL]. Phys. Rev. Lett., 1976, 36:1266-1268. https://link.aps.org/doi/10.1103/PhysRevLett.36.1266.

[66] Ader J P, Richard J M, Taxil P. DO NARROW HEAVY MULTI - QUARK STATES EXIST? [J/OL]. Phys. Rev. D, 1982, 25:2370. DOI: 10.1103/PhysRevD.25.2370.

[67] Aaij R, et al. Observation of structure in the J/ψ -pair mass spectrum[J/OL]. Sci. Bull., 2020, 65(23):1983-1993. DOI: 10.1016/j.scib.2020.08.032.

[68] Aubert B, et al. Observation of the bottomonium ground state in the decay $\upsilon_{3S} \to \gamma eta_b$[J/OL]. Phys. Rev. Lett., 2008, 101:071801. DOI: 10.1103/PhysRevLett.101.071801.

[69] Asner D M, et al. Observation of chi(b)(1P(J),2P(J)) decays to light hadrons[J/OL]. Phys. Rev. D, 2008, 78:091103. DOI: 10.1103/PhysRevD.78.091103.

[70] Briere R A, et al. Inclusive chi(bJ)(nP) Decays to D0 X[J/OL]. Phys. Rev. D, 2008, 78:092007. DOI: 10.1103/PhysRevD.78.092007.

[71] ATLAS Collaboration. ATLAS Pythia 8 tunes to 7 TeV data[M/OL]. 2014. https://cds.cern.ch/record/1966419.

[72] Ball R D, et al. Parton distributions for the LHC run II[J/OL]. JHEP, 2015, 04:040. DOI: 10.1007/JHEP04(2015)040.

[73] N. Davidson, T. Przedzinski and Z. Was. PHOTOS Interface in C++: Technical and physics documentation[J/OL]. Comput. Phys. Commun., 2016, 199:86. DOI: 10.1016/j.cpc.2015.09.013.

[74] S. Bolognesi et al. On the spin and parity of a single-produced resonance at the LHC[J/OL]. Phys. Rev. D, 2012, 86:095031. DOI: 10.1103/PhysRevD.86.095031.

[75] J. Pumplin et al. New Generation of Parton Distributions with Uncertainties from Global QCD Analysis[J/OL]. JHEP, 2002, 07:012. DOI: 10.1088/1126-6708/2002/07/012.

[76] Aad G, et al. Performance of the ATLAS muon triggers in Run 2[J/OL]. JINST, 2020, 15(09): P09015. DOI: 10.1088/1748-0221/15/09/p09015.

[77] Kostyukhin V. VKalVrt - package for vertex reconstruction in ATLAS.[R/OL]. 2003. https://cds.cern.ch/record/685551.

[78] Kostyukhin V. VKalVrt - package for vertex reconstruction in ATLAS.[J]. 2003.

[79] Collaboration T L. Measurement of Υ production in pp collisions at $\sqrt{s} = 13$ tev[J/OL]. Journal of High Energy Physics, 2018, 2018(7). https://doi.org/10.1007/JHEP07(2018)134.

[80] Aad G, et al. Measurement of upsilon production in 7 tev *pp* collisions at atlas[J/OL]. Phys. Rev. D, 2013, 87:052004. https://link.aps.org/doi/10.1103/PhysRevD.87.052004.

[81] Bai Y, Chen D Y. General mathematical analysis on multiple solutions of interfering resonances combinations[J/OL]. Phys. Rev. D, 2019, 99(7):072007. DOI: 10.1103/PhysRevD.99.072007.

[82] Cowan G, Cranmer K, Gross E, et al. Asymptotic formulae for likelihood-based tests of new physics[J/OL]. Eur. Phys. J. C, 2011, 71:1554. DOI: 10.1140/epjc/s10052-011-1554-0.

[83] Chen X, Xu Y, Wu Y, et al. Search for a generic heavy higgs at the lhc[J/OL]. Physics Letters B, 2020, 804:135358. http://www.sciencedirect.com/science/article/pii/S0370269320301623. DOI: https://doi.org/10.1016/j.physletb.2020.135358.

[84] Kuang Y P, Ren H Y, Xia L H. Model-independent probe of anomalous heavy neutral Higgs bosons at the LHC[J/OL]. Phys. Rev., 2014, D90:115002. DOI: 10.1103/PhysRevD.90.115002.

[85] Kuang Y P, Xia L H. Probing gauge-phobic heavy Higgs bosons at high energy hadron colliders [J/OL]. Phys. Lett. B, 2015, 747:193-199. DOI: 10.1016/j.physletb.2015.05.073.

[86] Aad G, et al. Search for heavy ZZ resonances in the $\ell^+\ell^-\ell^+\ell^-$ and $\ell^+\ell^-\nu\bar{\nu}$ final states using proton proton collisions at $\sqrt{s} = 13$ TeV with the ATLAS detector[J/OL]. Eur. Phys. J., 2018, C78:293. DOI: 10.1140/epjc/s10052-018-5686-3.

[87] Khachatryan V, et al. Search for a Higgs boson in the mass range from 145 to 1000 GeV decaying to a pair of W or Z bosons[J/OL]. JHEP, 2015, 10:144. DOI: 10.1007/JHEP10(2015)144.

[88] Aad G, et al. Combination of searches for heavy resonances decaying into bosonic and leptonic final states using 36 fb^{-1} of proton-proton collision data at $\sqrt{s} = 13$ TeV with the ATLAS detector[J/OL]. Phys. Rev., 2018, D98:052008. DOI: 10.1103/PhysRevD.98.052008.

[89] Khachatryan V, et al. Search for a heavy Higgs boson decaying to a pair of W bosons in proton-proton collisions at $\sqrt{s} = 13$ TeV[J]. CMS-PAS-HIG-17-033.

[90] The ATLAS collaboration. Searches for heavy ZZ and ZW resonances in the $\ell\ell qq$ and $\nu\nu qq$ final states in pp collisions at $\sqrt{s} = 13$ TeV with the ATLAS detector[J/OL]. JHEP, 2017, 03 (CERN-EP-2017-146):009. 52 p. https://cds.cern.ch/record/2281501. DOI: 10.1007/JHEP03 (2018)009.

[91] Alwall J, et al. The automated computation of tree-level and next-to-leading order differential cross sections, and their matching to parton shower simulations[J/OL]. JHEP, 2014, 07:079. DOI: 10.1007/JHEP07(2014)079.

[92] Sjöstrand T, et al. An Introduction to PYTHIA 8.2[J/OL]. Comput. Phys. Commun., 2015, 191: 159-177. DOI: 10.1016/j.cpc.2015.01.024.

[93] Alwall J, et al. Comparative study of various algorithms for the merging of parton showers and matrix elements in hadronic collisions[J/OL]. Eur. Phys. J., 2008, C53:473. DOI: 10.1140/ep jc/s10052-007-0490-5.

[94] Alloul A, et al. FeynRules 2.0 - A complete toolbox for tree-level phenomenology[J/OL]. Comput. Phys. Commun., 2014, 185:2250. DOI: 10.1016/j.cpc.2014.04.012.

[95] de Favereau J, et al. DELPHES 3, A modular framework for fast simulation of a generic collider experiment[J/OL]. JHEP, 2014, 02:057. DOI: 10.1007/JHEP02(2014)057.

[96] Cacciari M, Salam G P, Soyez G. FastJet user manual[J/OL]. Eur. Phys. J., 2012, C72:1896. DOI: 10.1140/epjc/s10052-012-1896-2.

[97] Aad G, et al. A search for heavy Higgs bosons decaying into vector bosons in same-sign two-lepton final states in pp collisions at $\sqrt{s} = 13$~TeV with the ATLAS detector[R/OL]. 2022. https://cds.cern.ch/record/2809720.

[98] Aad G, et al. Search for type-III seesaw heavy leptons in dilepton final states in pp collisions at $\sqrt{s} = 13$ TeV with the ATLAS detector[J/OL]. Eur. Phys. J. C, 2021, 81(3):218. DOI: 10.1140/epjc/s10052-021-08929-9.

[99] Evidence for $t\bar{t}t\bar{t}$ production in the multilepton final state in proton-proton collisions at $\sqrt{s} = 13$ TeV with the ATLAS detector[J]. 2020.

[100] Aad G, et al. Search for squarks and gluinos in final states with same-sign leptons and jets using 139 fb^{-1} of data collected with the ATLAS detector[J/OL]. JHEP, 2020, 06:046. DOI: 10.1007/JHEP06(2020)046.

[101] Aaboud M, et al. Observation of electroweak production of a same-sign W boson pair in association with two jets in pp collisions at $\sqrt{s} = 13$ TeV with the ATLAS detector[J/OL]. Phys. Rev. Lett., 2019, 123(16):161801. DOI: 10.1103/PhysRevLett.123.161801.

[102] Aad G, et al. Observation of WWW production in pp collisions at $\sqrts = 13 TeV with the ATLAS detector[J]. 2022.

[103] Artoisenet P, Frederix R, Mattelaer O, et al. Automatic spin-entangled decays of heavy resonances in Monte Carlo simulations[J/OL]. JHEP, 2013, 03:015. DOI: 10.1007/JHEP03(2013)015.

[104] Maltoni F, Mawatari K, Zaro M. Higgs characterisation via vector-boson fusion and associated production: NLO and parton-shower effects[J/OL]. Eur. Phys. J. C, 2014, 74(1):2710. DOI: 10.1140/epjc/s10052-013-2710-5.

[105] ATLAS Collaboration. Performance of pile-up mitigation techniques for jets in pp collisions at $\sqrt{s} = 8$ TeV using the ATLAS detector[J/OL]. Eur. Phys. J. C, 2016, 76:581. DOI: 10.1140/epjc/s10052-016-4395-z.

[106] ATLAS Collaboration. Electron and photon performance measurements with the ATLAS detector using the 2015–2017 LHC proton–proton collision data[J/OL]. JINST, 2019, 14:P12006. DOI: 10.1088/1748-0221/14/12/P12006.

[107] Aaboud M, et al. Observation of electroweak production of a same-sign W boson pair in association with two jets in pp collisions at $\sqrt{s} = 13$ TeV with the ATLAS detector[J/OL]. Phys. Rev. Lett., 2019, 123(16):161801. DOI: 10.1103/PhysRevLett.123.161801.

[108] ATLAS Collaboration. Luminosity determination in pp collisions at $\sqrt{s} = 13$ TeV using the ATLAS detector at the LHC[M/OL]. 2019. https://cds.cern.ch/record/2677054.

[109] Buttinger W. Using Event Weights to account for differences in Instantaneous Luminosity and Trigger Prescale in Monte Carlo and Data[R/OL]. Geneva: CERN, 2015. https://cds.cern.ch/record/2014726.

[110] Aad G, Abbott B, Abbott D C, et al. Observation of the associated production of a top quark and a z boson in pp collisions at $\sqrt{s} = 13$ tev with the atlas detector[J/OL]. Journal of High Energy Physics, 2020, 2020(7). http://dx.doi.org/10.1007/JHEP07(2020)124. DOI: 10.1007/jhep07(2020)124.

[111] Aaboud M, et al. Measurement of the $t\bar{t}Z$ and $t\bar{t}W$ cross sections in proton-proton collisions at $\sqrt{s} = 13$ TeV with the ATLAS detector[J/OL]. Phys. Rev. D, 2019, 99(7):072009. DOI: 10.1103/PhysRevD.99.072009.

[112] Aad G, et al. Evidence for the production of three massive vector bosons with the ATLAS detector[J/OL]. Phys. Lett. B, 2019, 798:134913. DOI: 10.1016/j.physletb.2019.134913.

[113] de Florian D, et al. Handbook of LHC Higgs Cross Sections: 4. Deciphering the Nature of the Higgs Sector[J/OL]. 2016, 2/2017. DOI: 10.23731/CYRM-2017-002.

[114] Baak, M. and Besjes, G. J. and Côté, D. and Koutsman, A. and Lorenz, J. and Short, D. HistFitter software framework for statistical data analysis[J/OL]. Eur. Phys. J. C, 2015, 75:153. DOI: 10.1140/epjc/s10052-015-3327-7.

[115] Barlow R J, Beeston C. Fitting using finite Monte Carlo samples[J/OL]. Comput. Phys. Commun., 1993, 77:219-228. DOI: 10.1016/0010-4655(93)90005-W.

APPENDIX A DISTRIBUTIONS IN FIT REGIONS

A.1 Di-J/ψ channel

Figure A.1 shows the constrained 4μ mass distribution without ΔR cuts, and Figure A.2 shows the mass distributions with different $p_{\mathrm{T}}^{\mathrm{di}-J/\psi}$ cuts.

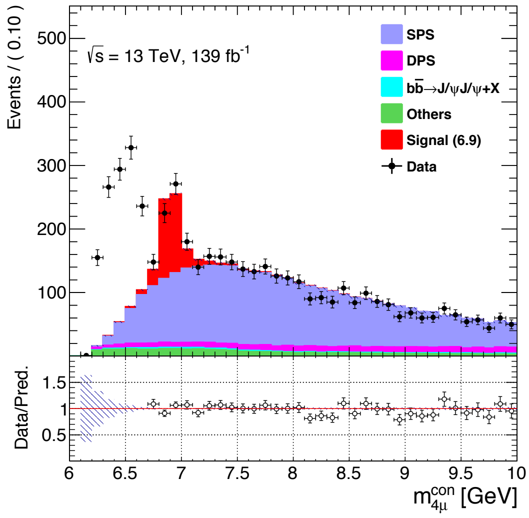

Figure A.1 The constrained 4μ mass spectra without $\Delta R(J/\psi, J/\psi)$ cut. The TQ signal has been scaled to match data around 6.9 GeV.

In the 6.7 GeV< $m_{4\mu}^{\mathrm{con}}$ < 7.1 GeV region, the data is compared with the signal plus background prediction. Similar to SPS, a large discrepancy in $p_{\mathrm{T}}^{\mathrm{di}-J/\psi}$ distribution is observed, as shown in Figure A.3. Figure A.4-A.5 show the other kinematic distributions after the correction. Good agreements between data and total prediction are seen in all the other variables after the signal correction on $p_{\mathrm{T}}(\mathrm{di}-J/\psi)$. Figure A.6-A.7 show similar kinematic distributions in the $m_{4\mu}^{\mathrm{con}} < 7.1$ GeV region.

A.2 J/ψ + $\psi(2S)$ channel

Figure A.8 shows the constrained 4μ mass without ΔR cut. Figure A.9-A.10 show some kinematic distributions in the $m_{4\mu}^{\mathrm{con}} < 7$ GeV region.

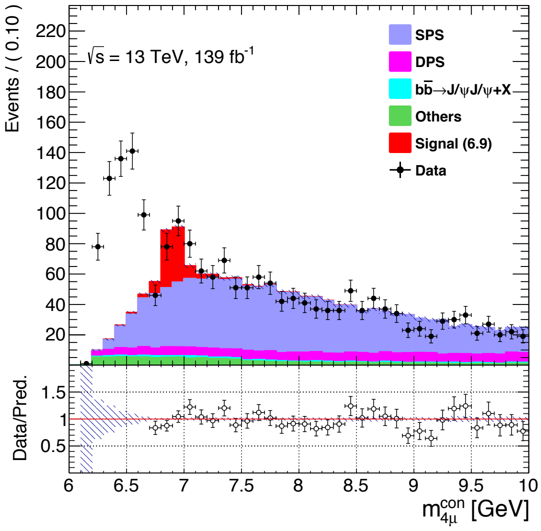

(a) Constrained 4μ mass with $p_{\mathrm{T}}^{\mathrm{di}-J/\psi} < 25$ GeV

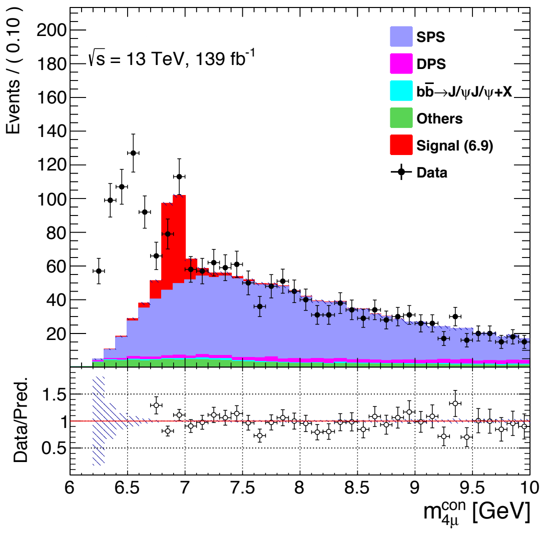

(b) Constrained 4μ mass with 25 GeV$\leq p_{\mathrm{T}}^{\mathrm{di}-J/\psi} <$ 35 GeV

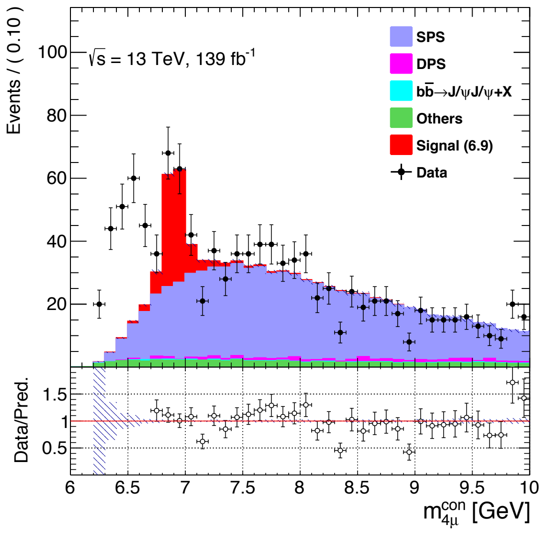

(c) Constrained 4μ mass with $p_{\mathrm{T}}^{\mathrm{di}-J/\psi} \geq 35$ GeV

Figure A.2 The constrained 4μ mass spectra with different $p_{\mathrm{T}}^{\mathrm{di}-J/\psi}$ cuts. The TQ signal has been scaled to match data around 6.9 GeV.

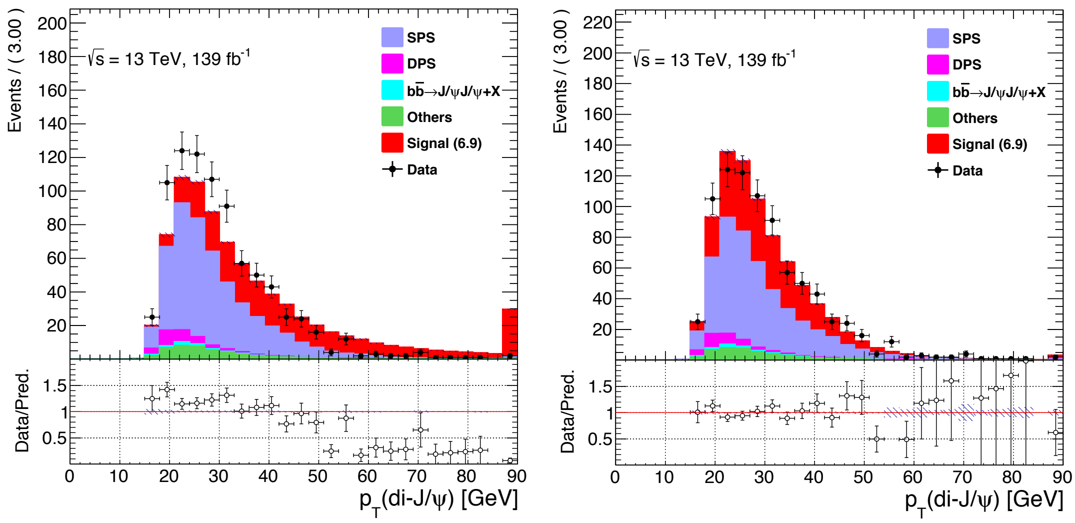

Figure A.3 The distributions of $p_{\mathrm{T}}^{\mathrm{di}-J/\psi}$ before (left) and after (right) the correction functions are applied on the 6.9 GeV TQ signal MC in the 6.7 GeV< $m_{4\mu}^{\mathrm{con}}$ < 7.1 GeV mass window in the di-J/ψ channel. The first and last bins in each plot are the underflow and overflow bins.

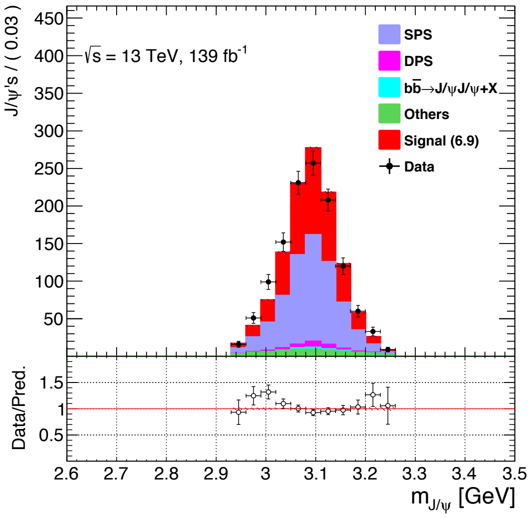

(a) J/ψ candidate mass

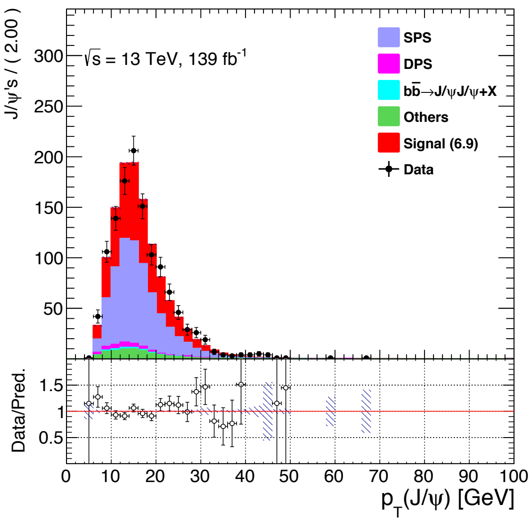

(b) J/ψ candidate p_{T}

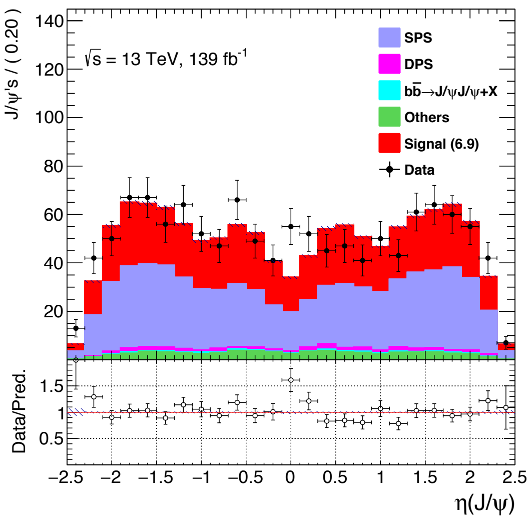

(c) J/ψ candidate η

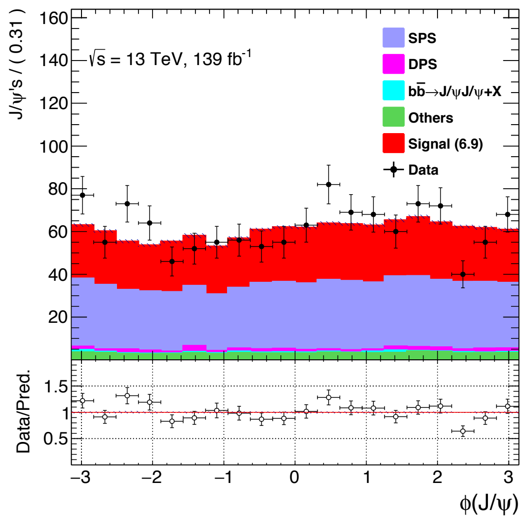

(d) J/ψ candidate ϕ

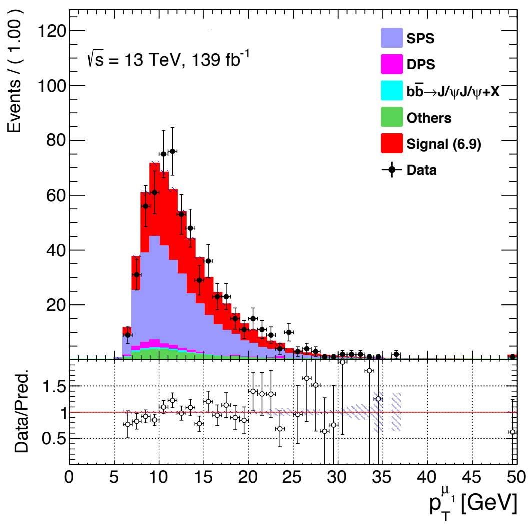

(e) Leading muon p_{T}

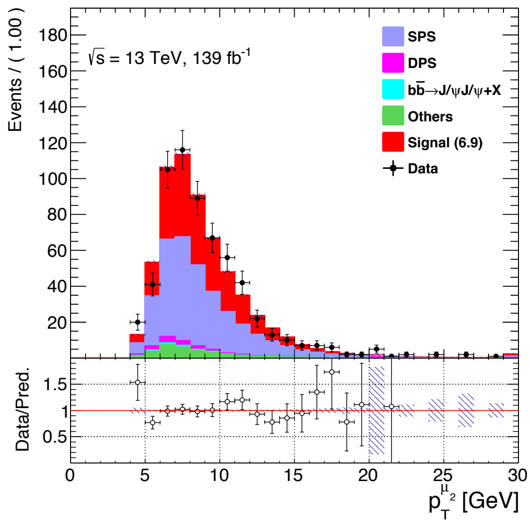

(f) Subleading muon p_{T}

Figure A.4 The kinematic distributions in the 6.7 GeV$< m_{4\mu}^{\mathrm{con}} <$ 7.1 GeV and $\Delta R(J/\psi, J/\psi) <$ 0.25 region after the signal $p_{\mathrm{T}}^{\mathrm{di}-J/\psi}$ correction in the di-J/ψ channel. The lower panel of each plot shows the ratio between data and total prediction. The bars and shaded areas represent statistical errors of data and prediction in each bin, respectively.

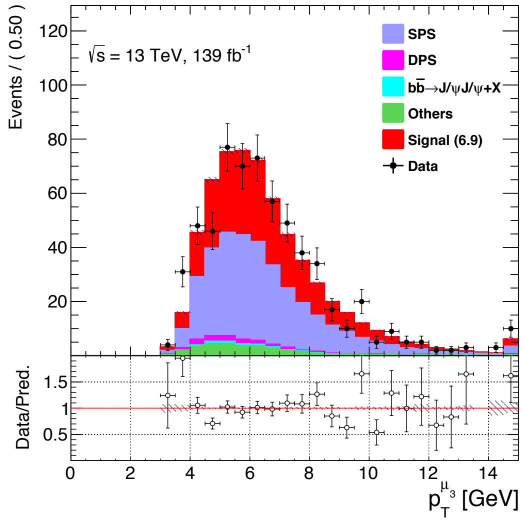

(a) 3rd muon p_{T}

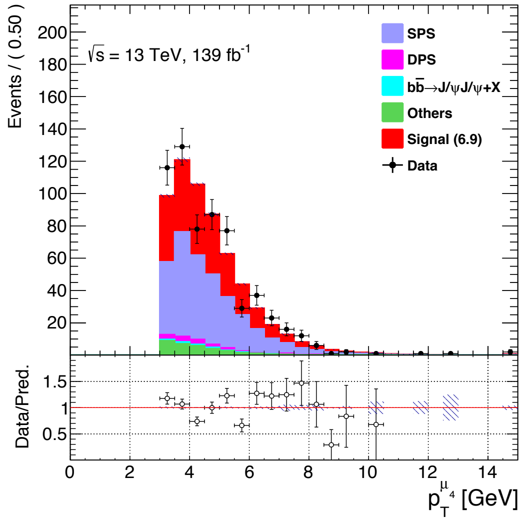

(b) 4th muon p_{T}

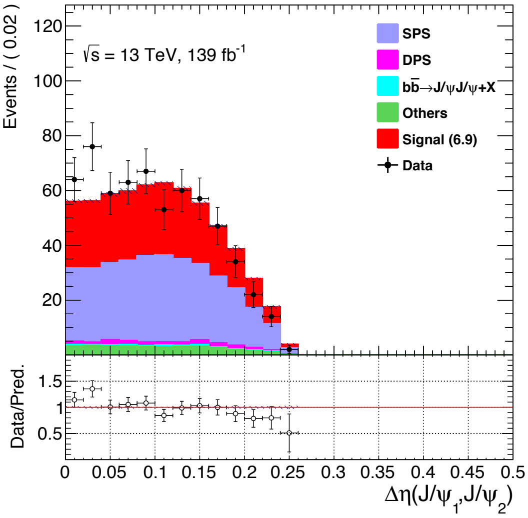

(c) $\Delta\eta$ between two J/ψ's

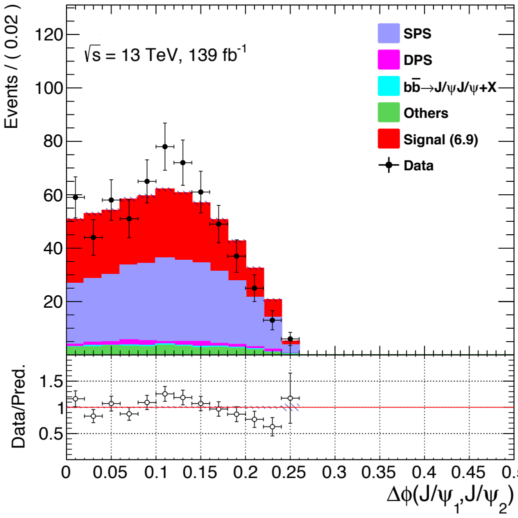

(d) $\Delta\phi$ between two J/ψ's

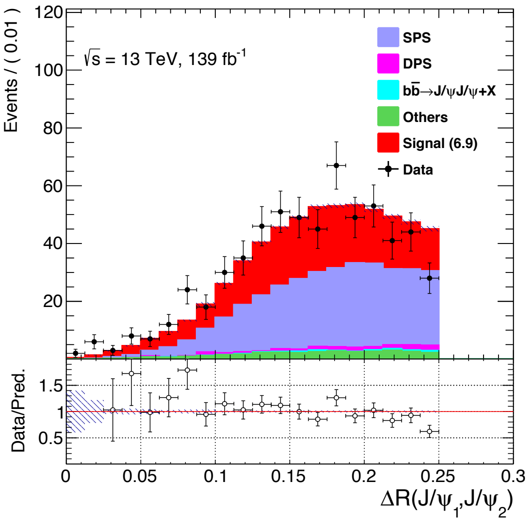

(e) ΔR between two J/ψ's

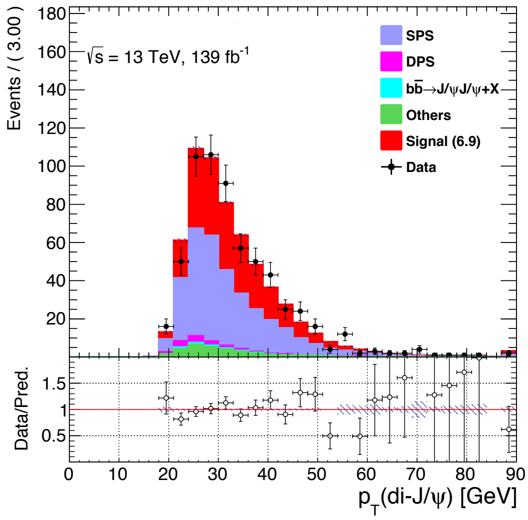

(f) $p_{\mathrm{T}}^{\mathrm{di}-J/\psi}$ of two J/ψ's system

Figure A.5 The kinematic distributions in the 6.7 GeV$< m_{4\mu}^{\mathrm{con}} <$ 7.1 GeV and $\Delta R(J/\psi, J/\psi) <$ 0.25 region after the signal $p_{\mathrm{T}}^{\mathrm{di}-J/\psi}$ correction in the di-J/ψ channel. The lower panel of each plot shows the ratio between data and total prediction. The bars and shaded areas represent statistical errors of data and prediction in each bin, respectively.

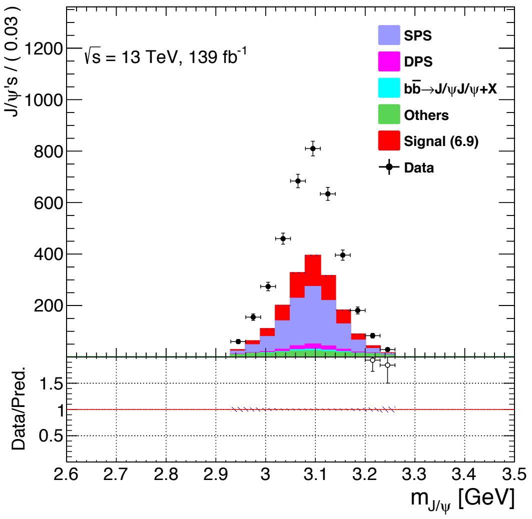

(a) J/ψ candidate mass

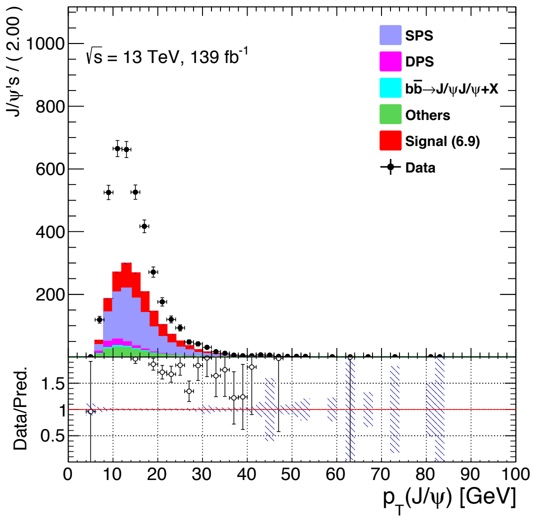

(b) J/ψ candidate p_{T}

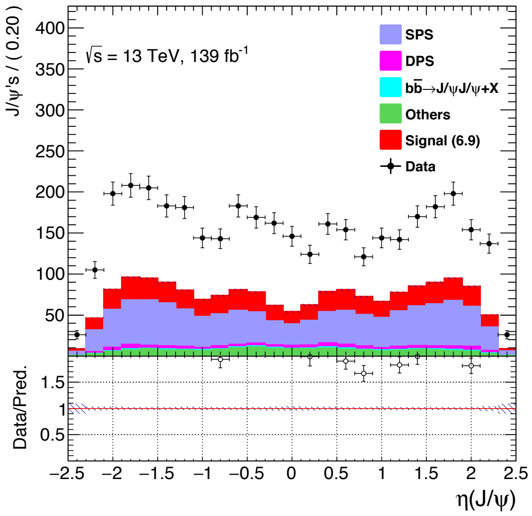

(c) J/ψ candidate η

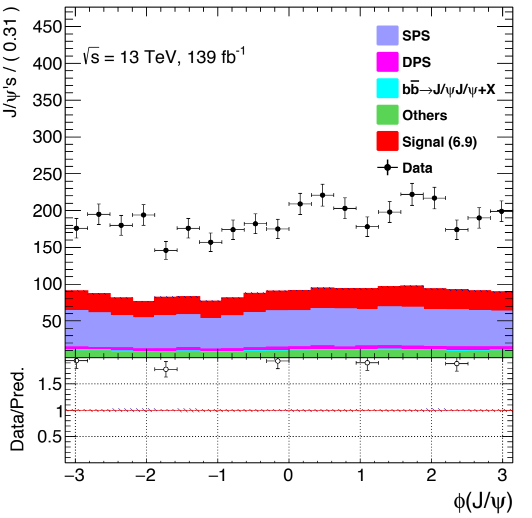

(d) J/ψ candidate ϕ

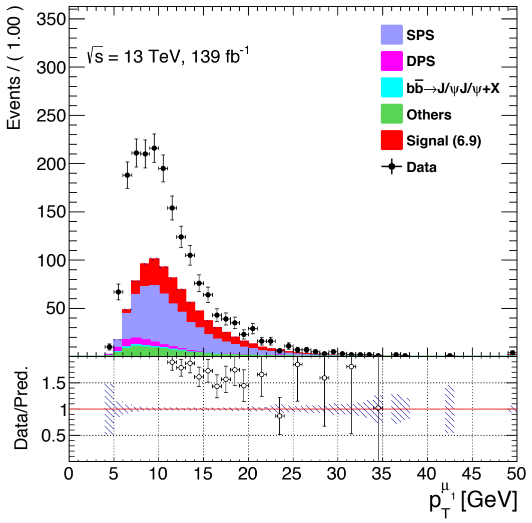

(e) Leading muon p_{T}

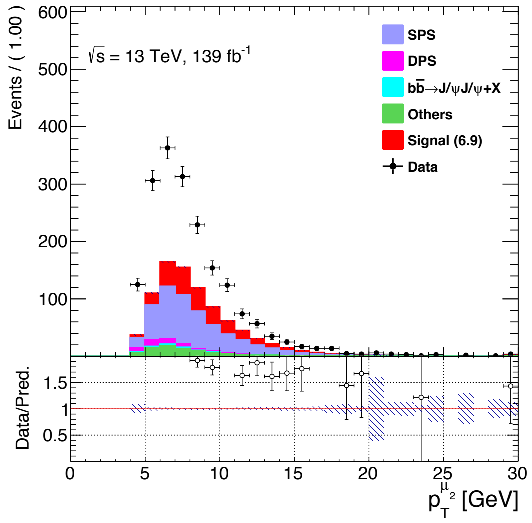

(f) Subleading muon p_{T}

Figure A.6 The kinematic distributions in the region of $m_{4\mu}^{\mathrm{con}} < 7.1$ GeV and $\Delta R(J/\psi, J/\psi) < 0.25$ after the signal $p_{\mathrm{T}}^{\mathrm{di}-J/\psi}$ correction in the di-J/ψ channel. The lower panel of each plot shows the ratio between data and total prediction. The bars and shaded areas represent statistical errors of data and prediction in each bin, respectively.

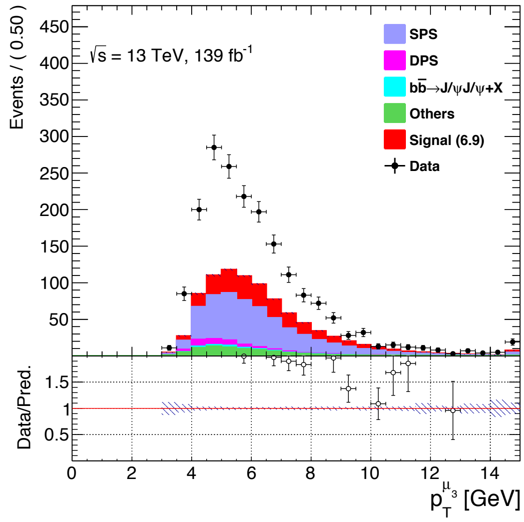

(a) 3rd muon p_{T}

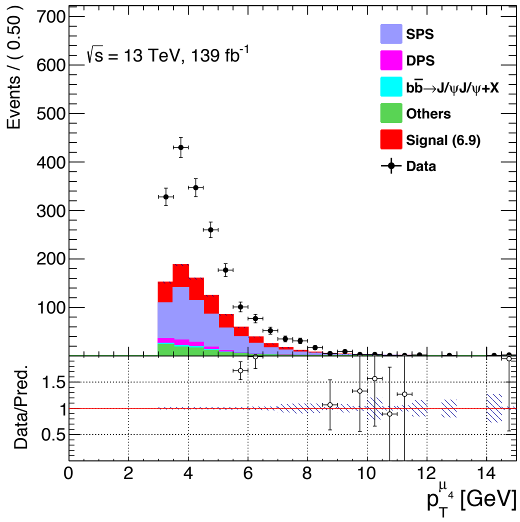

(b) 4th muon p_{T}

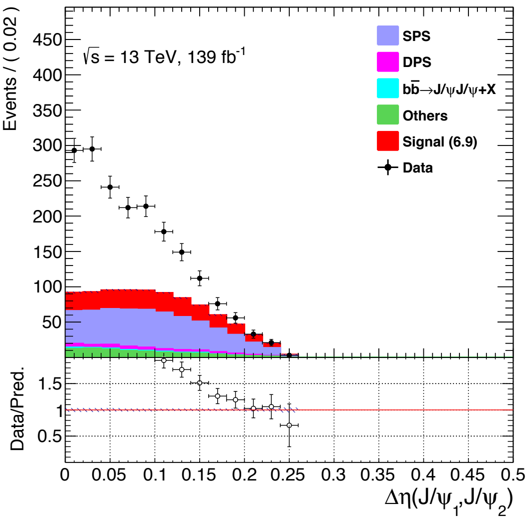

(c) $\Delta\eta$ between two J/ψ's

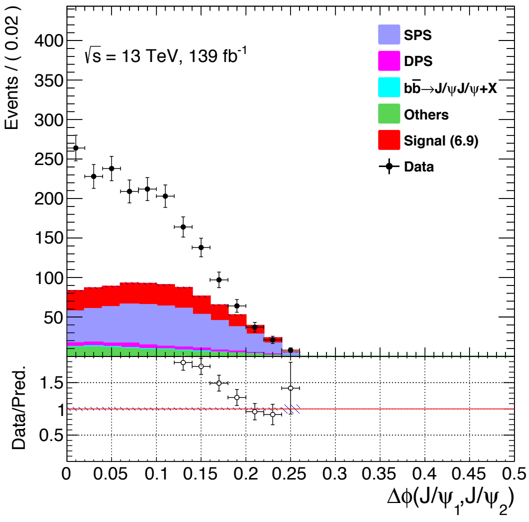

(d) $\Delta\phi$ between two J/ψ's

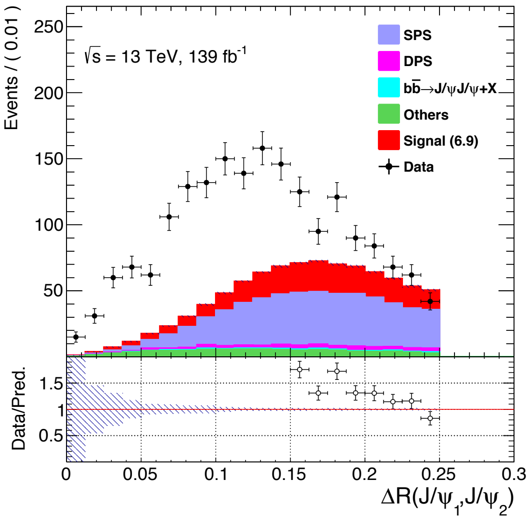

(e) ΔR between two J/ψ's

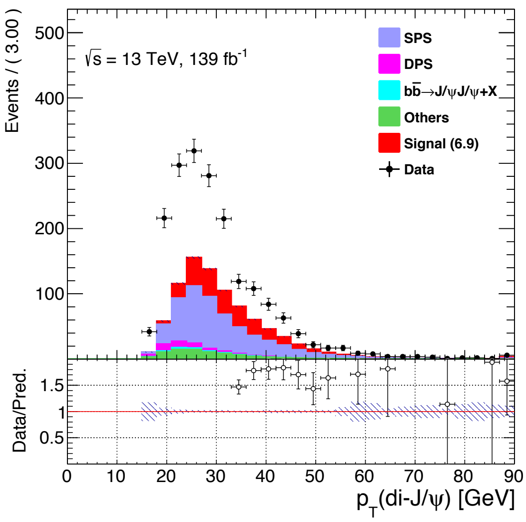

(f) $p_{\mathrm{T}}^{\mathrm{di}-J/\psi}$ of two J/ψ's system

Figure A.7 The kinematic distributions in the region of $m_{4\mu}^{\mathrm{con}} < 7.1$ GeV and $\Delta R(J/\psi, J/\psi) < 0.25$ after the signal $p_{\mathrm{T}}^{\mathrm{di}-J/\psi}$ correction in the di-J/ψ channel. The lower panel of each plot shows the ratio between data and total prediction. The bars and shaded areas represent statistical errors of data and prediction in each bin, respectively.

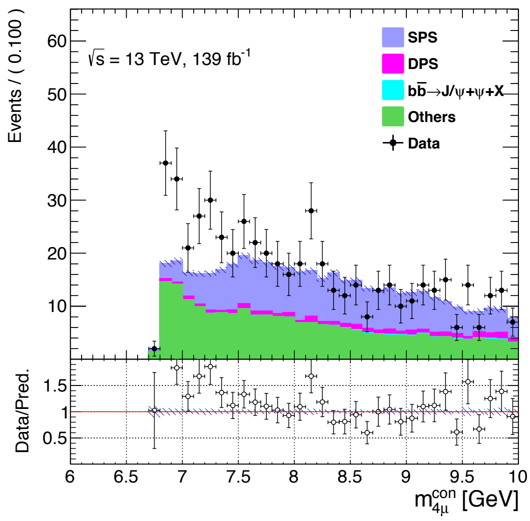

Figure A.8 The constrained 4μ mass spectra without $\Delta R(J/\psi, \psi)$ cut.

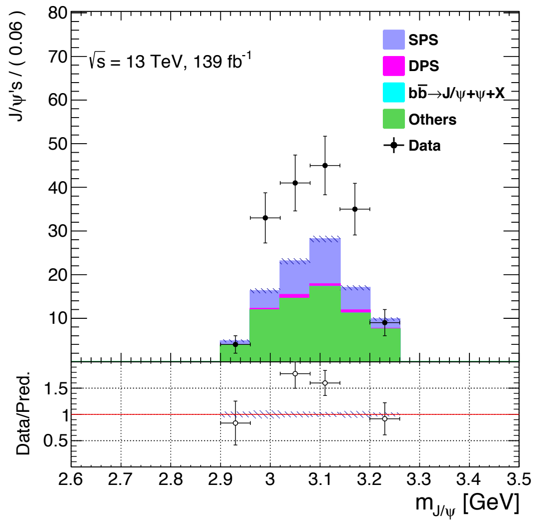

(a) J/ψ candidate mass

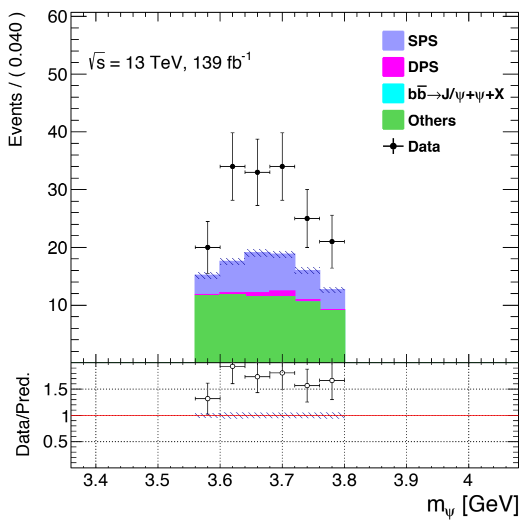

(b) J/ψ candidate p_{T}

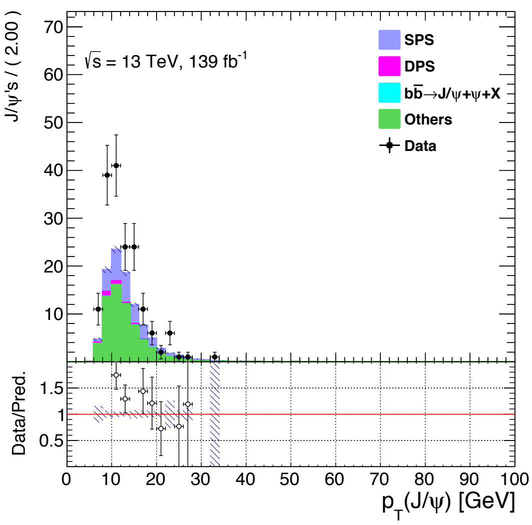

(c) J/ψ candidate η

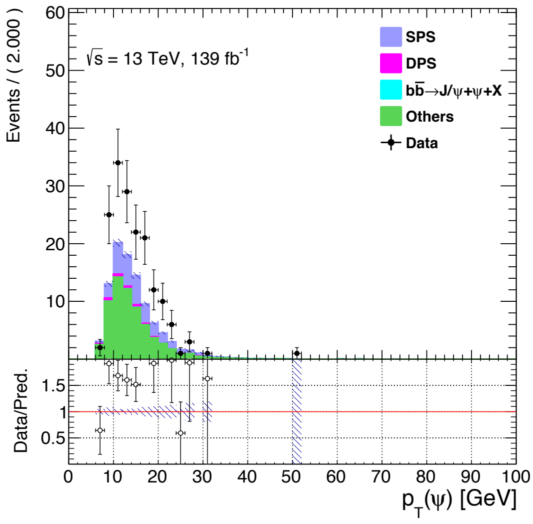

(d) J/ψ candidate ϕ

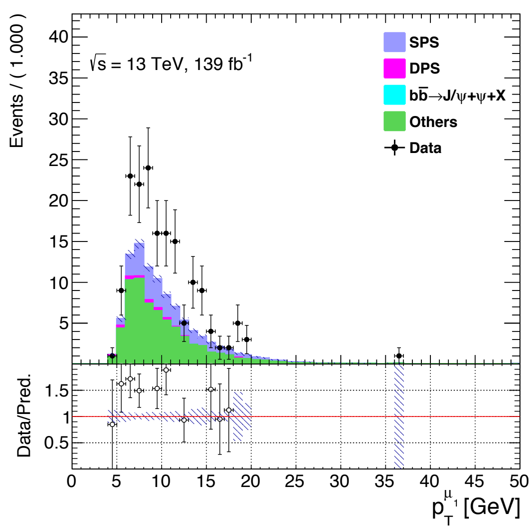

(e) Leading muon p_{T}

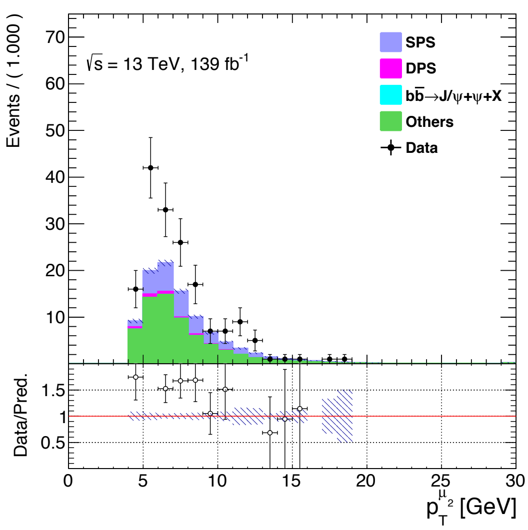

(f) Subleading muon p_{T}

Figure A.9 The kinematic distributions in the region of $m_{4\mu}^{\mathrm{con}} < 7.4$ GeV and $\Delta R(J/\psi, J/\psi) < 0.25$ in the J/ψ+$\psi(2S)$ channel. The lower panel of each plot shows the ratio between data and total prediction. The bars and shaded areas represent statistical errors of data and prediction in each bin, respectively.

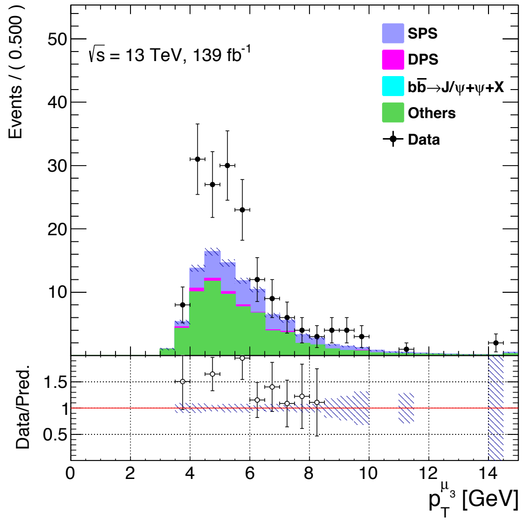

(a) 3rd muon p_{T}

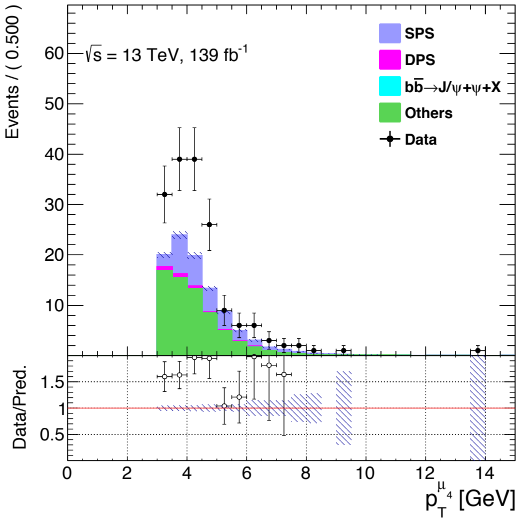

(b) 4th muon p_{T}

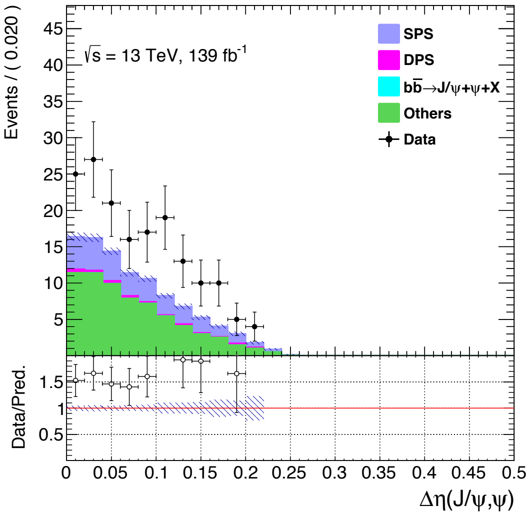

(c) $\Delta\eta$ between J/ψ and $\psi(2S)$

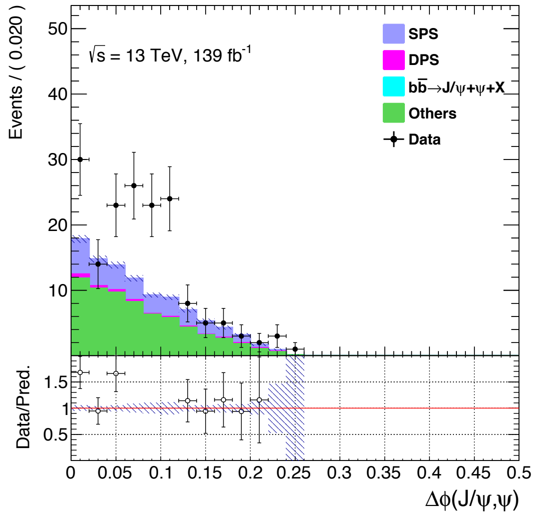

(d) $\Delta\phi$ between J/ψ and $\psi(2S)$

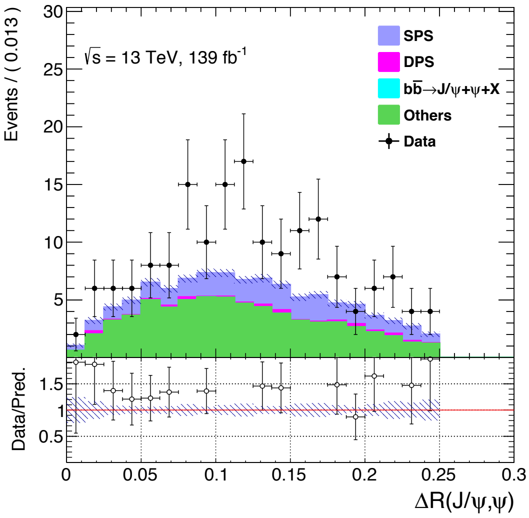

(e) ΔR between J/ψ and $\psi(2S)$

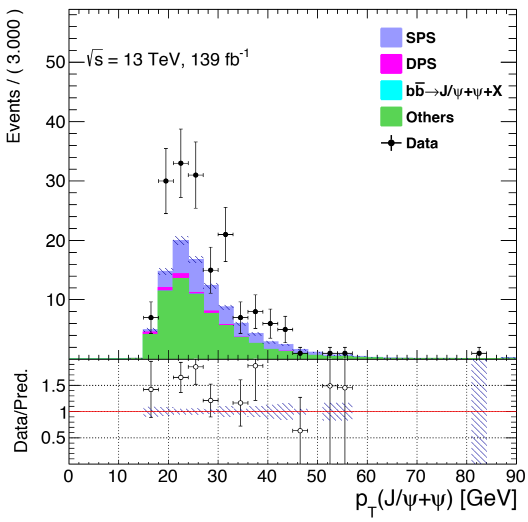

(f) $p_{\mathrm{T}}^{\mathrm{di-}J/\psi}$ of J/ψ+$\psi(2S)$ system

Figure A.10 The kinematic distributions in the region of $m_{4\mu}^{\mathrm{con}} < 7.4$ GeV and $\Delta R(J/\psi, J/\psi) < 0.25$ in the J/ψ+$\psi(2S)$ channel. The lower panel of each plot shows the ratio between data and total prediction. The bars and shaded areas represent statistical errors of data and prediction in each bin, respectively.

APPENDIX B FIT WITH TWO INTERFERING RESONANCES

A fit model of two interfering peaks is also tried, whose result is shown in Figure B.1. To compare the fit quality with the 3-peak fit in Figure 6.30(a)(b), a quantity χ^2/N is calculated, where $N = N_{\rm hist} + N_{\rm cons} - N_{\rm free}$ ($N_{\rm hist}$ is the total number of histogram bins in the signal and control regions, $N_{\rm cons}$ is the number of NP constraints, each of which is deemed as a subsidiary measurement, and $N_{\rm free}$ is the number of freely floating parameters), and χ^2 is defined as

$$\chi^2 = \chi^2_{\rm hist} + \sum_i \frac{\alpha_i^2}{\sigma_i^2}, \tag{B.1}$$

where α_i and σ_i are the fitted value and error of the i'th NP. This quantity is 2.17 (1.24) for the 2-peak (3-peak) fit. Therefore, the 3-peak model is preferred.

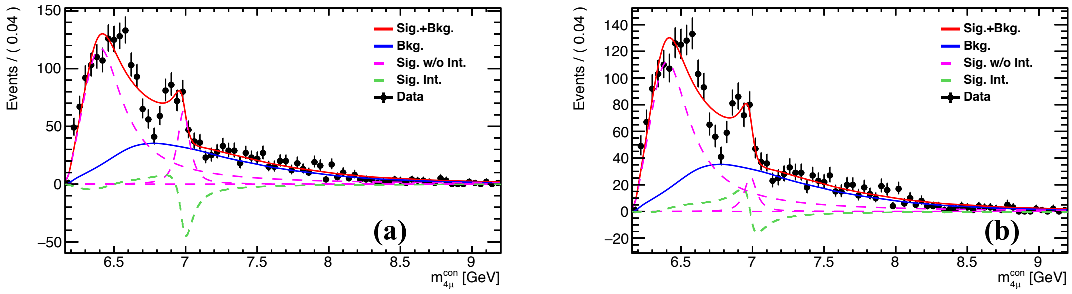

Figure B.1 The fitted mass spectra in the SR (a-b, corresponding to two degenerate solutions) in the di-J/ψ channel (2-peak signal model). The purple (green) dashed lines represent the components of individual resonances (interference between the two peaks).

APPENDIX C SIGNAL INJECTION TEST

In the analysis of heavy Higgs bosons, the signal injection test is performed to test the linearity of extracted signal strength and injected signal strength.

The linearity test is done as follows with all the systematics included:

- Randomly generate the pseudo data according to fit model for a certain signal strength μ_{Sig}, so called *signal injection*
- In signal regions, the M_{eff} distribution is sampled according to the background+signal pdf while the M_{eff} distribution is sampled according to the background pdf in control regions. The total generated events is determined by sampling from the Gaussian distribution, where the mean of the Gaussian is equal to the predicted number of events from MC and the width of the Gaussian is equal to the predicted number of events from MC times 0.05.
- Fit the pseudo data and extract the signal strength.
- Repeat above three steps with different random seeds. The process is called toy experiment method, and the number of repeat times is called number of toys
- Ideally, the mean of extracted signal strength from many toys will be about the value of injected signal strength, while the standard deviation of the extracted signal strength distribution gives the statistical uncertainty on extracted signal strength for the given signal strength.

In this analysis, 100 toys are performed for each injected μ_{Sig} (μ_{Sig} = 0.5, μ_{Sig} = 1.0, μ_{Sig} = 1.5, μ_{Sig} = 2.0 and μ_{Sig} = 3.0) and each test signal point (GHH300fW0fWW4600, GHH300fW0fWW6200, GHH420fW0fWW6200, GHH600fW0fWW6200).

Figure C.1 - C.4 show the distributions of extracted μ_{Sig} with a given injected μ_{Sig}. As expected, the extracted μ_{Sig} is around the injected value.

Figure C.5 shows the extracted μ_{Sig} as a function of injected μ_{Sig}. Extracted μ_{Sig} is linearly proportional to injected μ_{Sig}. The fit model used in this analysis performs well in the fit and does not introduce significant bias during fit.

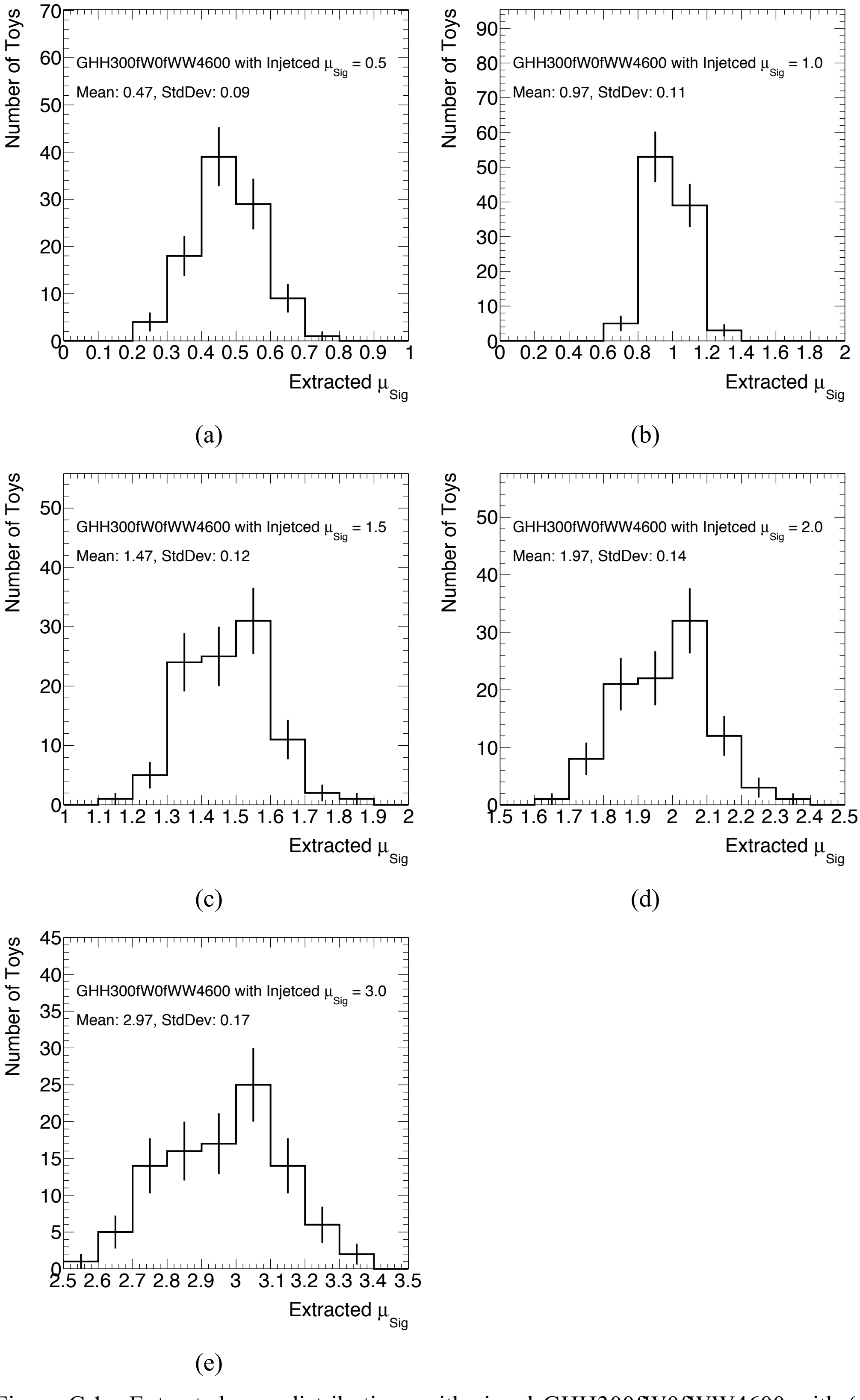

Figure C.1 Extracted μ_{Sig} distributions with signal GHH300fW0fWW4600 with (a) injected $\mu_{Sig} = 0.5$, (b) injected $\mu_{Sig} = 1.0$, (c) injected $\mu_{Sig} = 1.5$, (d) injected $\mu_{Sig} = 2.0$ and (e) injected $\mu_{Sig} = 3.0$.

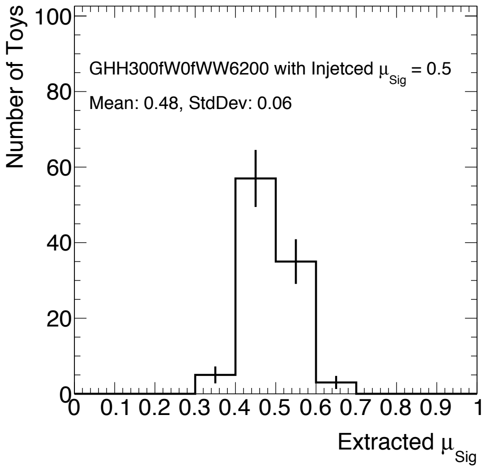

(a)

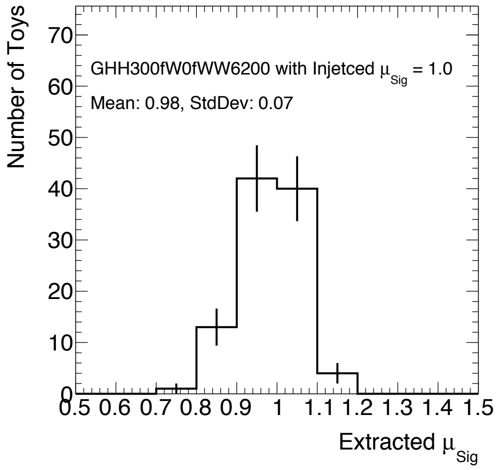

(b)

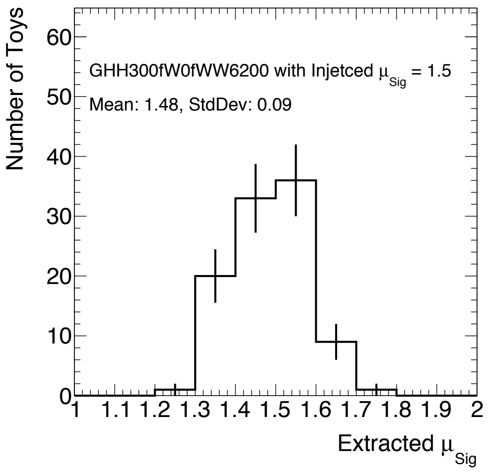

(c)

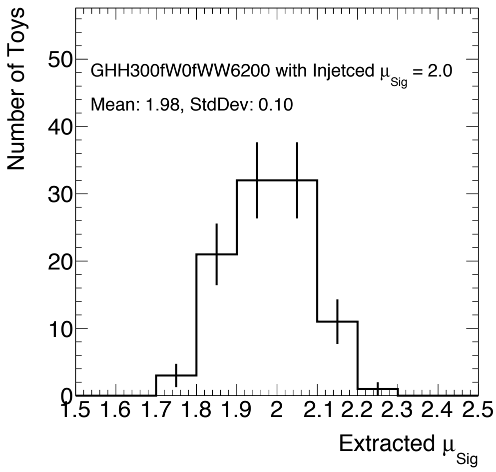

(d)

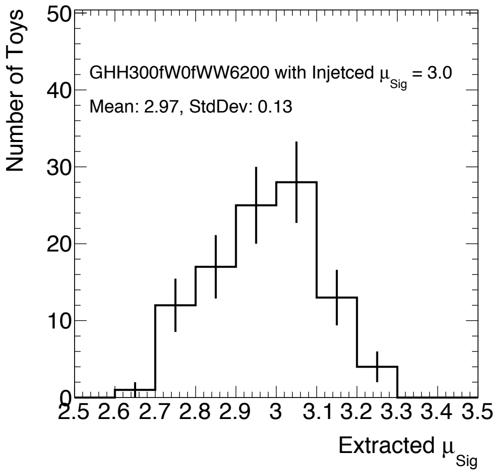

(e)

Figure C.2 Extracted μ_{Sig} distributions with signal GHH300fW0fWW6200 with (a) injected $\mu_{Sig} = 0.5$, (b) injected $\mu_{Sig} = 1.0$, (c) injected $\mu_{Sig} = 1.5$, (d) injected $\mu_{Sig} = 2.0$ and (e) injected $\mu_{Sig} = 3.0$.

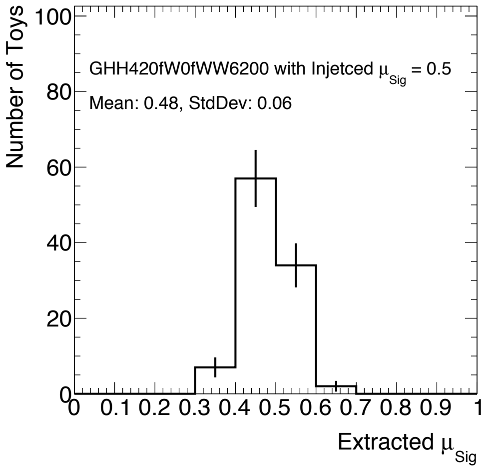

(a)

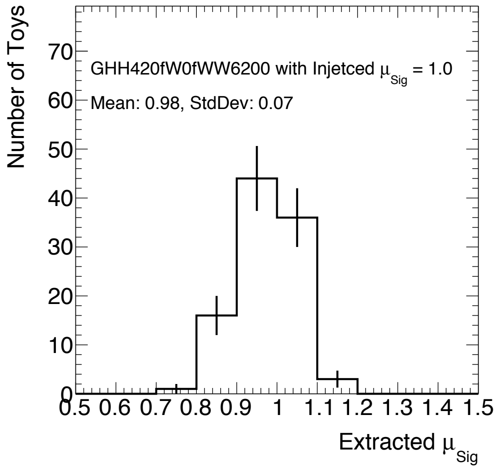

(b)

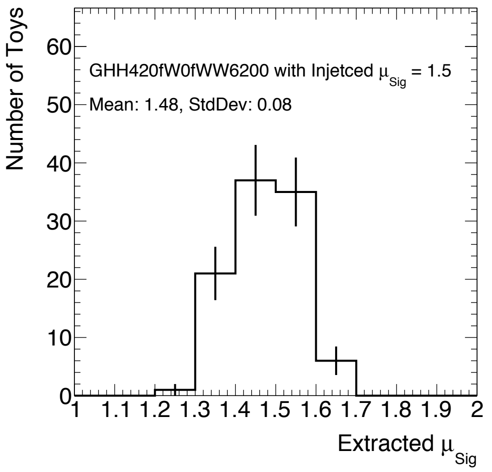

(c)

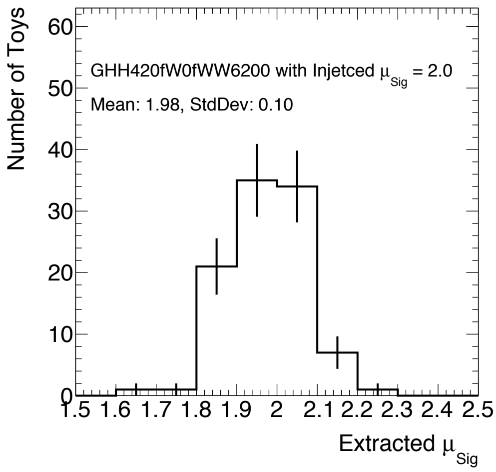

(d)

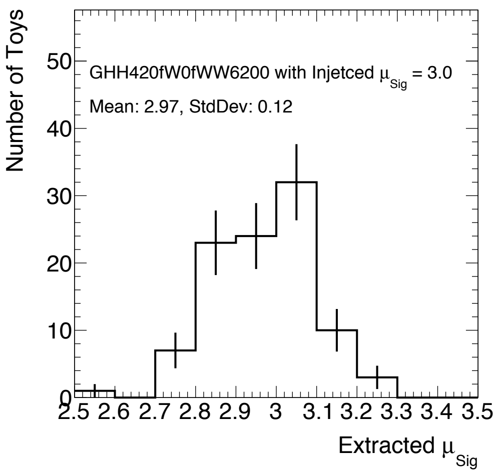

(e)

Figure C.3 Extracted μ_{Sig} distributions with signal GHH420fW0fWW6200 with (a) injected $\mu_{Sig} = 0.5$, (b) injected $\mu_{Sig} = 1.0$, (c) injected $\mu_{Sig} = 1.5$, (d) injected $\mu_{Sig} = 2.0$ and (e) injected $\mu_{Sig} = 3.0$.

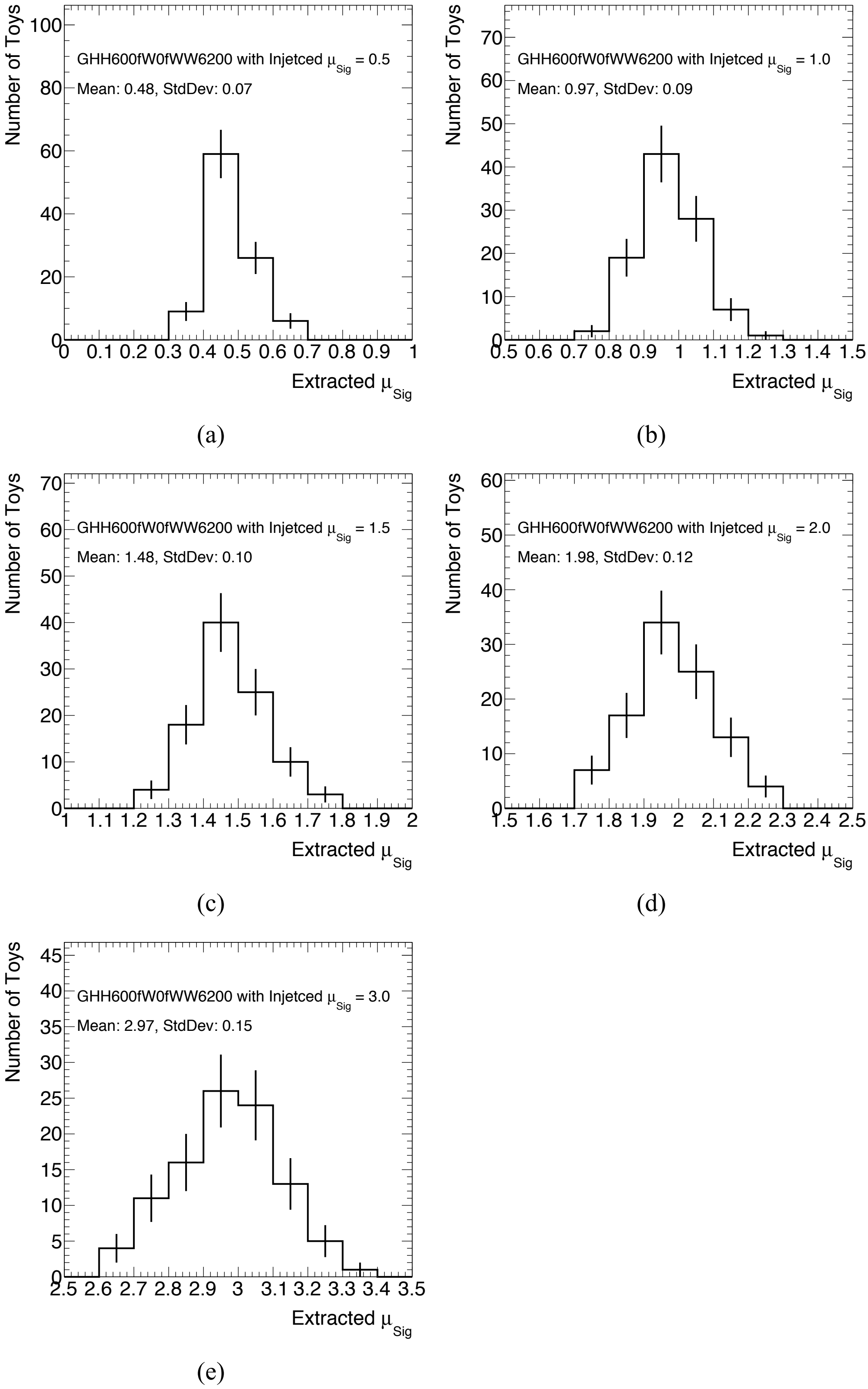

Figure C.4 Extracted μ_{Sig} distributions with signal GHH60fW0fWW6200 with (a) injected μ_{Sig} = 0.5, (b) injected μ_{Sig} = 1.0, (c) injected μ_{Sig} = 1.5, (d) injected μ_{Sig} = 2.0 and (e) injected $\mu_{Sig} = 3.0$.

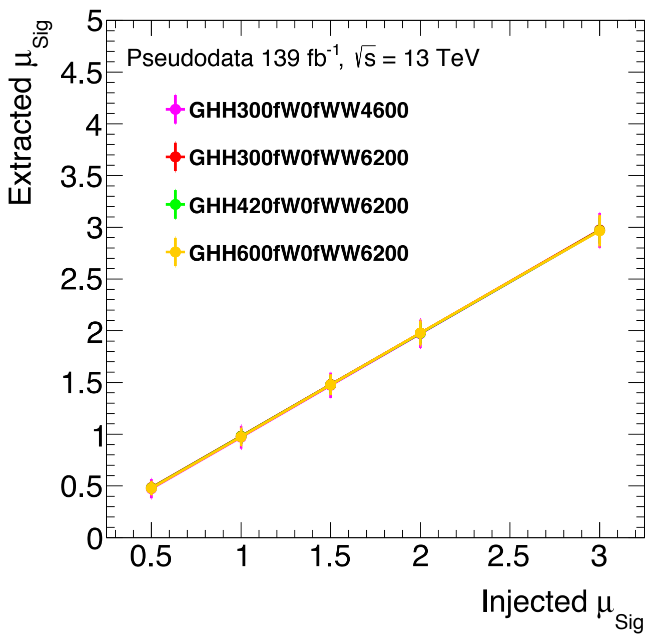

Figure C.5 Extracted μ_{Sig} vs. injected μ_{Sig} for signal GHH300fW0fWW4600, GHH300fW0fWW6200, GHH420fW0fWW6200 and GHH600fW0fWW6200.